

**FROM LABORATORY SCALE PROCESSING TO CONTINUOUS
PROCESSING OF CELLULOSE NANOFIBRIL (CNF) SHEETS FOR
STRUCTURAL AND PACKAGING APPLICATIONS**

by

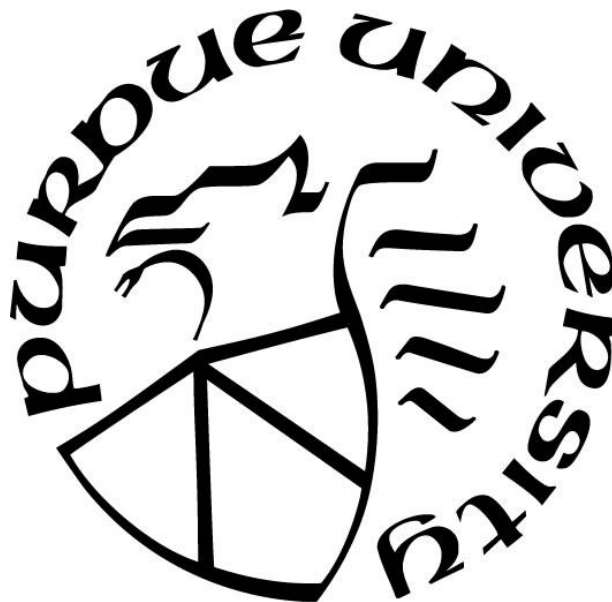
Sami M. El Awad Azrak

A Dissertation

Submitted to the Faculty of Purdue University

In Partial Fulfillment of the Requirements for the degree of

Doctor of Philosophy



School of Materials Engineering

West Lafayette, Indiana

May 2021

THE PURDUE UNIVERSITY GRADUATE SCHOOL
STATEMENT OF COMMITTEE APPROVAL

Dr. Jeffrey P. Youngblood, Chair

School of Materials Engineering

Dr. Robert J. Moon

Forest Products Laboratory

Dr. Chelsea S. Davis

School of Materials Engineering

Dr. John A. Howarter

School of Materials Engineering

Approved by:

Dr. David F. Bahr

This work is dedicated to my family and friends.
Le dedico esta tesis a mi familia y amigos, gracias por su apoyo todos estos años.

ACKNOWLEDGMENTS

I would like to thank my graduate research advisor, Prof. Jeffrey Youngblood. His open door policy and friendly attitude always gave me a window to voice my ideas and obtain valuable research and life advice. His broad knowledge, constructive criticism, and ample recommendations allowed me to continuously improve myself and critically steer my research into the right direction to answer the challenging scientific questions at hand. I would also like to thank my external research advisors and collaborators Dr. Robert Moon and Dr. Gregory Schueneman for their insightful ideas and conversations throughout these years, as well as their attention to detail when reviewing and revising the prepared manuscripts for publication. I would also like to acknowledge the financial support provided by the U.S. Forest Products Laboratory which made the research possible.

I would like to thank the all the staff in the MSE department including Rosemary Son, Lisa Stacey, and Aury Blanco for answering my numerous questions regarding graduate school paperwork and requirements and Vicki Cline for class registration and other enrollment paperwork. Additionally, I would like to thank Timothy VanMeter who was always happy to help all graduate students with any repairs and technical questions. His diligence in solving problems and fixing laboratory instruments allowed the research to continue without major delays.

I would also like to acknowledge my research colleagues. First, I would like to thank Dr. Caitlyn M. Clarkson, Dr. William J. Costakis, and Dr. Andrew Schlup who have been excellent friends and collaborators throughout my time at Purdue. Their help, advice, and fun lab conversations made the, sometimes long, lab hours more enjoyable. I would also like to thank graduate researchers Ana M. Ulloa Gomez, Anthony P. Becerril, Juan C. Verduzco Gastelum, Lysandra Perez, Jose F. Waimin, Maria C. Niño, and Brhayan S. Puentes Rodriguez for being more than friends and colleagues. They made my time at Purdue very memorable and helped me maintain a good work-life balance.

TABLE OF CONTENTS

LIST OF TABLES.....	9
LIST OF FIGURES	10
LIST OF COMMON SYMBOLS & ABBREVIATIONS.....	16
ABSTRACT.....	18
1. INTRODUCTION.....	19
1.1 Cellulose nanomaterials (CNMs) background	19
1.2 Processing of CNF films; current efforts and challenges	22
1.3 Research Objectives and Scope.....	24
2. PROCESSING AND CHARACTERIZATION OF THICK CNF SHEETS	25
2.1 Introduction	25
2.2 Experimental section; Materials, Methods, and Characterization.....	27
2.2.1 Materials.....	27
2.2.2 Preparation of CNF Sheets.....	27
2.2.3 Tensile properties and density of the CNF sheets	30
2.2.4 Scanning electron microscopy (SEM) of the CNF sheets.....	30
2.2.5 Optical profilometry	31
2.2.6 Statistical analysis of the tensile properties and density	31
2.3 Results and discussion	31
2.3.1 Sheet processing time and surface texture analysis.....	31
2.3.2 Cross sectional surface analysis.....	33
2.3.3 Thickness and pressing time effect on the mechanical properties of CNF sheets	35
2.3.4 Loading rate effect on the mechanical properties of CNF sheets	40
2.3.5 Pressing pressure rate effect on the mechanical properties of CNF sheets.....	42
2.3.6 Fracture analysis of CNF sheets	43
2.3.7 Benchmarking the performance of CNF sheets	44
2.4 Conclusion on the processing and performance of thick CNF sheets	45
2.5 Acknowledgements	46
3. CONTINUOUS PROCESSING OF CNF SHEETS.....	47
3.1 Introduction	47

3.2	Experimental section; Materials, Methods, and Characterization.....	49
3.2.1	Materials.....	49
3.2.2	Preparation of CNF/Processing Aid Suspensions for Centrifugation and Zeta Potential	50
3.2.3	Preparation of extrusion pastes	50
3.2.4	Solids content calculation.....	53
3.2.5	Preparation of cast CNF films.....	53
3.2.6	Torque Viscometry of CNF/CMC, CNF/XG, and CNF/aPAM	53
3.2.7	Zeta potential.....	55
3.2.8	Extruder configuration and extrusion parameters.....	55
3.2.9	Sample specimen preparation for mechanical tensile testing	57
3.2.10	Thermogravimetric analysis (TGA).....	58
3.2.11	Scanning electron microscopy (SEM)	58
3.2.12	Statistical analysis of tensile testing data.....	59
3.3	Results and discussion	59
3.3.1	Extrusion of pure CNF and processing aid selection	59
3.3.2	Extrusion of CNF/CMC, CNF/XG, and CNF/aPAM.....	64
3.3.3	Rheological analysis of pure CNF, CNF/CMC, CNF/XG, and CNF/aPAM.....	68
3.3.4	Mechanical and thermogravimetric analysis of CNF/CMC, CNF/XG, and CNF/aPAM sheets	74
3.3.5	Validation of Brabender mixing procedure for the preparation of CNF/CMC pastes	79
3.4	Conclusion	81
3.5	Acknowledgements	82
4.	CONTROLLING THE REDISPERSION AND SETTING BEHAVIOR OF CNF+CMC SYSTEMS.....	83
4.1	Introduction	83
4.2	Experimental section; Materials and Methods	85
4.2.1	Materials.....	85
4.2.2	Preparation of Highly Loaded CNF+CMC Pastes	85
4.2.3	CNF+CMC Filament/Cord Processing	86

4.2.4	Chemical Treatment	86
4.2.5	Pelletization.....	87
4.2.6	Zeta Potential	87
4.2.7	Titration.....	87
4.2.8	Turbidity	87
4.2.9	FTIR-ATR.....	88
4.2.10	Scanning Electron Microscopy (SEM)	88
4.3	Results and Discussion	89
4.3.1	CNF+CMC Bulk Processing and Pelletizing.....	89
4.3.2	CMC Adsorption onto CNF fibrils	91
4.3.3	Dispersibility and Setting Behavior of CNF+CMC	93
4.3.4	FTIR Analysis of Treated CNF+CMC	97
4.3.5	Water Uptake of Treated CNF+CMC	103
4.3.6	Ramifications of efforts.....	103
4.4	Conclusion	103
4.5	Acknowledgements.....	104
5.	PRELIMINARY PROCESSING OF FIBERS REINFORCED CELLULOSE NANOFIBRILS COMPOSITES (FR-CNF).....	105
5.1	Introduction	105
5.2	Experimental section; Materials and Methods	106
5.2.1	Materials.....	106
5.2.2	Processing of FR-CNF Composites.....	107
5.2.3	Mechanical Testing of FR-CNF Composites.....	107
5.3	Results and Discussion	108
5.3.1	FR-CNF Composites, First Impression	108
5.3.2	Alternative Design for Carbon Fiber Reinforced CNF Composites, First Impression and Testing.....	115
5.4	Summary and Future Work	117
6.	SUMMARY AND CONCLUSION.....	120
	APPENDIX A. PROCESSING AND CHARACTERIZATION OF THICK CNF SHEETS.....	123
	APPENDIX B. CONTINUOUS PROCESSING OF CNF SHEETS.....	130

APPENDIX C. CONTROLLED DISPERSION AND SETTING OF CNF+CMC PASTES	137
APPENDIX D. PROCESSING OF FIBER REINFORCED CELLULOSE NANOFIBRILS COMPOSITES (FR-CNF)	146
REFERENCES	147
PUBLICATIONS	165

LIST OF TABLES

Table 2.1 Wet stacking lamination approach compared with two common CNF film processing techniques.....	32
Table 2.2 Mechanical performance of CNF sheets with varying thicknesses. The reported values are averages between all three pressing times. The area under the stress versus strain curve was taken to be the apparent toughness or work-of-failure of the specimen in (MJ/m ³). The superscripts represent statistical similarity between different specimens with 1-layer being case “a” and 8-layer being case “g”.	35
Table 2.3 Comparison table containing the measured mechanical properties of PS, Nylon 6,6, Al 2024, Al 6061, and CNF sheets (4-layer). The units of specific strength, modulus, and toughness are MPa/(g/cm ³), GPa/(g/cm ³), and (MJ/m ³)/(g/cm ³)	45
Table 3.1 Summary table showing all the processed highly loaded extrusion pastes prepared. These pastes were extruded and hot pressed. Enough material for each batch was prepared to perform extrusion and rheological analysis.....	53
Table 3.2 Thickeners, viscosifiers, and gelling agents assessed based on their water-retention ability when incorporated into a CNF slurry. All the selected processing aids are soluble in water at room temperature conditions. Processing aids suspensions which did not experience any perceivable water separation after centrifugation are marked with (*).	61
Table 3.3 Paste concentrations and rheological constants obtained from torque rheometry analysis. A dry weight ratio of 0.1:1 (aid:CNF) was used for all pastes.	69
Table 4.1. Zeta potential and titration of dilute pure CNF and CNF+CMC suspensions. Each suspension was mixed, centrifuged, and resuspended in water 3 times to remove non-adsorbed CMC or other loose species. Eight measurements per sample were carried out for zeta potential analysis while 3 measurements per sample were performed for titration. The average and standard deviation of the samples are displayed. 5 mM NaOH was used for titration.	92
Table 4.2. Peak intensity normalized by the invariant peak intensity at 1024 cm ⁻¹	102

LIST OF FIGURES

Figure 1.1 Transmission electron microscopy (TEM) images of A) CNFs and C) CNCs, and photographs of scintillation vials filled with B) CNFs slurry at 3 wt.% and D) CNCs slurry at 12 wt.%. TEM images courtesy of Youngblood's research group.20

Figure 1.2. Images of solution cast films of A) CNF film next to a standard USA quarter, B) TOCNF film (reprinted with permission from ref. 34, copyright © 2020, Springer Nature B.V.), and C) CNC coating on a polyethylene terephthalate (PET) substrate (image courtesy of Youngblood's research group). The thickness of the CNF and TOCNF films is $\sim 75\ \mu\text{m}$ and $\sim 30\ \mu\text{m}$, respectively.....21

Figure 2.1 Process used to make CNF sheets. The process can be divided into 4 steps: press filtration, rolling, stacking, and hot pressing. Step 1, an CNF slurry at an initial concentration of $\sim 1\ \text{wt.}\%$ is filtered to $\sim 7\ \text{wt.}\%$ in a in house made dewatering frame. Step 2, the consolidated CNF web is press filtered through a slip roller to reach a concentration of $10\ \text{wt.}\%$. Step 3 the CNF layers are separated from the filtering mesh and stacked. Step 4) the layers are hot pressed into a multi-layer CNF sheet.29

Figure 2.2 A) Different thickness CNF sheets prepared using the layer-by-layer wet stacking technique described in Figure 2.1. For comparison, a solution cast CNF film ($\sim 90\ \text{mm}$ diameter) is placed at the center. Note it becomes much harder to see through the sheets as the number of layers increased. B) Cross-section of the thickest reported pure multi-layer CNF sheet ($\sim 1.65\ \text{mm}$), a US quarter is pressed against the surface for comparison.29

Figure 2.3 Optical profilometry (10x) of A) a single layer ($\sim 85\ \mu\text{m}$ thick) and B) an 8-layer ($\sim 547\ \mu\text{m}$ thick) CNF sheet. C) Surface texture imprint from the woven metal meshes onto a 1-layer pressed CNF sheet and D) an 8-layer sheet. The surface roughness does not change significantly as the sheet thickness increase from 1-layer ($S_q = 2.599\ \mu\text{m}$) to 8-layers ($S_q = 3.092\ \mu\text{m}$).33

Figure 2.4 Cross-sectional SEM microphotography of A) 1-layer sheet, B) 2-layer sheet, C) 6-layer sheet, and d) 8-layer sheet with their respective densities. The density values shown are for the specific specimen analyzed. The red arrow highlights one of the flat defects while the red lines highlight the edges of the given sheet.34

Figure 2.5 Scatter plot of A) ultimate strength verses thickness and B) density verses thickness for pure CNF sheets ranging from 1-layer to 8-layers thick for 35 minutes, 1 hour, and 2 hours press time. All the sheets were hot pressed at $0.36\ \text{MPa}$ and $126\ ^\circ\text{C}$. The numbers shown above and below the curves represent the numbers of layers and the average sheet thickness for all pressing times. The baseline represents a single CNF layer processed at a pressure of $0\ \text{MPa}$ and a temperature of $126\ ^\circ\text{C}$ for 35 minutes. The second dashed line represents an $80\ \mu\text{m}$ thick CNF solution cast film.....36

Figure 2.6 Linear regression of ultimate strength (MPa) versus Density (g/cc) of 49 tensile specimens from he prepared CNF sheets. The inner shaded region shows the 95 % confidence bands for the regression line. The outer lines show the 95 % prediction interval for individual sample units.....37

Figure 2.7 Scatter plot of A) Young's modulus verses thickness, B) strain verses thickness, and C) toughness verses thickness for 35 minutes, 1 hour, and 2 hours press time. All the sheets were hot pressed at 0.36 MPa and 126 °C. The baseline represents a single CNF layer processed at a pressure of 0 MPa and a temperature of 126 °C for 35 minutes. The second dashed line represents an 80 μm thick CNF solution cast film.	39
Figure 2.8 Photograph of four-layer CNF sheets pressed at a fast loading rate (A), slow loading rate (B) and optical profilometry (2.75x) of the center of the pressed sheets (C), and (D). Both sheets were pressed for 35 minutes at a temperature of 126 °C. The surface roughness at the center of the sheet increased significantly for the fast-pressed specimen ($S_q = 11.410 \mu\text{m}$ verses $S_q = 3.071 \mu\text{m}$).	41
Figure 2.9 Boxplots of A) ultimate strength vs loading rate and B) Young's modulus verses loading rate for 4-layer CNF sheets pressed at different loading rates. For each case, the sheet was pressed to 0.36 MPa for 35 minutes at a temperature of 126 °C. The dashed line is just a guide connecting the data sets.	42
Figure 2.10 Box plot of a) ultimate strength verses pressing pressure and b) density verses pressing pressure. All the 4-layer sheets were hot pressed for 35 minutes at temperature of 126 °C after reaching the respective pressure. The 0.36 MPa case is also shown and represents the baseline as it was the pressure utilized for all other studies.	43
Figure 2.11 SEM microphotography of the fracture surface of A) 1-layer, B) 2-layer, C) 6-layer, and D) 8-layer dogbone specimens. As seen, all the specimens presented a paper like fracture with fibrils pointing in the loading directions. The red lines highlight the analyzed fractured surface.	44
Figure 3.1 Recorded torque (Nm), temperature (°C), and mixing speed (rpm) during mixing of a CNF/CMC paste in a Brabender high shear torque mixer. The "A" points mark the addition of CMC while the "B" points mark the addition of water. The final paste solids concentration was 15.32 wt.% with a CMC to CNF dry weight ratio of 0.1:1. The plateau represents complete polymer incorporation into the paste and depend on the added polymer and final solids concentration of the paste.	52
Figure 3.2 CNF/CMC paste after mixing and complete CMC incorporation in the mixing chamber (A), wrapped around the mixing Banbury mixing blades (B), and removed from the mixer and shaped into a ball (C). The texture of the paste was very smooth and without any clumps or aggregates.	52
Figure 3.3 Brabender torque rheometer (ATR) unit but with an attached single screw extruder unit ($L/D = 25$, barrel diameter of 1.9 cm (3/4 inch), and 4 independent heating zones). The in-house made plunger used to push the highly viscous CNF/processing aid pastes can be seen in the hopper region.	56
Figure 3.4 Extruder configuration and processing parameters used to process highly loaded CNF/processing aid and pure CNF into wet sheets. The shown temperature is in °C. Unless otherwise stated the screw speed used was 7 rpm for all experiments.	57

Figure 3.5 Failed attempt at extrusion of pure CNF with a solids concentration of 17 wt.%. The material clogged the entrance of the sheet die (A) and the end of the barrel (C). The clogged and extracted water pooled in the hopped region (B).....	60
Figure 3.6 Extrudate of pure CNF originally at 30 wt.% solids concentration A) front view (width was ~50 mm), B) side view (thickness ~ 1.1 mm), and C) coming out of the slot die. The extrudate had a solids concentration of ~85 wt.% coming right out of the die. The total length of the pure CNF sheet was ~330 mm (13 inches). The sheet was very fragile and easily broken into pieces.	60
Figure 3.7 Zeta potential of pure CNF and suspensions of CNF plus processing aids. The dashed line shown is referenced to the mean of the pure CNF zeta potential ($\xi = -29.8$ mV). Six measurements were performed for each case and the average was calculated. The error bars represent one standard deviation away from the mean. The pH of all the samples was measured to be 6.4 except for PAA that had a pH of 6.0.	63
Figure 3.8 Solids concentration [wt.%] verses drying time [h] for an air dried CNF/CMC paste in a humidity controlled oven. To achieve a solids concentration of ~15 wt.% the paste had to be dried for over 38 days.....	64
Figure 3.9 Wet CNF/CMC sheet single screw extrusion (A), wet CNF/CMC extrudate (~15 wt.% total solids) exiting the rectangular sheet die (B), extrudate collected on a cardboard roll (C), and de-rolled extrudate laid flat on top of aluminum foil (D).	65
Figure 3.10 Extrusion delivery rate [kg/h] verses screw speed [rpm] for a CNF/CMC paste with a dry weight ratio of 0.1:1. Three aliquots of material were collected for each data point. The weight of the sample and delivery time were recorded in real time. A linear fit was applied to the data showing a strong correlation between the two variables ($R^2 = 0.997$). The red dot was excluded from the analysis for reasons explained in the main report. The error bars represent 1 standard deviation away from the mean.	66
Figure 3.11 Wet extrudates of CNF/CMC (A), CNF/XG (B), CNF/aPAM (C) pastes at ~15 wt.%, pressed and heated to fully dry sheets of CNF/CMC (D, G), CNF/XG (E, H), and CNF/aPAM (F, I). A strong back light was used to illuminate samples and highlight the defects like aggregation/aggregates or pinholes. A few of the observed defects are circled in red. Figures (A) through (F) were set to a grey scale to better appreciate the defects while figures (G), (H), and (I) were not color modified. The width of the sheets was ~51 mm.	68
Figure 3.12 Log (viscosity) - log (shear rate) dependence of pure CNF, CNF/CMC, and CNF/XG pastes with an aid to CNF ratio of 0.1:1 measured on the torque rheometer at 28 °C. The power law index is calculated by $n = (\text{slope} + 1)$ while the consistency index is the intercept point. All the analyzed pastes and pure CNF had a solids concentration of ~15.32 wt.%. Unfilled points represent unreliable data due to slipping or sticking to the mixing blades.	70
Figure 3.13 Log of apparent viscosity [Pa*s] verses log of shear rate [s^{-1}] for suspensions of pure CNF, CNF/CMC, CNF/XG, and CNF/aPAM. The table inset shows important rheological parameters computed from the power law fit on the obtained data. The equation on the top right corner represents the power law models.	72

Figure 3.14 Log (viscosity) - log (shear rate) dependence of CNF/CMC pastes with solids loading of ~15.32 wt.%, ~19 wt.%, and ~25 wt.% and pure CNF with a solids loading of ~30 wt.% measured on a torque rheometer at 28 °C. The processing aid to CNF ratio for the evaluated pastes was 0.1:1 (dry weight).....	72
Figure 3.15 Tensile mechanical response of cast CNF films, extruded CNF/CMC sheets, and extruded CNF/XG sheets with a processing aid to CNF ratio of 0.1:1. The error bars represent one standard deviation away from the mean. Typical stress-verses strain curves for these samples in included in Appendix B in Figure B. 10.	75
Figure 3.16 Scanning electron microscopy of the fractured surfaces of cast CNF (A), CNF/CMC at 0.1:1 (B), CNF/XG at 0.1:1 (C), and CNF/XG (D) at 0.15:1. The studied fractured surface is parallel to the tensile axis.	76
Figure 3.17 Tensile mechanical response of CNF/CMC pastes at two different dry weight ratios (0.1:1 and 0.15:1). The error bars represent one standard deviation away from the mean. The recorded responses are A) ultimate strength, B) Young's modulus, C) strain to failure, and D) density.	77
Figure 3.18 Tensile mechanical response of CNF/XG pastes at two different dry weight ratios (0.1:1 and 0.15:1). The error bars represent one standard deviation away from the mean. The recorded responses are A) ultimate strength, B) Young's modulus, C) strain to failure, and D) density.	78
Figure 3.19 Thermogravimetric analysis of cast CNF, extruded pure CNF, CNF/CMC, CNF/XG, and CNF/aPAM. The boiling point of water (100 °C) was selected as a comparison point. Prior to testing all the samples were preconditioned for over a week at 25 %RH.	79
Figure 3.20 Mechanical performance of Brabender mixed pastes (darker color) verses air dried pastes (lighter color) prepared using a humidity-controlled oven. The error bars represent one standard deviation away from the mean. The recorded responses are A) ultimate strength, B) Young's modulus, C) strain to failure, and D) density.	80
Figure 4.1 Single-screw filament/cord extrusion of a CNF+CMC paste (at ~18 wt.%) through a 2 mm nozzle (a), collected CNF+CMC wet cord extrudate on a cardboard roll (b), oven dried CNF+CMC cord (c), and pelletized cord (d).	89
Figure 4.2. Surface morphology of the extruded and dried untreated CNF+CMC cords with a varying degree of CMC carboxymethylation or substitution of 0.7 (a), 0.9 (b), and 1.2 (c).	91
Figure 4.3. Pelletized untreated CNF+CMC pellets at different stages of the rehydration process starting completely dry (a), ~30 s after adding water (b), 20 min after adding water (c), after being re-mixed in the Banbury shear mixer (d), and re-extruded into a filament/cord (e) and oven dried at 35 °C on a cardboard roll (f).	93
Figure 4.4. Dispersed never-dried CNF+CMC (a), redispersed dried-untreated CNF+CMC (b), redispersed HCl treated CNF+CMC (c), and redispersed PAE treated CNF+CMC (d) all in water after 24 hours of mechanical stirring and with a D.S. of 0.7. The turbidity response of treated and untreated CNF+CMC materials each prepared with CMC with three different degrees of substitution (D.S. = 0.7, 0.9, and 1.2) (e). Untreated, PEI, CaCl ₂ , HCl, and CDI treated samples were dried at 70 °C while PAE, PAmE treated samples were dried at 85 °C. The CNF+CMC pellets	

were stirred for 24 h in water at 25 °C before turbidity was collected and the pictures were taken. For each treatment type and D.S., a freshly prepared suspension was analyzed. Six measurements were carried out per sample. The mean and standard deviation error bars are displayed, respectively.94

Figure 4.5. Redispersion behavior at different points in time for CNF+CMC treated with PAE cured at 85 °C in 0.1 M NaOH (a) and turbidity response of different treated and untreated CNF+CMC materials in 0.1 M NaOH at two curing temperatures(b). The suspensions were stirred for 24 h before turbidity was collected. For each treatment type, two curing temperatures were evaluated while the CMC's D.S. remained constant at 0.7. A freshly prepared suspension was analyzed for each measurement. Six measurements were carried out per sample. The mean and standard deviation error bars are displayed, respectively.96

Figure 4.6. Optical micrographs of never-dried pure CNF dispersed in water (a), and dried-untreated CNF+CMC with a D.S. of 0.7 redispersed in water (b). Optical micrographs of CNF+CMC treated with CDI cured at 70 °C (c), CNF+CMC treated with HCl cured at 70 °C (d), CNF+CMC treated with PAE cured at 85 °C (e), and CNF+CMC treated with PAmE cured at 85 °C (f) all redispersed in 0.1 M NaOH and with a CMC D.S. of 0.7. The black scale bars in the top right have a length of 400 µm. Expanded (i.e., lower magnification) optical micrographs of the same dispersions are shown in Figure C.11 and Figure C.12.....97

Figure 4.7. FTIR analysis of CNF+CMC treated with; HCl cured at 25 °C and 70 °C (a), CDI cured at 25 °C and 70 °C (b), PAE cured at 25 °C and 85 °C (c), and PAmE cured at 25 °C and 85 °C (d) all with a CMC D.S. of 0.7. The control groups of pure CNF, pure CMC powder, and untreated CNF+CMC are also shown on the respective plots. The samples were conditioned under vacuum for 24 h at room temperature before testing. All the spectra shown were baseline corrected and 20 scans were collected. All intensities were all normalized by the invariant cellulose peak intensity at 1024 cm⁻¹. Dashed vertical lines mark the peak locations found in the treated CNF+CMC spectra while the dotted vertical lines mark peaks found in the pure compound spectra, respectively.98

Figure 4.8. Schematic of CNF with adsorbed CMC through hydrogen bonding with possible ester linkages (circled in green) formed due to treatment with HCl (a), anhydride linkages (circled in red) due to treatment with CDI (b), and ester linkages (circled in green) formed due to treatment with PAE and PAmE (c). Note that amide groups (circled in blue) are present in the PAE and PAmE backbone. All the schematics shows CMC with a D.S. of 1.100

Figure 5.1 Wet CNF web (~10 wt.% solids) with added PVA fibers being pulled apart. The PVA fibers can be clearly appreciated in the ruptured locations at the top and bridging the crack in the center of the wet web.....108

Figure 5.2 FR-CNF composites reinforced with abaca (a, e), flax (b, f), aramid/Kevlar (c, g), and rayon (d, h) fibers. For the images shown in the bottom half (e, f, g, and h), a strong backlight was applied to the back of the laminates to appreciate the level of fiber dispersion across through all the layers. A fiber content of 30 wt.% was used for all laminates shown. All of the laminates shown contained three layers and their thickness varied based on the fiber type. The scale bar for the figures in the bottom row is 10 mm.....109

Figure 5.3 Tensile mechanical performance of FR-CNF laminates; (a) ultimate strength, (b) strain to failure, and (c) tensile modulus versus fiber type. A fiber content of 30 wt.% was used for all

laminates. The black dots represent outlier data points. At least 6 samples were tested per laminate type. The numbers next to the fiber type represent the nominal fiber length. HT stands for high tenacity while L and S stand for 6.35 mm long and 3.175 mm.111

Figure 5.4 Mechanical performance of carbon FR-CNF laminates; (a) ultimate strength, (b) strain to failure, and (c) tensile modulus verses fiber treatment, respectively. A fiber content of 2.17 wt.% was used for all laminates. The black dots represent outlier data points. At least 6 samples were tested per laminate treatment. Unless otherwise stated the treatment, time was 24 hours. HPMC stands for hydroxypropyl methyl cellulose. SDS stands for sodium dodecyl sulfate. Pluronics 123 is a triblock copolymer surfactant made out of poly(ethylene oxide) (PEO) and poly(propylene oxide) (PPO) with a repeating structure of PEO-PPO-PEO.113

Figure 5.5 Mechanical tensile performance of CNF composites reinforced with rayon, aramid, or carbon fibers at three different fiber contents (~1, ~2, and ~4 wt.%). At least 6 samples were tested for each sample group and the error bars shown represent the standard deviation. No chemical treatment was applied to the reinforcing fibers. The fiber length used was 6.35 mm for all fiber types.....114

Figure 5.6 Schematic of the cross-section of a FR-CNF composite using a carbon fiber (CF) weave as the reinforcing phase. The blue sections represent pure CNF layers which sandwich the carbon fiber weave. The orange sections represent the polymer binder layers which sit between the carbon fiber weave and the pure CNF layers. The numbers inside the parenthesis next to the layer names represent the number of layers where 2x is two layers.115

Figure 5.7 Mechanical tensile performance of carbon fiber and flax weave reinforced CNF composites with different polymer binder layers. Rectangular specimens (6.35 mm by 115 mm) were cut with scissors from each composites. At least 12 samples were tested for each sample group and the average and standard deviation are displayed. The average values are displayed on top of their columns with a leader guide respectively.116

Figure 5.8 Schematic of the surface treatment processes for chopped carbon fibers.....119

LIST OF COMMON SYMBOLS & ABBREVIATIONS

List of Common Symbols

σ	Ultimate tensile strength or strength at break, MPa
E	Young's elastic modulus or tensile modulus, GPa
ε	Strain to Failure, %
ρ	Density, g/cc
ξ	Zeta potential, mV
η	Apparent viscosity, Pa * s
$\dot{\gamma}$	Shear rate, s^{-1}
g	Gravity, m/s^2

Common Abbreviations

CNMs	Cellulose nanomaterials
CNFs	Cellulose nanofibrils
CNCs	Cellulose nanocrystals
TEM	Transmission electrons microscopy
SEM	Scanning electron microscopy
DMA	Dynamic mechanical analysis
TGA	Thermogravimetric analysis
DI	Deionized
HCl	Hydrochloric acid
PAE	Polyamide epichlorohydrin
PAmE	Polyamine epichlorohydrin
CDI	Carbodiimide
NaOH	Sodium hydroxide
MC	Methyl cellulose
HEMC	Hydroxyethyl methyl cellulose
HEC	Hydroxyethyl cellulose
GG	Guar gum

KM	Konjac glucomannan
AS	Amphoteric starch
CMC	Carboxymethyl cellulose
XG	Xanthan gum
aPAM	Anionic polyacrylamide

ABSTRACT

First reported in the early 1980s, cellulose nanomaterials (CNMs) like cellulose nanofibrils (CNFs) have become a very attractive option to reinforce, replace, or reduce the need of oil-derived synthetic polymers. This is largely due to their inherent sustainability, abundance in nature, high crystalline contents, and ample surface chemistries possible (e.g., carboxylic acid, hydroxyls, esters, acetyls). Over the years, improved mechanical isolation processes (e.g., disk refining for isolation of the fibril-like CNFs) and acid hydrolysis processes (e.g., improved acid recovery for isolation of the rod-like cellulose nanocrystals (CNCs)) have increased industrial production capacity and allowed for CNMs to be readily accessible in both academic and industrial research settings. This, in turn, has accelerated research efforts regarding their processing into usable forms (e.g., films, fibers, coatings, etc.) which attain significantly higher properties when compared to synthetic polymer analogs. Although the reported CNM processing efforts are promising, further advances are still needed in order to galvanize the current polymer industry into processing CNMs and possibly ease their adoption in major markets like food packaging and construction.

Out of the different CNM types, this work focuses specifically on CNFs and encompasses four main projects, each targeted at solving a different CNF processing related challenge or limitation. The first project addresses the challenge of processing thick CNF sheets (thickness > 100 μm) through the development of a wet-stacking lamination technique. The results showed that high-strength multi-layer CNF structures with a thickness of up to ~ 1.7 mm can be produced. The second project addresses the challenge of bulk continuous processing of CNF sheets through conventional single-screw extrusion. The results showed that near pure CNF sheets (comprised of ~ 91 wt.% CNFs and $\leq \sim 9$ wt.% of a processing aid like carboxymethyl cellulose (CMC)) can be continuously extruded and calendered, and that traditional polymer compounders (e.g., Banbury mixer) can be used to prepare highly loaded CNF pastes (~ 25 wt.% solids) for extrusion. The third project addresses the susceptibility of CNFs to humid conditions through the use of different chemical treatments. The results showed that the redispersion and setting behavior of CNF with adsorbed CMC can be controlled and that new crosslinks were effectively formed due to the chemical treatment. Lastly, in hopes of further improving the mechanical performance and expand the possible end uses for CNFs and other CNMs, the fourth project presents preliminary research efforts into processing fiber reinforced CNF composites (FR-CNF).

1. INTRODUCTION

1.1 Cellulose nanomaterials (CNMs) background

Cellulose is an abundant, inexpensive, and naturally occurring polysaccharide. When bundled together, cellulose chains form highly-order domains which can be subsequently extracted as nano-particles. The extracted cellulose nanoparticles, generally termed cellulose nanomaterials (CNMs), boast high crystalline contents (up to 88 %, depending on the source), increased surface area, large aspect ratios (L/D of up to 500), and can easily form hydrogen bonds due to the native surface hydroxyl groups¹⁻⁴. When compared to inorganic nanoparticles, the properties of CNMs themselves are not unique, yet CNMs are sustainable, biodegradable, renewable, have a low environmental and health impact, can be harvested at an industrial scale at a low cost, and can be globally sourced⁵⁻⁸. These facts have made CNMs a very attractive option to reinforce, replace, or reduce the need of oil-derived synthetic polymers. Additionally, depending on the cellulosic source (e.g., wood verses bacterial), extraction or isolation method used, and chemical pre-treatment performed, different types of CNMs are possible each with own unique properties and functionalities which broadens their possible uses^{1,4,9,10}.

Cellulose nanofibrils (CNFs), often referred to as cellulose microfibrils (CMFs) in literature, are commonly extracted by mechanically fibrillating bleached wood pulp with the use of disk refiners, homogenizers, or enzymes^{3,4,8,11}. The extracted CNF nanoparticles boast large aspect ratios with fibril dimensions ranging from ~20 to 100 nm in diameter and 0.5 to 10 μm in length and contain both crystalline and amorphous domains, and a high degree of branching (e.g., thick central fibrils with thinner branched fibrils extending off)^{4,12}. CNFs have a strong tendency to form open network or aggregated structures due to poor fibril-fibril repulsion. A TEM image of CNFs extracted by mechanical fibrillation of bleached kraft pulp is shown in Figure 1.1 A. Due to the fibril's branched and aggregated nature, low solids suspensions of CNFs tend to have a white and non-transparent appearance as shown in Figure 1.1 B. However, different surface modification and chemical oxidation methods for CNFs has been reported in literature allowing for different surface chemistries (e.g., carboxylic acid, esters, acetyls)¹. A popular chemical oxidation method for CNFs employs the use of 2,2,6,6-tetramethylpiperidine-1-oxyl radical (TEMPO) to replace native surface hydroxyls with carboxylic or aldehyde groups without reducing its crystallinity^{8,13-15}.

TEMPO oxidized CNFs, often referred to as TOCNFs, carry the same fibril morphology as neat/untreated CNFs (i.e., branched, and long fibrils) except there are lower fibril-fibril entanglements and contacts due to the introduced negatively charged carboxylates. The improved stability through fibril-fibril repulsion makes TOCNFs suspensions transparent or clear when compared to unoxidized CNF suspensions.

Even though mechanically fibrillated CNFs were the first type of CNMs reported (~1980s), other types are possible when pre-treatments are used following mechanical fibrillation^{1–3}. Acid hydrolysis has been reported as a pre-treatment step to CNFs for the isolation of mostly the crystalline domains^{1,16}. In this case, the isolated nanoparticles are typically referred to as cellulose nanocrystals (CNCs) or cellulose nanowhiskers (CNWs). The elimination of the amorphous domains of the fibrils renders CNCs as short and rigid crystalline rods with a diameter ranging from 2 – 20 nm and a length of 20 to 500 nm, as shown in Figure 1.1 C^{1,16}. For the same reasons, CNCs have a much higher crystalline content (54 – 88%) when compared to CNFs (51 – 69%)¹. Acid hydrolysis also introduces negatively charged surface group functionalities to the crystalline rods which provides particle-particle repulsion. For example, hydrolysis with sulfuric acid (H₂SO₄), phosphoric acid (H₃PO₄), or hydrochloric acid (HCl) plus TEMPO oxidation, leads to the formation of negatively charged sulfate half esters (SO₄-CNC), phosphate half esters (PO₄-CNC), and carboxylic acids (COOH-CNC), respectively^{9,17}. As shown in Figure 1.1 D, the increased repulsion and virtually no entanglements, due to the rigidity of the crystalline rods, leads to higher clarity and transparency when in suspension^{1,16}.

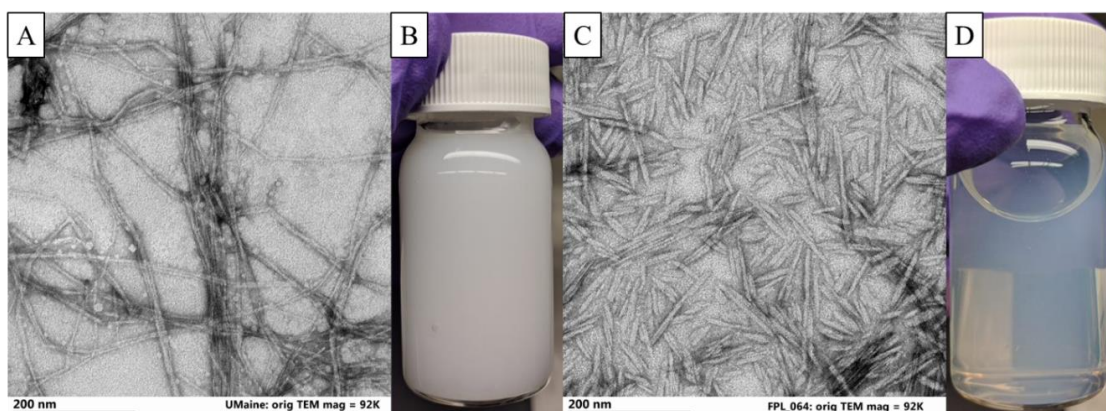


Figure 1.1 Transmission electron microscopy (TEM) images of A) CNFs and C) CNCs, and photographs of scintillation vials filled with B) CNFs slurry at 3 wt.% and D) CNCs slurry at 12 wt.%. TEM images courtesy of Youngblood's research group.

The broad morphological spectrum and functionalities possible for CNMs (e.g., Figure 1.1 A and C) has, in turn, accelerated research efforts regarding their processing into many different useable forms like films, fibers, coatings, and nanocomposites; all of which attain significantly higher properties when compared to synthetic polymer analogs^{18–24}. For example, due to CNF's long and flexible fibrils, self-standing neat isotropic films can be processed. When subjected to tensile testing, CNF films have been reported to achieve ultimate strength values of up to 232 ± 19 MPa and a Young's modulus of up to 13.4 ± 0.25 GPa with a density of 1.4 g/cc and a thickness of $60 \mu\text{m}$ ²⁰. An example of a cast CNF film is shown in Figure 1.2 A. Similarly, due to the improved fibril-fibril dispersion, isotropic and transparent films of TOCNF with an ultimate strength value of up to 312 ± 1 MPa and a density of 1.47 g/cc have been reported²⁵. An example of several cast TOCNF films stacked on top of each other is shown in Figure 1.2 B. CNFs have also found uses in foams, gels, coatings, as well as a reinforcement material in composite fibers and neat laminated sheets, to name just a few^{12,26–29}. On the other hand, due to CNC's rigid and crystalline morphology which makes for very brittle self-standing films, CNCs have been more popularly reported as reinforcement material in cellulose nanocomposites (both films and fibers) as well as coating materials as shown in Figure 1.2 C^{19,22,26,30–33}. Additionally, CNCs have found uses in packaging, construction, paints, cosmetics, pharmaceuticals, to name just a few¹⁷. Although the reported efforts show promising advances and innovative uses of CNMs, there are still significant limitation to the utilized methodologies for processing these materials.

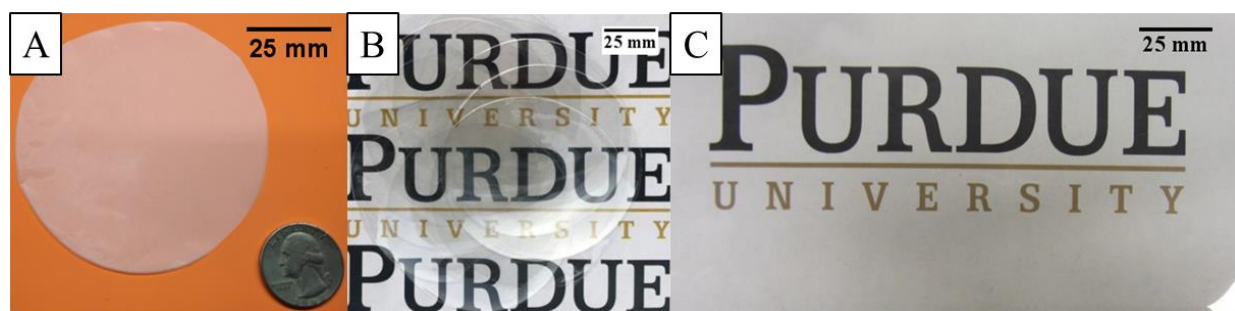


Figure 1.2. Images of solution cast films of A) CNF film next to a standard USA quarter, B) TOCNF film (reprinted with permission from ref. 34, copyright © 2020, Springer Nature B.V.), and C) CNC coating on a polyethylene terephthalate (PET) substrate (image courtesy of Youngblood's research group). The thickness of the CNF and TOCNF films is $\sim 75 \mu\text{m}$ and $\sim 30 \mu\text{m}$, respectively.

1.2 Processing of CNF films; current efforts and challenges

Due to the isolation processes used, CNFs are typically available in low solids concentration watery suspensions (1 – 30 wt.% solids, depending on CNF type, supplier, and isolation method used). For these reasons, waterborne fabrication techniques like solution casting or solvent casting have been widely used in laboratory settings to process CNFs into films or nanocomposites^{1,33}. In solution casting, a vessel (usually a petri dish) is first filled with a dilute CNF slurry. The vessel is then left (usually for two weeks) to dry under controlled conditions until all the water is evaporated and the structure is fully consolidated. For preliminary research purposes, solution casting is practical and inexpensive and provides for means of processing more specialized films. Yet, solution casting can only render small batches and requires very long drying times. Other laboratory processing methods which employ the use of vacuum assisted filtration, mechanical pressing, and heated pressing or a combination of all these to remove the water completely or partly from a CNF slurry have also been reported^{20,35}. These processing methodologies, here termed “hybrid methods”, reduce drying times to roughly a couple of hours as evaporation is no longer needed and thus significantly reduce total lead times. Yet, similar to solution casting, hybrid methods remain semiautomatic requiring trained personnel to move or pass the CNF slurry/suspension through all the processing stages and can only process a limited number of films at a time. Additionally, both solution casting and hybrid methods have a limit on the final dry film thickness which is dictated by the initial vessel volume which will be filtered and the starting solids concentration of the CNF suspension.

More recent research efforts have attempted to solve the semiautomatic nature of solution casting and hybrid methods through the use of pilot scale roll-to-roll (R2R) machines or other pilot scale coater machines (e.g., KTF-B Werner Mathis). For example, Claro et al. reported continuous processing of neat CNF films at a rate of 6 m/hr with a final dry film thickness of ~87 μm using a pilot scale coater^{36,37}. Otoni et al. also managed to continuously process CNF nanocomposite films at a rate of 6 m/hr, yet drying was problematic and significantly introduced film defects (e.g., water vapor bubbles) which reduced the mechanical properties of the films³⁸. However, continuous processing reports in literature are very scarce and still limit the final film thickness as complete drying will not be possible for thicker films.

In contrast to academic or pilot-scale efforts, industrial processing has focused on processing of conventional cellulose (i.e., non-fibrillated) instead of CNFs. For example, in papermaking,

CNFs have been added in small concentrations (~3 wt.%) to recycled paper which improved the tensile properties by roughly 30 % when compared to recycled pulp without CNFs³⁹. Additionally, established processing methods like that of regeneration also known as the Lyocell process have been used to produce regenerated cellulose films and fibers like rayon, Tencel™, or cellophane. Regeneration uses solvents like N-methylmorpholine N-oxide (NMMO) to dissolve native cellulose into a highly viscous dope/mass. The cellulose dope is then extruded through a die and into a precipitation bath (usually with a concentration of 75 % sulfuric acid in water, or sodium hydroxide) where the cellulose recrystallizes into the respective extruded shape (film or fiber)⁴⁰. The processed films or fibers are transparent unlike the films produced in papermaking. However, while both papermaking and regeneration processes have successfully continuously processed cellulose films, they have not been optimized for CNFs and carry inherent limitations and downsides.

Overall, there are four downsides to regeneration processes. First, they can be hazardous due to the volatility of NMMO or other solvents used⁴¹. Second, they are expensive due to the required washing and recycling of the solvent from the formed films or fibers. Third, hazardous and polluting byproducts like carbon disulfide and hydrogen sulfide are generated during the precipitation bath and must be managed. Lastly, regeneration changes the crystalline structure of cellulose (Cellulose I to Cellulose II polymorph change) making the films and fibers much weaker and introduces porosity (ultimate breaking strength ranging from 35 MPa to 75MPa with possible pore size ranging from 0.2 μm to 2 μm)^{40,42}. For these reasons, the regenerated cellulosic films and fibers must be coated with other polymers to serve as packaging material. This, in turn, reduces their biodegradability making them only industrially compostable^{43,44}. On the other hand, a major downside to the papermaking process is the small quantities of CNFs that can be incorporated which is dictated by the hydraulic capacity of the machines. The current machines will need to be modified to account for the greater water-retention ability (much greater surface area of CNFs) and the low solids content of CNF suspensions when compared to typical bleached kraft pulp slurries. This means papermaking machines will need to have longer pressing sections and drying ovens. It is important to point out that conventional papermaking machines are already on average over 140 meters long without modification⁴⁵. Due to these limitations, further advances are needed in the development of continuous processing approaches for CNFs. These methods must be able

to satisfy the functionality needed for industry (e.g., mechanical, optical, thermal, etc.), and must be fast and inexpensive.

1.3 Research Objectives and Scope

Out of the different CNM types discussed, this work focuses specifically on mechanically fibrillated CNFs which have not been pre-treated and thus still conserve their native surface hydroxyl groups. Furthermore, this work encompasses four main projects each targeted at solving a different CNF processing related challenge or limitation. More specifically, Chapter 2 addresses the main limitation of solution casting and hybrid methods (introduced in Section 1.2) which is the processing of thicker CNF structures (thickness $> 100\text{ }\mu\text{m}$) through a novel wet-stacking lamination technique. The results showed that high-strength multi-layer CNF structures with a thickness of up to $\sim 1.7\text{ mm}$ can be produced, and that the mechanical performance was improved by $\sim 37\%$ in terms of tensile ultimate strength. Chapter 3 addresses the challenge of bulk continuous processing of CNF sheets through conventional single-screw extrusion. The results showed that near pure CNF sheets (comprised of $\sim 91\text{ wt.}\%$ CNFs and $\leq \sim 9\text{ wt.}\%$ of a processing aid like carboxymethyl cellulose (CMC) or xanthan gum (XG)) can be continuously extruded and calendered, and that traditional polymer compounders (e.g., Banbury mixer) can be used to prepare highly loaded CNF pastes ($\sim 25\text{ wt.}\%$ solids) for extrusion. Chapter 4 addresses the susceptibility of CNFs to humid conditions through the use of different chemical treatments. The results showed that the redispersion and setting behavior of CNFs with adsorbed CMC can be controlled and that ester, N-acyl urea, and anhydride linkages were effectively formed due to the chemical treatment. Lastly, in hopes of further improving the mechanical performance and expand the possible end uses for CNFs and other CNMs, Chapter 5 builds on the knowledge gained from Chapter 2 and presents preliminary research efforts into processing fiber reinforced CNF composites (FR-CNF). The results show that different fiber types (synthetic and natural fibers) and lengths (3, 6, 10, and 13 mm long) can be incorporated into CNF, but the overall tensile mechanical performance decreases.

Solving the stated processing challenges and limitations will ultimately galvanize the current polymer industry into processing CNFs and possibly ease their adoption in major markets like food packaging and construction. Ideally, CNFs will serve as a more biofriendly and sustainable alternative to oil-derived synthetic polymers in the near future.

2. PROCESSING AND CHARACTERIZATION OF THICK CNF SHEETS

In the presented work, all the laboratory experiments and work in this chapter was performed by Sami M. El Awad Azrak. The manuscript writing and submission was done by Sami El Awad Azrak. Dr. Caitlyn Clarkson took part of the SEM micrographs and revised the manuscript. Dr. Youngblood, Dr. Moon, and Dr. Schueneman provided guidance on the research direction and on all writing.

This chapter contains content reproduced with permission from El Awad Azrak, S. M.; Clarkson, C. M.; Moon, R. J.; Schueneman, G. T.; Youngblood, J. P. *ACS Appl. Polym. Mater.* **2019**, *1* (9), 2525–2534. Copyright 2019 ACS Applied Polymer Materials.

2.1 Introduction

For CNF, the solution casting film making process often starts with a slurry (0.1 wt.% to 3 wt.% in water) which is evenly dispersed using shear mixers and/or sonicators. The mixture is then poured in a vessel or reservoir (usually a petri dish) where the solvent (usually water) is removed through evaporation and the web consolidates at the bottom. The total film processing time varies based on the method used to remove the solvent and ranges from roughly an hour for hot pressing operations, up to a couple of weeks for controlled room temperature evaporation. Moreover, depending on the vessel/reservoir dimensions, the variety of processing methods can yield different size films. For example, those films produced using solution casting and evaporation techniques rely on the use of standard petri dishes with a 90 mm diameter. On the other hand, the thickness of the films can be controlled by the amount of slurry initially added in the mold. Standard thicknesses reported for neat CNF films range from 0.033 mm (33 μm) to at most 0.1 mm (100 μm)^{35,46,47}. However, thickness is practically limited by cracking and curling during evaporation due to residual stresses and the long evaporation/filtration time required to consolidate and dry the films which requires free water to escape through the dense fibrillar network as the escape path becomes increasingly tortuous due to the formation of fiber-fiber hydrogen bonds and humidity gradients^{45,48}. For example, it takes roughly 45 minutes to filter CNF slurry through a 0.65 μm pore size membrane to create a film with a final thickness of 0.06 mm²⁰. This problem is well known in established industries such as papermaking; where evaporation rates are fastest during the initial sheet warming step and then significantly decrease during the later stages of drying where extensive structural changes occur to the web^{49,50}. As processing time increases with

thickness, this presents a challenge for the creation of thicker CNF sheets or plaques which could serve as structural and other packaging materials.

One solution for creating thicker nanocellulose structures (0.1 mm to 3.2 mm) without significantly increasing processing time is to create polymer nanocomposites. In these structures a polymer matrix is often used, and cellulose nanomaterials (CNMs) will be added as the reinforcing phase. Two major drawbacks of using composite systems to make thicker structures is the poor compatibility between the different phases and the low dispersibility of the hydrophilic material (CNMs) in a highly hydrophobic matrix. This often limits the amount of material which can be added or dispersed, leading to peak composite performance at relatively low solids loadings (<10 wt.%) of CN due to particle aggregation. Additionally, low solids loading also defeats the initial goal of reducing the dependence on oil-derived polymers. Thus, there is still a need to find a better way to process thicker CN structures and study their mechanical properties.

In this chapter, a four-step wet stacking technique was developed and used for the creation of multi-layer CNF sheets with varying thicknesses and without the use of additional solvents or binders. Wet stacking allowed increased thickness of the CNF sheets without significantly increasing total processing time which represents a significant advantage over other conventional film making processes like solution casting. Additionally, the use of this technique allowed for the creation of the thickest reported pure multi-layer CNF sheet with a working area of 117 mm by 117 mm and thickness of 1.65 ± 0.02 mm. The effect of thickness on the mechanical performance of the sheets was investigated by varying the number of stacked CNF layers from 1 layer to 8 layers thick. The results were contrasted with commodity polymers commonly used for packing applications and metals used in structural applications like poly(styrene), nylon 6,6, Al 2024, and Al 6061. Pressing time, pressing pressure, and loading rate were varied to gauge their effect on the mechanical performance of the produced sheets. To elucidate why thicker sheets performed better than the thinner ones, SEM photomicrography was utilized to view the cross-sectional area of the sheets as well as the fracture surface.

2.2 Experimental section; Materials, Methods, and Characterization

2.2.1 Materials

5-gallon buckets of CNF from Kraft pulp were bought directly from University of Maine, Orono, ME, USA (batch #98; 3 wt.% CNF-water slurry; 90 % fines). These fibrils had a mean diameter of 38 nm as taken from a transmission electron microscopy image (see Appendix A, Figure A. 1 TEM image of the CNF fibrils used to make the sheets. The diameter of the fibrils was measured with imageJ an open source software. Note, individual fibrils were measured rather than the agglomerated structures that appear as darker regions. Figure A. 1). Over 15 particle diameters were measured using an open source software (imageJ). The material was used as delivered and diluted to 1 wt.% with deionized water. The process of making the cellulose slurry is explained more in detail by C.A. de Assis et al⁸.

The materials used for building the dewatering frame were: two stainless steel filtering wire cloths/sieves (“Dutch weave”, 316SS) with a mesh size of 165x1400; one filter felt (polyester) with a 10 µm pore size, one polyurethane super absorbing foam/sponge (Aquazone™); perforated staggered hole 0.635cm thick PVC sheet (50 % open area and 1.27 cm hole diameter); and four 5x10 cm wood studs cut to a length of 40.64cm. A wooden frame was constructed to hold the perforated PVC sheet. The filter felt was then laid on top of the PVC sheet, followed by the metal filter mesh (Figure S2). The total dewatering frame working area is 929 cm² (WxL = 30.48x30.48 cm). Additionally, aluminum 2024 (T3 tempered), aluminum 6061 (T6 tempered), poly(styrene) and nylon 6,6, sheets were bought to use as comparison materials. All materials were bought directly from McMaster Carr Supply Company, Elmhurst, IL, USA with exception of the wood studs which were sourced in house.

2.2.2 Preparation of CNF Sheets

For all case studies, the initial CNF concentration of 3 wt.% was diluted to 1 wt.% by adding deionized (DI) water at a ratio of 1 to 2 (CNF to water). To make a single layer, 300 g of CNF slurry (at 3 wt.%) and 600 g of DI water were added into a larger plastic container and vigorously mixed by hand for 3 to 4 minutes. The contents were then poured in a zig-zag fashion over the metal filtering mesh which was placed inside the frame. The frame and mixture were slightly shaken to make sure that the CNF slurry was evenly distributed across the surface of the filtering

mesh. A second metal filter mesh was then carefully laid on top of the CNF slurry followed by the sponge. The slurry remained in the frame for 10 minutes to allow for filtration by gravity and capillary suction to occur. To aid capillary suction, evenly distributed pressure was then applied to the sponge by using a painter roller in a rowing fashion for 10 minutes. When the sponge was completely soaked it was squeezed and placed back on top of the filtering mesh where the pressure was applied a second time. This process was repeated as needed until no more water was extracted by the sponge. The CNF web, now consolidated to ~7 wt.%, was removed from the frame and carried between the two metal meshes. The CNF sandwich was then passed through a 30.48 cm wide, tabletop slip roller (WFSR1.0) seven times. The rolling gap width was decreased slightly after each pass to gradually apply more pressure to the web and further increase the solids loading of the CNF web. After rolling, the solids loading reached ~10 wt.% and the CNF web was capable of being separated from the meshes by hand. Large films with an initial area of 30.48 cm by 30.48 cm were sectioned into four smaller sections (15.24 cm by 15.24 cm). These smaller sections were stacked, and the sides were trimmed to a final sheet area of 11.7 cm by 11.7 cm. Finally, the stacked layers were hot pressed at a temperature of 126 °C until dry (~99 wt.%) for different pressing times (35 min, 1 h, and 2 h) using a hydraulic heated laboratory press model No. 3690 (Carver). The final thickness of the sheet is dependent on the number of layers stacked before the final hot-pressing step.

Figure A. 2 and Figure A. 3 portray each step in this process while Figure 2.1 shows a graphical illustration summary of the major steps taken. Step 2 in the process is optional, yet it was incorporated to further reduce the water content of the layers as the heated press used in the final step did not have any drainage system for liquid water. Moreover, the initial press filtration step could be carried out by other means instead of gravity and capillarity (sponge) like vacuum pumps or mechanical presses, but this could represent a costlier and more complex route. The total solids concentrations were calculated by dividing the weight of the completely dry web by the weight of the wet web.

The process outlined in Figure 2.1 was used to produce pure multi-layer CNF sheets of varying thicknesses as shown in Figure 2.2 A. The use of this technique allowed for the creation of the thickest reported pure multi-layer CNF sheet with a working area of 117 mm by 117 mm and a thickness of 1.65 ± 0.02 mm made out of 24 layers of CNF (Figure 2.2 B). Yet, thicker sheets could be made by stacking additional layers. It is worth pointing out that Steps 1 and 2 (Figure 2.1)

are very similar to the process used to create hand sheets of paper from hydrated paper pulp by using a sheet machine where a single large layer is formed and dried⁵¹.

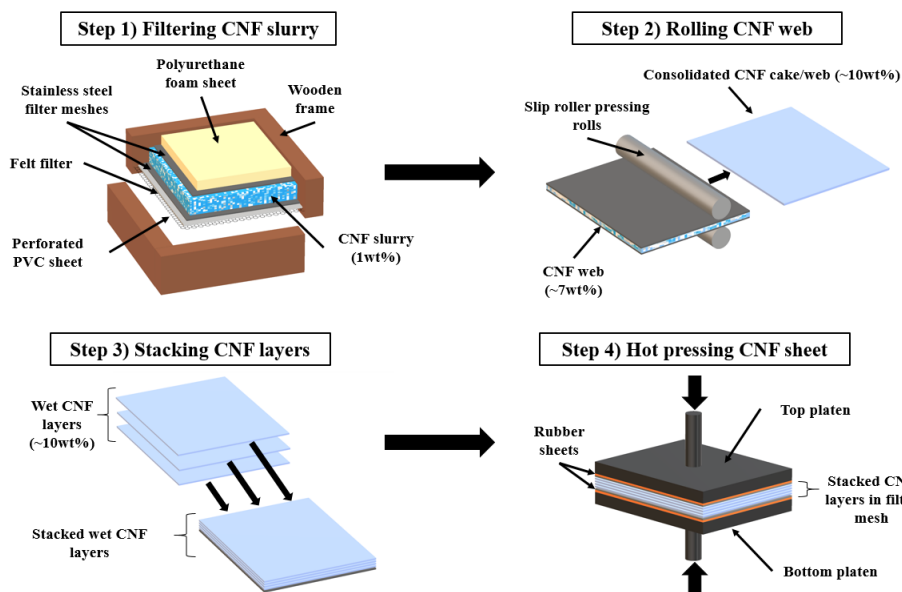


Figure 2.1 Process used to make CNF sheets. The process can be divided into 4 steps: press filtration, rolling, stacking, and hot pressing. Step 1, an CNF slurry at an initial concentration of ~1 wt.% is filtered to ~7 wt.% in a in house made dewatering frame. Step 2, the consolidated CNF web is press filtered through a slip roller to reach a concentration of 10 wt.%. Step 3 the CNF layers are separated from the filtering mesh and stacked. Step 4) the layers are hot pressed into a multi-layer CNF sheet.

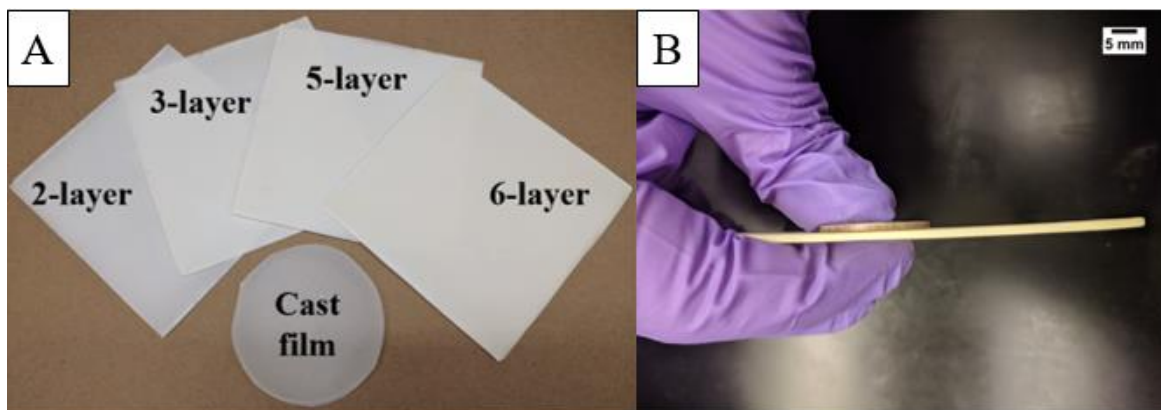


Figure 2.2 A) Different thickness CNF sheets prepared using the layer-by-layer wet stacking technique described in Figure 2.1. For comparison, a solution cast CNF film (~90 mm diameter) is placed at the center. Note it becomes much harder to see through the sheets as the number of layers increased. B) Cross-section of the thickest reported pure multi-layer CNF sheet ($t \sim 1.65$ mm), a US quarter is pressed against the surface for comparison.

2.2.3 Tensile properties and density of the CNF sheets

Following ASTM D638 dogbone specimens were cut from prepared CNF sheets using a laser cutter PLS6MW MW (Universal Laser Systems™) with a 10.6 CO₂ source and 2 MW optics. Several laser passes were needed to cut thicker samples. The tensile specimens were 92 mm long and had a neck width of 4.80 mm. After laser cutting, all the specimens were conditioned in a desiccator at 23 %RH for at least 2 days before mechanical testing. An electromechanical testing machine (MTS Insight) was used for tensile testing of dogbone specimens with a 1000 N load cell and serrated film clamps. Sandpaper was added at the grips to avoid specimen slippage. The crosshead speed was set to 1mm/min for all samples. All the samples were preloaded to 1 N. The ambient relative humidity could not be controlled and varied from 30 %RH to 50 %RH during mechanical testing, but large sample groups were tested together to reduce variation. The ultimate strength was taken to be the strength at failure. The Young's modulus was obtained by steepest slope method and the strain was measured based on crosshead displacement (no extensometer was used); all the values were gathered from the built-in software (TestWorks4®). Grip compliance was measured using a thick 1020 steel specimen and was subtracted from the results. The area under the stress verses strain curve was taken to be the apparent toughness or work-of-failure (MJ/m³) of the specimen and was integrated using a built-in function in OriginPro™. Density was measured on smaller square samples (8 mm by 8 mm) which were cut from the same sheet as the specimens. A micrometer and a caliper were used for measuring thickness and width while mass was measured with an analytical balance (VWR).

2.2.4 Scanning electron microscopy (SEM) of the CNF sheets

CNF sheet surface texture, cross-sectional area, and fracture surfaces were imaged using a Quanta 650 FEG field emission electron microscope. Prior to imaging, samples were secured to a conductive metal stub with copper and carbon tapes and then sputter coated (SPI sputter coater) with a platinum-gold target for 60 s. No polishing or sanding was used. Samples were imaged at 2-7 KeV and spot size of 3-5. The working distance varied from 8-32 mm depending on whether sample topography or resolution was the objective. For the cross-sectional area analysis, a total surface length of 8 mm (i.e., the entire length of the density samples) was scanned before taking any SEM image.

2.2.5 Optical profilometry

CNF sheet surface roughness was imaged using a Zygo Corporation (NewView 8000) optical profilometer. A 10x or 2.75x magnification was used for all the images taken. Due to the nonreflective nature of CNF, the studied samples were sputter coated (SPI sputter coater) with a platinum-gold target for 60 seconds. A cylindrical baseline/plane correction was applied to all captured surfaces from which the roughness values (S_a , S_q , S_z) were automatically calculated.

2.2.6 Statistical analysis of the tensile properties and density

At least 8 samples per CNF sheet were tested for each data point and a minimum of 13 samples were tested to generate the baseline (1-layer, 0 MPa) and 8 samples were tested of the 80 μm thick cast CNF film, which were depicted as dashed lines. For metal and commodity polymer specimens (Al 2024, Al 6061, poly(styrene), and nylon 6,6) at least 3 samples were tested. All specimens were visually inspected for excessive roughness or burn marks prior to testing. Only those with significant defects were removed from the analysis. Statistical analysis was done using OriginProTM. A normality test was performed on all sample data sets to verify normal distribution. The error bars shown represent a single STD away from the mean. Student's t-test with a 95% confidence interval was used to determine if there was significant statistical difference/similarity between data sets. For the density versus ultimate strength analysis, residual analysis was utilized to remove any outliers which are highlighted in red. Data points with a standardized residual above or below ± 10 STD were excluded from the linear fit.

2.3 Results and discussion

2.3.1 Sheet processing time and surface texture analysis

A significant advantage of processing thicker CNF sheets in a wet stacking lamination approach, Figure 2.1, is the fact that dewatering time is not significantly increased. This is due to the ease at which water can escape through the thinner pre-stacked layers (Step 1 and 2, Figure 2.1) rather than a thicker CNF web (Step 3, Figure 2.1). In this way, the pre-dewatered CNF layers (~10 wt.%) are simply stacked on top on each other and hot pressed to form a final consolidated thicker structure. This differs from some of the most common techniques like solution casting and vacuum filtration plus hot drying, where the final thickness of the CNF sheet depends on the

amount of material that was initially added into the reservoir for filtration and a thick CNF cake forms at the bottom. Table 2.1 compares two common processing techniques used to make CNF sheets with that of the wet stacking lamination approach. The total processing times are estimated based on laboratory trials and extrapolated from what has been reported in literature. The time reported includes preparation, filtration, and drying time. Solution casting could not produce structures with a thickness greater than 0.28 mm without excessive wrinkling and warping.

Table 2.1 Wet stacking lamination approach compared with two common CNF film processing techniques.

	Total processing time to create a CNF sheet with a thickness of:				
Processing technique	0.28 mm	0.34 mm	0.42 mm	0.55 mm	1.65 mm
Wet stacking lamination plus hot pressing (126°C)	~ 1 hour	1 - 2 hours	1 - 2 hours	1 - 2 hours	6 - 7 hours
Vacuum filtering plus hot drying (90°C) ²⁰	3 - 4 hours	4 - 5 hours	5 - 6 hours	6 - 7 hours	20 - 21 hours
Solution casting (23°C)	~ 1 week	N/A	N/A	N/A	N/A

The prepared CNF sheets in this work had some degree of translucency and flexibility both of which significantly decreased as the number of layers increased (Figure 2.2 A). Additionally, the sheets were flat and smooth to the touch even though the filtering mesh did impart small scale texturing to the surface which was identical to the crosshatched pattern of the woven metal filtering mesh (Figure 2.3 C and Figure 2.3 D). SEM analysis of the surface showed that this type of texturing imprint was also seen for the 2- and 6-layer sheets and is assumed to be present in the 3-,4-, and 5- layer sheets (Figure A. 4). Furthermore, optical profilometry confirmed that the surface roughness did not change significantly ($S_q = 2.6 \mu\text{m}$ versus $S_q = \sim 3.1 \mu\text{m}$) as the thickness increased from 85 μm to 547 μm (Figure 2.3A and Figure 2.3B). This means that surface defects are not being generated as thickness increases and surface quality remains the same.

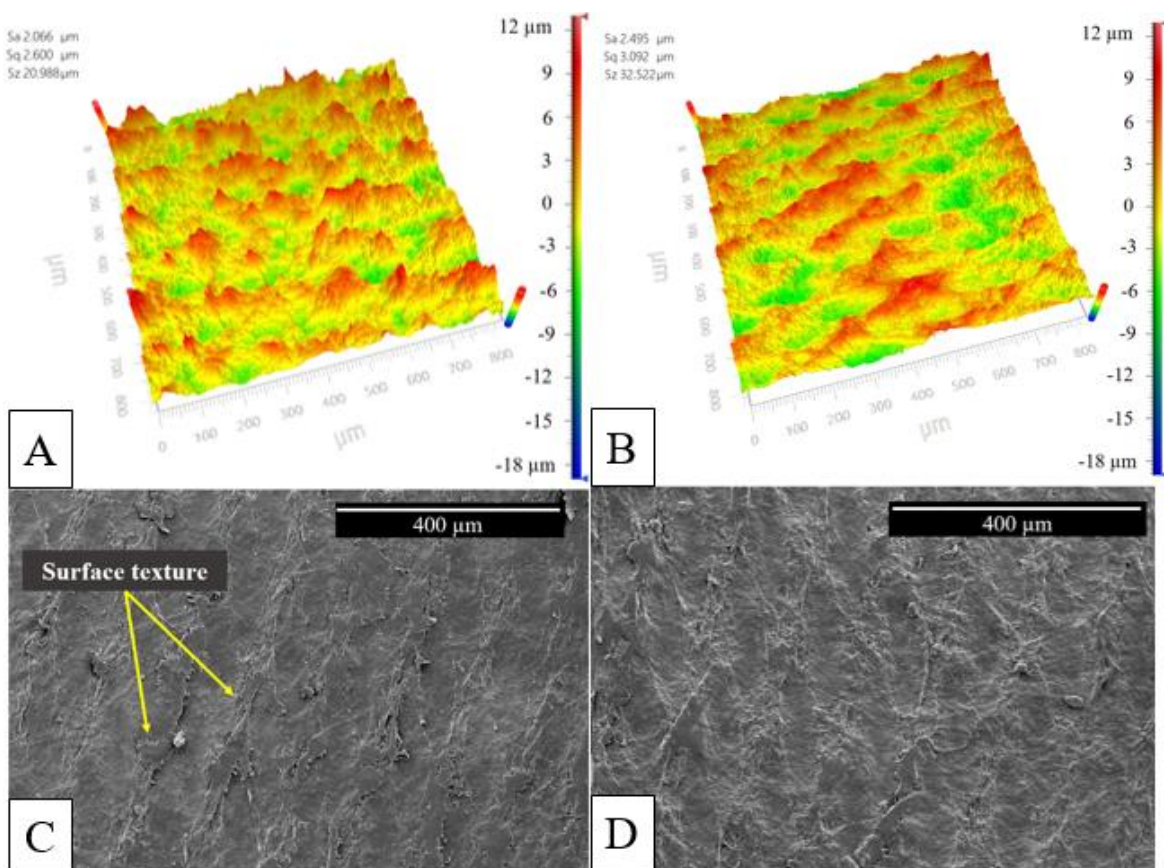


Figure 2.3 Optical profilometry (10x) of A) a single layer ($\sim 85 \mu\text{m}$ thick) and B) an 8-layer ($\sim 547 \mu\text{m}$ thick) CNF sheet. C) Surface texture imprint from the woven metal meshes onto a 1-layer pressed CNF sheet and D) an 8-layer sheet. The surface roughness does not change significantly as the sheet thickness increase from 1-layer ($S_q = 2.599 \mu\text{m}$) to 8-layers ($S_q = 3.092 \mu\text{m}$).

2.3.2 Cross sectional surface analysis

Water retention within the layers was very important throughout this process as it is well known that removing water from cellulose slurries causes irreversible structural changes through heavy aggregation also known as hornification^{49,50,52}. In this case, the wet CNF layers retained a significant amount of water ($\sim 90 \text{ wt.}\%$), which should have deterred the formation of a greater number of fibril-fibril hydrogen bonds or aggregates. Thus, when wet CNF layers are stacked and hot pressed together, hydrogen bonding can occur between them and the layers consolidate to form a single sheet with no discernable interfaces. The entire cross-section of CNF specimens composed of 1-, 2-, 4-, 6-, and 8-layers were analyzed with SEM to check for possible defects between the pressed layers. Defects could have resulted from incomplete contact between layers as a result of

surface roughness/texture brought by the woven filtering mesh⁵³ (Figure 2.4). Unfortunately, laser cutting caused significant damage to the cut surface (e.g., melting, etc.), which extends approximately 10 μm into the bulk of the sample (see Figure A. 5). As a result, the cross-section surface was full of pin-hole porosity and flat defects (Figure 2.4). For the thicker sheets (6- and 8-layers), flat defects are clearer, and run parallel to the sheet stacking. At this early stage it is unclear if these flat defects are associated at the layer-layer interface (Figure 2.4 C, Figure 2.4 D, and Figure A. 6) as they appear throughout the cross-section.

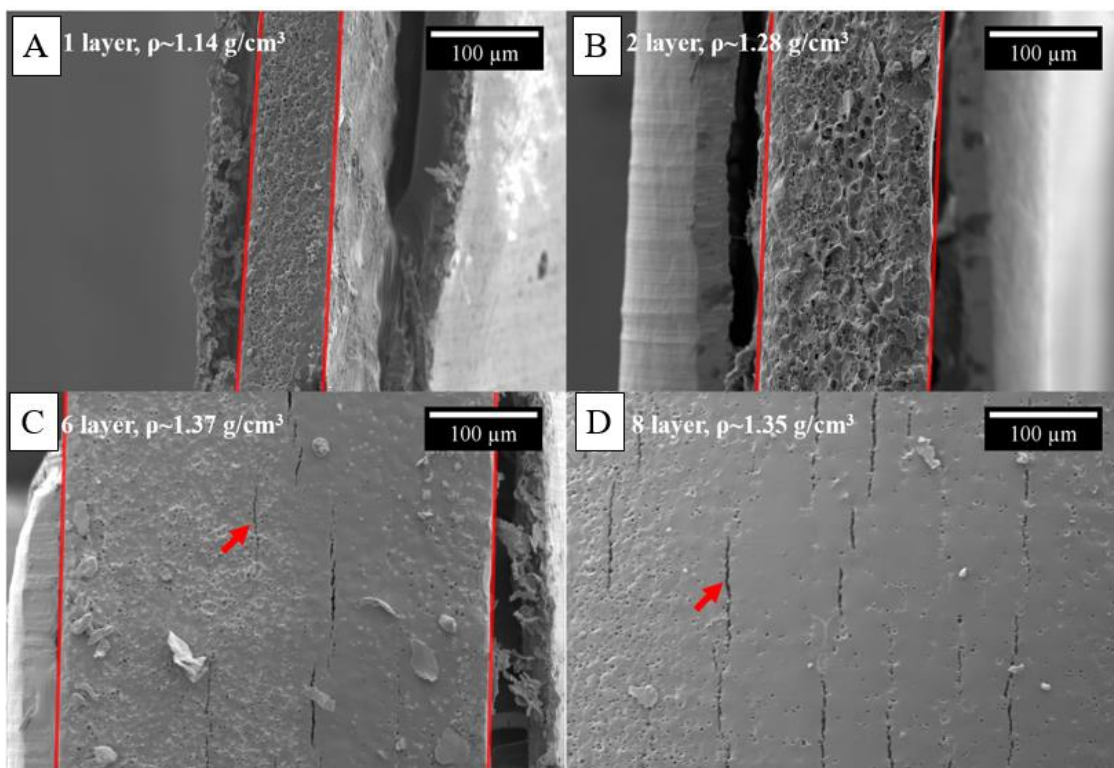


Figure 2.4 Cross-sectional SEM microphotography of A) 1-layer sheet, B) 2-layer sheet, C) 6-layer sheet, and d) 8-layer sheet with their respective densities. The density values shown are for the specific specimen analyzed. The red arrow highlights one of the flat defects while the red lines highlight the edges of the given sheet.

It is well known that there exists a nano-porous network present in all neat CNF films^{1,54}. In this case the porosity's magnitude or size must have decreased as the thickness of the sheets increased. This could explain the increase in density experienced by the 3-, 4-, 5-, 6-, and 8- layer sheets when compared to the 1- and 2-layer specimens. Table 2.2 shows a complete summary of the average density values for all CNF sheet thicknesses probed in this study.

Table 2.2 Mechanical performance of CNF sheets with varying thicknesses. The reported values are averages between all three pressing times. The area under the stress versus strain curve was taken to be the apparent toughness or work-of-failure of the specimen in (MJ/m³). The superscripts represent statistical similarity between different specimens with 1-layer being case “a” and 8-layer being case “g”.

Number of Layers	Thickness (mm)	Density (g/cm ³)	Ultimate Strength (MPa)	Young's Modulus (GPa)	Strain to Failure (%)	Toughness (MJ/m ³)
1	0.085±0.002	1.14±0.03 ^a	151.8±8.7 ^a	10.7±0.03 ^{acdef}	2.01±0.15 ^{ab}	1.75±0.3 ^a
2	0.153±0.004	1.28±0.01 ^b	195.4±1.9 ^{bfg}	12.0±0.5 ^{bcd}	2.34±0.22 ^{abcdefg}	2.95±0.4 ^{bcd}
3	0.220±0.002	1.33±0.02 ^{cdefg}	205.6±3.7 ^{cdef}	11.5±1.3 ^{abc}	2.55±0.21 ^{bcdefg}	3.36±0.4 ^{bcd}
4	0.279±0.003	1.35±0.01 ^{cdefg}	209.2±6.6 ^{cdef}	10.7±1.2 ^{abc}	2.61±0.21 ^{bcdefg}	3.84±0.3 ^{cdefg}
5	0.344±0.013	1.35±0.01 ^{cdefg}	209.0±5.8 ^{cdef}	10.4±0.3 ^{ac}	2.59±0.08 ^{bcdefg}	3.96±0.3 ^{cdefg}
6	0.420±0.013	1.37±0.02 ^{cdefg}	204.2±5.1 ^{cdef}	10.7±0.9 ^{abc}	2.37±0.28 ^{bcdefg}	3.51±0.5 ^{bcd}
8	0.547±0.029	1.35±0.01 ^{cdefg}	184.8±10.9 ^{bg}	8.90±0.3 ^{dg}	2.51±0.2 ^{bcdefg}	3.58±0.6 ^{bcd}

2.3.3 Thickness and pressing time effect on the mechanical properties of CNF sheets

Based on the statistical difference between data sets for different thicknesses (t-test with 95% confidence interval), mechanical tensile testing showed that as the sheet thickness increased from $85 \pm 2 \mu\text{m}$ (1-layer) to $153 \pm 4 \mu\text{m}$ (2-layers) the ultimate strength increased from $151.8 \pm 8.7 \text{ MPa}$ to $195.5 \pm 1.9 \text{ MPa}$. The strength then remained constant at roughly $207 \pm 2.5 \text{ MPa}$ for thicker sheets (3-, 4-, 5-, and 6-layers) (Figure 2.5 A). Moreover, for all the sheets produced (1- to 8-layers), the ultimate strength results are significantly higher than that of the two different comparison baselines used ($80 \mu\text{m}$ thick solution cast film and a 1-layer loosely constrained ($\sim 0 \text{ MPa}$) hot pressed sheet) which should carry the base mechanical properties of the most popular methods of making CNF films (cast and hot pressing). Other authors have shown a similar trends for films prepared from bamboo CNF; where there was an initial increase in strength ($\sim 125 \text{ MPa}$ to 175 MPa) and then a plateau for thicker specimens (up to $205.5 \mu\text{m}$)⁵⁵. For the $547 \pm 29 \mu\text{m}$ thick sheets (8-layer), the strength decreased slightly to $184.8 \pm 10.9 \text{ MPa}$. It is also interesting to note that the effective layer thickness decreased as the number of layers increased. For example, for the 1-layer sheet the effective layer thickness was $\sim 85 \mu\text{m}/\text{layer}$ while for the 8-layer sheet it was $\sim 68 \mu\text{m}/\text{layer}$. These differences may be a result of the compression of surface roughness on each layer during hot pressing (Step 4, Figure 2.1). Table 2.2 lists all the measured average values relating to the tensile mechanical performance of the produced CNF sheets.

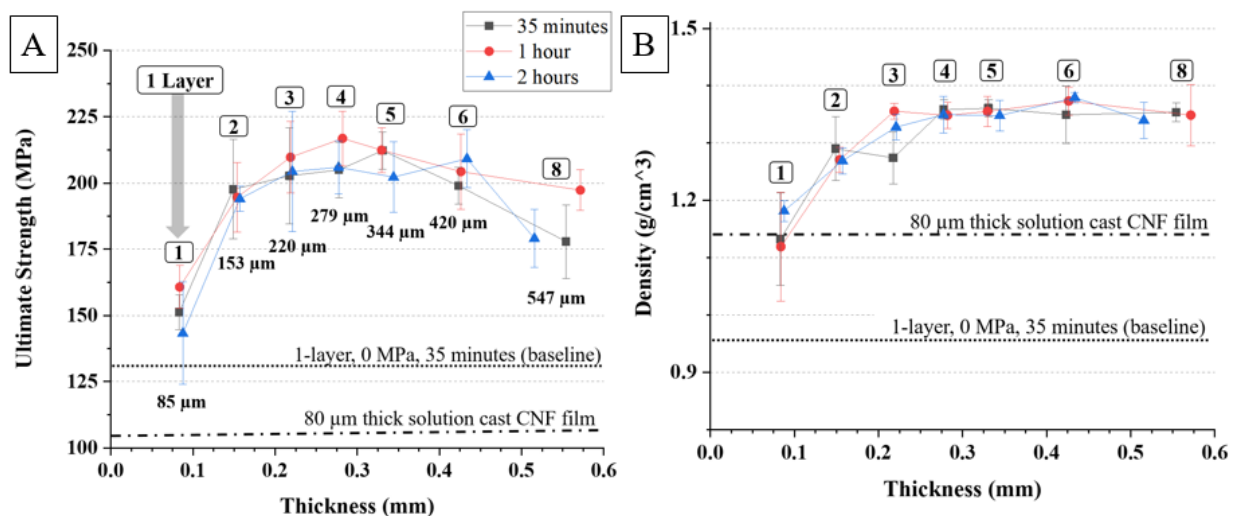


Figure 2.5 Scatter plot of A) ultimate strength versus thickness and B) density versus thickness for pure CNF sheets ranging from 1-layer to 8-layers thick for 35 minutes, 1 hour, and 2 hours press time. All the sheets were hot pressed at 0.36 MPa and 126 °C. The numbers shown above and below the curves represent the numbers of layers and the average sheet thickness for all pressing times. The baseline represents a single CNF layer processed at a pressure of 0 MPa and a temperature of 126 °C for 35 minutes. The second dashed line represents an 80 μm thick CNF solution cast film.

To gain a better assessment of the mechanical properties of the produced sheets, the empirical relationship between ultimate strength and fibril diameter was used. This relationship was reported in the work done by Zhu et al⁵⁶. In the current study, the obtained ultimate strength values were on average 207 ± 2.5 MPa. These values were above the empirically found maximum possible for CNF films made with mean fibril diameters of 38 nm, which is estimated to be ~ 162.2 MPa⁵⁶. This approximation is made by taking the inverse of the square of the mean fibril diameter (Figure A. 1 and Equation A. 1). The deviation from the empirical relationship was directly related to an increase in density with sheet thickness, following the same trend seen for ultimate strength (Figure 2.5 B). For example. 3-, 4-, 5-, 6- and 8-layer sheets with a thickness greater than 153 μm had average higher densities in the range of 1.35 ± 0.02 g/cc, while 1- and 2-layer sheets had a density of 1.14 ± 0.03 g/cc and 1.28 ± 0.01 g/cc (Table 2.2). To assess the strength-density relationship, a plot of ultimate strength versus density was made (Figure 2.6) and linear regression was performed. A linear fit to the results showed an $R^2 = 0.968$, demonstrating a strong correlation between the two variables. Though not explicitly stated, the increase in density with sheet thickness and its correlation with the ultimate strength was also reported by other authors⁴⁷.

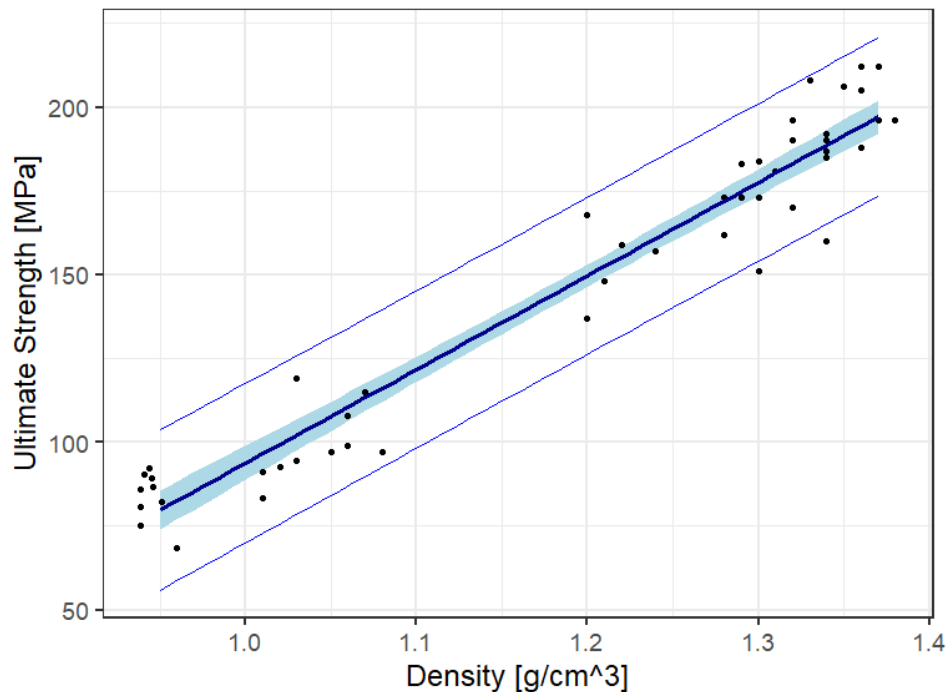


Figure 2.6 Linear regression of ultimate strength (MPa) versus Density (g/cc) of 49 tensile specimens from the prepared CNF sheets. The inner shaded region shows the 95 % confidence bands for the regression line. The outer lines show the 95 % prediction interval for individual sample units.

Pressing times were investigated to assess effect on sheet strength, in which longer pressing times would allow for more complete water removal and web consolidation, resulting in higher sheet densities (Figure 2.5 B) and thus higher sheet strength (Figure 2.5 A). For the 1- through 6-layer sheets longer pressing times did not affect the density nor the tensile strengths. In contrast, the 8-layer sheet was influenced by pressing time where pressing for 1 hour developed a higher strength (197 ± 7.7 MPa) which was above the 35 minutes case (177.9 ± 13.9 MPa), and the 2 hours case (179.1 ± 11.0 MPa). The decrease in strength experienced by the 8-layer sheets was likely generated during sheet processing, a result of having a greater volume or mass of water being pressed together and removed from the structure. When the stacked wet structure was pressed, the CNF layers started sliding out of the mold (Figure A. 7). The mass movement likely formed different aggregates within the sheet, which after full consolidation of the web, developed into weaker sites where failure is more likely to occur. Furthermore, the movement of CNF when pressing will usually manifest as a slightly rougher sheet surface, which was observed in all 8-layer sheets. A solution to this is to apply slow and controlled pressing to compress the layers more

slowly as the water evaporates. Additionally, the density of all the specimens was not affected and remained statistically equivalent between all pressing times, hence water was not likely retained within the thicker specimens.

For sheets with 1-, 2-, 3-, 4-, 5-, and 6-layers the tensile elastic modulus remained constant at around 11.0 ± 0.9 GPa and decreased to 8.86 ± 0.3 GPa for the 8-layer sheets for all pressing times. The modulus for all sheets (e.g., hot pressed, constrained drying) was slightly lower than that of the baseline (1-layer, 0 MPa unconstrained drying) with a modulus of 12.6 ± 0.8 GPa, yet equivalent to that of the 80 ± 3 μm thick solution cast CNF film (11.04 ± 1.7 GPa) (Figure 2.7 A). Overall, the values obtained for the sheets (1- through 6-layers) were equivalent to what other authors have obtained for thin solution cast and pressed-dry CNF films⁵⁷⁻⁵⁹. The higher modulus obtained for the baseline (loosely constrained (~ 0 MPa) 1-layer sheet) was unexpected as it did not possess noticeable fibrillar alignment, which could have led to a higher modulus, as verified by SEM of the surface (Figure A. 8)^{59,60}. In contrast, there was a slight decrease in modulus seen for the 8-layer sheets, as compared to the thinner sheets (1- through 6- layers), which could possibly result from the formation of defects and nonbonded sites throughout the laminated structure or slippage at the grip sections during tensile testing due to the increase of load required to test the thicker specimens. Moreover, other authors have shown that constrained drying (i.e. hot-pressing) does not have an effect on the elastic modulus⁶⁰. When comparing between the different pressing times there appears to be no statistical difference for the elastic modulus between specimens with 1-, 2-, 5-, and 8-layers. The exceptions were the 3-layer/2-hours that was higher than the 35 minutes and 1 hour, the 6-layer/1-hour case that was lower than that of the 35-minutes and 2-hours, and the 4-layer/1-hour that was higher than the other two pressing times.

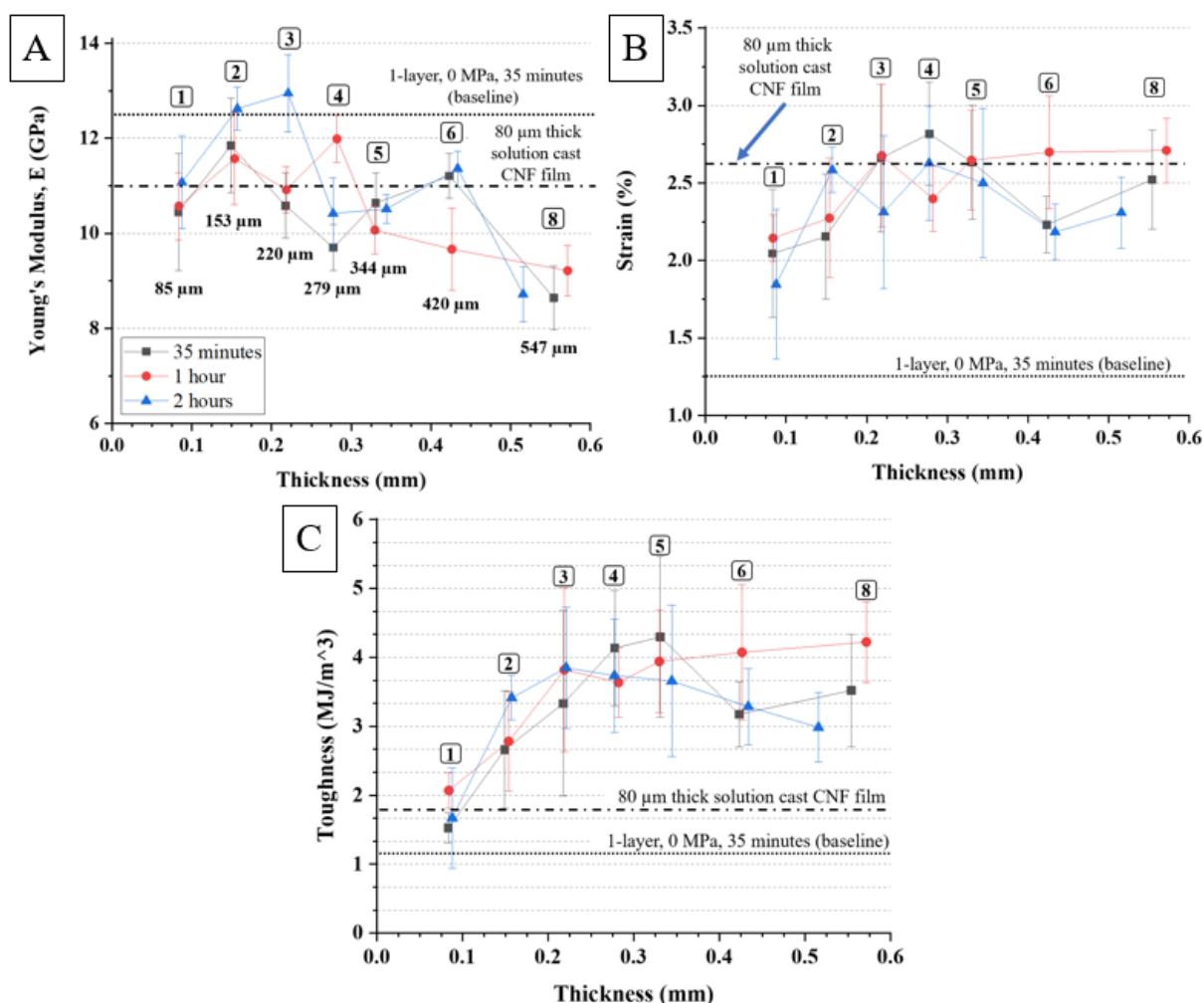


Figure 2.7 Scatter plot of A) Young's modulus versus thickness, B) strain versus thickness, and C) toughness versus thickness for 35 minutes, 1 hour, and 2 hours press time. All the sheets were hot pressed at 0.36 MPa and 126 °C. The baseline represents a single CNF layer processed at a pressure of 0 MPa and a temperature of 126 °C for 35 minutes. The second dashed line represents an 80 μ m thick CNF solution cast film.

For all pressing times, strain to failure increased from $\sim 2.01 \pm 0.15$ % for 1-layer sheets to a constant value of $\sim 2.50 \pm 0.21$ % for 2-, 3-, 4-, 5-, 6-, and 8-layers sheets, which was equivalent to that of the solution cast CNF film (~ 80 μ m thick) with a strain to failure of 2.58 ± 0.55 % (Figure 2.7 B). The increase in strain to failure for the 2- to 8-layer sheets could originate from the fact that the more efficiently packed fibrils (e.g., higher density sheets) utilize more of their active surface area and better distribute the load (e.g., effectively lowering stress concentrations within sample) or that the nonbonded sites within the multi-layer sheets give more flexibility to the structure. These results also indicate that while constrained drying lowers strain to failure for 1-

layer sheets, it can be recovered if the CNF structure is made thicker by adding more sheets. Furthermore, other authors have shown that CNF films with lower densities experienced greater axial strain variations over the specimen surface which could lead to early failure⁶⁰. This phenomenon is likely due to higher porosity and defects which act as stress concentration zones and could explain why 1-layer specimens fail first. Conversely, lower strain variations and smaller porosity/defects experienced by thicker sheets (greater than 1-layer) translate to a better distribution of the applied load which suppresses early crack initiation and failure. When comparing different pressing times there appears to be no statistical difference for the strain to failure between specimens with 1-, 2-, 3-, 4-, and 5- layers. The exceptions were for the 6-layer and 8-layer sheets where the 1-hour pressing time resulted in higher strain to failure than the 35 minutes and 2 hours, pressing times. It is unclear why this is the case at this time.

Similarly, for all pressing times, the apparent toughness (work-of-failure) of the sheets increased from $1.75 \pm 0.28 \text{ MJ/m}^3$ (1-layer) to $3.53 \pm 0.36 \text{ MJ/m}^3$ for sheets with more than 1-layer (Figure 2.7 C). The increase is likely physically linked to the higher density, and lower critical defect size in a similar manner to strength as it is known that toughness scales with strength in brittle materials from Griffith's energy criterion⁶¹. When comparing different pressing times, there appears to be no statistical difference for the apparent toughness of the specimens with 1-, 2-, 3-, 4-, and 5-layers. The exceptions were for the 6-layer and 8-layer sheets where the 1-hour pressing time resulted in higher apparent toughness than the 35 minutes and 2 hours, pressing times. It is unclear why this is the case at this time.

2.3.4 Loading rate effect on the mechanical properties of CNF sheets

The loading rate at which the wet sheets are pressed is a crucial processing parameter that must be carefully monitored to avoid any mass movement before full web consolidation. Ideally, the loading rate is fast enough to keep the desired pressure on the surface of the sheet but not so much as to initiate any mass moment (i.e., over pressing). Achieving this balance becomes increasingly challenging as water evaporates from the CNF sheets at uncontrolled rates. This is especially true for multiple layer sheets as more water (90 wt.% per layer) is essentially stacked together and over pressing is easily initiated which causes severe damage to the structure of the sheet (Figure A. 7). Two 4-layer sheets (279 μm thick) pressed at two different rates show how the sheet quality is affected (Figure 2.8). For the fast loading rate, an applied pressure of 0.36 MPa

was reached within 20 seconds (Figure 2.8 A) while for the slow pressed case it took 4 minutes (Figure 2.8 B). A very bright light was applied to the back of the 20 second sheet to better view the in-bulk aggregates formed due to the mass movement and the formation of a nonhomogeneous structure. It is important to note that the CNF movement is suppressed at the center of the 20 second sheet while it increases at the edges which is typical for materials undergoing elongational flow and more specifically biaxial flow⁶². Optical profilometry captured the surface roughness of the fast pressed and slow pressed sheets at the center and edge (Figure 2.8 C, Figure 2.8 D, Figure A. 9 A, and Figure A. 9 B). When the two sheets are compared, the roughness increased from $\sim 3.1 \mu\text{m}$ to $\sim 11.4 \mu\text{m}$ at the center and from $\sim 2.8 \mu\text{m}$ to $\sim 13 \mu\text{m}$ at the edge which confirms the excessive CNF movement and deformation caused in the bulk of the fast-pressed sheet.

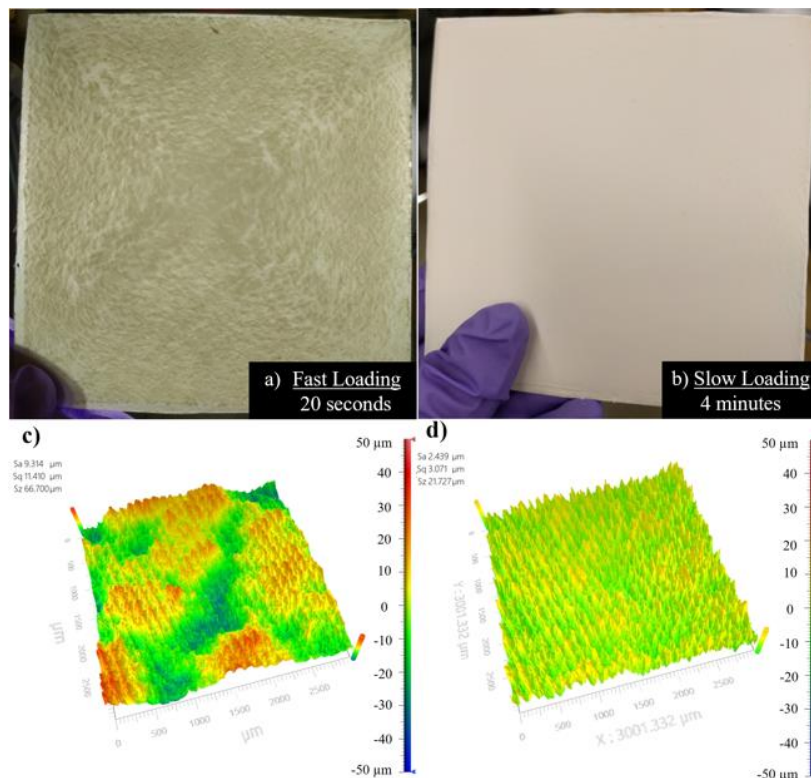


Figure 2.8 Photograph of four-layer CNF sheets pressed at a fast loading rate (A), slow loading rate (B) and optical profilometry (2.75x) of the center of the pressed sheets (C), and (D). Both sheets were pressed for 35 minutes at a temperature of 126 °C. The surface roughness at the center of the sheet increased significantly for the fast-pressed specimen ($S_q = 11.410 \mu\text{m}$ versus $S_q = 3.071 \mu\text{m}$).

Additionally, the results for three 4-layer sheets pressed at different rates show that the fastest loading rates lower the ultimate strength (Figure 2.9 A). Similarly, the elastic modulus appears to decrease slightly as the loading rate is increased (Figure 2.9 B). The decrease in mechanical properties at higher loading rates can be explained by the much greater surface roughness in the 20 second pressed sheet, as compared to the 4-minute specimen. The increase in surface roughness can be linked to a larger surface defect size that act as larger critical stress concentration points, and thus attain a lower ultimate strength as fracture will occur at a lower applied load.

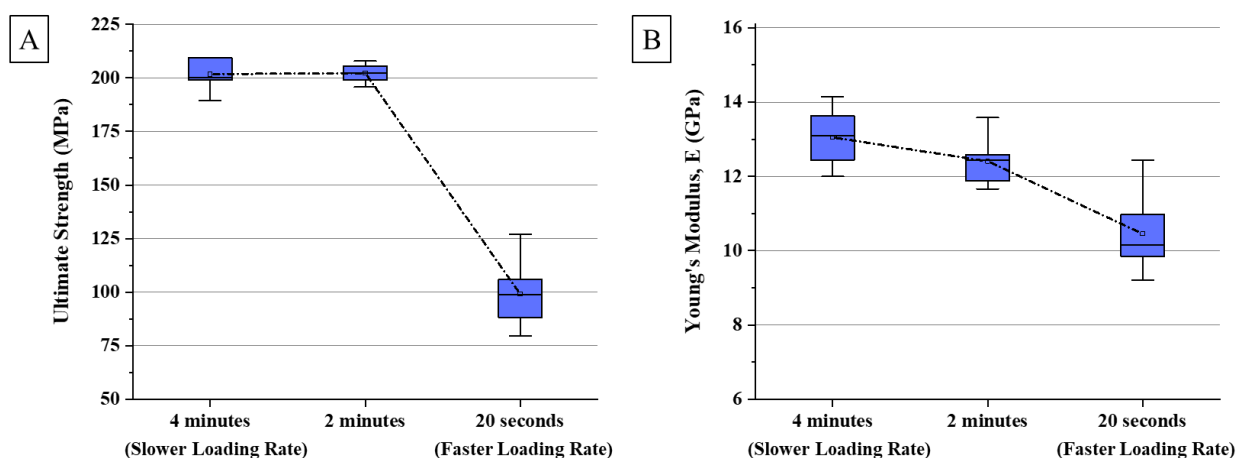


Figure 2.9 Boxplots of A) ultimate strength vs loading rate and B) Young's modulus verses loading rate for 4-layer CNF sheets pressed at different loading rates. For each case, the sheet was pressed to 0.36 MPa for 35 minutes at a temperature of 126 °C. The dashed line is just a guide connecting the data sets.

2.3.5 Pressing pressure rate effect on the mechanical properties of CNF sheets

Due to the strong correlation between strength and density (Figure 2.6), densification was desired hence higher pressing pressures of up to ~5.17 MPa were probed. The results show that the strength started to decrease at pressures higher than 1.43 MPa (Figure 2.10 A). Moreover, at higher pressures (5.17 MPa or greater) the rubber pads started deforming and impregnating the metal mesh which damaged the CNF sheets (Figure A. 10 A). This caused the strength to decrease to a value of 124.3 ± 8.4 MPa. Loosely constrained (~0 MPa) 4-layer samples showed the appearance of bubbles within the sheet; hence some pressure is ultimately required to suppress bubbles and other defects like wrinkling (Figure A. 10 B). It is important to note that the sheet

defects heavily decreased the mechanical performance, yet the density was not affected until the pressure was above 3.59 MPa or below 0.36 MPa. For example, the 3.59 MPa specimens had a density of 1.34 ± 0.03 g/cc which was equivalent to that of the loosely constrained (~ 0 MPa) specimens (1.35 ± 0.08 g/cc) (Figure 2.10 B). On the other hand, the ultimate strength of the 3.59 MPa specimens was 197.8 ± 7.3 MPa which is higher than that of the loosely constrained (~ 0 MPa) pressed samples (173.4 ± 8.55 MPa). The results also show that an applied pressure of 0.36 MPa is enough to develop the highest ultimate strength and hence it was selected to process all previous hot-pressed sheets in the thickness study. Though densification at higher pressures was not achieved in this study, it may be possible if high pressure bearing rubber pads and meshes are used. Sample area can also be further reduced to increase pressure, yet fewer samples will be generated per sheet.

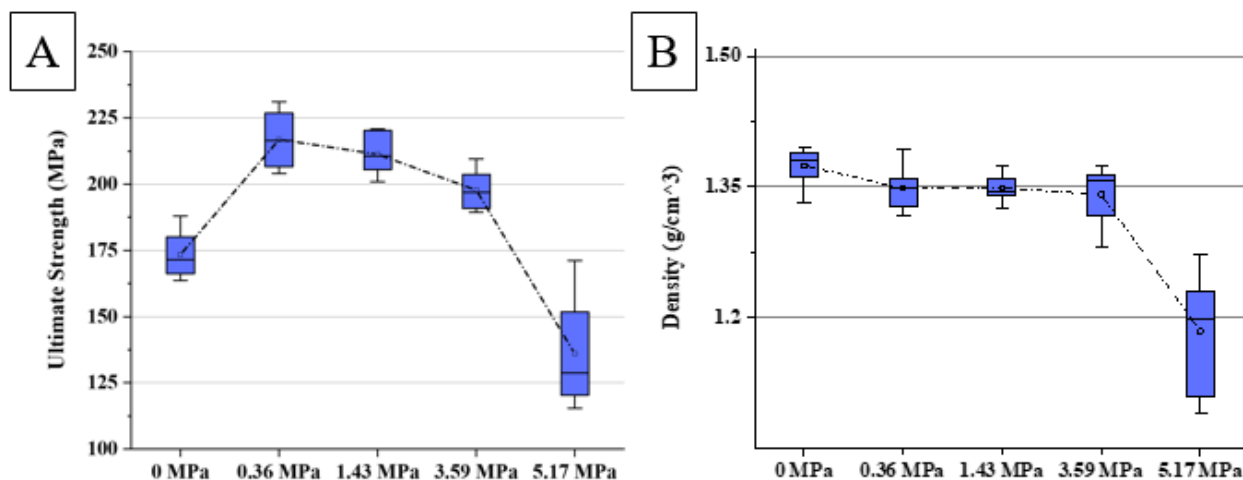


Figure 2.10 Box plot of a) ultimate strength versus pressing pressure and b) density versus pressing pressure. All the 4-layer sheets were hot pressed for 35 minutes at temperature of 126 °C after reaching the respective pressure. The 0.36 MPa case is also shown and represents the baseline as it was the pressure utilized for all other studies.

2.3.6 Fracture analysis of CNF sheets

The fracture surface of the specimens was analyzed to gain a better understanding of the possible causes for early failure of the 1-layer sheets (i.e., lower strain %). As seen, the 1- and 2-layer specimens presented a fibrillar fracture surface with fibrils pointing in the loading direction which was identical to that of the 6- and 8-layer specimens (Figure 2.11). The fracture surfaces appear to have a layered structure which is similar to the fracture surfaces of CNF films prepared

by other methods like solution casting as reported by other authors³⁵. Due to the similarity between the fracture surfaces, there was no discernable influence of the presence of the layers nor interfacial defects, to cause early failure or lower strength values for thinner specimens. Hence, making the thicker specimens seems to conserve the fracture behavior and no interlayer delamination is observed in the fracture zone.

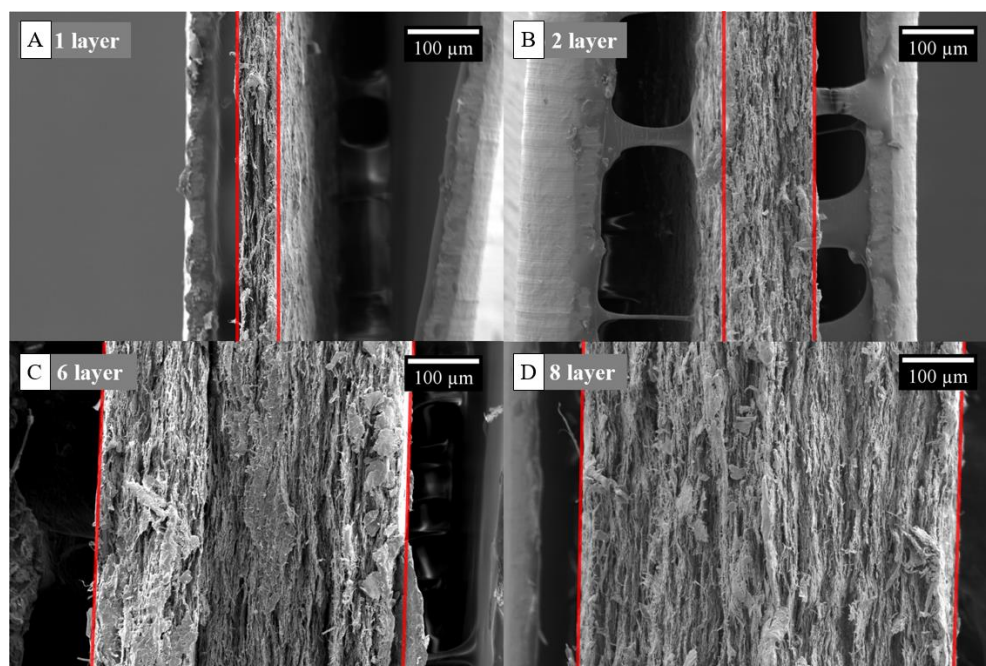


Figure 2.11 SEM microphotography of the fracture surface of A) 1-layer, B) 2-layer, C) 6-layer, and D) 8-layer dogbone specimens. As seen, all the specimens presented a paper like fracture with fibrils pointing in the loading directions. The red lines highlight the analyzed fractured surface.

2.3.7 Benchmarking the performance of CNF sheets

Commodity polymers like poly(styrene) (PS), and nylon 6,6, and structural metal alloys like aluminum 2124 (T3), and aluminum 6061 (T6) were tested for comparison. Based on the thickness studies previously presented, a 4-layer CNF sheet was selected because the mechanical performance is assumed to be fully developed at this thickness. Table 2.3 below compiles all the mechanical properties of the different materials studied. The results show that the CNF sheet is superior to PS and Nylon 6,6 in both ultimate strength and elastic modulus. The opposite is true when the sheet is compared to Al 2024, and Al 6061. However, when the density of the materials

is considered, as for specific strength, the results show that the CNF sheet is comparable to Al 2024 (T3). This means that CNF sheets are a strong light weight material which could serve in structural applications. When looking at toughness, the results show that the CNF sheet was on average ~6.7 times tougher than PS. On the other hand, nylon 6,6, Al 2024, and Al 6061 had a toughness which was roughly 9, 11, and 6 times higher than that of the 4-layer CNF sheet (Table 2.3). The reduced toughness is linked to the small strain to failure seen for the CNF specimens which was expected due to the short nature of the CNF fibers as the mechanism for failure is fibrillar sliding and rupture³⁵. The stress-strain curves of the compared materials (CNF sheet, PS, Nylon 6,6, Al 2024, and Al 6061) can be found in Appendix A (see Figure A. 11).

Although the direct comparison of CNF sheets to tempered aluminum alloys (2024 and 6061) showed inferior properties in term of toughness, the extraction of CNF and its processing places a significantly lower burden on the environment. This is due to the extraction of bauxite which requires mining and its processing (Hall-Heroult process) that requires significant electrical energy (12.9 - 17.0 kWh/kg for aluminum verses 2.5 kWh/kg for CNF)^{8,63}. Additionally, the inherent sustainability of CNF holds a major advantage over tougher commodity polymers like nylon 6,6.

Table 2.3 Comparison table containing the measured mechanical properties of PS, Nylon 6,6, Al 2024, Al 6061, and CNF sheets (4-layer). The units of specific strength, modulus, and toughness are MPa/(g/cm³), GPa/(g/cm³), and (MJ/m³)/(g/cm³)

Material	Density (g/cm ³)	Ultimate Strength (MPa)	Young's Modulus (GPa)	Strain to Failure (%)	Toughness (MJ/m ³)	Specific Strength	Specific Modulus	Specific Toughness
CNF sheet (4-layer)	1.35	209.2±6.6	10.7±1.2	2.61±0.21	3.84±0.3	154.96	7.93	2.84
Poly(styrene)	1.05	10.9±1.3	1.8±0.02	4.53±0.80	0.57±0.13	10.38	1.71	0.54
Nylon 6,6	1.31	44.9±0.3	1.36±0.08	74.5±5.67	34.80±1.85	34.27	1.04	26.56
Al 2024 (T3)	2.78	431.3±29.6	58.5±0.3	106±2.82	41.55±0.92	155.14	21.04	14.95
Al 6061 (T6)	2.7	254.3±24.1	61.4±2.3	7.57±0.55	22.95±1.1	94.19	22.74	8.50

2.4 Conclusion on the processing and performance of thick CNF sheets

In this study, the fabrication of multi-layered CNF sheets was assessed. The developed four-step process allowed for the creation of mechanically strong (ultimate strength = 207 ± 2.5 MPa), light weight ($\rho = 1.35 \pm 0.02$ g/cc), and tough (3.53 ± 0.36 MJ/m³) pure CNF sheets in under two hours. These sheets could serve in high-strength and low-density structural applications where

aluminum alloys (2024 and 6061) and packing materials/containers where commodity polymers like poly(styrene) are currently used. A significant advantage of wet stacking lamination over conventional CNF film making techniques was found to be that it enabled the filtration through pre-stacked wet CNF layers rather than a thick CNF cake. Pre-stacked filtration avoided extending processing times, hence a CNF sheet with a thickness of 1.65 ± 0.02 mm (24-layers) was made in under 7 hours. Evaluation of the mechanical properties of the produced sheets showed that a plateau in ultimate strength of 207 ± 2.5 MPa was reached at a critical thickness between 85 ± 2 μ m (1-layer) and 153 ± 4 μ m (2-layers) for all pressing times investigated (35 min, 1 hour, 2 hours). On the other hand, sheets with a thickness 547 ± 29 μ m (8-layers) appeared to have a slightly lower mechanical performance possibly due to CNF movement during pressing. It is believed that the observed inferior mechanical behavior of thinner specimens (1-layer sheets) could be explained by the greater axial strain variations, larger porosity, and lower densities which lead to an early fracture. Additionally, loading rates greater than 2 minutes and pressing pressures of 0.36 MPa proved to be the optimal values to develop the highest possible mechanical properties. Moreover, this study demonstrated that sustainable and biofriendly nanosized polymers like CNF can be turned into larger structures with improved mechanical performance.

2.5 Acknowledgements

The authors would like to acknowledge the financial support from the US Endowment and the Public-Private Partnership for Nanotechnology (Grant Number: 109217) and the National Science Foundation-Integrative Graduate Education and Research Traineeship: Sustainable Electronics (Grant Number: 1144843).

Additionally, the authors would like to thank Dr. Srinivasan Chandrasekar for making the optical profilometer equipment available and Mojib Sae for conducting and guiding the optical profilometry analysis and characterization.

3. CONTINUOUS PROCESSING OF CNF SHEETS

In the presented work, all the laboratory experiments and work in this chapter was performed by Sami M. El Awad Azrak. The manuscript writing and submission was done by Sami M. El Awad Azrak. Dr. William Costakis performed the torque rheometer rheological analysis and revised the manuscript. Dr. Youngblood, Dr. Moon, and Dr. Schueneman provided guidance on the research direction and on all writing.

This chapter contain content reproduced with permission from El Awad Azrak, S. M.; Clarkson, C. M.; Moon, R. J.; Schueneman, G. T.; Youngblood, J. P. *ACS Appl. Polym. Mater.* **2019**, *1* (9), 2525–2534. Copyright 2019 ACS Applied Polymer Materials.

3.1 Introduction

Current laboratory techniques like solution casting used to process self-standing CNM films often require long lead times (hours to weeks) for complete water removal through controlled evaporation. Other methods employ the use of vacuum filtration or heated pressing (or a combination of the two) to accelerate water removal and consolidate the structure^{1,20,35,46,64}. While laboratory methods can process more specialized batches of materials for research purposes, they remain largely semiautomatic and are not industrially viable. In contrast, continuous papermaking methodologies can indeed offer a solution to small batches, but the current machines have a difficult time of effectively dewatering CNMs due to CNM's increased water retention capacity when compared to typical bleached pulp⁶⁵. This means that current papermaking lines will need to be modified and the initial capital investment will be higher, which might deter industrial adoption. Alternatively, approaches to continuously process CNMs in bulk through melt processing techniques have been reported but there are still limitations.

Bulk processing of CNMs have mainly focused on the formation of cellulose nanocomposite films or sheets by first compounding CNMs and a matrix polymer using an extruder and subsequently compression or injection molding the compounded material into shape⁶⁶. These methods have been successful at incorporating CNF, using a twin screw extruder, into different polymeric matrices like thermoplastic starch (TPS), polyvinyl acetate (PVAc), polylactic acid (PLA), and others^{33,67–70}. Though successful at continuous processing, extrusion of cellulose nanocomposites is largely limited by the incompatibility between the hydrophilic reinforcing phase (e.g., CNMs) and the hydrophobic matrix (e.g., synthetic polymer). Hence, the addition of higher contents (>20 wt.%) of CNMs into a synthetic polymer matrix eventually leads to aggregation and

the low contents of the CNM needed for processing lowers the mechanical properties of the nanocomposites³³. Furthermore, extrusion processes typically require a meltable phase while CNMs and cellulose derivatives reach their degradation temperature (T_d) before reaching their melting temperature (T_m) which limits both the processing temperature window and the possible synthetic matrices ($T_{m, \text{polymer matrix}} < 200\text{ }^{\circ}\text{C}$)^{71,72}.

One solution to this complex processing problem is to bulk process CNMs without the use of any synthetic polymer matrix (i.e., ~100 % pure CNMs structures). This eliminates incompatibility issues with hydrophobic polymer matrices and gives the ability to take full advantage of the impressive CNM properties. It also allows processing of CNM at a lower temperature. However, processing ~100 % pure CNMs structures introduces new challenges; the first being the inability of pure CNMs to melt and form entangled polymer networks, hence similar viscoelastic properties to polymer melts are hard to achieve and have not been reported. Second, due to the isolation processes used to extract CNMs, a significant amount of water is retained by CNMs (>80 wt.% water) and must be removed, hence a high hydraulic capacity is needed during processing and forming¹. Freeze drying methodologies to remove almost all of the water (can achieve ~96 wt.% solids content) have been developed, yet careful control is needed to avoid permanent aggregation of the CNMs and surfactants are sometimes needed and must be removed following rehydration^{73,74}. Lastly, CNM slurries are two phase materials composed of cellulose nanoparticles and water, which makes the rheological control more complex during processing⁷⁵. Although challenging, extrusion of mostly pure CNMs will open up new ways towards bulk continuous processing that are otherwise not be possible with batch based or semiautomatic techniques currently used.

In this chapter we report both the first continuously processed wet CNF sheet using conventional single-screw extrusion and the first preparation of highly loaded CNF pastes (~91 wt.% CNF, up to 25 wt.% solids) using a shear mixer. The results showed that highly loaded CNF pastes containing small concentrations of a processing aid (≤ 9 wt.% of carboxymethyl cellulose (CMC), xanthan gum (XG), or anionic polyacrylamide (aPAM)) can be produced in under 40 minutes using a standard shear mixer saving up to 40 days in preparation and drying time. The mixing procedure was validated against typical air drying to achieve higher solids loadings in CNF/processing aid pastes. Extrusion of the prepared pastes showed that cohesive sheets could be produced continuously at output rates of ~7.45 kg/h (or ~1.14 kg/h dry) without the introduction

of surface defects. Wet extrudates with an average length of 0.61 m (~2 ft), width of 5.1 cm (2 inches), and thickness of 1.46 ± 0.05 mm were continuously processed, limited only by the system in use. Tensile testing of the pressed and heated extrudates revealed equivalent mechanical properties to cast CNF films prepared through conventional solution casting. More broadly, the results presented show that it is possible to utilize common polymer processing methods for CNF from beginning to end of the processing chain allowing the potential to significantly increase processing rate and lower cost associated with typical CNF processing.

3.2 Experimental section; Materials, Methods, and Characterization

3.2.1 Materials

Carboxylated methyl cellulose sodium salt powder (e.g., CMC) was purchased from Alfa Aesar (Lot#R07E012, D.S 0.69, $\eta = 660$ mPa*s at 1% v/v at 25 °C, $M_w \sim 150,000$ to 180,000). An anionic polyacrylamide (aPAM) “water in oil” type emulsion (Nalclear™ 7768) was kindly supplied by Nalco Water (EcoLab). The solids content of the aPAM emulsion was found to be ~32 wt.%. The average molecular weight of the polyelectrolyte (aPAM) was not measured, but it is generally expected to be at least in the millions range and has a linear molecular structure⁷⁶. Xanthan Gum (XG) from *Xanthomonas campestris* was purchased from Sigma-Aldrich (Lot#SLBZ5317, $\eta = 800$ to 1200 mPa*s at 1% v/v at 25 °C, M_w was not supplied but has been reported to vary between 300,000 and 7.5×10^6)⁷⁷. Hydroxyethyl methyl cellulose powder (product no. 435015), hydroxyethyl cellulose powder (product no. 09368), poly(ethyleneimine) solution (50 % H₂O, $M_w = 750,000$), and polyacrylic acid sodium salt solution (45 % H₂O, $M_w = 8,000$) were purchased from Sigma-Aldrich. Tragacanth gum powder (product no. A18502-22) and methyl cellulose powder (product no. 43483) were purchased from Alfa Aesar. Amphoteric starch powder (Chargemaster® R25F, D.S. 0.027) and cationic starch powder (Chargemaster® R33F, D.S 0.032) were kindly supplied by Grain Processing Corporation. Carbopol 940 (powder) was kindly supplied by Lubrizol. Carrageenan-lambda (Viscarin GP 5015) was kindly supplied by DuPont. Food grade konjac glucomannan powder and guar gum powder were both purchased from regional stores. Mechanically fibrillated CNFs produced at the Process Development Center (PDC) were bought from University of Maine, Orono, ME, USA at two different solids concentration, 3.1 wt.% (Batch #110, 90% retained fines) and ~23.5 wt.% (Batch #122) both in water⁷⁸. This variety

of CNF is more coarse (e.g., diameter ~ 20 to 100 nm) and branched (e.g., thicker central fibril with thinner fibrils extending off), this material often has been referenced in the literature as cellulose microfibrils (CMF)⁴. The process of isolating/making the CNF slurry is explained in detail by C.A. de Assis et al⁸. The CNF was used as delivered without any surface or solvent modification/exchange and mixed with the respective processing aids at different ratios by dry weight.

Two stainless steel meshes (“Dutch weave”, 316SS) with a mesh size of 165x800, and two temperature resistant silicone rubber sheets with a hardness of 60A were purchased from McMaster Carr Supply Company, Elmhurst, IL, USA. Both materials were cut down to a square size of 115x115 mm (LxW) and used for pressing the extrudates.

3.2.2 Preparation of CNF/Processing Aid Suspensions for Centrifugation and Zeta Potential

CNF plus processing aid suspensions for centrifugation/separation column test were prepared by first fully dissolving the processing aid in water and then mixing it with a CNF slurry at 3.1 wt.%. Two different dry weight ratios of processing aid to CNF of 0.1:1 and 0.05:1 were prepared. The suspensions were shear-mixed using a SpeedMixerTM (Flacktek Inc.) system at 2500 rpm for 15 minutes. Subsequently, 35 ml of the suspensions were loaded into 50 ml centrifugation tubes (Falcon®) and centrifuged (HERMLE Z300, Hermie Labortechnik GmbH, Germany) at 4500 rpm for 30 minutes (RCF ~3500). The separated water was weighed on an analytical balance and recorded.

Suspensions for zeta potential analysis were prepared identically to the suspensions intended for centrifugation with a processing aid ratio to CNF of 0.05:1 yet diluted with deionized water from a ~3 wt.% solids concentration to 0.13 wt.%. Once the water was added the suspensions were shear mixed at 4500 rpm for 3 minutes. A transfer pipette (3 ml) was used to transfer the suspensions into the disposable capillary cells.

3.2.3 Preparation of extrusion pastes

Pure CNF with a solids concentration of 10, 17, 20, 24, and 30 wt.% were prepared by air drying an initial 3.1 wt.% CNF slurry at room temperature. Following drying, the pastes were

blended using a common household blender until fully homogenous. The pastes were then extruded.

CNF/processing aid pastes (CNF/CMC, CMC/XG, and CNF/aPAM) with solids concentration of ~15.32 wt.% or greater were prepared using a high shear torque mixer (Plasti-Corder PL 2100 Electronic Torque Rheometer, C. W. Brabender, South Hackensack, NJ) equipped with Banbury type mixing blades. Geometrical data as well as a detailed schematic of the setup are presented in other literature⁷⁹. All the CNF/processing aid pastes were prepared by first adding 52 grams of CNF with a solids concentration of ~23.5 wt.% into the mixer. The added CNF was mixed at 120 rpm and a temperature of 60 °C until the output torque curve reached a plateau, which on average took ~5 to 8 minutes as shown in Figure 3.1. After reaching the torque plateau, the required amount of processing aid was gradually added in smaller discrete steps to the paste until a ratio of 0.05:1 or 0.1:1 was reached (aid:CNF, both dry weight). It is important to note that adding the processing aid caused a significant drop in torque. Water was added as needed into the paste to control the final solids concentration and replace the lost water during mixing (~1 wt.% solids increase for a mixing time of 40 min). During mixing, the rotor speed was held at 120 rpm for CNF/CMC pastes and was lowered to 20 rpm for CNF/XG and CNF/aPAM pastes to avoid improper mixing due to the material sticking or slipping at the mixing blades. The pastes were mixed until the processing aid was fully incorporated into the paste. For all processing aids, full incorporation was signaled by a steady rise in torque and a secondary plateau (Figure 3.1). It is important to point out that if the torque plateaus are not reached the processing aid will not be fully incorporated into the CNF slurry and the resulting pastes will have a grainy consistency (Figure 3.1). Samaniuk et al. investigated in more detail the observed relationships between torque drop, drop time, and processing aid concentration for corn stover pastes in a similar torque rheometer⁸⁰. The total paste preparation time for a single batch (~66 grams at ~15 wt.%) was roughly between ~30 to 40 minutes depending on how quickly the plateaus were reached (Figure 3.1). Unlike CMC and XG, lower concentrations for aPAM were used (0.026:1 and 0.013:1) as aPAM could not be incorporated completely at a ratio of 0.1:1 or 0.05:1 (i.e., the torque plateau will not be reached and resulted in grainy and inhomogeneous paste, Figure B. 1). Figure 3.2 shows a highly loaded paste of CNF/CMC after removal from the mixing cavity. For all concentrations, the mixing procedure was repeated three times to yield enough material to perform both extrusion and rheological analysis. Table 3.1 shows the different pastes prepared for extrusion.

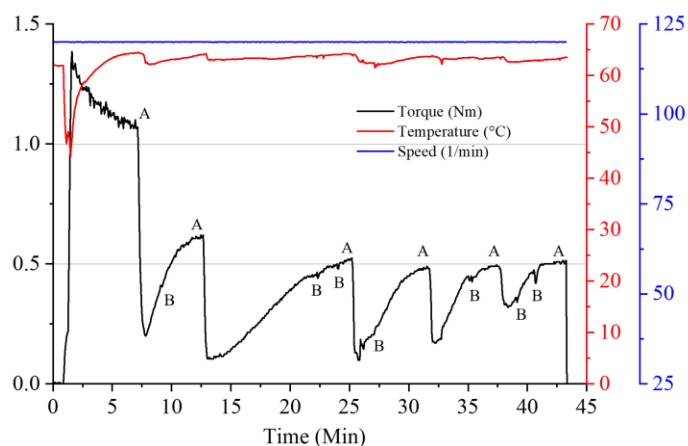


Figure 3.1 Recorded torque (Nm), temperature (°C), and mixing speed (rpm) during mixing of a CNF/CMC paste in a Brabender high shear torque mixer. The “A” points mark the addition of CMC while the “B” points mark the addition of water. The final paste solids concentration was 15.32 wt.% with a CMC to CNF dry weight ratio of 0.1:1. The plateau represents complete polymer incorporation into the paste and depend on the added polymer and final solids concentration of the paste.



Figure 3.2 CNF/CMC paste after mixing and complete CMC incorporation in the mixing chamber (A), wrapped around the mixing Banbury mixing blades (B), and removed from the mixer and shaped into a ball (C). The texture of the paste was very smooth and without any clumps or aggregates.

CNF/CMC air dried pastes denoted by “AD” were prepared by first fully dissolving CMC powder in water to reach a concentration of ~2.0 % (w/v). The viscous CMC solution was then added to a CNF slurry with a solids concentration of 3.1 wt.% to match a dry weight ratio of 0.1:1 (CMC:CNF). Subsequently, the solution was mixed using a planetary SpeedMixer™ (Flacktek Inc.) system at 2500 rpm for 2 minutes and cast into large glass baking trays, crystallization dishes, or 400 ml beakers (Figure B. 2). The pastes were left to dry slowly inside a humidity-controlled chamber (Mettler GmbH + Co. KG, humidity Chamber HCP240) at a temperature of 35 °C, and humidity of 95 %RH until reaching the desired solids concentration.

Table 3.1 Summary table showing all the processed highly loaded extrusion pastes prepared. These pastes were extruded and hot pressed. Enough material for each batch was prepared to perform extrusion and rheological analysis.

Extrusion Paste	Mixture Ratio (processing aid to CNF)	Final Solids Concentration [wt.%]
CNF/CMC	0.1 : 1	15.32
CNF/CMC	0.1 : 1	19.14
CNF/CMC	0.1 : 1	25.31
CNF/CMC	0.05 : 1	15.32
CNF/XG	0.1 : 1	15.32
CNF/XG	0.05 : 1	15.32
CNF/aPAM	0.026 : 1	15.32
CNF/aPAM	0.013 : 1	15.32

It is important to point out that throughout this chapter the word “paste” will refer to CNF/processing-aid mixtures which have a high total solids content and are intended to be extruded. On the other hand, the word “suspension” will be used for low total solids (≤ 3 wt.%) content aqueous-based mixtures like those used for centrifugation, and zeta potential.

3.2.4 Solids content calculation

For all the suspensions and pastes processed, the total solids concentration or solids loading (wt.%) was calculated by weighing roughly 1 g of the suspension, paste, or extrudate and then drying in an oven overnight (> 12 h) at $110\text{ }^{\circ}\text{C}$ with subsequent re-weighing.

3.2.5 Preparation of cast CNF films

Cast CNF films were prepared by casting 40 grams of a CNF/water suspension with a total solids concentration of 1 wt.% into a 90 mm diameter polypropylene Petri dish. The Petri dishes were left to dry at in a humidity controlled chamber (35 %RH, $25\text{ }^{\circ}\text{C}$) for over 7 days. Once dried the films were easily delaminated from the petri dish.

3.2.6 Torque Viscometry of CNF/CMC, CNF/XG, and CNF/aPAM

A Brabender torque rheometer (Plasti-Corder PL 2100 Electronic Torque Rheometer, C. W. Brabender, South Hackensack, NJ), equipped with roller head blades, was used to measure the viscosity-shear rate dependence of the CNF/CMC, CNF/XG and CNF/aPAM pastes. Examples

from the literature^{79,81–86} have shown that small chambered torque rheometers are a practical means to obtain the viscosity-shear rate behavior of polymer-based systems. Recently, Santi et al.⁸⁶ proposed that the torque-temperature dependence must be characterized to correct the final viscosity data for viscous dissipation effects. The analysis used in this study was slightly modified from the process described by Costakis et al.⁸⁷ and the details are explained below.

For the analysis, the sample chamber was loaded to 70 % of the total volume (60 cm³) with the CNF/processing aid paste and mixed at an initial temperature of 21 °C with a roller speed of 10 rpm for 7 minutes. Once the torque and temperature were stable, the torque data was collected at 21, 28, and 32 °C for three minutes to characterize the torque-temperature dependence. The viscosity temperature sensitivity constant (b) was obtained from an exponential fit of the torque vs temperature graph. This constant was used in Equation 3.1 to correct the measured viscosity data for temperature increases due to viscous dissipation:

Equation 3.1

$$\Gamma(T) = \Gamma(T_0) \exp[-b(T - T_0)]$$

where $\Gamma(T)$ is torque as a function of temperature, T is the set temperature, and T_0 is the measured temperature of the blend.^{86,87} After the torque-temperature analysis, the sample was removed and replaced with another sample from the same batch to reduce drying effects. Then, the temperature was set to 28 °C and the roller speed was decreased to 10 rpm. Torque data was collected at 10, 20, 30, 50, 70, and 90 RPM in three-minute intervals to obtain the torque-rpm dependence of each blend. The calibration and analysis suggested by Bousmina et al.⁸³ was applied to obtain the shear-rate and viscosity data. The details for the calibration process and calculating the effective equivalent internal radius (R_i) are explained in detail by Costakis et al.⁸⁷ Once R_i was obtained it was used in the following equations to calculate the shear rate from Equation 3.2 and viscosity from Equation 3.3 for each paste. The log(viscosity) dependence on log(shear rate) was linearly fit to obtain the power law index (n) and melt consistency index (m) for each paste.

Equation 3.2

$$\dot{\gamma} \approx \frac{2\pi N}{\ln\left(\frac{R_c}{R_i}\right)}$$

$$\eta = \frac{\Gamma}{N} \frac{\left(\frac{R_c}{R_i}\right)^2 - 1}{8\pi^2 L R_c^2 \cdot (1 + g^2)}$$

In addition to this analysis, a controlled shear stress response rheometry was performed using a Malvern Bohlin Gemini HR Nano Rheometer with a cup and bob fixture (C25 DIN 53019). Aliquots of the highly loaded extrusion pastes (CNF/CMC, CNF/XG, CNF/aPAM) were diluted to 1 wt.%. The diluted suspensions were loaded using a syringe, roughly 12 ml was added. A gap of 150 μm was set for all experiments. A pre-shear of 1 s^{-1} for 60 sec was applied to erase the loading history. A shear range of 0.1 to 100 s^{-1} was probed with an integration time of 10 seconds, a delay time of 10 seconds, and 30 sample points. The temperature of the fixture was controlled at 25°C.

3.2.7 Zeta potential

Dilute suspensions of CNF plus processing aid with a final concentration of 0.13 % (w/v) were prepared for zeta potential analysis. A dry-weight ratio of CNF to processing aid of 1:0.05 was used (except for aPAM with a ratio of 0.025:1 due to the high viscosity). A larger CNF content in suspension allowed a good number of particles for scattering (> 100,000 counts/sec) and a lower processing aid content did not significantly increase the viscosity of the suspensions. The viscosity of each different suspension was not measured but assumed to be that of water. The pH of each suspension was measured with a pH meter (HANNA® Instruments). Unless stated otherwise, the pH of the suspensions prepared was 6.4. A total of 6 zeta potential measurements were collected using a Zetasizer Nano ZS (Malvern Panalytical) and disposable folded capillary cells (DTS1070). The average value between all six measurements was taken to be the final zeta potential and the standard deviation was calculated for the measurements.

3.2.8 Extruder configuration and extrusion parameters

The pastes were extruded using the Brabender torque rheometer (ATR) unit with an attached single screw extruder unit (L/D = 25, barrel diameter of 1.9 cm (3/4 inch), and 4 independent heating zones) as shown in Figure 3.3 and Figure 3.4. A conventional 3:1 compression screw was used to extrude all pastes. An adjustable 2-inch-wide slot die/sheet die was attached to

the end of the extruder to form the extrudates into rectangular sheets. The initial width of the slot die (i.e., wet sheet thickness) was adjusted to be 1.131 mm by using feeler gages. For all extrusions performed ~75 grams of the paste were loaded into the feeder section with the use of an in-house made plunger as the ~15 wt.% pastes were too viscous to be gravity fed (Figure 3.3). Roughly 61 cm long sheets were produced for each experiment performed. Unless stated differently, all the extrusions were performed at screw speed of 7 rpm and a temperature of 25 °C in all heating zones (low temperature setting in Figure 3.4). The pressure before the die, screw torque, and barrel temperature was recorded during extrusion.

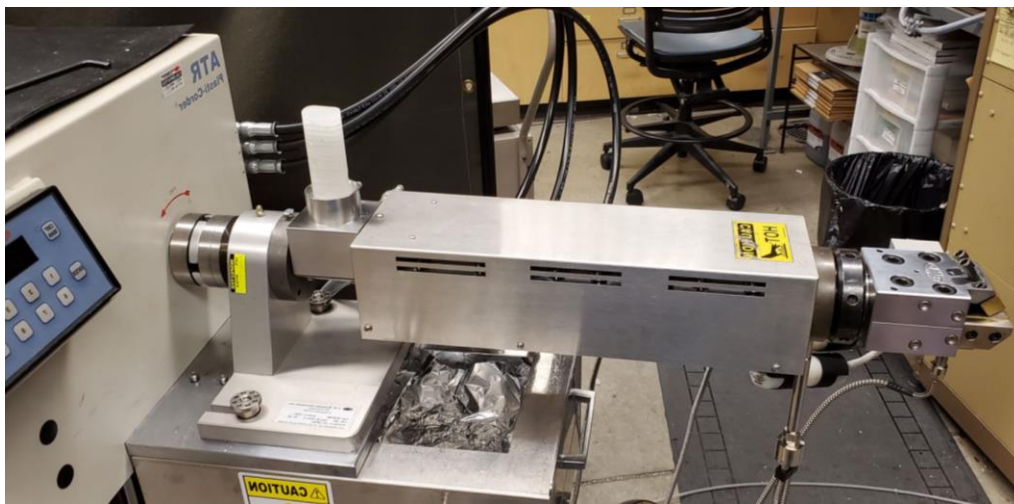


Figure 3.3 Brabender torque rheometer (ATR) unit but with an attached single screw extruder unit ($L/D = 25$, barrel diameter of 1.9 cm (3/4 inch), and 4 independent heating zones). The in-house made plunger used to push the highly viscous CNF/processing aid pastes can be seen in the hopper region.

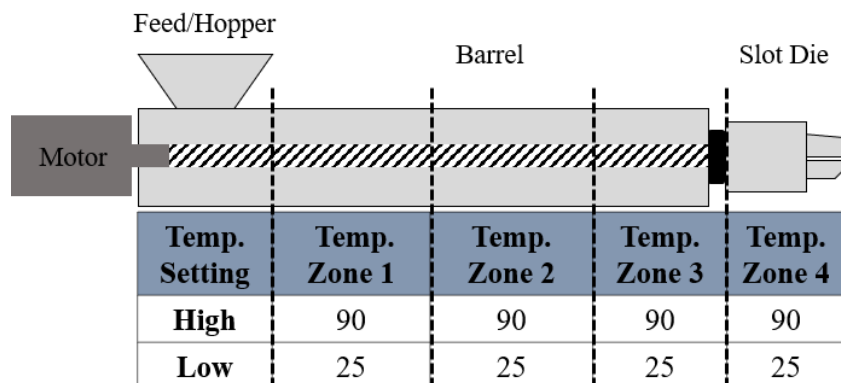


Figure 3.4 Extruder configuration and processing parameters used to process highly loaded CNF/processing aid and pure CNF into wet sheets. The shown temperature is in °C. Unless otherwise stated the screw speed used was 7 rpm for all experiments.

3.2.9 Sample specimen preparation for mechanical tensile testing

The ~61 cm long wet extrudates were cut into smaller ~116 mm long segments. Subsequently two smaller segments were sandwiched between two stainless steel meshes and two silicone sheets (Figure B. 3) and warm pressed at a temperature of 126°C for 30 minutes using a hydraulic heated laboratory press model No. 3690 (Carver). After drying, tensile test dogbones were cut from the sheets in the machine direction (MD) following ASTM D638. The total dogbone length was 92 mm with a neck width of 4.80 mm and a gauge length of 26.40 mm. The dogbones were cut using a laser cutter (Muse Desktop Laser, Full Spectrum LASER, Las Vegas, NV) equipped with a 10.6 μm CO₂ 40 W laser. One to three passes (varied based on solids content of the paste) at 35 % power and 100 % speed were used to cut the samples and reduce damage. For sample conditioning, the cut samples were placed in a desiccator at ~25 %RH for at least 2 days before mechanical testing.

The conditioned dogbones were tested in tension using an electromechanical testing machine (MTS Insight) equipped with a 2000 N load cell and serrated film clamps. To avoid sample slippage during testing, sandpaper was added at the grips. For all samples tested, a preload force of 1 N was applied. The crosshead speed was set to 1 mm/min. The ambient humidity could not be controlled and varied between 30 %RH to 50 %RH, yet large batches of samples (6 to 24 samples) were tensile tested on the same day to reduce variation amongst data sets. Once tested, the ultimate stress or strength (MPa) and strain to failure (%) were taken from the last data point collected. Young's modulus was determined through the steepest slope method. Strain was

measured based on crosshead displacement without the use of an extensometer. The obtained mechanical testing data was collected by the built-in software (TestWorks4®). Grip compliance was measured using a thick 1020 steel specimen and sample data was adjusted accordingly. For density measurement, smaller 8 mm by 8 mm specimens were cut from the same sheet as the dogbones. A caliper and micrometer were used to measure the width and thickness of the squares while the mass was measured using an analytical balance (VWR™).

Lastly, cast CNF films were cut with the same laser cutter but with a reduced 25 % power and a single pass. The dogbone specimens were smaller (37 mm long, a neck width of 1 mm, and a gauge length of 6.50 mm) yet still followed ASTM D638 (type IV). The specimens were tested using a dynamic mechanical analyzer (DMA) model Q800 from TA® Instruments (TA Instruments Inc., Wood Dale, IL). A strain-controlled mode used with a preload force of 0.010N and a strain rate of 0.5 mm/min until failure. Samples were tested at 35 %RH.

3.2.10 Thermogravimetric analysis (TGA)

Thermogravimetric analysis was performed using a thermogravimetric analyzer (TGA) model Q50 from TA® Instruments (TA Instruments Inc., Wood Dale, IL). Roughly 40 to 50 mg of the cast CNF, or warm pressed extrudates were loaded into a platinum pan. Prior to testing all the samples were preconditioned for over a week at 25 %RH. Samples were tested from a temperature of 25 °C to 300 °C at a heating rate 10 °C/min in an oxygen atmosphere.

3.2.11 Scanning electron microscopy (SEM)

Fractured surfaces of the tensile tested specimens were imaged using a Quanta 650 FEG field emission electron microscope. The fractured surfaces were positioned normal to the aluminum stub and secured using carbon tape. The samples were sputter coated (SPI sputter coater) with a platinum-gold target for 60 seconds. No polishing or sanding was used. Samples were imaged at 4 KeV and a spot size of 4. The working distance varied between 9 to 10 mm for highest resolution.

3.2.12 Statistical analysis of tensile testing data

Unless otherwise stated, 6 sample units were tested for each CNF/processing aid paste sample shown in the respective bar graphs. The laser cut specimens were visually inspected for any excessive burn marks or surface defects before performing mechanical testing. Only those with any evidence of defects or any edge burn marks were removed from the sample set. Additional samples were processed to account for any removed sample unit in a sample set. Statistical analysis was performed using OriginPro™. The error bars shown represent one standard deviation (STD) away from the mean value for the data set. A normality test (Shapiro-Wilk, $\alpha = 0.05$) was performed on the data sets to verify a normal distribution followed by a Student's t-test (95 % confidence interval) to determine statistical similarity/difference among data sets or an analysis of variance (ANOVA) with the same confidence level, respectively.

3.3 Results and discussion

3.3.1 Extrusion of pure CNF and processing aid selection

With the primary goal of processing 100% pure CNF sheets, initial attempts to extrude CNF were performed without the use of any processing aid. Extrusion of pure CNF was assessed at six different solids concentrations; 3.1, 10, 17, 20, 24, and 30 wt.% and at two different extrusion temperatures (i.e., 25°C and 90°C processing temperatures, see Figure 3.4). Results show that pure CNF pastes with a solids concentration of 3.1, 10, 17, 20, and 24 wt.% all experienced significant amounts of dewatering. The dewatering raised the total solids concentration of the pastes to roughly ~85 wt.% which clogged the slot die and stopped the process (Figure 3.5 A and Figure 3.5 C). The increased solids loading easily raised the die pressures to the extruder's maximum limitation of ~ 69 MPa (10,000 psi). Furthermore, due to the lack of drainage/solvent ports in the barrel, the extracted water traveled opposite to the extrusion direction and pooled in the hopper region (Figure 3.5 B). The pooling of water caused rehydration of the newly fed material which was unable to push the dewatered material (~85 wt.%) at the slot die. On the other hand, CNF at ~30 wt.% also experienced dewatering yet to a much lower extent and was capable of being extruded into a ~330 mm (13 inch) long sheet (Figure 3.6).

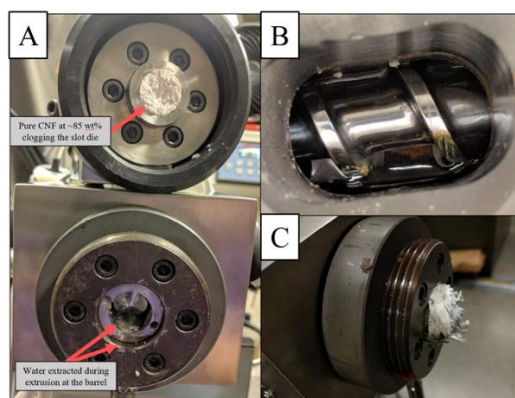


Figure 3.5 Failed attempt at extrusion of pure CNF with a solids concentration of 17 wt.%. The material clogged the entrance of the sheet die (A) and the end of the barrel (C). The clogged and extracted water pooled in the hopped region (B).

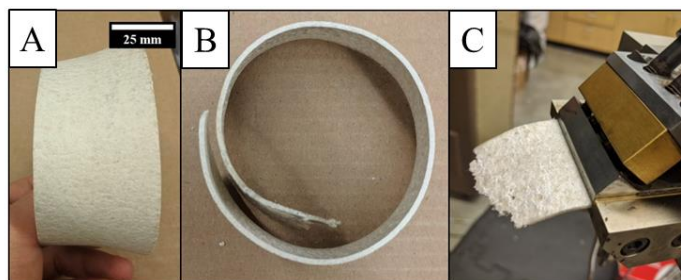


Figure 3.6 Extrudate of pure CNF originally at 30 wt.% solids concentration A) front view (width was ~50 mm), B) side view (thickness ~ 1.1 mm), and C) coming out of the slot die. The extrudate had a solids concentration of ~85 wt.% coming right out of the die. The total length of the pure CNF sheet was ~330 mm (13 inches). The sheet was very fragile and easily broken into pieces.

Extrusion of the 30 wt.% CNF was likely due to the greater water-retention ability of the CNF which reduced both pooling in the hopper and water adsorption/hydration (i.e., it was much harder for CNF to lose or gain water throughout the extrusion process). The increased water retention in cellulose is a phenomenon commonly seen in the papermaking industry where drying rates significantly decrease as the paper web dries. During drying, the paper web experiences permanent structural changes (e.g., hornification) due to the formation of fibril-fibril bonds and a reduction of pore size making for a tortuous path of escape for water⁴⁹. For pure CNF at 30 wt.% it appears that a higher water-retention ability facilitated processability as it was the only paste that did not significantly dewater. On the other hand, hornification could have also restricted the ability of the CNF to reform hydrogen bonds and homogenize (i.e., re-take shape) once the conveyed

material reached the slot die for forming. The inability to retake shape after exiting the die caused an excessive amount of agglomeration/inhomogeneity in the sheet, which made the structure very fragile. Permanent hornification is a problem that has been present in paper recycling where the mechanical properties are reduced due to the irreversible hornification processes and mechanical, and chemical treatments must be used to partly restore the properties^{88,89}.

For pure CNF, a lower solids concentration could possibly be needed for forming and homogenization (i.e., fiber swelling) to occur during extrusion. Additionally, for all CNF loadings assessed, using higher processing temperatures of 90 °C seemed to exacerbate all the problems seen for lower processing temperatures 25 °C. Hence, all subsequent extrusions were done using the lower processing temperature of 25 °C. Due to the prevailing problems during extrusion of pure CNF, a processing aid was desired to address dewatering. Thickeners, viscosifiers, and gelling agents have been used to viscosify suspensions and could serve to aid water retention⁹⁰. Table 3.2 below shows the selected candidates as well as the surface charge and acronym which will be used throughout the report.

Table 3.2 Thickeners, viscosifiers, and gelling agents assessed based on their water-retention ability when incorporated into a CNF slurry. All the selected processing aids are soluble in water at room temperature conditions. Processing aids suspensions which did not experience any perceivable water separation after centrifugation are marked with (*).

Processing Aid	Charge at pH 6 - 7	Acronym
Methyl cellulose	Nonionic	MC
Hydroxyethyl methyl cellulose	Nonionic	HEMC
Hydroxyethyl cellulose	Nonionic	HEC
Guar gum	Nonionic	GG
Konjac glucomannan	Nonionic	KM
Amphoteric starch	+ & -	AS
Cationic starch	+	CS
Poly(ethyleneimine)	+	PEI
Polyacrylic acid sodium salt	-	PAA
Carrageenan-lambda	-	CG-λ
Carbopol 940	-	CP940
Tragacanth gum	-	TG
Carboxymethyl cellulose sodium salt*	-	CMC
Xanthan gum*	-	XG
Anionic polyacrylamide*	-	aPAM

*processing aids which fully suppressed water separation

As a first approach, water-retention ability of the suspensions containing viscosifiers was assessed through centrifugation. This approach is essentially an accelerated separation column test which bypasses particle diffusion and hence the long wait times associated with standard gravity separation. Additionally, if separation occurs at the pressures associated with the centrifugal forces, as they are not as high as in an extruder, indicate that a processing aid will not be suitable. Centrifugation showed that suspensions containing CMC, XG, or aPAM at a dry weight ratio of 0.1:1 aid to CNF did not experience any perceivable water separation or solid-liquid separation (Figure B. 4). All the other suspensions (not marked with an asterisk, Table 3.2) experienced a slight level of dewatering (~2 to 3 ml of water extracted; MC, HEMC, HEC, GG, CG- λ , CP940, and TG) or had a similar water separation behavior to pure CNF (~20 ml of water separated; KM, AS, CS, PEI, and PAA). Similar results are produced for suspensions with a reduced ratio of processing aid to CNF of 0.05:1, where CMC, XG, and aPAM containing suspensions did not dewater, yet all other suspensions experienced dewatering at an even greater extent. Additionally, processing aids like KM formed irreversible gels when mixed with water which could not be fully incorporated into CNF hence KM was not further studied⁹¹. The water retention provided by CMC, XG, and aPAM could not necessarily be linked to the surface charge as other negatively surface charged polymers did not suppress dewatering to the same extent (e.g., TG, CP940, CG- λ , and PAA). Similarly, water retention could not be directly linked to molecular weight (M_w) as CMC containing suspensions did not dewater and had a much lower M_w (~150,000 to 180,000) when compared to XG (M_w ~300,000 to 7.5×10^6)⁷⁷, aPAM (in the millions)⁷⁶, or even to CP940 (M_w ~ 7×10^5 to 4×10^9)⁹² which did dewater.

In order to further gauge the stability of the centrifuged suspensions and possibly explain the water retention behavior, zeta potential was measured on dilute suspensions of CNF plus processing aid. The results showed that CMC, XG, aPAM, CP940, CG- λ , and PAA containing suspensions experienced the lowest zeta potential (i.e., largest magnitude of charge). CMC, XG, aPAM, and CG- λ all lowered the zeta potential below -50 mV with the strongest reduction being caused by CMC ($\xi = -58 \pm 5.63$ mV). This represents a relatively large increase in stability when compared to pure CNF ($\xi = -29.8 \pm 4.35$ mV) which tends to phase separate at room temperature conditions and without any centrifugation. Aids like TG, CS, and AS did not have any effect on the zeta potential when compared to pure CNF, while HEC, MC, and HEMC all increased it towards zero, hence theoretically reducing stability (Figure 3.7). Zeta potential results matched

with the centrifugation behavior seen for CMC, XG, and aPAM indicating that colloidal stability is the origin of dewatering results. However, this supposition did not match for other processing aids. For example, MC, HEMC, HEC, and GG containing suspensions experienced the same low level of dewatering as those containing CG- λ ($\xi = -52.1 \pm 3.83$ mV), and CP940 ($\xi = -37.4 \pm 6.59$ mV) when compared against pure CNF. Furthermore, the PAA containing suspension ($\xi = -49.2 \pm 4.09$ mV), experienced the same dewatering behavior as pure CNF. Additionally, strongly positively charged polymers like PEI flipped the sign of the zeta potential yet did not provide water retention during centrifugation trials. Hence, zeta potential cannot directly explain the dewatering behavior of CNF/aid suspensions yet can still serve as a first approximation. Lastly, it is important to point out that while it is indeed possible to achieve no water separation during centrifugation for the slightly dewatering suspensions (i.e., those that contain MC, HEMC, HEC, GG, CG- λ , CP940, or TG) by adding more polymer (e.g., a ratio of 0.15:1 or 0.2:1, aid:CNF) the intent in this work is to produce extruded sheets with the highest CNF purity. Hence, only CMC, XG, and aPAM were selected for further study in extrusion.

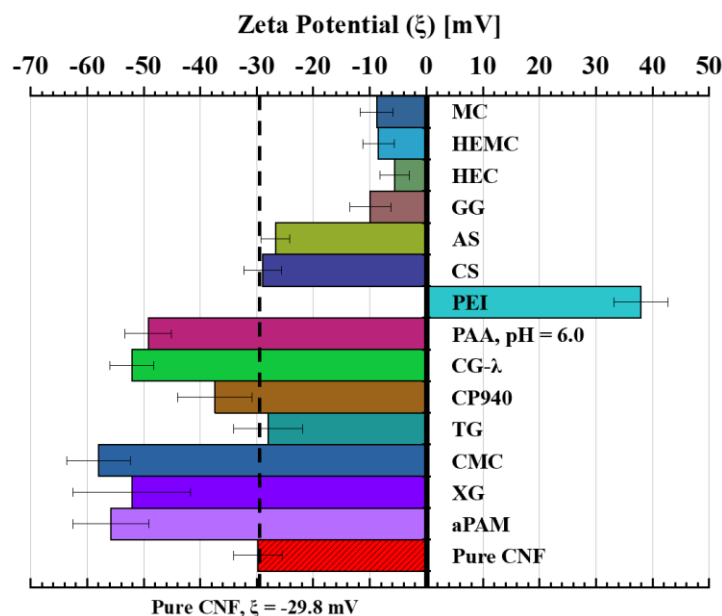


Figure 3.7 Zeta potential of pure CNF and suspensions of CNF plus processing aids. The dashed line shown is referenced to the mean of the pure CNF zeta potential ($\xi = -29.8$ mV). Six measurements were performed for each case and the average was calculated. The error bars represent one standard deviation away from the mean. The pH of all the samples was measured to be 6.4 except for PAA that had a pH of 6.0.

3.3.2 Extrusion of CNF/CMC, CNF/XG, and CNF/aPAM

Based on an initial extrusion trial of three different solids loadings (~3, ~7.6, and ~15 wt.%) of a CNF/CMC paste (0.1:1 of aid to CNF), it was determined that a total solids concentration of ~15 wt.% is needed to form cohesive sheets. Lower solids concentration would extrude yet the extrudate was too watery and not cohesive enough to be transported or handled. Based on the results, ~15 wt.% total solids concentration was selected for all extrusion pastes unless otherwise stated.

To achieve a ~15 wt.% concentration, the watery suspensions (~3 wt.%) had to be air dried for roughly 38 days, which is not industrially viable (see Figure 3.8). These long drying times are caused by the enhanced water retention brought by the processing aids and has been known to reduce drainage in typical papermaking^{93,94}. Due to the enhanced water retention, typical dewatering/drying techniques often used to consolidate pure CNF such as vacuum filtration, mechanical pressing, and oven drying cannot effectively extract water from CNF/aid pastes^{20,35,64}.

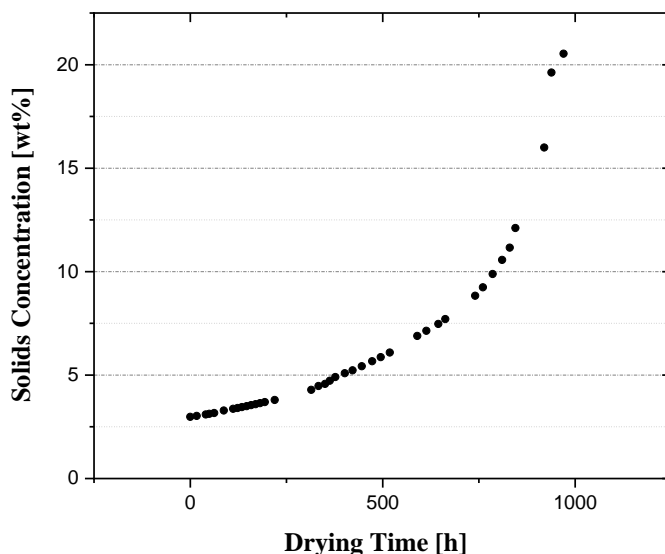


Figure 3.8 Solids concentration [wt.%] versus drying time [h] for an air dried CNF/CMC paste in a humidity controlled oven. To achieve a solids concentration of ~15 wt.% the paste had to be dried for over 38 days.

To circumvent the long drying times, concentrated pastes containing CMC, XG, and aPAM were prepared by using a standard polymer Banbury-style high shear mixer, the procedure for which is explained in detail in the experimental section. The high shear mixing process utilized a

bottom up approach to achieve the higher solids loadings by using vendor pre-dewatered pure CNF (~23 wt.% instead of the more dilute ~3 wt.% slurry). The needed processing aid and water were then added to tune the final solids concentration. In the literature, a similar approach was used to produce ultra-high consistency pulp/biomass pastes (20 to 40 wt.%) with the addition of processing aids or water soluble polymers (WSP) like CMC, HPMC, XG, agar, HPC, and others⁹⁵. Out of all the WSP sampled, CMC was found to provide highest paste stability while HPMC provided a thermo-reversible aspect which could be important for downstream dewatering after sheet forming. Thus, this mixing process can save many days that would otherwise be required for air drying.

Extrusion of CNF/CMC (0.05:1 of aid to CNF), CNF/XG(0.05:1), or CNF/aPAM (0.013:1) pastes failed due to dewatering at the slot die and did not form homogenous sheets (Figure B. 5). This shows that while centrifuging is a good initial screening test for processing aids (e.g., a list of 15 candidates was reduced to 3, Table 3.2, it clearly does not replicate the complex pressure profiles and shear forces in an extruder or the behavior of highly loaded pastes. On the other hand, CNF/CMC, CNF/XG pastes at 0.1:1 and aPAM pastes at 0.026:1 of aid to CNF did not dewater and were capable of being formed into wet sheets. Extrudates/sheets with an average length of 0.61 m (~2 ft), width of 5.1 cm (2 inches), and wet thickness of 1.46 ± 0.05 mm were processed for each paste type, CNF/CMC, CNF/XG, and CNF/aPAM (see Figure 3.9). It is important to note that the length of the extrudate was only limited by the amount of material at hand and by the lack of collection rolls, hence longer extrudates can be produced if needed.

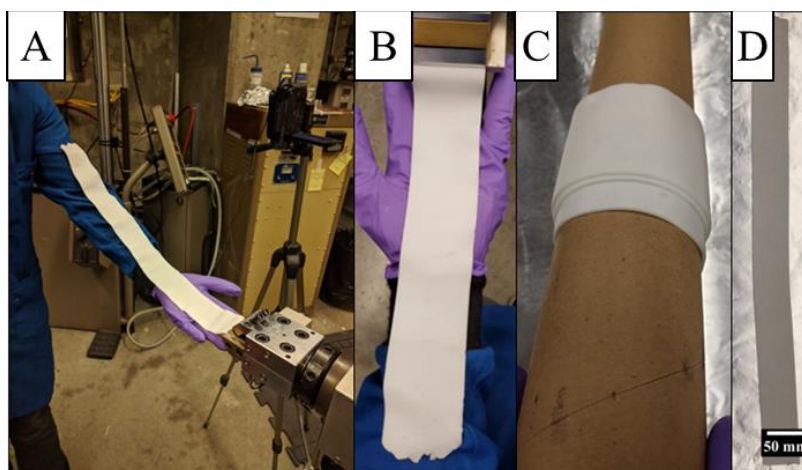


Figure 3.9 Wet CNF/CMC sheet single screw extrusion (A), wet CNF/CMC extrudate (~15 wt.% total solids) exiting the rectangular sheet die (B), extrudate collected on a cardboard roll (C), and de-rolled extrudate laid flat on top of aluminum foil (D).

Wet sheet production rates at a screw speed of 7 rpm were in the range of 0.45 ± 0.02 kg/h (or 0.07 ± 0.002 kg/h dry) while the maximum possible production rate was found to be 7.45 ± 0.47 kg/h (or 1.14 ± 0.072 dry) at a screw speed of 110 rpm for CNF/CMC pastes (~ 15.32 wt.% solids). Figure 3.10 shows a plot of the production rate (kg/h) versus screw speed (rpm) for a CNF/CMC (0.1: 1 of aid to CNF) paste at ~ 15 wt.%. There was a strong ($R^2=0.997$) linear relationship between the extrusion/delivery rate and the screw speed until the maximum screw speed (120 rpm) was reached, which experienced a decrease in the rate to 6.24 ± 0.12 kg/h (0.96 ± 0.02 kg/h dry). The reduction of the delivery rate could possibly be caused by the shear thinning response of the paste. If the shear is high enough to cause shear thinning of the material pressed against the barrel walls the screw's ability to deliver material to the slot die will be hindered⁹⁶. Hence, it is expected that the maximum possible production rates will depend on both the processing aid type and the total solids concentration as the rheological response will change (as seen in the next section).

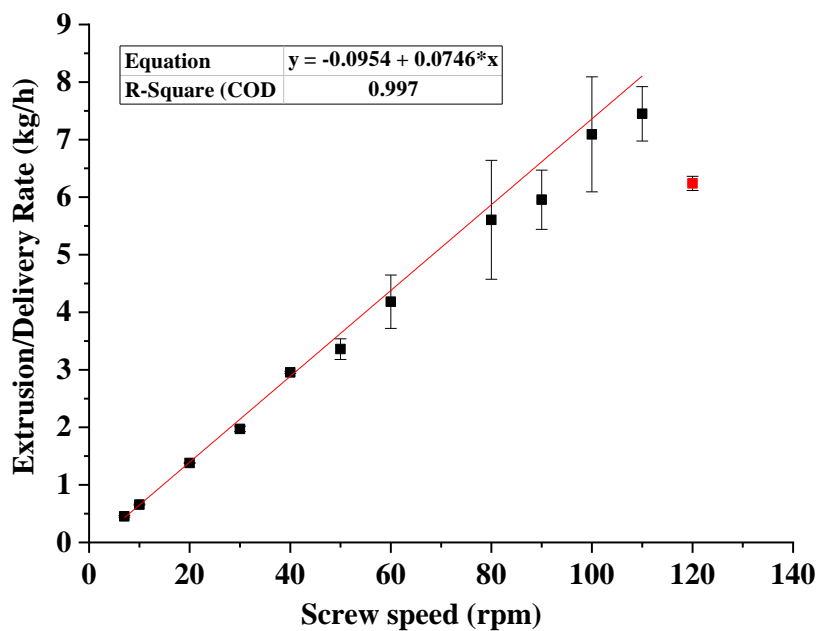


Figure 3.10 Extrusion delivery rate [kg/h] versus screw speed [rpm] for a CNF/CMC paste with a dry weight ratio of 0.1:1. Three aliquots of material were collected for each data point. The weight of the sample and delivery time were recorded in real time. A linear fit was applied to the data showing a strong correlation between the two variables ($R^2 = 0.997$). The red dot was excluded from the analysis for reasons explained in the main report. The error bars represent 1 standard deviation away from the mean.

The obtained processing rates are much lower than typical industrial single-screw extrusion lines with a throughput of approximately 40 kg/h at 122 rpm (approximation by Fang et al.⁹⁷ for processing LDPE), yet current efforts only employ a laboratory scale extruder with a relatively small barrel diameter (1.9 cm) and small width (5.1 cm) sheet die. It is also important to point out that at all the screw speeds there was no ‘sharkskin’ nor ridged pattern observed at the extrudate’s surface. It is possible that the lubricating water layer or depletion layer that forms between two phase materials and solid surfaces suppressed the stick-slip behavior common in capillary dies^{98,99}. On the other hand, a small amount of die swell was observed as the extrudates were on average slightly thicker (1.46 ± 0.05 mm) than the set die gap width (1.13 mm).

When compared against laboratory processing techniques (e.g., solution casting) the major benefit that comes from using the proposed methodology (shear mixer to produce pastes and an extruder to continuously process sheets) is the significant reduction in processing time. The results show a decrease in processing time of ~97 % when compared to typical casting (assuming a 7 day drying period). On the other hand, when compared to previously reported extruded cellulose nanocomposites, the proposed methodology allows for processing of sheets with very high solids and CNF loading (up to ~91 wt.% CNF and ~9 wt.% processing aid) compared to nanocomposites (a maximum of 20 wt.% CNF content)^{33,67–70}. Processing nearly pure CNF parts conserves 100% of the inherent mechanical properties of CNF. Additionally, problems dealing with matrix incompatibility and matrix selection are essentially eliminated.

When comparing wet extrudates it was found that CNF/CMC extrudates were the most homogenous and contained no perceivable surface or bulk defects such as pinholes, aggregation, inhomogeneity, etc. (Figure 3.11 A). CNF/XG extrudates contained pin holes and agglomerated structures while CNF/aPAM extrudates contained numerous defects (Figure 3.11 B, and C). Collectively, for all wet extrudates, larger defects were partly transferred to the fully dry state after pressing and heating (Figure 3.11 D, E, F, G, H, and I), which ultimately lead to lower mechanical performance as shown in the mechanical testing section. Additionally, similar defect patterns were observed inside of the sheet die after extrusion and during cleaning (Figure B. 6).

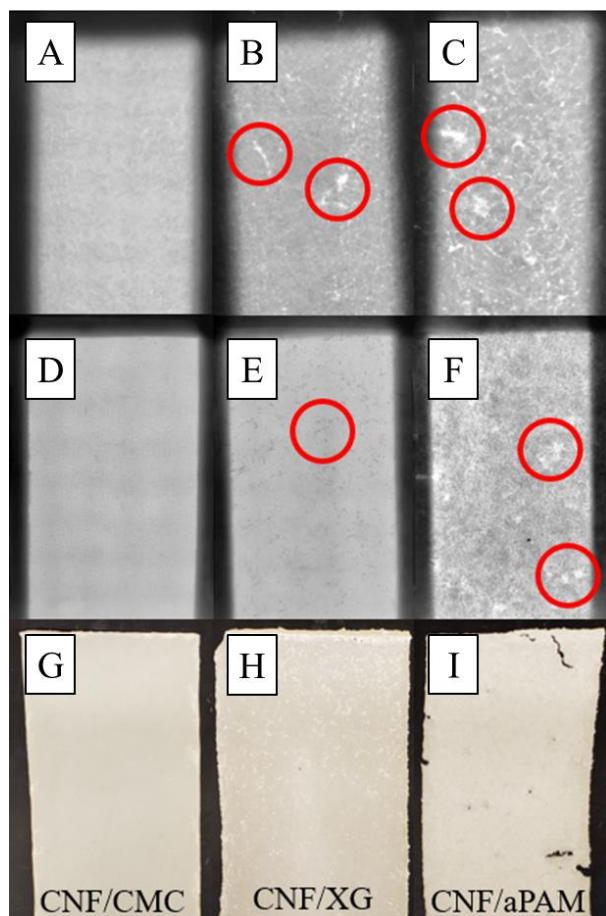


Figure 3.11 Wet extrudates of CNF/CMC (A), CNF/XG (B), CNF/aPAM (C) pastes at ~15 wt.%, pressed and heated to fully dry sheets of CNF/CMC (D, G), CNF/XG (E, H), and CNF/aPAM (F, I). A strong back light was used to illuminate samples and highlight the defects like aggregation/aggregates or pinholes. A few of the observed defects are circled in red. Figures (A) through (F) were set to a grey scale to better appreciate the defects while figures (G), (H), and (I) were not color modified. The width of the sheets was ~51 mm.

3.3.3 Rheological analysis of pure CNF, CNF/CMC, CNF/XG, and CNF/aPAM

Rheological analysis of highly concentrated pastes was carried out on a Brabender torque rheometer. The measured viscosity-temperature sensitivity constants (b , used to correct the measured torque data), were measured for each blend and are shown in Table 3.3. From here the torque and roller speed were converted to viscosity and shear rate through the Equations 1-3 and plotted in Figure 3.12.

Table 3.3 Paste concentrations and rheological constants obtained from torque rheometry analysis. A dry weight ratio of 0.1:1 (aid:CNF) was used for all pastes.

Paste Type	Total solids [wt.%]	Aids [wt.%]	CNF [wt.%]	H ₂ O [wt.%]	b [°C ⁻¹]	R ²	n	log (m)	R ²
Pure CNF	15.32	0	15.32	84.68	0.0085	0.944	0.13	3.533	1.000
	30	0	30	70	0.0145	0.982	0.06	4.470	1.000
CNF/CMC	15.32	1.39	13.93	84.68	0.0119	0.941	0.42	2.991	0.995
	19	1.73	17.27	81	0.0107	0.963	0.30	3.359	0.998
	25	2.27	22.72	75	0.0040	0.729	0.26	3.494	0.999
CNF/XG	15.32	1.39	13.93	84.68	0.0049	0.722	-0.31	3.666	0.982

Figure 3.12 shows the log(viscosity) dependence on log(shear rate) at 28 °C for 15.32 wt.% pastes containing CMC, XG, aPAM, and pure CNF. The solid lines correspond to linear curve fits with all $R^2 > 0.98$. The power law index (or shear thinning exponent, n) and melt consistency index (m) were calculated from the power law fits and are shown in Table 3.3. Figure 3.12 and the values in Table 3.3 show that the addition of CMC suppressed the shear thinning behavior when compared to pure CNF. The power law index increased from $n = 0.13$ for pure CNF to $n = 0.42$ for CNF/CMC at ~15.32 wt.%. For the CNF/XG paste, issues due to slippage at the mixing blades started to occur at ~50 to 70 rpm (data points are not filled in to signify unreliable data, Figure 3.12) and hence the power law and consistency index could not be reliably calculated or compared (note n is negative, Table 3.3, Figure 3.12). Slippage was most likely caused by XG's highly shear thinning rheological behavior when compared to other thickeners. This behavior is possibly caused by the weak association between XG molecules and their relatively stiff conformation¹⁰⁰. XG molecules take on a stiff right-hand five-fold helical conformation with a large hydrodynamic size and with a persistence length, $q > 100 \text{ nm}^{100-102}$. This is in contrast to more flexible linear molecules like CMC or Guar gum ($q \sim 10 - 30 \text{ nm}$) that take on a ribbon-like conformation and are also characterized by a pseudoplastic behavior¹⁰⁰. XG's conformation allows for higher viscosities at lower shear rates. Slippage also occurred for CNF/aPAM, yet in a more significant manner at lower rpms ($\leq 5 \text{ rpm}$). Hence, CNF/aPAM could not be characterized using the Brabender. One rheological study showed that adding trace amounts (10 g/m^3) of aPAM to paper pulp highly increased the elongational viscosity and drainage time while keeping the shear viscosity the same⁹⁴. Perhaps for the CNF/aPAM pastes prepared for extrusion (~15.32 wt.% total solids with a ratio aid to CNF of 0.026:1), the high aPAM concentration (~4500 g/m^3) could have influenced the

shear viscosity as it does the elongational viscosity for trace amounts in dilute suspensions, thus exacerbating slippage.

When compared to the extrudates (Figure 3.11) it appears that pastes with a reduced shear thinning behavior or stronger Newtonian behavior present less defects and hence have a greater sheet homogeneity. A plausible reason that having a stronger Newtonian behavior reduces sheet defects is that during forming the complex shear profiles inside the die will have a weaker effect on the final part shape (i.e., reduced shear sensitivity of the paste). In fact, this is why in conventional commodity polymer extrusion lines there is a unique die for each polymer being processed. Individual die designs account for the vastly different flow characteristics (e.g., shear thinning exponent (n), melt flow index (MI), and die swell) of the polymers and ensure high quality parts¹⁰³. However, for the prepared pastes, CMC appears to impart both good rheological properties and strong dispersion to CNF pastes and allows for successful extrusion without defects.

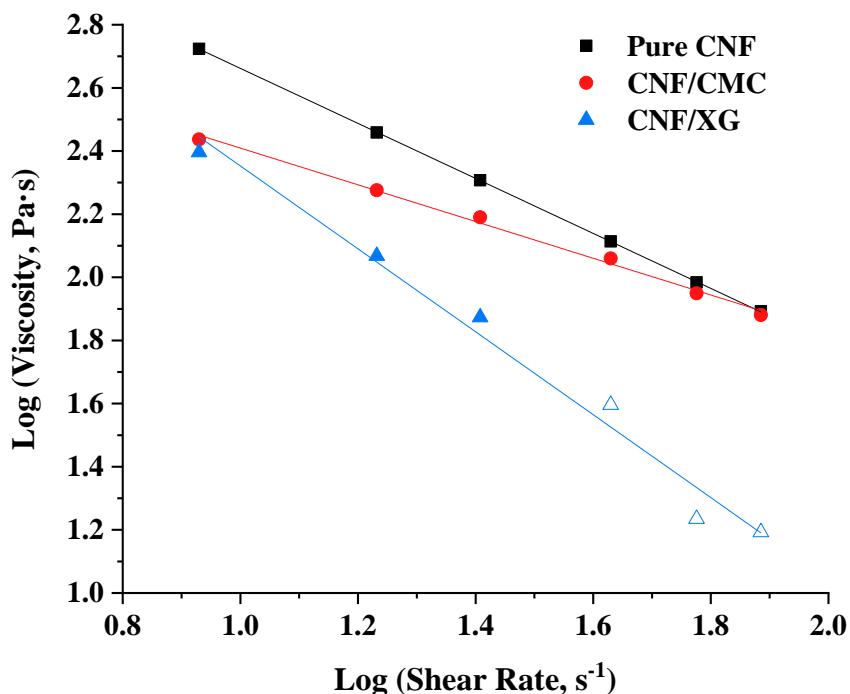


Figure 3.12 Log (viscosity) - log (shear rate) dependence of pure CNF, CNF/CMC, and CNF/XG pastes with an aid to CNF ratio of 0.1:1 measured on the torque rheometer at 28 °C. The power law index is calculated by $n = (\text{slope} + 1)$ while the consistency index is the intercept point. All the analyzed pastes and pure CNF had a solids concentration of ~15.32 wt.%. Unfilled points represent unreliable data due to slippage or sticking to the mixing blades.

For all shear rates studied and for both processing aids added (CMC and XG), there was a marked decrease of the apparent viscosity of the pastes when compared to pure CNF (see Figure 3.12). Classically in synthetic polymer extrusion, the same effect is caused by processing aids that act as internal lubricants. For example, polyglycerol ester (C_{16} to C_{22}) fatty acid are added to reduce the characteristic high melt viscosity of poly(vinyl chloride), poly(propylene), or acrylonitrile-butadiene-styrene¹⁰⁴. For CNF/aid pastes the decrease in viscosity is possibly caused by the reduction of fibril-fibril contacts and fibril-fibril friction as the dispersed/dissolved polymer molecules adsorb to fibrils and improve dispersion¹⁰⁵. More specifically for CMC, the frictional reduction and dispersion effects has been studied extensively for more dilute papermaking suspensions (1 to 3 wt.% total solids) that contain CMC as a wet-end additive in the dispersed phase or adsorbed CMC onto the pulp fibers^{93,106–108}. Because CNFs have the same surface chemistry as bleached kraft pulp often used in papermaking suspensions it is believed that the reported effects were carried over to the extrusion pastes. Contrary to CMC, XG has not been studied as an additive in papermaking suspensions yet similar effects could be occurring in terms of fibril-fibril friction and contact reduction as well as adsorption.

Typical rotational shear rate controlled rheometry with a cup and bob fixture served as a secondary analysis/comparison and was performed on very dilute suspensions (1 wt.%) of CNF/CMC, CNF/XG, CNF/aPAM, and pure CNF due to the high viscosity of highly-loaded suspensions making them unmeasurable in our system, see Figure 3.13. The obtained trends for the very dilute suspensions match those obtained for the highly loaded pastes (~15 wt.%) evaluated on the Brabender. Where adding CMC reduced the shear thinning behavior ($n = 0.11$ for pure CNF, and $n = 0.30$ for CNF/CMC, Figure 3.13). In contrast to the torque rheometer analysis, CNF/XG and CNF/aPAM watery suspensions could be analyzed without slippage. The behavior of CNF/XG and CNF/aPAM was similar in that both suppressed the shear thinning behavior ($n = 0.26$ for CNF/XG and $n = 0.24$ for CNF/aPAM) when compared to pure CNF. The apparent viscosity of CNF/XG and CNF/aPAM was also lower than that of CNF/CMC at all shear rates studied. Interestingly, a power law transition in pure CNF at $\sim 5 \text{ s}^{-1}$ disappeared with the addition of processing aids. While the reason is not clear, it was deemed beyond the scope of this paper. It is also important to point out that these results only serve as indirect comparisons to the torque rheometer results and greater importance is given to highly loaded pastes as those are the concentrations desired for extrusion.

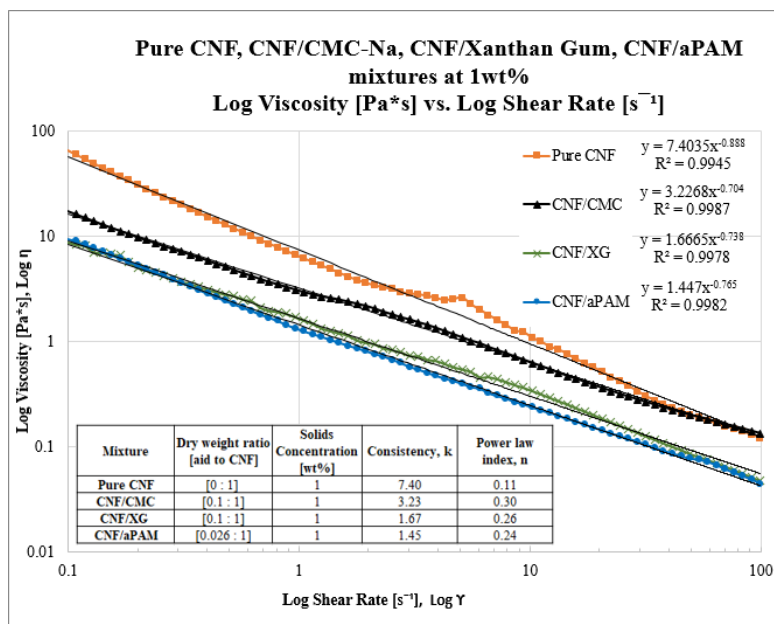


Figure 3.13 Log of apparent viscosity [Pa*s] versus log of shear rate [s⁻¹] for suspensions of pure CNF, CNF/CMC, CNF/XG, and CNF/aPAM. The table inset shows important rheological parameters computed from the power law fit on the obtained data. The equation on the top right corner represents the power law models.

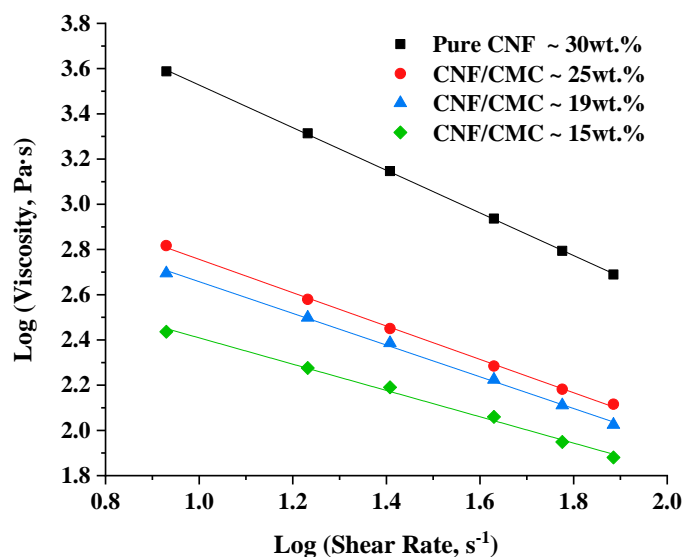


Figure 3.14 Log (viscosity) - log (shear rate) dependence of CNF/CMC pastes with solids loading of ~15.32 wt.%, ~19 wt.%, and ~25 wt.% and pure CNF with a solids loading of ~30 wt.% measured on a torque rheometer at 28 °C. The processing aid to CNF ratio for the evaluated pastes was 0.1:1 (dry weight).

Additional analysis, using the torque rheometer, of the two higher concentration ~19 wt.% and ~25 wt.% CNF/CMC pastes (at 0.1:1) showed that a higher total solids concentration reduced the power law index and hence increased the shear thinning response ($n = 0.42$ for ~15 wt.%, $n = 0.3$ for ~19 wt.%, and $n = 0.26$ for ~25 wt.%, Figure 3.14 and Table 3.3). As expected, there is also a general trend where higher solids concentration leads to higher apparent viscosities for all shear rates probed due to the higher density of particle interactions. It is important to note that the only “successful” extrudate of pure CNF at ~30 wt.% showed an order of magnitude higher viscosities when compared to ~25 wt.% CNF/CMC, and a stronger shear thinning behavior ($n = 0.06$) when compared to the ~15 wt.% pure CNF paste ($n = 0.13$). It is also important to point out that while testing pure CNF samples (~15 and ~30 wt.%) slight dewatering occurred, which might have affected the rheological response, this was not quantified as the amount of water lost as a result of coating the surfaces of the mixer.

Due to the lack of literature on steady-state rheometry of highly loaded CNF pastes the results were indirectly compared with that of corn stover biomass pastes tested under dynamic conditions. Highly loaded corn stover pastes (20 wt.% solids) tested using a vane rheometer showed a similar shear thinning behavior to CNF pastes with a linearly decreasing complex viscosity (η^*) ranging from 10,000 Pa*s (0.3 Hz) to 50 Pa*s (100 Hz)^{109,110}. The measured elastic (G') modulus was on average an order of magnitude higher than the storage (G'') modulus and both were found to be relatively insensitive to frequency. The reported solid like behavior ($G' \gg G''$) for corn stover can be explained due to the increased particle interactions (i.e., higher solids). This solid like behavior is expected to be intensified for highly loaded pure CNF pastes as the particle sizes are much smaller than corn stover biomass (i.e., more interactions). On the other hand, Samaniuk et. al. showed that CMC was an excellent corn stover processing aid when compared to other aids like poly(ethylene) oxide (PEO), nonionic polyacrylamide (PAM), and XG^{80,111}. Adding 2 wt.% CMC achieved a reduction of yield stress (τ_y) of ~67% (~55 kPa to ~18 kPa) for 25 wt.% corn stover pastes⁸⁰. Additionally, the degree of substitution of CMC (0.7 to 1.2) was found to be inversely proportional to the reduction in yield stress. The obtained results are consistent with previously stated theories regarding the reduction of fibril-fibril contacts and friction through processing aid adsorption to the surfaces of the insoluble particles in the paste¹¹². The reduction in friction reduces fiber entanglements or fiber flocs and explains the stronger Newtonian behavior seen for CNF/CMC pastes (Figure 3.12, and Figure 3.14). The fibril-fibril friction theory could

also explain why as the solids loading increases for the CNF/CMC pastes the shear thinning exponent (n) decreases from $n = 0.42$ for 15 wt.% to $n = 0.26$ for 25 wt.% solids (Table 3.3).

3.3.4 Mechanical and thermogravimetric analysis of CNF/CMC, CNF/XG, and CNF/aPAM sheets

Mechanical testing of the pressed and dried extrudates with an aid to CNF dry weight ratio of 0.1:1 showed that CNF/CMC sheets outperformed CNF/XG sheets in terms of ultimate strength (110.6 ± 7.30 MPa and 60.1 ± 19.5 MPa, respectively) and strain to failure (1.80 ± 0.08 % and 0.75 ± 0.26 %, respectively) as shown in Figure 3.15 A and Figure 3.15 C. These results were not surprising as CNF/XG sheets contained more defects than CNF/CMC sheets (Figure 3.11). The CNF/aPAM sheets were not tested mechanically, because the properties are expected to be much lower when compared to any of the other extruded sheets due to the significantly higher level of defects as seen in Figure 3.11 I. Additionally, there seems to be no significant difference between the mean densities for cast CNF films, and extrudates of CNF/CMC and CNF/XG (one-way ANOVA: $F_{2,16} = 3.47$, $P = 0.056$, $R^2 = 0.302$, Figure 3.15d). The density between sample groups is better appreciated in the boxplots shown in Figure B. 7.

When compared against cast CNF films prepared through typical solution casting, the extruded CNF/CMC sheets were statistically the same in terms of ultimate strength (110 ± 8.2 MPa for cast CNF films verses 110.6 ± 7.30 MPa for extruded CNF/CMC sheets) and density (1.13 ± 0.11 g/m³ for cast CNF films verses 1.19 ± 0.03 g/m³ for CNF/CMC) as shown in Figure 3.15 . Collectively, for both CNF/CMC and CNF/XG, the extruded sheet's strain to failure was lower than that of cast CNF films (2.57 ± 0.6 %), yet this is probably an artifact of the constrained drying applied to the extruded sheets verses the room temperature unconstrained/free drying used for cast films. In terms of Young's modulus, all the extruded sheets were statistically similar to cast CNF films (Figure 3.15 B).

SEM analysis of the extruded sheets and cast CNF film did not reveal any additional information as shown in Figure 3.16. All the tested sheets and films presented a paper-like layered structure with fibrils pointing towards the tensile direction. The fractured surfaces looked similar to previous work on thicker multi-layered neat CNF sheets which was shown in Chapter 2¹².

Table B. 6-1 summarizes the mechanical response including the specific strength, and specific modulus of all the extruded and pressed sheets as well as cast CNF films. Furthermore, preliminary attempts at calendering of the wet extrudates of CNF/CMC showed that full extrudate consolidation can be achieved and a more translucent sheet is developed (Figure B. 8). The mechanical properties of the calendered sheets were not evaluated, but a higher density is expected.

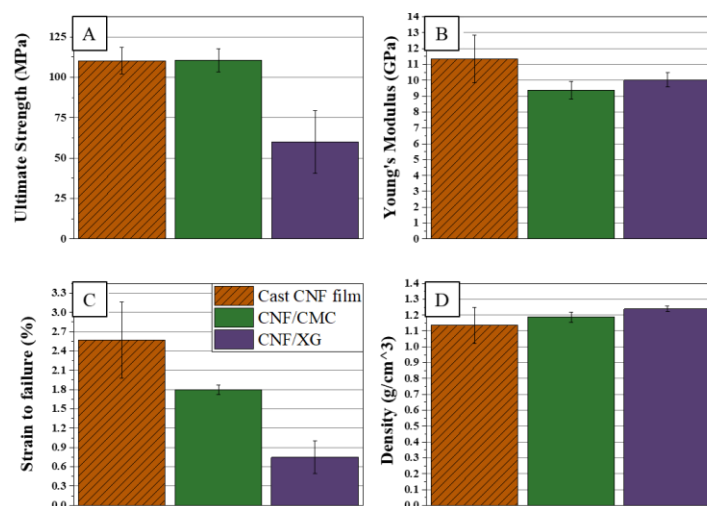


Figure 3.15 Tensile mechanical response of cast CNF films, extruded CNF/CMC sheets, and extruded CNF/XG sheets with a processing aid to CNF ratio of 0.1:1. The error bars represent one standard deviation away from the mean. Typical stress-verses strain curves for these samples in included in Appendix B in Figure B. 10.

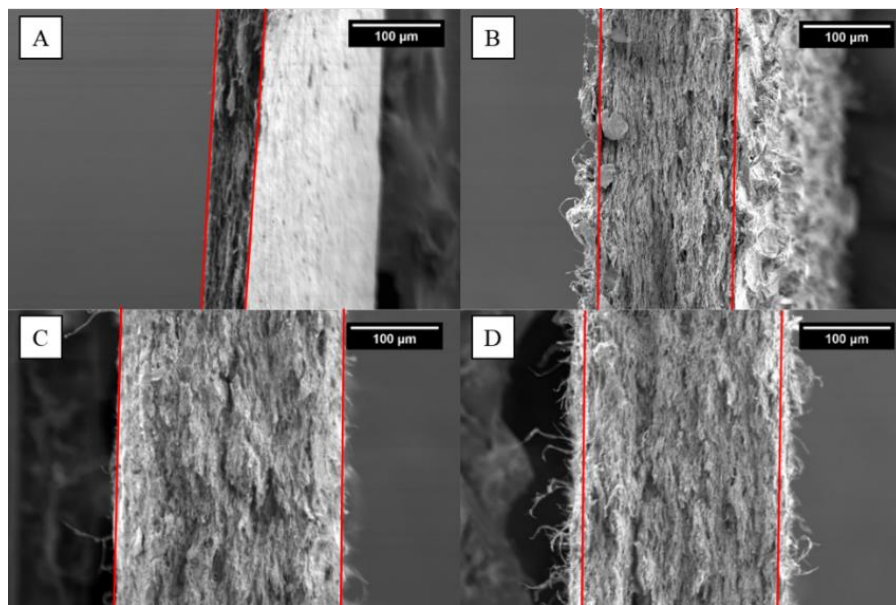


Figure 3.16 Scanning electron microscopy of the fractured surfaces of cast CNF (A), CNF/CMC at 0.1:1 (B), CNF/XG at 0.1:1 (C), and CNF/XG (D) at 0.15:1. The studied fractured surface is parallel to the tensile axis.

Higher processing aid concentrations were also probed in order to better gauge the effect of the processing aid on the mechanical properties. The results showed that adding CMC at a ratio of 0.15:1 (aid to CNF) lowered all the mechanical properties, possibly due to over plasticization as shown in Figure 3.17. Surprisingly, the addition of XG at a ratio of 0.15:1 (aid to CNF) improved all the mechanical properties when compared to pressed sheets with a XG to CNF ratio of 0.1:1 as shown in Figure 3.18. The addition of more XG appeared to reduce macroscopic defects like pinholes and aggregates possibly due to improved CNF dispersion. A comparison between CNF/CMC and CNF/XG both with a ratio of 0.15:1 was also made which shows the marked increase for CNF/XG sheets (Figure B. 9).

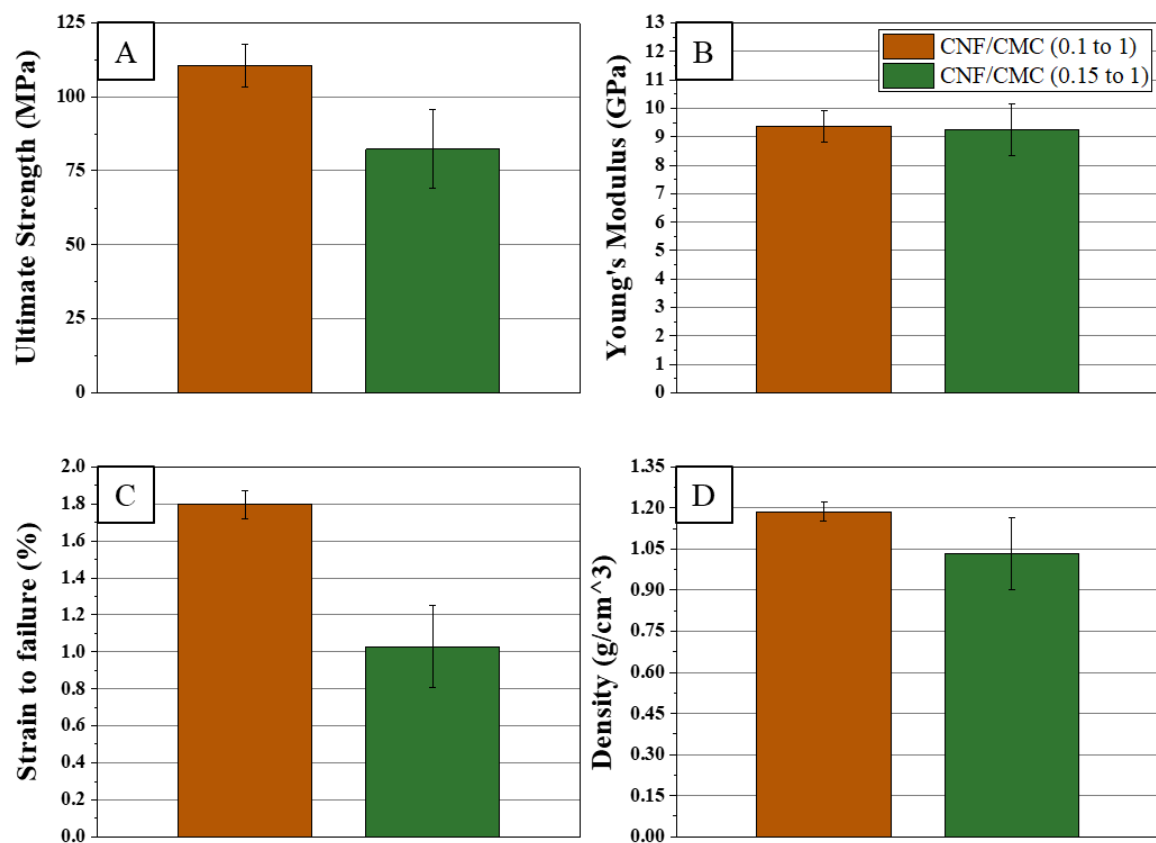


Figure 3.17 Tensile mechanical response of CNF/CMC pastes at two different dry weight ratios (0.1:1 and 0.15:1). The error bars represent one standard deviation away from the mean. The recorded responses are A) ultimate strength, B) Young's modulus, C) strain to failure, and D) density.

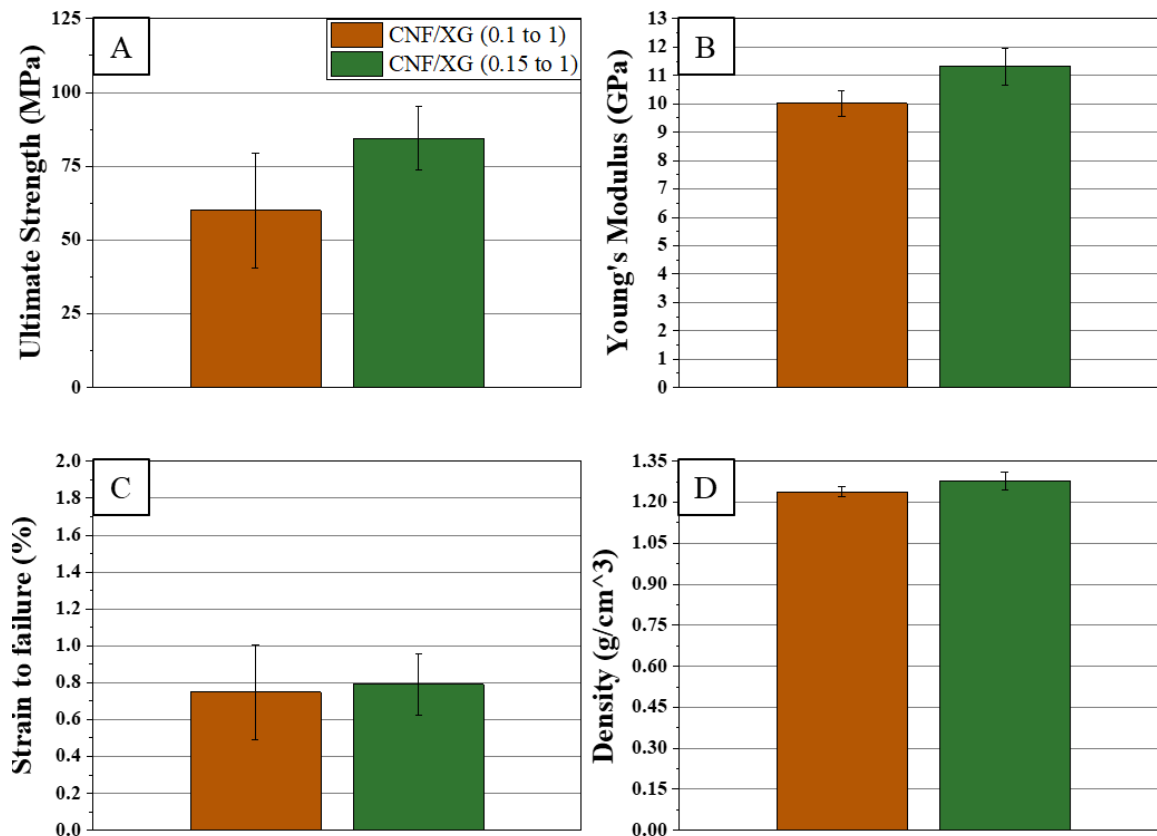


Figure 3.18 Tensile mechanical response of CNF/XG pastes at two different dry weight ratios (0.1:1 and 0.15:1). The error bars represent one standard deviation away from the mean. The recorded responses are A) ultimate strength, B) Young's modulus, C) strain to failure, and D) density.

Thermogravimetric analysis (TGA) of the pressed and heated extrudates revealed a similar degradation behavior between CNF/aPAM and the ~30 wt.% pure CNF extrudate with a pronounced weight loss reaching over 2 % at 100 °C as shown in Figure 3.19. On the other hand, CNF/CMC and CNF/XG sheets behaved more like cast CNF films with a less pronounced weight loss reaching 1 % at 100 °C. For all cases, the weight loss could be linked to how well the material retains water as there is always some amount of free and bound water left and CNF starts degrading at 180 °C while aids like CMC start degrading at 200 °C^{72,88,113}. CMC and XG could have acted as a stronger CNF dispersant and thus enabled more surface area making it harder for water to diffuse and escape through a more homogenous structure. This is in contrast to CNF/aPAM and pure extruded CNF sheets whose structure looked heavily agglomerated even in the macroscopic state (Figure 3.6 and Figure 3.11 F). Examples in literature for this water retention behavior can

be seen between the more agglomerate fibrillar nature of CNF verses the highly dispersed TEMPO oxidized CNF (TOCNF) fibrils. The higher fibrillar dispersion of TOCNF makes for much stronger and more viscous gels which binds or retains water more strongly^{13,114}. Furthermore, cast CNF films achieve a good level of homogeneity as the drying process is very slow compared to pressing which allows for CNF fibrils to find the best possible packing.

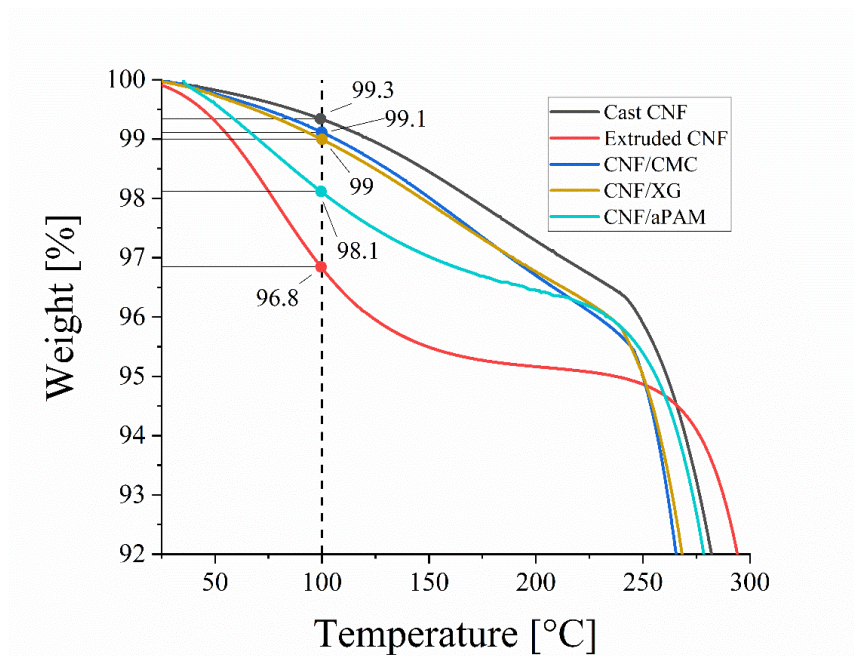


Figure 3.19 Thermogravimetric analysis of cast CNF, extruded pure CNF, CNF/CMC, CNF/XG, and CNF/aPAM. The boiling point of water (100 °C) was selected as a comparison point. Prior to testing all the samples were preconditioned for over a week at 25 %RH.

3.3.5 Validation of Brabender mixing procedure for the preparation of CNF/CMC pastes

To verify that the Brabender mixing method is not damaging the CNF fibrils and to show that it is an industrially viable high volume method for preparing pastes for extrusion, CNF/CMC pastes at three solids loadings (~15, ~19, and ~25 wt.%) were prepared, extruded, pressed, and heated, and tested mechanically in tension as shown in Figure 3.20. These “mixer-pastes” were compared against air-dried pastes “AD-pastes” with roughly the same solids concentration. The results show that the ultimate strength for ~15 wt.% and ~19 wt.% mixer-pastes is equivalent to AD-pastes, while at ~25 wt.% mixer-pastes outperformed AD-pastes (ultimate strength of 101 ± 14.12 MPa for mixer-pastes at ~25 wt.% versus 70 ± 7.76 MPa for AD-pastes at 24 wt.%). In terms of strain to failure, mixer-pastes outperformed AD-pastes at all concentrations. It is plausible that

the decrease in properties for AD-pastes is due to the uneven surface drying that incorporates microscopic aggregates into the sheets once extruded. Yet for both types of processes, the strain to failure decreases with an increase in solids concentration hence lower solids concentration might be optimal for extrusion of tougher sheets. Collectively for both types of pastes (mixer and AD), the density appears to increase as concentration increases and then plateaus at a value of $1.37 \pm 7.76 \text{ g/m}^3$. Furthermore, the Young's modulus of the mixer-pastes and AD-pastes appear to be equivalent to each other at all probed concentrations. Surprisingly for both types of pastes, the modulus appears to vary between $\sim 9 \text{ GPa}$ to $\sim 11 \text{ GPa}$ as a function of concentration. The reason for the modulus fluctuations is unknown and will be investigated in future publications.

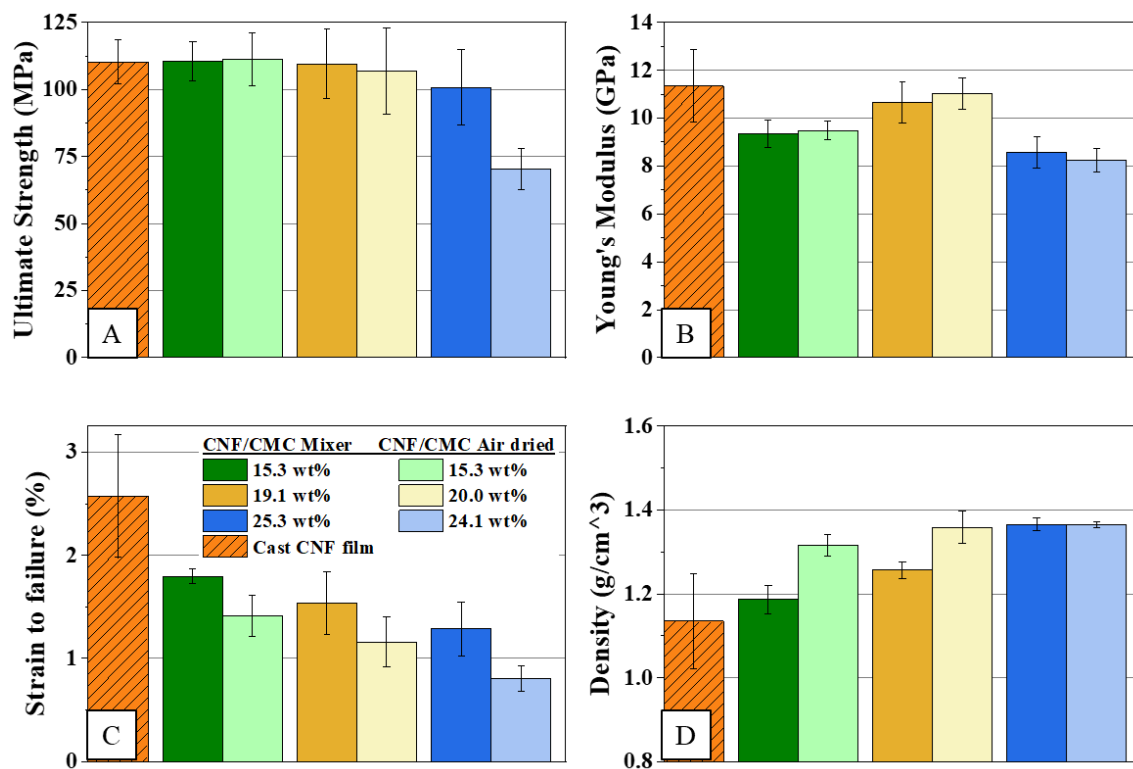


Figure 3.20 Mechanical performance of Brabender mixed pastes (darker color) versus air dried pastes (lighter color) prepared using a humidity-controlled oven. The error bars represent one standard deviation away from the mean. The recorded responses are A) ultimate strength, B) Young's modulus, C) strain to failure, and D) density.

3.4 Conclusion

In this chapter the processing of CNF sheets through conventional single screw extrusion was presented and assessed. Results showed that the problems associated with extrusion of pure CNF, such as, dewatering and aggregation were completely suppressed with the addition of processing aids like CMC, XG, and aPAM at low concentrations (~ 9 wt.% processing aid and 91 wt.% CNF both in dry weight equivalents) and that these processing aids can be added using standard polymer high shear mixing in a much faster and more controlled process than air-drying. Wet extrudates with an average length of 0.61 m (~2 ft), width of 5.1 cm (2 inches), and thickness of 1.46 ± 0.05 mm were processed using a single screw extruder. The length of the extrudate was only limited by the amount of material at hand and by the lack of collection rolls. Out of the three processed paste types, CNF/CMC extrudates appeared to be the most homogenous and contained the least number of defects like aggregates and pinholes. This was possibly due to the stronger Newtonian rheological response of CNF/CMC ($n = 0.42$) when compared against pure CNF ($n = 0.13$). On the other hand, CNF/XG and CNF/aPAM extrudates contained more defects and developed a strong shear thinning response. After pressing and heating, tensile testing of the processed CNF/CMC extrudates revealed equivalent mechanical properties in terms of ultimate strength, density, and modulus when compared to cast CNF films prepared by typical solution casting. Additionally, calendering of the wet extrudates showed that full consolidation can be achieved, which eliminates the need to use discrete pressing steps.

More broadly, the results obtained show that it is possible to utilize common polymer processing methods for CNF from beginning to end of the processing chain allowing the potential to significantly increase production rate and lower cost. Banbury high-shear mixing, extrusion and calendering provide an elegant way to both continuously process CNF and take advantage of the already developed polymer melt-processing industry, while at the same time, taking advantage of their relatively lower cost as compared to typical paper production methods. Though the work performed employed the use of a single screw extruder, it is envisioned that the use of other more advanced extruder configurations would add utility, such as twin screw extruders that can handle more viscous polymer melts allowing more concentrated CNF/aid pastes (above 25 wt.% total solids) or single screw extruders with mixing stages or twin-screw mixing extruders allowing continuous mixing of the processing aid in line with extrusion in a single step, as is performed commercially with polymer melts, currently.

3.5 Acknowledgements

The authors would like to thank the US Endowment and the Public-Private Partnership for Nanotechnology (Grant Number: 109217) and Army Research Office for funding this research (Grant Number: W911NF-17-0203).

Additionally, the authors would like to thank Dr. Carlos Martinez for the advice given with regards to the zeta potential measurements.

4. CONTROLLING THE REDISPERSION AND SETTING BEHAVIOR OF CNF+CMC SYSTEMS

In the presented work, all the laboratory experiments and work in this chapter was performed by Sami M. El Awad Azrak. The manuscript writing and submission was done by Sami M. El Awad Azrak. Jared A. Gohl performed and collected the titration results and revised the manuscript. Dr. Davis revised the manuscript. Dr. Youngblood, Dr. Moon, Dr. Schueneman provided guidance on the research direction and on all writing.

This chapter contains work has been submitted for review in Cellulose under the title of “Controlled Dispersion and Setting of Cellulose Nanofibril (CNF) - Carboxymethyl Cellulose (CMC) Pastes”.

4.1 Introduction

Unlike CNFs which are produced by mechanical fibrillation, carboxymethyl cellulose (CMC) is an ionic ether derived from cellulose prepared from the esterification reaction between alkaline cellulose and monochloroacetic acid^{115,116}. This reaction causes the substitution of some of the hydroxyl groups in the glucose repeat unit for negatively charged carboxymethyl groups ($-\text{CH}_2-\text{COO}^-$)¹¹⁶. The average number of hydroxyl groups substituted per glucose unit is referred to as the degree of substitution (D.S.), where a D.S. of one would mean that on average one out of three -OH groups were replaced. Owing to its nontoxic nature and its ability to fully dissolve in water, CMC has found uses in the food, cosmetic, and pharmaceutical industries as a highly effective thickener, viscosifier, gelling agent, and rheological modifier^{100,117}. CMC has even been reported to significantly reduce the yield stress by 60 – 80 % of highly loaded lignocellulosic biomass pastes (up to 25 wt.% solids) from corn stover which, in turn, facilitated their processing for use as plausible liquid fuel alternatives^{80,111}. More recently, CMC has shown to be an excellent water-soluble processing aid to highly loaded CNF pastes (up to 25 wt.% solids) and in turn allowed for continuous extrusion of CNF sheets without reducing the mechanical performance¹¹⁸.

CMC's effectiveness as a processing aid in CNF systems could be tied to its ability to adsorb irreversibly to the surface of the fibrils¹⁰⁵. This adsorption occurs due to the attachment of unsubstituted CMC cellulose units onto the surface of exposed cellulose chains on CNF fibrils. In the wet state (i.e., suspension), the adsorbed CMC carboxylates reduce fibril-fibril contacts and fibril-fibril friction and entanglements¹¹². A reduction in apparent viscosity has been reported in highly loaded CNF+CMC and corn-stover+CMC pastes which agrees with the stated theories^{80,118}.

This absorption behavior has also been observed for low solids (1 – 3 wt.%) pulp systems that contain CMC as a wet end additive^{106,108,119,120}. Furthermore, fully dried CNF with adsorbed CMC have been reported to be redispersible possibly due to the reduced number of hydrogen bonds formed and the added negative surface charges which facilitates swelling¹⁰⁵.

Considering that most CNMs processed today contain no more than 30 wt.% solids, the ability of a CNM system, like that of CNF, to fully redisperse after being dried can significantly aid their commercialization by reducing the costs associated with transportation. In this way, CNFs can be transported in the dry state and redispersed at the manufacturing plant to the desired solids concentration for further processing. Additionally, understanding the possible methods or pretreatments that will allow for a semi-permanent setting of CNFs after being processed into the desired shape (e.g., clamshells, cups, sheets, etc.) can in turn expand their possible uses in the dry state by reducing their susceptibility to humid conditions. For these reasons, understanding and having the ability to control the redispersion and setting behavior of CNFs becomes very important.

In this paper highly loaded (~18 wt.% solids) CNF+CMC pastes were prepared using a high shear Banbury mixer. Subsequently, a single-screw extruder was used to form the prepared pastes into wet filament/cord and proved to be an effective bulk processing technique for CNF+CMC. Three different CMC degrees of substitution were evaluated (0.7, 0.9, and 1.2), all with the same molecular weight of 250,000. Zeta potential and titration were used to quantify the surface charge (mV) and the amount of active carboxylic groups (mmol/g) adsorbed on CNF fibrils, respectively. The re-dispersibility of the dry and pelletized CNF+CMC pastes was qualitatively assessed by remixing and re-extrusion and quantitatively assessed through turbidity measurements both in DI water and in an alkaline solution (0.1 M NaOH). To investigate the possible setting of CNF+CMC, different chemical treatments were assessed including two popular waterborne wet strength enhancers (polyamide epichlorohydrin (PAE) and polyamine epichlorohydrin (PAmE)) and a waterborne carbodiimide crosslinker (CDI). Treatment with hydrochloric acid (HCl), the multivalent cationic salt calcium chloride (CaCl₂) and the polycationic polymer polyethyleneimine (PEI) was also investigated. Similarly, the effectiveness of the setting behavior of the different chemical treatments was assessed through turbidity. Lastly, FTIR was used to elucidate the possible mechanisms behind the suppressed redispersion behavior observed for each chemical treatment.

4.2 Experimental section; Materials and Methods

4.2.1 Materials

Hydrochloric acid (HCl) solution at 37 %, calcium chloride (CaCl_2) powder, and branched polyethyleneimine (PEI, $M_w \sim 800$) were procured from Sigma-Aldrich. Standardized 0.1 M NaOH solution was purchased from Fisher Scientific. Picassian[®] XL 702, a waterborne polycarbodiimide (CDI) crosslinker with a solids content of 40%, was kindly provided by Stahl Polymers. Two waterborne crosslinking resins of polyamide epichlorohydrin (Polycup[™] 9200, Lot#0002475278, 20 % solids, PAE) and polyamine epichlorohydrin (Polycup[™] 7360A, Lot# 2459303, 38 % solids, PAmE), were kindly supplied by Solenis LLC. Powders of carboxymethyl cellulose sodium salt (CMC-Na) with three different degrees of substitution (D.S.) of 0.7, 0.9, and 1.2 and with a molecular weight of $M_w = 250,000$ (Lot# MKCK7917, Lot# MKCF4819, and Lot# MKCF8509) were purchased from Sigma Aldrich. Mechanically fibrillated CNFs were procured from University of Maine, Orono, ME, USA at a concentration of ~ 23.5 wt.% solids in water (Batch #122, 90 % fines retained). The process of isolating this specific type of CNFs is explained in detail by C.A. de Assis et al⁸. Two TEM images of the mechanically fibrillated CNF used are shown Figure C. 1. Purified water was produced using a Barnstead system and used for all experiments. Unless otherwise stated, solutions of HCl, CaCl_2 , PEI, PAE, and PAmE were prepared with water.

4.2.2 Preparation of Highly Loaded CNF+CMC Pastes

The preparation of highly loaded CNF+CMC pastes has been explained in detail in a previous publication¹¹⁸. In brief, 52 g of CNF (at ~ 23.5 wt.%) was loaded into a high shear torque mixer (Plasti-Corder PL 2100 Electronic Torque Rheometer, C. W. Brabender, South Hackensack, NJ) equipped with Banbury type mixing blades and mixed at 55 °C and 120 rpm. While the CNF was being mixed, CMC powder was gradually added until reaching a dry weight CMC:CNF ratio of 0.1:1. Water was added to adjust the paste's solids concentration to ~ 18 wt.%. The paste was mixed until complete CMC incorporation, which was signaled by a constant torque reading/plateau. The entire mixing process took on average less than 40 min and yielded approximately 66 g of wet CNF+CMC paste. This mixing process was repeated for each of the different CMC degrees of substitution (0.7, 0.9, and 1.2). The prepared CNF+CMC pastes were kept in the refrigerator to

avoid any microbiological growth and used as quickly as possible. It is important to note that the word “paste” is used throughout the report to refer to these highly loaded CNF+CMC mixtures. The word “suspension” is used to refer to dilute suspensions prepared from the wet or dried pastes, respectively.

4.2.3 CNF+CMC Filament/Cord Processing

The prepared CNF+CMC pastes were extruded using a Brabender torque rheometer (ATR) with an attached single-screw extruder unit (L/D = 25, barrel diameter of 1.9 cm, and a conventional 3:1 compression screw). A filament head attachment with a 2 mm nozzle was used. Extrusion was carried out at 25 °C and at a screw speed of 10 rpm. The filament/cord was collected using a cardboard roll.

4.2.4 Chemical Treatment

The extruded wet CNF+CMC cords were cut into ~100 mm long segments with an approximate wet diameter of 2 mm (see Figure C. 2). Treatment solutions of 0.1 M HCl, 0.1 M CaCl₂, 10 % PEI, 10 % PAE, and 10 % PAmE were freshly prepared. The still wet cord segments were carefully submerged into the different treatment solutions, respectively. Treatment time, solution concentration, and drying/curing temperature were optimized through preliminary experimental trials with HCl and assumed to also apply for CaCl₂ (see Figure C. 3, Figure C. 4, and Figure C. 5). It was determined that a concentration of 0.1 M was ideal to retain the cord's dimensions while a soak time of 20 min allowed for the treatment to penetrate a distance of 2 mm (i.e., the cord's diameter). After the respective treatment, excess solution was drained off and the cord segments were oven dried at 70 °C for 1 h, to avoid any oxidation or browning. For treatment with PEI, PAE, and PAmE, the cord segments were cured in the oven at 70 °C for PEI, and 85 °C or 25 °C for PAE and PAmE (per supplier recommendations). Due to CDI's reactivity at room temperature conditions and the required acidic conditions for correct activation, the treatment process was slightly adjusted. CDI was mixed directly into the CNF+CMC paste at a dry weight ratio of CMC:CDI of 1:1. Subsequently, the CNF+CMC+CDI cord segments were submerged for 20 minutes in 0.1 M HCl and cured at 70 °C or 25 °C. Lastly, oven dried CNF+CMC cord segment without any treatment, termed “untreated” were also prepared and dried at 70 °C for 1 h.

4.2.5 Pelletization

For all treatments and degrees of substitution, the dried and cured CNF+CMC cords were cut by hand using scissors into pellets with an approximate length of ~1 mm. Longer untreated CNF+CMC cords were pelletized using a commercial pelletizer (Davis Standard, Pawcatuck, CT, Model PK-102) running at 30 rpm for the rehydration and remixing analysis.

4.2.6 Zeta Potential

The prepared CNF+CMC pastes (D.S. = 0.7, 0.9, and 1.2 all at ~18 wt.%) were diluted to 1 wt.%. CNFs adsorbed with CMC were precipitated by centrifugation (10,000 RFC) with any unbound CMC remaining in the supernatant. The supernatant was discarded and the CNF fibrils were resuspended by shear mixing in purified water. This process was repeated 3 times. Subsequently, the washed suspensions were further diluted to a final concentration of 0.025 wt.%. Zeta potential measurements were carried out using a Zetasizer Nano ZS (Malvern Panalytical) and disposable folded capillary cells (Model: DTS1070). The viscosity of the suspensions was not measured but was assumed to be that of water due to the low solids concentration. The pH of all the suspensions was measured to be 6.6 (HANNA® Instruments). Eight measurements were recorded, and the average was reported along with \pm STD error bars. Quality criteria were met for all suspensions analyzed, yet the count rate varied for pure CNF suspensions.

4.2.7 Titration

From the ~1 wt.% CNF+CMC suspensions prepared for zeta potential analysis, 5 mL were added to 250 mL beakers and diluted with 50 mL of deionized water. 500 μ L of 0.1 M HCl was added to fully protonate the carboxylic acid groups on the CNFs. The resulting mixture was titrated with 5 mM NaOH solution. The pH was monitored using an Oakton Acorn pH meter. Representative titration curves (pH verses titrant volume) can be seen in Figure C. 6. The volume between the two inflection points on the curve was used to calculate the amount of COOH present on the nanofibers.

4.2.8 Turbidity

0.17 g of the treated or untreated CNF+CMC pellets were added into a scintillation vial followed by 17 mL of purified water or 17 mL of a 0.1 M NaOH solution (i.e., a target

concentration of 1 wt.% solids). The pellets were stirred in solution for 24 h at 1000 rpm and 25 °C. This was repeated for each different degree of substitution and treatment type. Additionally, 1 wt.% never-dried CNF+CMC and pure CNF suspensions were prepared as control groups. Following stirring, 100 μ L of the supernatant, with an unknown solids concentration of redispersed CNFs, was diluted with an additional 17 mL of purified water. Dilution was performed to be in the most accurate reading range of the turbidity meter. The dilute suspensions were analyzed using a nephelometric turbidimeter (Vernier®, Beaverton, OR) consisting of a 90° photodiode detector and an 890 nm infrared LED light source. The turbidity meter was calibrated using a 100 NTU Formazin standard and DI water (i.e., 0 NTU) in a glass cuvette. Before collection, a 10 mm stir bar was added to the sample glass cuvette, and the turbidity meter was placed on top of a stir plate. Turbidity was continuously collected every 0.5 s for 650 s while the suspension was being stirred at 400 rpm. Six measurements were carried out per sample group with a fresh diluted sample loaded for every measurement. The average between all 6 measurements is reported along with \pm STD error bars as stated under the figures, respectively.

4.2.9 FTIR-ATR

Treated and untreated CNF+CMC pellets, CMC powder (D.S. = 0.7), and a pure cast CNF film were conditioned in a vacuum oven for 24 h at room temperature. The samples were placed in direct contact with the ATR crystal and a 550 cm^{-1} to 4000 cm^{-1} spectra was captured using an FTIR-ATR system (PerkinElmer) with a resolution of 4 cm^{-1} . 20 sample scans were collected, and background subtraction was performed, respectively. Baseline correction was applied to all the spectra for fair comparison.

4.2.10 Scanning Electron Microscopy (SEM)

~25 mm long dry segments of untreated CNF+CMC cord were secured to a conductive aluminum stub with carbon tape and then sputter coated (SPI sputter coater) with a platinum-gold target for 60 s. No polishing or sanding was used. The samples were imaged using a Quanta 650 FEG field emission electron microscope at 3 KeV and a spot size of 5. The working distance varied from 39 – 41 mm to achieve the highest resolution.

4.3 Results and Discussion

4.3.1 CNF+CMC Bulk Processing and Pelletizing

Extrusion-based processes are one of the most versatile, commercially available, and easily scalable processing methods used for current commodity polymers. For these reasons, a single-screw extruder was employed to continuously extrude the highly loaded (~18 wt.%) CNF+CMC pastes. Results show that wet filament with a diameter of ~2 mm (~1 mm dry) can be successfully processed without any restrictions on its final length. The extruded cord was collected and oven dried on a cardboard roll as shown in Figure 4.1a and Figure 4.1b. Constrained drying was necessary for the CNF+CMC cord to retain its shape and avoid shrinking/warping (see Figure 4.1c versus Figure C. 6). Following drying, the cord was easily pelletized by using a commercial pelletizer running at 30 rpm as shown in Figure 4.1d. The processed CNF+CMC pellets had an average length of 6.73 ± 2.5 mm. Roughly 10 g of dry cord were processed and presented in Figure 4.1d.

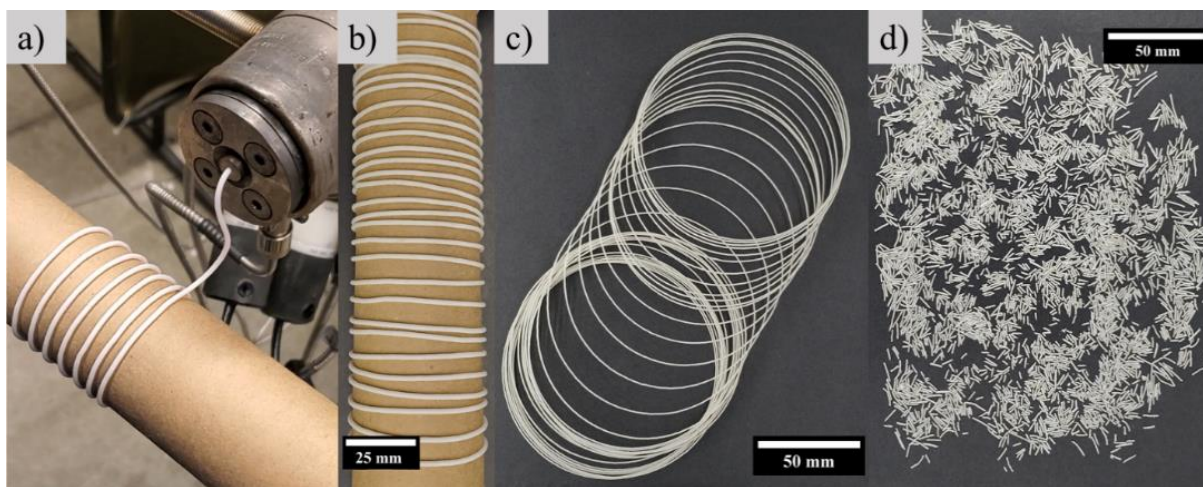


Figure 4.1 Single-screw filament/cord extrusion of a CNF+CMC paste (at ~18 wt.%) through a 2 mm nozzle (a), collected CNF+CMC wet cord extrudate on a cardboard roll (b), oven dried CNF+CMC cord (c), and pelletized cord (d).

With the current set up used, dry CNF+CMC extrusion output rates of up to 0.25 ± 0.072 kg/h and nozzle speeds of up to 7.68 ± 2.22 m/min were possible at a screw speed of 110 rpm. Although the nozzle speeds are lower than those typically reported in conventional spinning processes (20 – 150 m/min)¹²¹, filament die extrusion can process larger diameter cord (> 1 mm) versus those typically seen for spinnerets (10 – 500 μ m)¹²², making it a more effective bulk

processing methodology. Additionally, larger diameter cord allowed for easier handling and collection as the wet cord extrudate was relatively fragile and does not strain harden as conventional synthetic polymeric filament.

The mechanical properties of the processed CNF+CMC cords are not expected to be higher than those typically observed for CNF, (2,2,6,6-tetramethylpiperidin-1-yl)oxidanyl (TEMPO) oxidized CNF or composite fiber filaments prepared using wet- or dry- spinning methodologies^{18,123,124}. This is due to the lower shear rates typically observed in larger nozzles and the lack of filament drawing, both of which facilitate CNF fibril alignment in the axial direction and improve the mechanical properties. However, the intent of this report is to understand the redispersion and setting behavior of highly loaded CNF+CMC systems rather than improve the mechanical performance of the extruded filament/cord.

The surface morphology of the oven dried and untreated CNF+CMC cords with a varying CMC degree of substitution (D.S. = 0.7, 0.9, and 1.2) is shown in Figure 4.2 below. It is evident that there is a lack of fibril alignment when Figure 4.2 is compared to other reported drawn CNF filament micrographs^{125,126}. Furthermore, there appears to be no difference between cords prepared with CMC with a D.S. of 0.7 and 0.9 (Figure 4.2a and Figure 4.2b, respectively), while the cord prepared with a D.S. of 1.2 appeared to have a slightly rougher surface (Figure 4.2c).

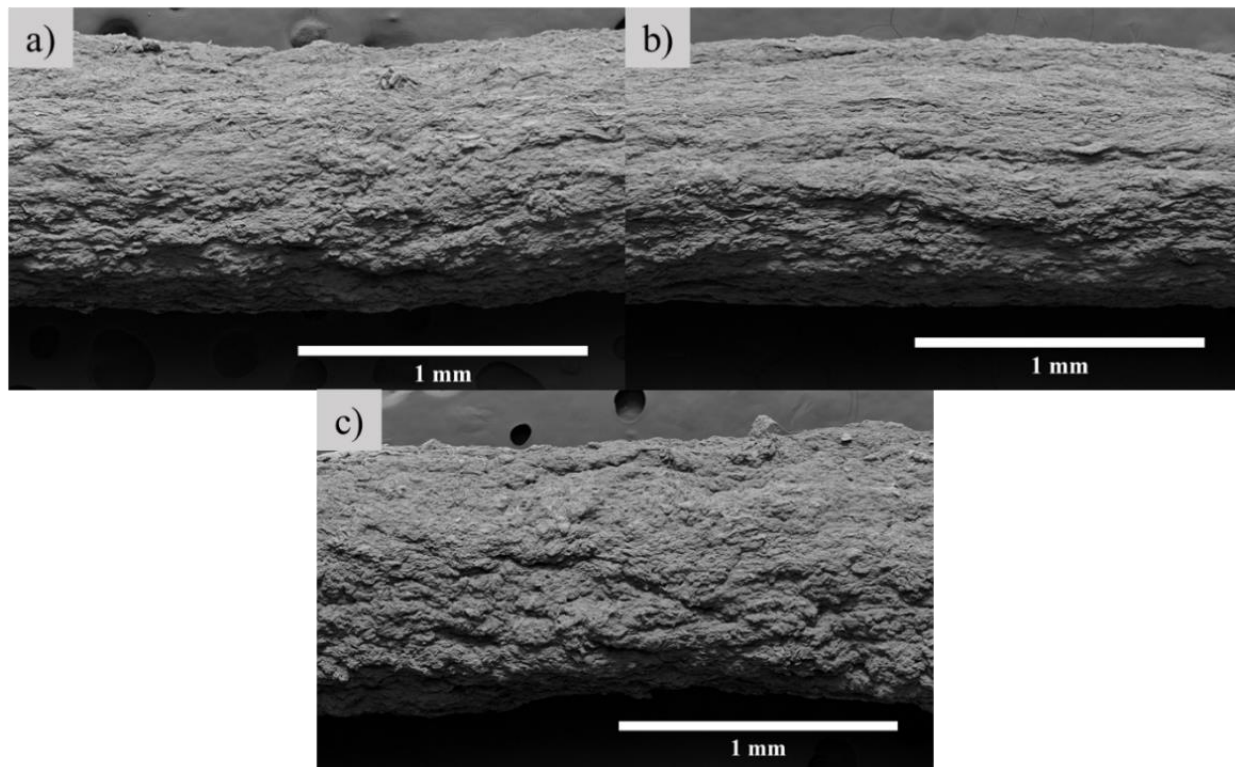


Figure 4.2. Surface morphology of the extruded and dried untreated CNF+CMC cords with a varying degree of CMC carboxymethylation or substitution of 0.7 (a), 0.9 (b), and 1.2 (c).

4.3.2 CMC Adsorption onto CNF fibrils

As mentioned in the introduction, CMC has been reported to adsorb irreversibly to the surface of CNF even under mild heating conditions (22 °C) in low solids (~1 wt.%) suspensions in water¹⁰⁵. This adsorption occurs due to the attachment of unsubstituted CMC cellulose units onto the surface of exposed cellulose chains on CNF fibrils through hydrogen bonding and can be improved if cations (e.g., Ca^{2+}) are added to the CNF suspension^{127,128}. In this work, both the Banbury high-shear mixing process and the relatively high mixing temperatures (55 °C) used to prepare CNF+CMC pastes also caused CMC to adsorb irreversibly to the surface of CNF even at high solids loadings (~18 wt.%). This was confirmed through zeta potential and titration measurements on dilute CNF+CMC suspensions prepared from the different pastes. As shown in Table 4.1, CMC adsorption caused an increase in surface charge from -36.8 ± 2.04 mV for pure CNF to -59.3 ± 1.31 mV for CNF+CMC (D.S. = 0.7). Additionally, there was no statistical difference between the three CMC degrees of substitution with respect to zeta potential (one-way

ANOVA: $F_{2,21} = 2.22$, $P = 0.133$, $R^2 = 0.175$). This could mean that the surfaces were completely saturated even with a more negative CMC with a D.S. of 1.2.

As shown in Table 4.1, titration of the different CNF+CMC suspensions with NaOH revealed the presence of weak acid functionalities from the adsorbed CMC's carboxylic acids. More specifically, surface charge increased from 0.094 ± 0.005 mmol/g COOH for pure CNF to 0.166 ± 0.035 mmol/g COOH for CNF+CMC with a degree of substitution of 0.9. However, while zeta potential revealed a change in magnitude of surface charge (mV) for all D.S. in CNF+CMC when compared to pure CNF, titrated surface charges for CNF+CMC with a D.S. of 0.7 and 1.2 were not significantly different to pure CNF (0.104 ± 0.024 and 0.082 ± 0.012 mmol/g COOH, respectively). As expected, the titrated charges for pure CNF and CNF+CMC are lower than those typically observed for TEMPO oxidized CNF (up to 1.5 mmol/g)^{129,130} due to the lower level of carboxylic functionalities.

Table 4.1. Zeta potential and titration of dilute pure CNF and CNF+CMC suspensions. Each suspension was mixed, centrifuged, and resuspended in water 3 times to remove non-adsorbed CMC or other loose species. Eight measurements per sample were carried out for zeta potential analysis while 3 measurements per sample were performed for titration. The average and standard deviation of the samples are displayed. 5 mM NaOH was used for titration.

Suspension Type	Ave. Zeta Potential [mV] \pm STD	Surface Charge [mmol/g COOH] \pm STD
Pure CNF	-36.8 ± 2.04	0.094 ± 0.005
CNF+CMC (D.S. = 0.7)	-59.3 ± 1.31	0.104 ± 0.024
CNF+CMC (D.S. = 0.9)	-58.1 ± 2.02	0.166 ± 0.035
CNF+CMC (D.S. = 1.2)	-58.4 ± 2.06	0.082 ± 0.012

Given that CMC adsorption was present, it's plausible that the CNF fibril's ability to form irreversible hydrogen bonds between themselves was suppressed. Hence, the pelletized and untreated cord was able to rehydrate itself rapidly (under 20 min) without any stirring/mixing as shown in Figure 4.3(a-c). These rehydrated pellets were re-mixed using the same Banbury mixer and reformed into the original ~18 wt.% paste as shown in Figure 4.3d. Complete re-mixing was confirmed by an equivalent torque reading on the mixer when compared to a freshly prepared CNF+CMC paste (see Figure C. 7). It is important to note that the torque plateau for the rehydrated CNF+CMC pellets was reached in less than 2 min versus the original ~19 min (see Figure C. 7), hence complete re-mixing was easily and quickly achieved. Furthermore, this paste was re-

extruded into a cord without any difficulty and dried as shown in Figure 4.3e and Figure 4.3f and appeared identical to the original cord before pelletizing (Figure 4.1c). Importantly, this shows that by adding CMC, the material can be extruded, dried, pelletized, rehydrated, and extruded to the same consistency to “close the loop”, which conceptually allows dry shipment of material.



Figure 4.3. Pelletized untreated CNF+CMC pellets at different stages of the rehydration process starting completely dry (a), ~30 s after adding water (b), 20 min after adding water (c), after being re-mixed in the Banbury shear mixer (d), and re-extruded into a filament/cord (e) and oven dried at 35 °C on a cardboard roll (f).

4.3.3 Dispersibility and Setting Behavior of CNF+CMC

To evaluate the dispersibility and setting behavior of highly loaded CNF+CMC pastes, different chemical treatments were selected and applied to the extruded wet cords. The treatments assessed were HCl, CaCl₂, PEI, CDI, PAE, and PAmE. Light scattering techniques like turbidity are often used to monitor the degree of fibrillation/quality during CNF manufacturing

processes^{131,132} and, in this work, served to gauge the level of redispersion achieved by the treated and untreated dry CNF+CMC materials in water. Turbidity results in Figure 4.4e show that complete redispersion is observed when the dried-untreated CNF+CMC samples (~29 NTU) are compared to the never-dried CNF+CMC dilute suspensions (~30 NTU), regardless of CMC's degree of substitution. On the other hand, chemical treatment with HCl, CDI, PAE and PAmE all significantly suppressed the level of redispersion achieving a value of less than 1 NTU when compared to the control groups of never-dried pure CNF (~29 NTU), never-dried CNF+CMC (~30 NTU), and dried-untreated CNF+CMC (~29 NTU). As shown in Figure 4.4(a-d) and Figure C. 9, complete redispersion was assessed visually where no observable macroscopic pellets were left in the suspension after mixing versus clearly visible pellets that did not redisperse (i.e., semi-permanent setting). Furthermore, pellets treated with HCl, CDI, PAE, or PAmE did not show any sign of redispersion even after 4 weeks of being immersed in water.

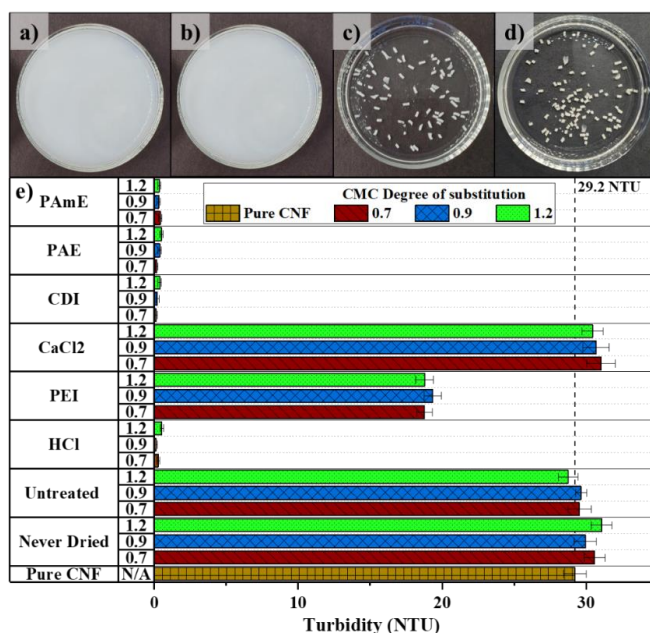


Figure 4.4. Dispersed never-dried CNF+CMC (a), redispersed dried-untreated CNF+CMC (b), redispersed HCl treated CNF+CMC (c), and redispersed PAE treated CNF+CMC (d) all in water after 24 hours of mechanical stirring and with a D.S. of 0.7. The turbidity response of treated and untreated CNF+CMC materials each prepared with CMC with three different degrees of substitution (D.S. = 0.7, 0.9, and 1.2) (e). Untreated, PEI, CaCl₂, HCl, and CDI treated samples were dried at 70 °C while PAE, PAmE treated samples were dried at 85 °C. The CNF+CMC pellets were stirrer for 24 h in water at 25 °C before turbidity was collected and the pictures were taken. For each treatment type and D.S., a freshly prepared suspension was analyzed. Six measurements were carried out per sample. The mean and standard deviation error bars are displayed, respectively.

Unlike PAmE, PAE, CDI, and HCl, treatment with PEI and CaCl_2 did not seem to suppress the redispersion behavior of CNF+CMC possibly due to the inability of these treatments to form crosslinks between CNF fibrils which then permitted the adsorbed CMC to redisperse them as shown in Figure C. 9. It is important to note that the lower turbidity values observed for the PEI treatment (~19 NTU) are due to the strong cationic nature of the ammonium groups which caused the negatively charged fibrils to flocculate while in suspension rather than the lack of pellet redispersion. This was confirmed through a solids contents measurement of the supernatant (~1 wt.%) after redispersion which matched with the original target concentration (1 wt.%) when water was added to the dry pellets. Additionally, for all treatments studied, the degree of carboxymethylation or substitution (D.S. = 0.7, 0.9, and 1.2) of CMC appears to have no significant effect on the level of redispersion.

For the best performing setting treatments (HCl, CDI, PAE, and PAmE) dispersion in a strong alkaline solution (0.1 M NaOH, pH > 10) was also performed. The different treatments were assessed at two curing temperatures. Dispersion in NaOH helped isolate the effect of the different treatments on crosslinking by promoting negative surface charges on CMC by neutralizing any acid present, thus improving the swelling and dispersion behavior of CNF+CMC fibrils¹³³. This then revealed differences between treatments which were not evident in water (pH ~7). The results in Figure 4.5b show that HCl was effective regardless of the curing temperature achieving low turbidity values (6.7 NTU for 25 °C and 6.0 NTU for 70 °C, respectively) while PAmE and CDI were only effective at their higher curing temperatures of 85 °C and 70 °C achieving turbidity values of ~4 NTU and ~3 NTU, respectively. PAE was not effective regardless of the curing temperature hence high turbidity values were observed (23.9 NTU for 25 °C and 17.7 NTU for 85 °C), however there was a difference between the dispersion behavior observed for a cure temperature of 85 °C and 25 °C, (one-way ANOVA: $F_{1,10} = 74.3$, $P = 6.1 \times 10^{-6}$, $R^2 = 0.881$). The difference in dispersion behavior observed between the two different curing temperatures for CDI, PAE and PAmE suggests the formation of physical crosslinks rather than purely structural irreversibly changes that might have occurred during drying (i.e., hornification), while at higher temperatures chemical crosslinking occurs¹³⁴. As shown in Figure C. 10 and Figure 4.5a small pellet fragments were visible for all treatments hence some level of dispersion was still possible in the studied time period (24 h).

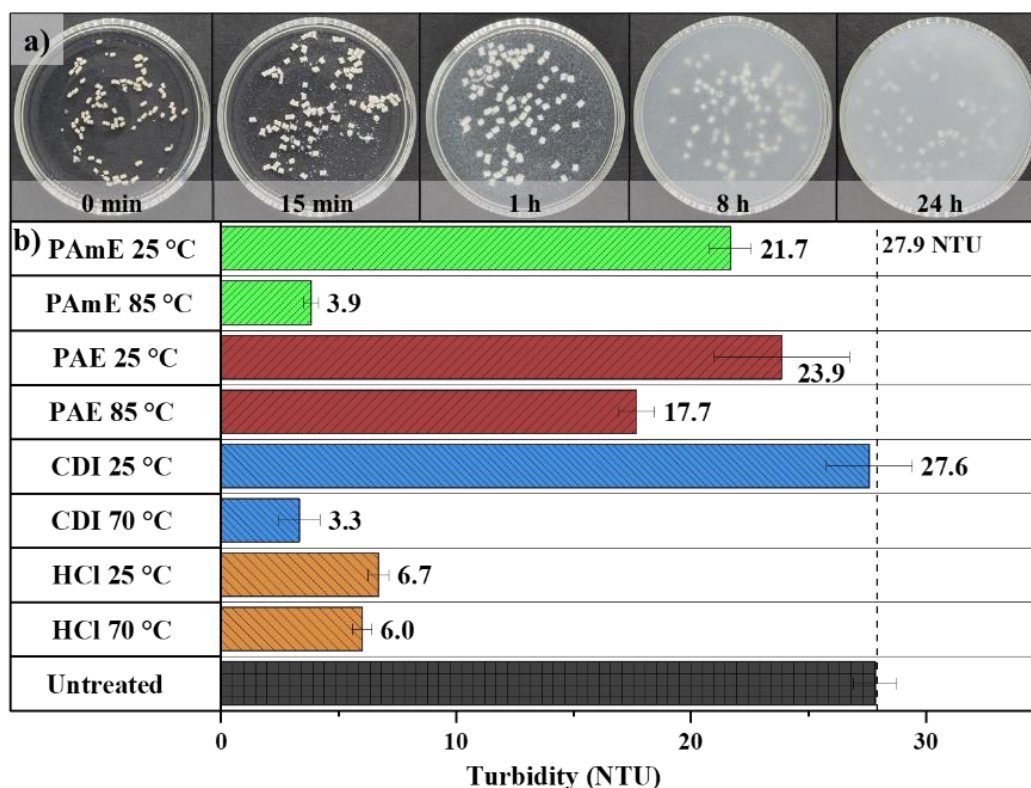


Figure 4.5. Redisperison behavior at different points in time for CNF+CMC treated with PAE cured at 85 °C in 0.1 M NaOH (a) and turbidity response of different treated and untreated CNF+CMC materials in 0.1 M NaOH at two curing temperatures(b). The suspensions were stirrer for 24 h before turbidity was collected. For each treatment type, two curing temperatures were evaluated while the CMC's D.S. remained constant at 0.7. A freshly prepared suspension was analyzed for each measurement. Six measurements were carried out per sample. The mean and standard deviation error bars are displayed, respectively.

Optical micrographs, shown in Figure 4.6, of the redisperised CNF+CMC fibrils in water and 0.1 M NaOH revealed that the fibril's morphology remained intact before and after redisperison when compared to never-dried pure CNF (Figure 4.6a) and dried-untreated CNF+CMC (Figure 4.6b). It is important to note that the reduced presence of CNF fibrils displayed in the micrographs for CDI (Figure 4.6c), HCl (Figure 4.6d), PAE (Figure 4.6e), and PAmE (Figure 4.6f) match with the results obtained for turbidity. Perhaps only non-crosslinked and or smaller fibrils were able to be redisperised back into the solution. Furthermore, expanded optical micrographs show the same behavior (see Figure C. 11 and Figure C. 12).

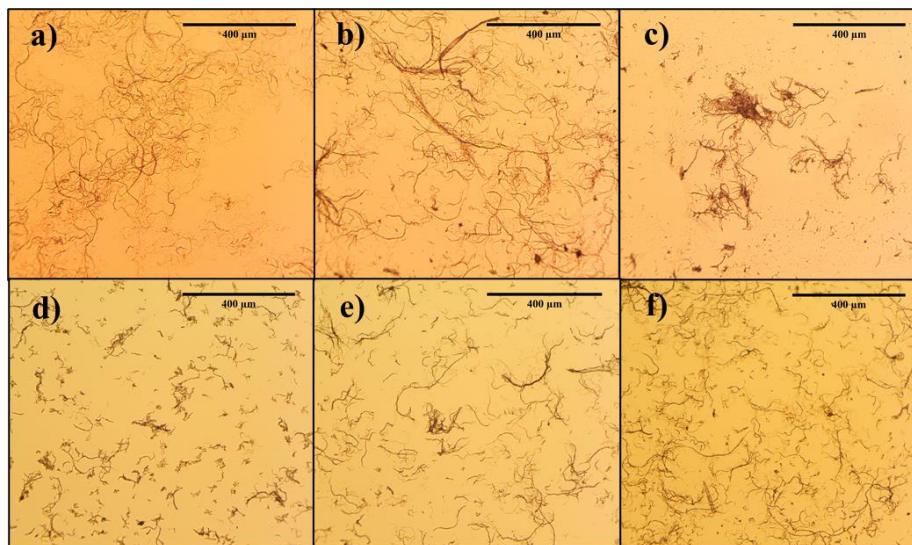


Figure 4.6. Optical micrographs of never-dried pure CNF dispersed in water (a), and dried-untreated CNF+CMC with a D.S. of 0.7 redispersed in water (b). Optical micrographs of CNF+CMC treated with CDI cured at 70 °C (c), CNF+CMC treated with HCl cured at 70 °C (d), CNF+CMC treated with PAE cured at 85 °C (e), and CNF+CMC treated with PAmE cured at 85 °C (f) all redispersed in 0.1 M NaOH and with a CMC D.S. of 0.7. The black scale bars in the top right have a length of 400 μm . Expanded (i.e., lower magnification) optical micrographs of the same dispersions are shown in Figure C. 11 and Figure C. 12.

4.3.4 FTIR Analysis of Treated CNF+CMC

To understand the possible setting mechanism behind the chemical treatments (HCl, CDI, PAE, and PAmE) which significantly suppressed the dispersibility of CNF+CMC, FTIR was used. As shown in Figure C. 13 through Figure C. 16, complete spectra (550 cm^{-1} to 4000 cm^{-1}) were captured for each treatment at two curing temperatures. As expected for all samples, common cellulose IR peaks at 3335 cm^{-1} , 2899 cm^{-1} , 1429 cm^{-1} , 1368 cm^{-1} , 1335 cm^{-1} , 1024 cm^{-1} , and 896 cm^{-1} were observed. These peaks were assigned to the O-H hydroxyl stretching, C-H stretching, and bending and stretching of $-\text{CH}_2$, $-\text{CH}$, $-\text{OH}$, and C-O bonds in cellulose, respectively^{135,136}.

Further analysis of the 1000 cm^{-1} to 1800 cm^{-1} spectrum region, shown in Figure 4.7, revealed key peak differences between the treated CNF+CMC samples and the control groups of pure CMC powder, pure CNF, untreated CNF+CMC, and cured pure compounds of CDI, PAE, and PAmE. As shown in Figure 4.7a treatment with HCl caused the formation of a strong peak at 1731 cm^{-1} which was assigned to the carbonyl stretching of newly formed ester linkages (i.e., COOC) or, equally likely, the carbonyl stretching of protonated carboxylates (i.e., COOH)¹³⁷. This occurred for both curing temperatures ($25\text{ }^{\circ}\text{C}$ and $70\text{ }^{\circ}\text{C}$). The peak at 1591 cm^{-1} which was

observed only for CMC powder and untreated CNF+CMC was assigned to the asymmetric stretching vibration of the carboxylate (COO^-) moiety^{138–140}. It is important to note that the peak at 1591 cm^{-1} was not present for HCl 25°C or HCl 70°C , indicating a possible replacement of COO^- groups with ester linkages or, due to the high acidity of 0.1 M HCl treatment, the protonation of the carboxylate that caused a shift of the 1591 cm^{-1} peak to 1731 cm^{-1} as shown by Cuba-Chiem et. al¹³⁸. Protonation and esterification could not be separated due to the similarity of the peak locations for the $\text{C}=\text{O}$ stretching vibration which typically lies between $1760\text{--}1700\text{ cm}^{-1}$. However, esterification crosslinking between CNF fibrils with adsorbed CMC could possibly explain the suppressed dispersibility behavior observed for both cure temperatures during turbidity measurements (Figure 4.5b). A schematic of the possible ester linkages between CNF fibrils with adsorbed CMC is shown in Figure 4.8a^{137,141}. The weak peak observed at 1645 cm^{-1} was assigned to the (O-H) bending vibration of adsorbed/bound water on CNF fibrils which was present in all samples CNF+CMC samples and pure CNF^{139,142,143}.

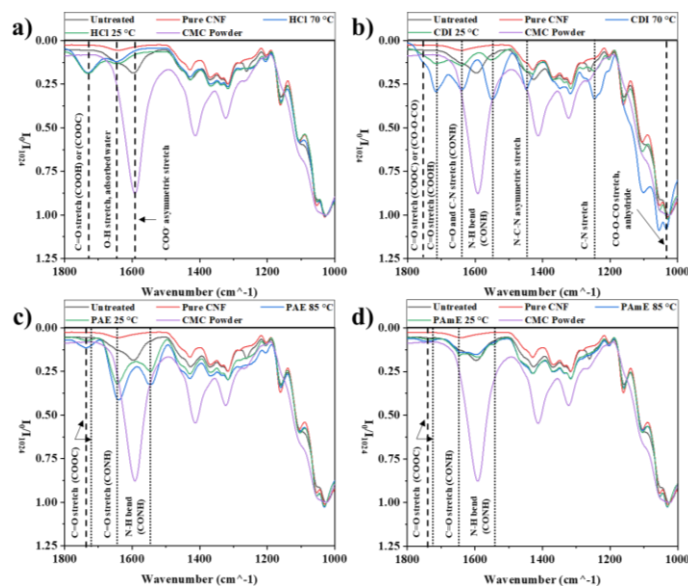


Figure 4.7. FTIR analysis of CNF+CMC treated with; HCl cured at 25°C and 70°C (a), CDI cured at 25°C and 70°C (b), PAE cured at 25°C and 85°C (c), and PAmE cured at 25°C and 85°C (d) all with a CMC D.S. of 0.7. The control groups of pure CNF, pure CMC powder, and untreated CNF+CMC are also shown on the respective plots. The samples were conditioned under vacuum for 24 h at room temperature before testing. All the spectra shown were baseline corrected and 20 scans were collected. All intensities were all normalized by the invariant cellulose peak intensity at 1024 cm^{-1} . Dashed vertical lines mark the peak locations found in the treated CNF+CMC spectra while the dotted vertical lines mark peaks found in the pure compound spectra, respectively.

As shown in Figure 4.7b, treatment with CDI lead to prominent absorption peaks located at 1754 cm^{-1} , 1716 cm^{-1} , 1639 cm^{-1} , 1549 cm^{-1} , 1448 cm^{-1} , 1247 cm^{-1} , and 1033 cm^{-1} . The appearance of these peaks could be understood through two possible reaction pathways between carbodiimides and CMC's protonated carboxylates, both of which start with the formation of unstable O-acyl urea as a reaction intermediate. The first reaction route leads to the formation of stable N-acyl urea linkages formed from the rearrangement of O-acyl urea^{144,145}. The formation of new N-acyl urea linkages between the adsorbed CMC repeat units can then possibly explain the observed 1639 cm^{-1} (C=O stretching, CONH) and 1549 cm^{-1} peak (N-H bending)^{145,146}. However, because these peaks were also present in the spectra for pure CDI cured at $70\text{ }^{\circ}\text{C}$ (shown by the dotted vertical lines in Figure 4.7b), they could simply originate from the added presence of the resin in the CNF+CMC system. The second CDI-carboxylic acid reaction route leads to the formation of anhydride linkages and urea as byproduct from the reaction between O-acyl urea and a additionally available carboxylic acid¹⁴⁵. The formation of anhydride linkages can then possibly explain the observed strong 1033 cm^{-1} peak (CO-O-CO stretching) and the 1754 cm^{-1} peak (C=O stretching), which were not present in the pure CDI spectra (shown by the dashed lines in Figure 4.7b), while the 1448 cm^{-1} (N-C-N asymmetric stretching) and the 1247 cm^{-1} peak (C-N stretching, amine) can be linked to the urea byproduct^{147,148}. A schematic of the possible anhydride linkages formed between CNF fibrils with adsorbed CMC is shown in Figure 4.8b¹⁴⁵.

There is also the possibility that ester linkages were formed between CMC units through a subsequent reaction between anhydride linkages and a nucleophile like that of a hydroxyl from either CMC or CNF leading to intra- or inter-molecular linkages which could also explain the appearance of the 1754 cm^{-1} peak/shoulder (C=O stretching, COOC) which was not present for the pure CDI compound (see dashed line in Figure 4.7b)^{145,149}. The peak observed at 1716 cm^{-1} (C=O stretching) could belong to carboxylic acids which were not converted during the CDI reaction. It is important to note that both reaction routes can occur simultaneously and the ratio between N-acyl urea and anhydride/urea has been reported to be dependent on the mobility of the reactive groups and ratio of concentration between carbodiimide and carboxyl groups¹⁴⁵. Additionally, similar to treatment with HCl, the lack of the 1592 cm^{-1} peak for either CDI $25\text{ }^{\circ}\text{C}$ and CDI $70\text{ }^{\circ}\text{C}$ points to a possible consumption of the (COO⁻) groups for the formation of N-acyl urea, anhydride, and ester linkages as well as the possible protonation of the carboxylates due to the low pH at treatment (0.1 M HCl). Although both CDI $25\text{ }^{\circ}\text{C}$ and CDI $70\text{ }^{\circ}\text{C}$ appeared to contain

the same major peaks in the 1000 cm^{-1} to 1800 cm^{-1} region, the disappearance of the 2117 cm^{-1} peak (assigned to the -N=C=N- stretching vibration of carbodiimides¹⁵⁰) shown in Figure C. 17, confirmed that a higher curing temperature ($70\text{ }^{\circ}\text{C}$) was necessary for complete CDI resin reaction/activation. Hence, the lack of complete CDI activation could possibly explain the much higher turbidity values observed for the CDI treatment cured at $25\text{ }^{\circ}\text{C}$ (27.6 NTU) when compared to the CDI treatment cured at $70\text{ }^{\circ}\text{C}$ (3.3 NTU) as shown in Figure 4.5b.

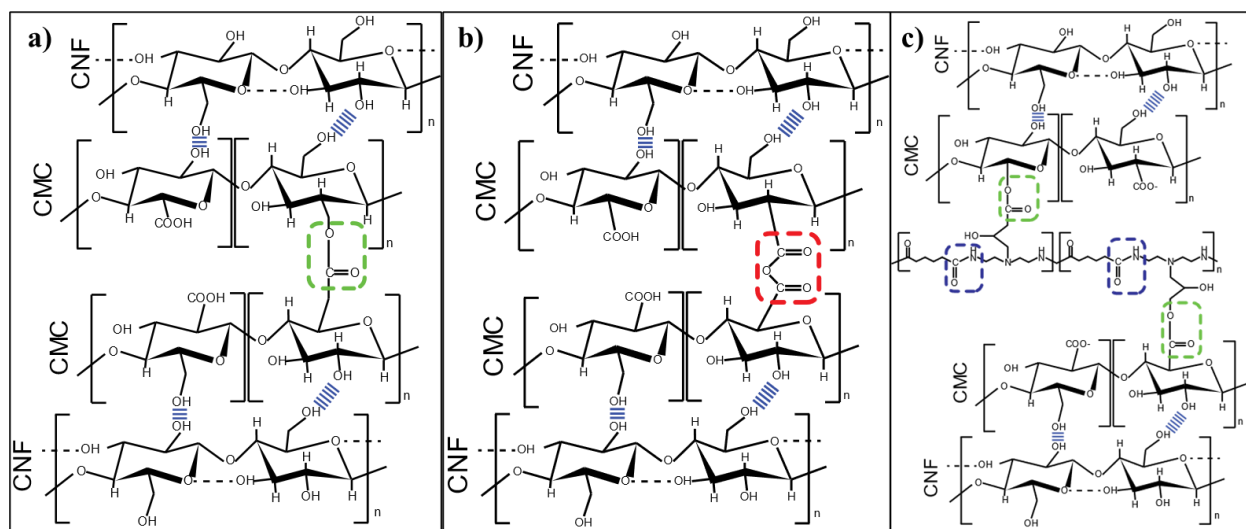


Figure 4.8. Schematic of CNF with adsorbed CMC through hydrogen bonding with possible ester linkages (circled in green) formed due to treatment with HCl (a), anhydride linkages (circled in red) due to treatment with CDI (b), and ester linkages (circled in green) formed due to treatment with PAE and PAmE (c). Note that amide groups (circled in blue) are present in the PAE and PAmE backbone. All the schematics shows CMC with a D.S. of 1.

Treatment with PAE, shown in Figure 4.7c, revealed amide I and amide II peaks at 1641 cm^{-1} (C=O stretching, CONH) and 1546 cm^{-1} (N-H bending), respectively. These were also present in the spectra for pure PAE cured at $85\text{ }^{\circ}\text{C}$ (see vertical dotted lines in Figure 4.7c and Figure 4.8c for the backbone structure) and are likely due to the added presence of the resin in the CNF+CMC system rather than the formation of new amide linkages between CMC units. However, carbonyl stretching vibrations of ester linkages (COOC) were observed at two different adsorption bands, one for PAE treated CNF+CMC (1742 cm^{-1} , dashed line) and one for pure PAE cured at $85\text{ }^{\circ}\text{C}$ (1732 cm^{-1} , dotted line). For PAE treated CNF+CMC, esterification has been reported to be the primary crosslinking mechanism behind the wet strength development or improvement in other

(COO⁻) containing nanocellulose systems like that of TEMPO oxidized CNF and cellulose ethers like CMC^{151–154}. The ester bonds are formed from the thermally induced reaction between (COO⁻) and the azetidinium groups in the PAE resin¹⁵⁴. A schematic of the possible ester linkages between CNF fibrils with adsorbed CMC is shown in Figure 4.8c¹⁵⁵. On the other hand, pure PAE has been reported to crosslink with itself forming ester linkages though its tail end carboxylates or, as a secondary crosslinking reaction, form 2-propanol linkages between the azetidinium groups on its backbone^{151,156,157}. Hence, PAE esterification with CMC and self-crosslinking could possibly explain the shift or appearance of the two ester absorption bands as shown in Figure 4.7c. It is important to note that while HCl and CDI treatment may have led to protonation of CMC's carboxylate groups, treatment with PAE or PAmE did not require a low pH and hence the peaks observed are likely ester carbonyl stretching vibrations. When the two cure temperatures (25 °C and 85 °C) are compared, the ester band (1742 cm⁻¹) is almost not present for the 25 °C cured sample possibly due to a reduced number of linkages formed, hence it was much easier for CNF+CMC to redisperse as seen in the higher turbidity values (see Figure 4.5b, 23.9 NTU for 25 °C versus 17.7 NTU for 85 °C).

As shown in Figure 4.7d, a similar spectrum to the PAE treatment was observed for treatment with PAmE. Again, the amide peaks simply confirmed the presence of the PAmE resin in the CNF+CMC system as these were also present in the pure PAmE cured at 85 °C spectra (dotted lines). Similar to PAE, two different absorptions bands for carbonyl stretching of esters were observed, one at 1742 cm⁻¹ (dashed line) for PAmE treated CNF+CMC and one at 1732 cm⁻¹ (dotted line) for pure PAmE cured at 85 °C. This is possibly due to the fact that both resin systems (PAE and PAmE) can react with the same functional groups (carboxylates, hydroxyls, thiols, and amines) which led to identical crosslinking linkages. Perhaps the only difference between the two resin spectra (PAE versus PAmE) is the lower peak intensities observed for PAmE. However, the performance of PAmE was superior in terms of redispersion suppression to that of PAE, as observed in Figure 4.5b. The reason for this is unknown but could be linked to the high cationic charge of PAmE which might have allowed for the resin to interact more strongly with the exposed (COO⁻) groups in CMC or other slightly negative charges on the surface of CNF fibrils as well as go into the nanopores between fibrils¹⁵². Furthermore, it is important to note that unlike all other treatments, the carboxylate peak (1592 cm⁻¹) was not consumed significantly for either cure temperature (25 °C and 85 °C). When the two cure temperatures are compared for treatment with

PAmE, the intensity for the 1732 cm^{-1} peak for a cure temperature of 25 $^{\circ}\text{C}$ were of weaker intensity when compared to the spectra for 85 $^{\circ}\text{C}$, which might explain the much higher turbidity value of 21.7 NTU when compared to 3.9 NTU, respectively (see Figure 4.5b).

Table 4.2. Peak intensity normalized by the invariant peak intensity at 1024 cm^{-1} .

Treatment type and cure temperature ($^{\circ}\text{C}$)	1033/1024 (CO-O-CO stretch, anhydride)	1549/1024 (Amide II, N-H bend, CONH)	1591/1024 (COO^- asymmetric stretch)	1641/1024 (Amide I, C=O stretch, CONH or H-O stretch)	1731/1024 (C=O stretch, COOC or COOH)	1754/1024 (C=O stretch, COOC or CO-O-CO)
HCl 70 $^{\circ}\text{C}$	0.996	0.045	0.058	0.118	0.186	0.138
HCl 25 $^{\circ}\text{C}$	0.988	0.066	0.080	0.133	0.188	0.147
CDI 70 $^{\circ}\text{C}$	1.082	0.336	0.112	0.278	0.203	0.124
CDI 25 $^{\circ}\text{C}$	1.018	0.109	0.071	0.141	0.113	0.084
PAE 85 $^{\circ}\text{C}$	1.024	0.323	0.226	0.413	0.112	0.100
PAE 25 $^{\circ}\text{C}$	1.018	0.245	0.194	0.316	0.073	0.064
PAmE 85 $^{\circ}\text{C}$	1.021	0.087	0.151	0.139	0.076	0.074
PAmE 25 $^{\circ}\text{C}$	1.018	0.095	0.167	0.153	0.065	0.061
Pure CNF	1.003	0.027	0.036	0.056	0.027	0.026
Pure CMC	0.996	0.338	0.877	0.299	0.081	0.084
Untreated CNF+CMC	0.982	0.079	0.182	0.129	0.057	0.054

Table 4.2 summarizes the FTIR results shown in Figure 4.7 where the intensity of the main peaks of interest (1033 cm^{-1} , 1549 cm^{-1} , 1591 cm^{-1} , 1641 cm^{-1} , 1731 cm^{-1} , and 1754 cm^{-1}) was normalized by that of the intensity of the invariant 1024 cm^{-1} peak assigned to the C-O stretching in cellulose^{158,159}. Overall, due to the numerous different reaction routes, treatment with CDI could have led to the formation of ester, N-acyl urea, anhydride, or all of the above linkages which made it a very effective treatment for the setting of CNF+CMC. PAmE was an equally effective setting treatment possibly due to the formation of ester linkages and, unlike PAE, had a high cationic charge which might have improved its interaction with CMC's carboxylate groups. However, both of these treatments were only effective when cured at higher temperatures (70 $^{\circ}\text{C}$ and 85 $^{\circ}\text{C}$, respectively). On the other hand, HCl was effective even when cured at room temperature (25 $^{\circ}\text{C}$). Lastly, PAE was the least effective setting treatment for CNF+CMC regardless of the curing temperature.

4.3.5 Water Uptake of Treated CNF+CMC

Water uptake of the differently treated CNF+CMC with a D.S. of 0.7 agreed with both the observed turbidity behavior and the possibly newly formed linkages detected through FTIR. For example, the best performing setting treatments of HCl and CDI (both cured at 70 °C) absorbed on average only 20.1 ± 0.19 %, and 17.5 ± 0.58 % of their weight in water, respectively. PAE and PAmE treated CNF+CMC (both cured at 85 °C) absorbed 41.6 ± 0.32 % and 59.7 ± 1.1 % of their weight in water, respectively. The higher water uptake for the PAE and PAmE treated CNF+CMC led to a much more flexible structure which could, in turn, be more susceptible to redispersion by mechanical stirring (i.e., softer structure). On the other hand, HCl and CDI treated materials were much more rigid and possibly less susceptible to redispersion by stirring. The flexibility of the treated CNF+CMC materials is qualitatively shown in Figure C. 18. Unlike HCl and CDI, hydrated PAE and PAmE treated CNF+CMC cord segments could be folded onto itself without fracturing into two pieces.

4.3.6 Ramifications of efforts

More broadly, the results obtained show that the redispersion and setting behavior of CNF with adsorbed CMC can be controlled through different chemical treatments. Industrially, redispersion grants the ability to transport CNF in a dry state, thus providing a significant reduction in weight and transportation cost. On the other hand, semi-permanent setting of CNF+CMC systems allows for CNF products (e.g., sheets, cups, lids, clamshells, etc.) to retain their shape after being processed while at the same time reducing their susceptibility to high humidity conditions, and hence extending the life of use and expanding their possible applications. Furthermore, bulk processing of CNF+CMC through conventional polymer processing equipment like a Banbury high-shear mixer, a single-screw extruder, and a commercial pelletizer takes advantage of the already developed polymer melt-processing industry and reduces the initial capital investment destined for new processing equipment.

4.4 Conclusion

Highly loaded CNF+CMC pastes (~18 wt.%) were prepared and continuously processed into cord using a single-screw extruder. Output rates of up to 0.25 ± 0.072 kg/h (dry) and nozzle speeds

of up to 7.68 ± 2.22 m/min were possible with the current set up. Thus, proving to be a successful bulk processing technique for highly loaded CNF+CMC systems. Zeta potential of never dried and dilute CNF+CMC suspensions showed a change in surface charge from -36.8 mV for pure CNF to -59.3 mV for CNF+CMC (D.S. = 0.7). Titration of the CNF+CMC suspensions with NaOH revealed the presence of weak acid functionalities attributed to the adsorbed CMC's carboxylic acids and showed an increase in surface concentration from 0.094 ± 0.005 mmol/g COOH for pure CNF to 0.166 ± 0.035 mmol/g COOH for CNF+CMC (D.S. = 0.9). Due to the adsorbed CMC on the CNF fibrils, dried-untreated CNF+CMC could be completely redispersed in water at room temperature conditions and allowed for complete remixing and re-extrusion back into a cord. Turbidity measurements confirmed that dried-untreated CNF+CMC fully redispersed, reaching values of ~29 NTU when compared to never-dried CNF+CMC (~30 NTU). On the other hand, chemical treatment with HCl, CDI, PAE, and PAmE almost entirely suppressed the dispersibility of dried-untreated CNF+CMC achieving turbidity values of less than 1 NTU. Overall, the dispersibility observed for dried untreated and treated CNF+CMC was not dependent on the degree of substitution of CMC. Subsequently, dispersion in a strongly alkaline solution (0.1 M NaOH) showed that HCl treatment was effective regardless of the curing temperature achieving low turbidity values (6.7 NTU for 25 °C and 6.0 NTU for 70 °C) while CDI and PAmE treatments were effective only at the higher curing temperatures (85 °C and 70 °C) achieving turbidity values of ~3 NTU and ~4 NTU, respectively. Treatment with PAE was the least effective, hence relatively high turbidity values were observed (23.9 NTU for 25 °C and 17.7 NTU for 85 °C) when compared to the other chemical treatments at either cure temperatures. Depending on the chemical treatment used, FTIR analysis of the treated CNF+CMC samples revealed the presence of possible ester, N-acyl urea, and anhydride linkages which could possibly explain the suppressed redispersion behavior. Lastly, water uptake of the differently treated and dried CNF+CMC materials agreed with both turbidity and FTIR results.

4.5 Acknowledgements

The authors would like to acknowledge the financial support provided by the US Endowment and the Public-Private Partnership for Nanotechnology (Grant Number: 109217)

5. PRELIMINARY PROCESSING OF FIBERS REINFORCED CELLULOSE NANOFIBRILS COMPOSITES (FR-CNF)

All laboratory work in this chapter was performed by Sami El Awad. All writing was done by Sami El Awad.

5.1 Introduction

Fiber reinforced composites (FRC) are materials which typically consist of two parts; a high strength reinforcing fiber phase that bears the majority of the applied load and a continuous phase/matrix which transfers the load to the fibers and also shields the fibers from environmental damage (e.g., swelling, oxidation). The combination of these two distinct materials can, in turn, lead to enhanced mechanical properties when compared to the properties of the constituents acting alone (i.e., a synergistic effect). The reinforcing fiber phase can be synthetic (e.g., nylon, PVA, aramid, carbon, rayon, Tencel), inorganic (e.g., fiber glass), or natural (e.g., flax, kenaf, ramie, and others). Each fiber type has its own advantages, for example, natural fibers are sustainable, low cost, low density, and have comparable specific tensile properties to synthetic fibers. However, synthetic fibers typically outperform natural fibers and have the added benefit of a high level of dimensional consistency (i.e., a high fiber quality, as there is an engineering control over diameter, lengths, and size). Common matrix materials include thermosetting phenolic, epoxy, and polyester resins and thermoplastic polymers like PP, PE, and PVC^{160–162}. Considering the growing concept of a circular economy¹⁶³, one of the biggest challenges to using natural fibers in composites is the poor compatibility between the hydrophilic fiber and the hydrophobic matrix, thus significant research efforts have been devoted to improving the compatibility as well as other aspects¹⁶⁴. Being that CNF is naturally sourced and shares the same surface chemistry as most natural fibers (surface neutral hydroxyl groups), it will likely have a much better compatibility to natural fibers and act to effectively transmit the load if used as a matrix material due to its strong tendency to form tangled/aggregated networks.

One of the most common forms of a composite for structural applications is a laminate due to the added control over the layer stacking sequence. Generally, laminates are formed by stacking or layering films/sheets of a stronger and stiffer material (e.g., ceramic) while a softer resin layer (e.g., PVB or EVA) is added between the sheets to bond the layers together imparting toughness

and flexibility to the structure^{165–167}. Contrary to the standard lamination process, previous work (shown in Chapter 2) has proven that CNF laminates of varying thicknesses can be made using a novel layer-by-layer wet stacking technique without the use of solvents or binders other than water. Neat CNF laminates with a working area of 117 mm by 117 mm and a thickness of 1.65 mm (24 layers of CNF) have been produced, yet even thicker structures can be made if desired. When the density of the CNF laminates is considered ($\sim 1.35 \text{ g/cm}^3$), as for specific strength, the results show that CNF laminates are comparable to Al 2024 and perform better than Al 6061, Nylon 6,6 and poly(styrene). However, the addition of a fiber reinforcement phase could further improve the toughness and strength of CNF laminates. To date, no work found in literature has shown such efforts regarding fiber reinforced CNF (FR-CNF) laminate processing or testing.

This chapter discusses the initial investigation into the processing and testing of FR-CNF composites. This investigation will help in the development of datasets to select the best fiber system to incorporate into cellulose nanofibril laminates to mitigate their inherent brittleness. The central hypothesis is that there will be an optimal fiber dimension (e.g., 3.175 mm, 6.35 mm, 12.7 mm, 25.4 mm long), type/source (e.g., inorganic, natural, synthetic), and concentration (in wt.% or vol.%) that will lead to the best CNF laminate performance. The optimal combination of fiber parameter and type will manifest in improved toughness, and possibly, ultimate strength and elastic modulus values for the laminate. This will ultimately affect the viability of using CNF laminates as structural materials.

5.2 Experimental section; Materials and Methods

5.2.1 Materials

Mechanically fibrillated CNFs were bought from University of Maine, Orono, ME, USA at a concentration of 3.1 wt.% in water (Batch #110, 90 % retained) and used as received to make the laminates (i.e., the matrix). The process of isolating the CNFs is explained in detail by C.A. de Assis et al⁸. Natural fibers (~ 10 mm long) of Flax, Abaca, Jute, and Kenaf were procured from Bast Fibers LLC. Synthetic fibers of Kevlar/aramid, viscous rayon, and nylon all with a length of 6.35 mm were obtained from MiniFIBERS Inc. Glass fibers with a length of 6.35 mm were obtained from Fibre Glast LLC. Lastly, poly(vinyl alcohol) fibers with a length of 6.35 mm were sourced in house. The obtained fibers served as the reinforcing phase in the laminate. Additionally,

unsized polyacrylonitrile (PAN) based chopped carbon fibers with a length of 3 mm, and 6 mm were kindly supplied by Zoltek® (PX35 type 02, $\rho = 1.81 \text{ g/cc}$,). Isopropanol, acetone, and ethanol were procured from Thomas Scientific and used as received. Potassium persulfate ($\text{K}_2\text{S}_2\text{O}_8$), silver nitrate (AgNO_3), tetrahydrofuran (THF), lithium aluminum hydride (LiAlH_4), acetic acid, 3-aminopropyl triethoxysilane (APTS), N,N-dimethylacetamide (DMAc), succinic anhydride, diethanolamine, and ethanolamine were purchased from Sigma-Aldrich and used as received. All de-ionized water used for this work was generated in house using a Barnstead system.

5.2.2 Processing of FR-CNF Composites

FR-CNF composites were prepared using the methodology previously used for neat unreinforced CNF laminates (see Section 2.2.2) except for the addition of fibers. In short, the initial CNF suspension (at 3 wt.%) was diluted to 1 wt.% and a predetermined amount of reinforcing fibers (in grams) was subsequently incorporated into the dilute CNF slurry in smaller steps and shaken vigorously by hand. 900 ml of the CNF+fiber slurry was then poured in a dewatering frame (Figure 2.1) and filtered for roughly 10 minutes. The filtered web (~7 wt.% solids) was then passed through a tabletop slip roller and dewatered to achieve a solids concentration of ~10 wt.%. After pressing, the CNF+fiber web was delaminated from the filter mesh cut into three smaller square sections (15.24 cm by 15.24 cm) which were stacked on top of each other. Finally, the stacked wet layers were hot pressed at a temperature of 126 °C until dry (~99 wt.%) using a hydraulic heated laboratory press model No. 3690 (Carver) forming the FR-CNF composite.

5.2.3 Mechanical Testing of FR-CNF Composites

Following ASTM D638 dogbone specimens were cut from prepared FR-CNF composites using a clicker press with a dogbone die type ASTM D638 IV (Ace Steel Rule Dies®). All the specimens were conditioned in a desiccator at 23 %RH for at least 2 days before mechanical testing. An electromechanical testing machine (MTS Insight) was used for tensile testing of dogbone specimens with a 1000 N load cell and serrated film clamps. Sandpaper was added at the grips to avoid specimen slippage. The crosshead speed was set to 1 mm/min for all samples. All the samples were preloaded to 1 N. Large sample groups were tested together to reduce any possible confounding variables in the study. The ultimate strength was taken to be the strength at failure.

The Young's modulus was obtained by steepest slope method and the strain was measured based on crosshead displacement (no extensometer was used); all the values were gathered from the built-in software (TestWorks4®). Grip compliance was measured using a thick 1020 steel specimen and was subtracted from the results. A micrometer and a caliper were used for measuring the exact thickness and width of the individual specimens.

5.3 Results and Discussion

5.3.1 FR-CNF Composites, First Impression

As shown in Figure 5.1 CNF-fiber wet webs (~10 wt.% solids) were successfully formed by directly mixing the fibers with the slurry and dewatering it. As shown in Figure 5.2 (a, b, c, and d), three of these webs were stacked and heated pressed until dry forming the FR-CNF composite for each fiber type, respectively. Additionally, efforts at processing FR-CNF composites were made by layering neat CNF layers and then dispersing the fibers between the layers. In this way the fibers were still randomly oriented in plane in the CNF matrix. However, attempts at making these neat layer-fiber layer-neat layer laminates failed as the higher concentration of fibers between the neat CNF layers resulted in delamination the CNF layers after heated pressing.



Figure 5.1 Wet CNF web (~10 wt.% solids) with added PVA fibers being pulled apart. The PVA fibers can be clearly appreciated in the ruptured locations at the top and bridging the crack in the center of the wet web.

As observed using a strong backlight in Figure 5.2 (e, f, g, and h), fiber dispersion is not homogeneous for the fiber types shown. This is especially true for abaca and aramid fibers (Figure 5.2e and Figure 5.2g, respectively). The heterogeneity is possibly due to fiber length (6.35 mm for aramid and 10 mm for abaca) which has been reported to influence the level of fiber entanglement and decrease some mechanical properties like elastic modulus and tensile strength¹⁶⁸. However, synthetic rayon fibers with a length of 6.35 mm did appear to disperse more evenly throughout the CNF matrix possibly due to the fact that they are purely cellulosic regenerated materials (i.e., a lower chemical dissimilarity to the CNF matrix), yet fiber entanglement could still be present.

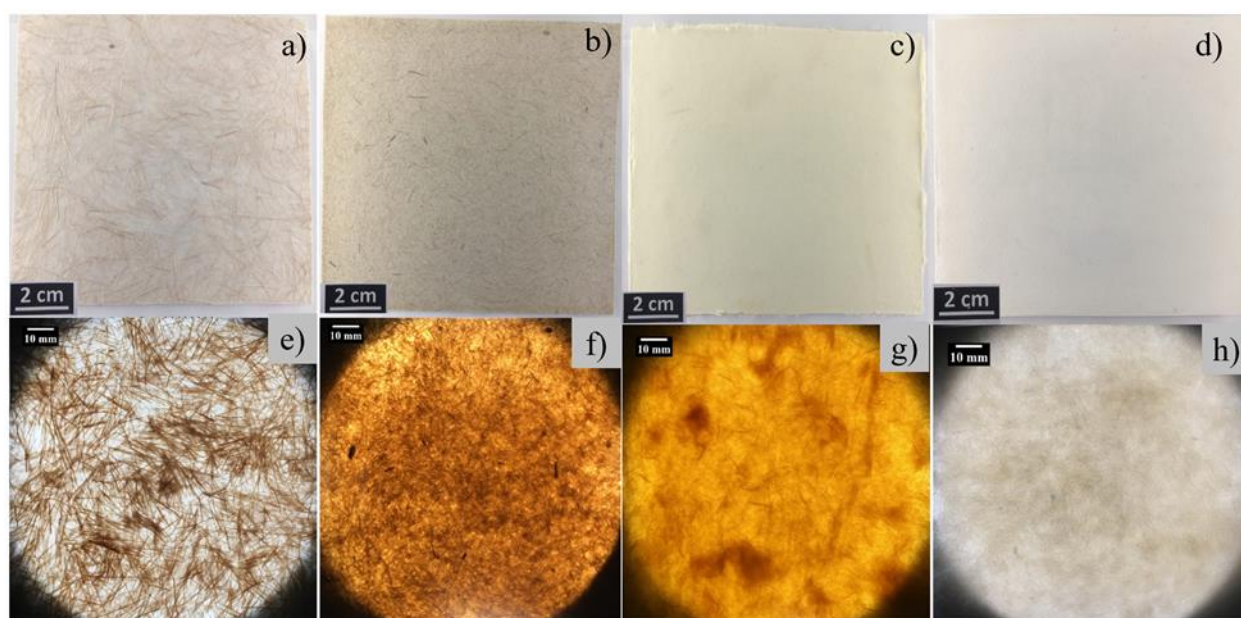


Figure 5.2 FR-CNF composites reinforced with abaca (a, e), flax (b, f), aramid/Kevlar (c, g), and rayon (d, h) fibers. For the images shown in the bottom half (e, f, g, and h), a strong backlight was applied to the back of the laminates to appreciate the level of fiber dispersion across through all the layers. A fiber content of 30 wt.% was used for all laminates shown. All of the laminates shown contained three layers and their thickness varied based on the fiber type. The scale bar for the figures in the bottom row is 10 mm.

Mechanical tensile testing of the processed FR-CNF composites showed that all of the fibers types (abaca, flax, jute, kenaf, PVA, and rayon), reduced the mechanical performance (i.e., ultimate strength [MPa], strain to failure [%], and Young's modulus [GPa]) when compared to the unreinforced pure CNF laminate, as shown in Figure 5.3. More specifically, viscous rayon (regular tenacity) caused the smallest decrease in the tensile mechanical performance with an average

reduction in ultimate strength of ~54 %, elastic modulus of ~49 %, and an average increase of the strain to failure by ~50 % when compared to unreinforced CNF. On the other hand, reinforcement with aramid fibers (with a length of 3.175 mm) caused the largest decrease in performance and reduced the ultimate strength by ~80 %, the elastic modulus by ~68 %, and the strain to failure by ~49 %, respectively. Similarly, abaca fibers decreased the ultimate strength by ~78 %, the elastic modulus by ~18 %, and the strain to failure by ~54%. The stronger decrease in tensile performance for aramid and abaca FR-CNF composites is possibly due to the lower fiber dispersion achieved within the layers which creates stress/weak points in the laminate and, in turn, causes early failure. For the different PVA fibers assessed, the shortest length (6 mm) decreased the performance the least when compared to fibers with a length of 8 mm and 13 mm. Considering the much higher elastic modulus of the reinforcing fibers, the lower elastic moduli observed for FR-CNF composites, in turn, means that the fibers were not effectively interacting with the CNF matrix and thus the load was not effectively transferred.

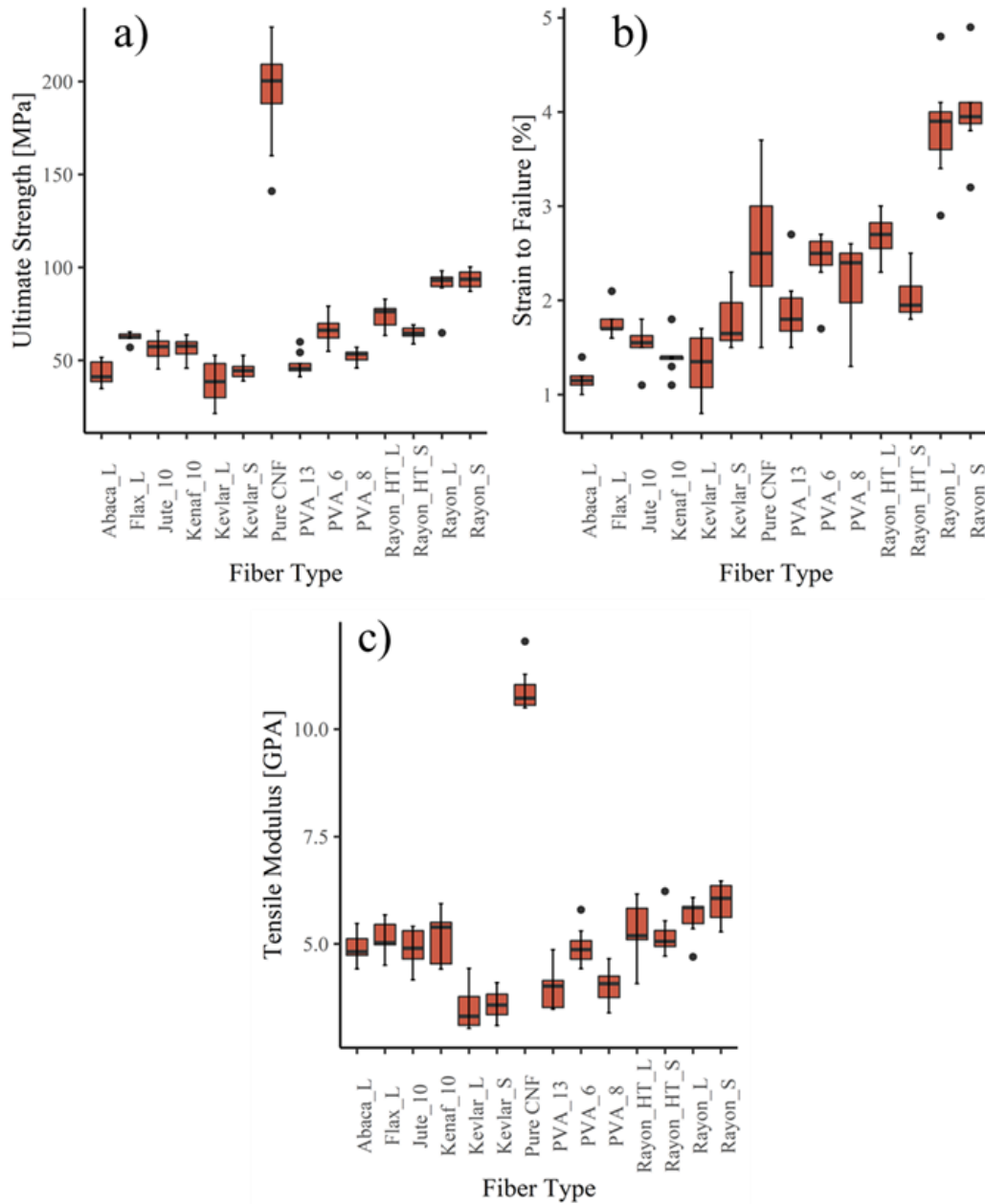


Figure 5.3 Tensile mechanical performance of FR-CNF laminates; (a) ultimate strength, (b) strain to failure, and (c) tensile modulus verses fiber type. A fiber content of 30 wt.% was used for all laminates. The black dots represent outlier data points. At least 6 samples were tested per laminate type. The numbers next to the fiber type represent the nominal fiber length. HT stands for high tenacity while L and S stand for 6.35 mm long and 3.175 mm.

Carbon fibers were especially hard to disperse when added to the CNF slurry (shown in Figure D. 1), and large fiber bundles were present throughout the composite structure at 30 wt.% fiber loading. To address this problem, different acid treatments and surfactants were applied to

the carbon fibers before being mixed with the CNF slurry and the fiber loading was reduced to ~2 wt.%. Acid treatments have been reported to induce the formation of surface carboxylic groups (-COOH) through oxidation^{169,170}. These newly formed carboxylic groups could then possibly interact with the hydroxyls (-OH) on CNF fibrils through hydrogen bonding and reduce the interfacial chemical dissimilarity between the two materials (i.e., hydrophobic-hydrophilic) and, in turn, reduce the tendency for fibers to agglomerate. On the other hand, surfactants have been used to improve the dispersion of carbon fibers in cement and could also possibly help their dispersion in a CNF slurry^{171,172}.

Mechanical testing of the processed carbon fiber reinforced CNF composites prepared using the differently treated carbon fibers are shown in Figure 5.4. As observed with previous fiber types, the addition of carbon fibers reduced the tensile mechanical performance regardless of the acid treatment or surfactant used. More specifically, reinforcement with untreated carbon fibers lead to average ultimate strength values of ~161 MPa, elastic modulus of ~7.2 GPa, and a strain to failure of ~3.6 % which represents a performance decrease of ~17 % and ~34 % for strength and modulus and an increase of ~40 % in strain to failure, when compared to the unreinforced CNF. From the obtained results, the best performing treatment was nitric acid. 24 hour treatment with nitric acid reduced the strength by ~26 % (~144 MPa), elastic modulus by ~38 % (~6.8 GPa) yet increased the strain to failure of the composite by ~85 % (~4.7 %) when compared to unreinforced CNF. The large increase in strain to failure, while still maintaining a reasonable elastic modulus, points to the improvement fiber-matrix interactions¹⁷³. A similar mechanical performance was observed for treatment with nitric acid applied for 48 hours which achieved average ultimate strength values of ~144 MPa, modulus of ~6.7 GPa, and strain to failure of ~4.2 %. Perhaps the only difference between the treatment times is the lower variation or error observed in the strain to failure for the 48 hour treatment with a relative standard deviation of ~35 % verses ~24 % for 24 hours. This in turn could suggest a more even surface treatment on the carbon fibers, yet their individual strength may have been lowered due to formation of defects through the longer oxidative process¹⁶⁹. On the other hand, surfactants severely reduced the mechanical performance of the composites. As shown, carbon fiber treatment with SDS lead to an average ultimate strength value of ~75 MPa, elastic modulus of ~5.4 GPa, and a strain to failure of ~1.6 % which represents a performance decrease of ~61 % in strength, ~50 % in modulus, and a ~38 % in strain to failure

when compared to the unreinforced CNF. Treatment with hydroxypropyl methyl cellulose had a similarly low performance yet had the benefit of being a more sustainable/biofriendly option.

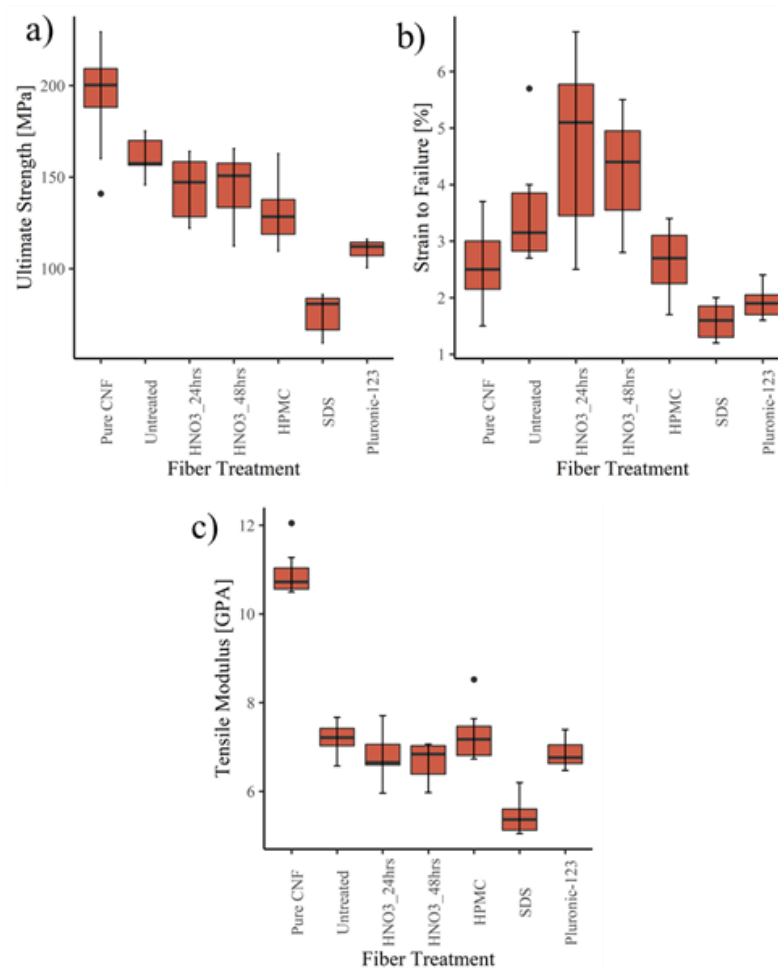


Figure 5.4 Mechanical performance of carbon FR-CNF laminates; (a) ultimate strength, (b) strain to failure, and (c) tensile modulus verses fiber treatment, respectively. A fiber content of 2.17 wt.% was used for all laminates. The black dots represent outlier data points. At least 6 samples were tested per laminate treatment. Unless otherwise stated the treatment, time was 24 hours. HPMC stands for hydroxypropyl methyl cellulose. SDS stands for sodium dodecyl sulfate. Pluronics 123 is a triblock copolymer surfactant made out of poly(ethylene oxide) (PEO) and poly(propylene oxide) (PPO) with a repeating structure of PEO-PPO-PEO.

Optimization of the fiber content for the “best” performing fiber types (rayon, and carbon) as well as aramid fibers (due to their high strength) was also performed. As shown in Figure 5.5a and Figure 5.5b, there is not much difference between the different fiber types and fiber loadings when considering the ultimate strength or elastic modulus with the exception of aramid fibers at a

content of ~2 wt.% which achieved a strength value of ~171 MPa and a modulus of ~7 GPa. However, there is a clear trend when looking at the strain to failure where on average the optimum performance is consistently achieved at a ~2 wt.% loading for all fiber types. The reasons for this are unknown as due to the different fiber-matrix interface chemistries present, there should be a different optimum fiber loading for each fiber type, hence this could more likely be a processing effect (i.e., a higher fiber loading forces more fiber-fiber interactions which do not allow for effective load transfer from the matrix to the fibers). However, more samples need to be tested as there is significant error in the ~1 wt.% loading sample group. It could be that the optimum loading lies between ~1 wt.% and ~2 wt.% for the different fiber types.

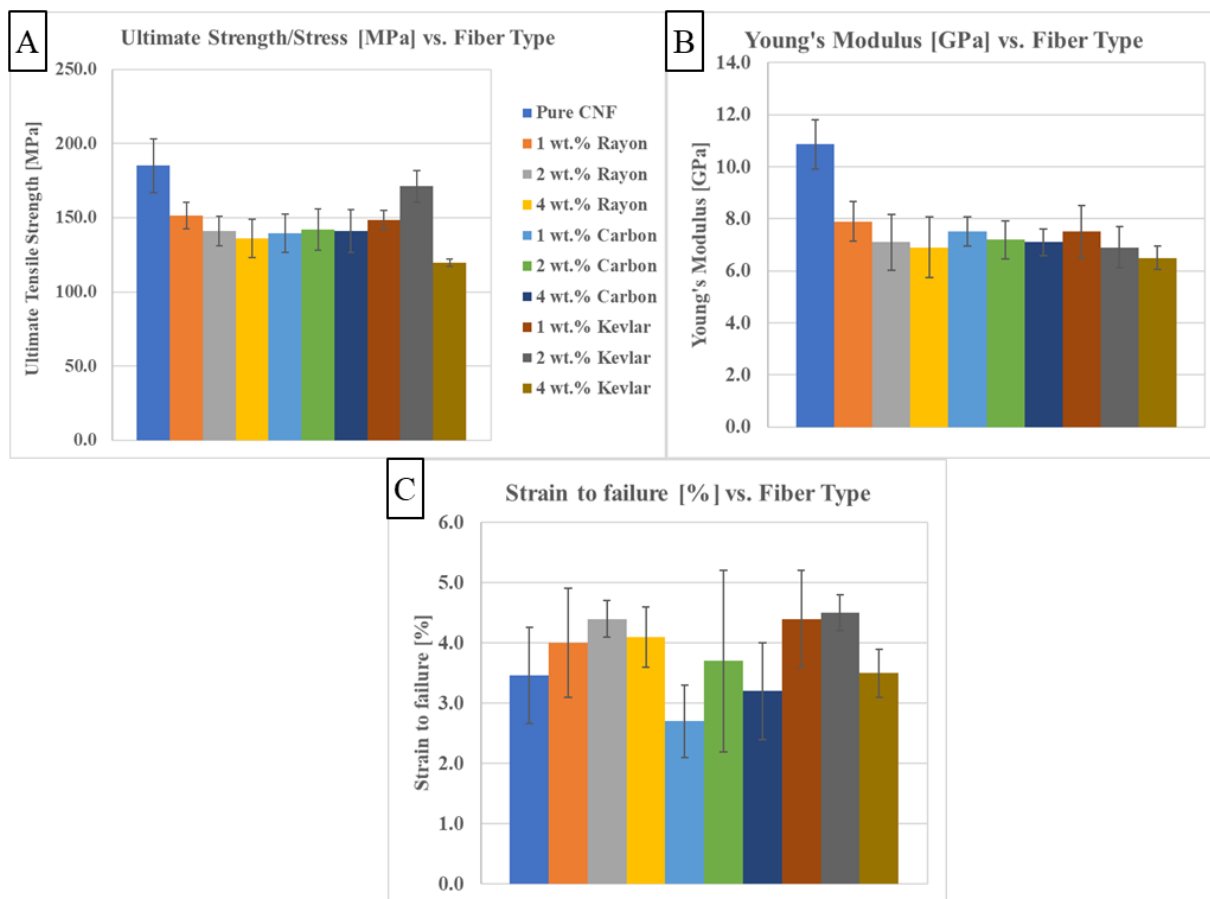


Figure 5.5 Mechanical tensile performance of CNF composites reinforced with rayon, aramid, or carbon fibers at three different fiber contents (~1, ~2, and ~4 wt.%). At least 6 samples were tested for each sample group and the error bars shown represent the standard deviation. No chemical treatment was applied to the reinforcing fibers. The fiber length used was 6.35 mm for all fiber types.

5.3.2 Alternative Design for Carbon Fiber Reinforced CNF Composites, First Impression and Testing

In hopes of improving the tensile mechanical performance, an alternative design to the carbon fiber reinforce CNF composites was evaluated. As shown in Figure 5.6, the alternative design employed a carbon fiber weave rather than the chopped carbon fibers previously used in the composites in Section 5.3.1. Using a weave configuration rather than chopped fibers made the processing of the composites much simpler as homogenous fiber dispersion was no longer a concern. However, it is important to note that the alternative design also incorporates a secondary polymer layer between the carbon fiber weave and the CNF layers. This polymer layer essentially acts as a binder between the weave and the CNF so that the load is effectively transferred, hence the mechanical performance will ultimately be based on the effectiveness of the binder layer.

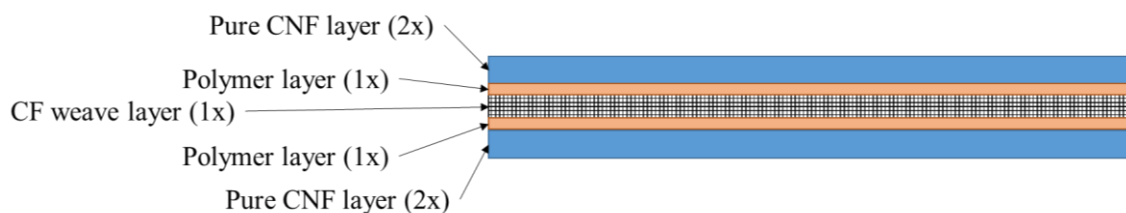


Figure 5.6 Schematic of the cross-section of a FR-CNF composite using a carbon fiber (CF) weave as the reinforcing phase. The blue sections represent pure CNF layers which sandwich the carbon fiber weave. The orange sections represent the polymer binder layers which sit between the carbon fiber weave and the pure CNF layers. The numbers inside the parenthesis next to the layer names represent the number of layers where 2x is two layers.

Two different polymeric binder layers were assessed, polyvinyl alcohol (PVA) and a blocked isocyanate resin system (BIC). Additionally, in the hopes of reducing the susceptibility of CNF to humid conditions, citric acid was added to the PVA to induce crosslinking. Mechanical performance of the weave composites is shown in Figure 5.7. Using PVA as a binder layer led to a Young's modulus value of ~27 GPa which represent a performance increase of ~109 % when compared to the unreinforced CNF composite, while maintaining an average ultimate strength of 223 MPa. As expected, the strain to failure was reduced to ~1 % from the initial ~3 % due to the increased stiffness/modulus of the composite. The lower performance of the control group of CNF+PVA (without the carbon weave), revealed that the observed properties of CNF+PVA+CF were attributed to the carbon fibers and that the load was effectively being transferred from the

CNF outer layers to the inner carbon fiber weave. Surprisingly, the addition of PVA to CNF on its own did in fact improve the modulus from ~13 GPa to ~16 GPa (i.e., a ~23 % increase). Furthermore, the addition of citric acid to the PVA did not significantly change the performance of the composite and achieved on average a modulus of ~25 GPa, a strain to failure of ~1%, and an ultimate strength of 212 MPa. Using BIC as a polymeric binder layer to a Young's modulus of ~16 GPa which was statistically equivalent to the modulus obtained for only adding PVA to CNF without the carbon fiber weave and represented a performance increase of ~23 % when compared to the unreinforced CNF composite.

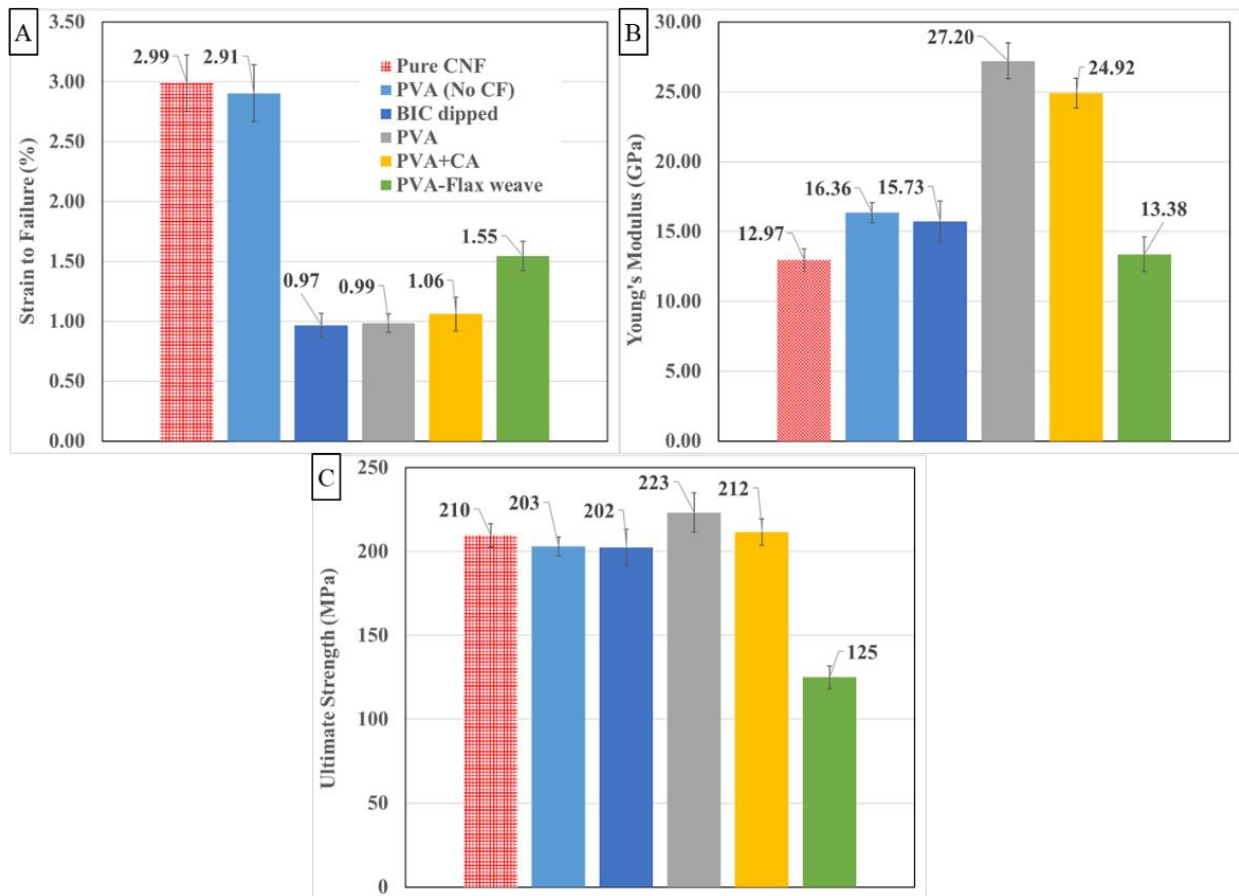


Figure 5.7 Mechanical tensile performance of carbon fiber and flax weave reinforced CNF composites with different polymer binder layers. Rectangular specimens (6.35 mm by 115 mm) were cut with scissors from each composite. At least 12 samples were tested for each sample group and the average and standard deviation are displayed. The average values are displayed on top of their columns with a leader guide, respectively.

Using a flax fiber weave rather than a carbon fiber weave led to reduced properties in terms of strain to failure (~1.5 %) and ultimate strength (125 MPa), yet a statistically equivalent modulus of ~13 GPa was observed when compared to the unreinforced CNF composite. It is important to note that the ultimate strength of the weave reinforced composites was limited by the strength of the outer CNF layers with an average strength of 210 MPa, and hence none significantly outperformed the unreinforced CNF. Lastly, the lower strain to failures observed for all weave reinforced composites showed that both PVA (flax and carbon) and BIC provided a good load transfer from the matrix to the fibers.

5.4 Summary and Future Work

FR-CNF composites were successfully processed using our previously developed wet-stacking technique (see Chapter 2) with the addition of different types of reinforcing fibers. When considering the tensile mechanical response of the chopped fiber reinforced CNF composites, the best performing fiber types were found to be that of rayon and carbon fibers. However, both natural and synthetic fibers reduced the tensile mechanical performance when compared to the unreinforced CNF laminates previously prepared (see Chapter 2). Natural fibers of abaca, flax, jute, and kenaf reduced the properties the most, where ultimate strength was found to decrease by ~78 %, ~68 %, ~71 %, and ~71 % respectively when compared to unreinforced CNF. Additionally, when adding these fibers, the modulus was found to decrease by ~55 %, ~53 %, ~55 %, and ~53 %, respectively. On the other hand, viscous rayon (regular tenacity) fibers caused a smaller decrease in ultimate strength of ~54 %, elastic modulus of ~49 %, and an increase of the strain to failure by ~50 % when compared to unreinforced CNF. Additionally, reinforcement of CNF with chopped carbon fibers which have been treated with nitric acid (for 24 hours) reduced the ultimate strength by only ~26 % and elastic modulus by ~38 % yet increased the strain to failure of the composite by ~85 % when compared to unreinforced CNF, thus was the most successful fiber type. The large increase in strain to failure along with a relatively small decrease in modulus points to a possible improvement of the matrix-fiber interactions possibly through the formation of carboxylic groups (COOH) and hydrogen bonds which, in turn, allows for more effective load transfer from the matrix to the carbon fibers. Furthermore, fiber content optimization showed the optimal performance is consistently achieved at a ~2 wt.% loading for rayon, aramid, and carbon fibers.

An alternative composite design which employed the use of a carbon fiber weave proved to outperform both the chopped FR-CNF composites as well as the unreinforced CNF control group. More specifically, using PVA as a binder layer between the carbon fiber weave and the CNF outer layers led to a Young's modulus value of ~27 GPa which represent a performance increase of ~109 % when compared to the unreinforced CNF composite while maintaining an average ultimate strength of 223 MPa. Using a blocked isocyanate resin (BIC) as a binder layer did not increase the properties of the composite significantly which reached only a Young's modulus of ~16 GPa (i.e., a performance increase of ~23 %) when compared to the unreinforced CNF composite. Lastly, using a flax weave with a PVA binder layer did not improve the properties of the composite and a modulus of ~13 GPa was observed along with a reduced ultimate strength of 125 MPa and strain to failure of ~1.5 %.

Considering that chemical oxidation did in fact improve the mechanical response of chopped carbon FR-CNF composites, future efforts will attempt to surface modify the carbon fibers to further improve their chemical compatibility to the CNF matrix. Two surface modification methods will be assessed. A schematic of the modification processes is shown in Figure 5.8 below. For the first method (top), the carbon fibers will be initially treated with aminopropyl tri-ethoxy silane (APTES) in order to attach primary amines to the surface. Subsequently, a hyperbranched polymer with terminal hydroxyl groups will be polymerized from succinic anhydride and diethanolamine at the primary amines. Increasing the number of hydroxyl groups on the surface of the carbon fibers will then allow for hydrogen bond formation with the CNF matrix. This modification process is based on previously reported efforts from Li et. al., where hyperbranched polymers were grown on zirconium nanoparticles^{174,175}.

The second modification method (bottom, in Figure 5.8) will also prime the carbon fiber surfaces with primary amines through APTS modification. Subsequently, dimethylaminopropyl carbodiimide (CDI or EDC) will be used to activate the surfaces of CNF which, in turn, will allow for direct crosslinking of the hydroxyls on the CNF fibrils with the primary amines on the carbon fibers. The crosslinked CNF on the surface of the carbon fibers will essentially act as a sizing agent which will improve the chemical compatibility (i.e., hydrogen bonding with the matrix) and possibly also mechanically entangle with the CNF matrix improving the interfacial shear strength. This modification method is loosely based and adapted from previous research efforts from Batista

6. SUMMARY AND CONCLUSION

Overall, this thesis covered four major projects which were all related to the processing and characterization of cellulose nanofibril (CNF) sheets. Although each project had its very own hypothesis to test or objective to achieve, the underlying big-picture goal for all these projects was to provide an industrially viable and scalable processing method while, at the same time, aiming to improve or maintain the already observed mechanical properties of the CNF sheets or composites.

In the first project, a four-step wet stacking lamination technique was developed and used for the creation of the pure multi-layer CNF sheets with varying thicknesses. This technique allowed for the processing of the thickest reported ($t \sim 1.7$ mm) pure CNF sheet, where most other CNF films reported in literature have a thickness ranging from ~ 60 to ~ 200 microns. It was found that for CNF sheets with a thickness above ~ 150 μm (i.e., two layers) the ultimate strength increased by ~ 100 % when compared to thinner CNF sheets (thickness < 150 μm) while, at the same time, maintaining an equivalent Young's modulus and strain to failure. Due to the increased ultimate strength and low density (~ 1.4 g/cm^3), the specific strength of the processed multi-layer CNF sheets was found to be equivalent to that of aluminum 2024 (T3 tempered) which is commonly used for structural applications. Furthermore, due to the simplicity of the process and the fact that no binders or solvents (other than water) were needed, wet-stacking can lend itself to be scaled up industrially without any specialized equipment. Perhaps, some of the current papermaking machines could, in the future, be adapted to carry out the wet-stacking lamination process continuously.

In the second project, highly loaded (up to 25 wt.% solids) pastes of CNF with different processing aids like xanthan gum (XG), anionic polyacrylamide (aPAM), and carboxymethyl cellulose (CMC) were prepared using a Banbury high-shear mixer. For CMC, the mixing process was validated by preparing pastes with different solids contents and comparing them to pastes that were air dried to achieve the same solids content. High-shear mixing proved to effectively incorporate CMC into high solids CNFs cake, reducing the drying time significantly. Rheological analysis of the CNF+CMC pastes showed that a stronger Newtonian response and lower apparent viscosity (when compared to pure CNF) were developed due to addition of CMC. Furthermore, in order to address the semiautomatic nature observed for the wet-stacking process in the first project,

a single-screw extruder was used to continuously process the highly loaded pastes into wet sheets which were subsequently dried by heated pressing. However, calendering of the wet extrudates showed that full consolidation can be achieved, which eliminates the need to use discrete pressing steps for drying. Lastly, tensile testing of the CNF+CMC sheets revealed an equivalent ultimate strength (~ 110 MPa) and density (~ 1.1 g/cm³) when compared to solution cast CNF films, hence proving that extrusion is an industrially viable processing method which maintains the mechanical properties of CNF.

From the knowledge gained from the second project, the third project investigated the possibility of controlling the redispersion and setting behavior of highly loaded CNF+CMC systems. Through turbidity analysis, it was found that complete redispersion (in water) of fully dried CNF+CMC materials was possible regardless of the CMC's degree of substitution (D.S. = 0.7, 0.9, and 1.2). Redispersion was made possible due to the adsorption of CMC onto the CNF fibrils which increased the surface charge by ~ 61 % (from -36.8 mV for pure CNF to -59.3 mV for CNF+CMC and 0.094 mmol/g COOH for pure CNF to 0.166 mmol/g COOH for CNF+CMC (D.S. = 0.9)) due to the added carboxylates. Additionally, adsorbed CMC allowed for fully dried CNF+CMC pellets to be rehydrated, re-mixed, and re-extruded without any limitations. On the other hand, chemical treatment of CNF+CMC with hydrochloric acid, a carbodiimide crosslinker, a polyamide epichlorohydrin resin, or a polyamine epichlorohydrin resin completely suppressed the redispersible behavior observed for untreated CNF+CMC systems. FTIR analysis revealed the presence of newly formed ester, N-acyl urea, and anhydride linkages which could possibly explain the suppressed redispersion/setting behavior. Overall, the results from this project could benefit the CNF processing industry. For example, CNF+CMC could be shipped in the dry state providing significant savings in transportation, subsequently redispersed to the desired solids concentration, processed into the desired shape, and finally set by chemical treatment.

Lastly, born from the first project, the fourth project focused on improving the mechanical performance of CNF even further through the addition of high strength reinforcing fibers. Both synthetic and natural fibers were incorporated into CNF. Tensile testing of the processed chopped fiber reinforced CNF composites (FR-CNF) revealed that on average the mechanical performance was reduced, especially for composites reinforced with natural fibers (an average reduction of ~ 70 % in ultimate strength was observed). However, carbon fibers were found to be the best fiber type if chemical oxidation through nitric acid is first performed. Nitric acid pre-treatment did in fact

improve the compatibility of the carbon fibers with the CNF matrix, resulting in a ~85 % increase in strain to failure when compared to unreinforced CNF. Additionally, an alternative composite design which employed the use of a carbon fiber weave and a PVA binder layer led to a Young's modulus value of ~27 GPa which represent a performance increase of ~109 % when compared to the unreinforced CNF, while maintaining an average ultimate strength of 223 MPa. Based on these preliminary results, future efforts in this project will be devoted to the chemical surface modification of carbon fibers in the hopes of improving their chemical compatibility with CNF and their dispersion in a CNF slurry.

More broadly speaking, the research efforts presented in this thesis show that the commercialization of CNF is not a farfetched idea, as high strength CNF sheets can be produced inexpensively and continuously. Again, having the advantage of using conventional polymer processing equipment like that of an extruder and a Banbury shear mixer as well as calender rolls, can significantly lower the initial capital investment needed or cost associated with scaling up production. Additionally, the presented results can help galvanize future researchers interested in processing fiber reinforced CNF composites and expand the possible end uses for CNFs as well as other nanocellulose materials.

APPENDIX A. PROCESSING AND CHARACTERIZATION OF THICK CNF SHEETS

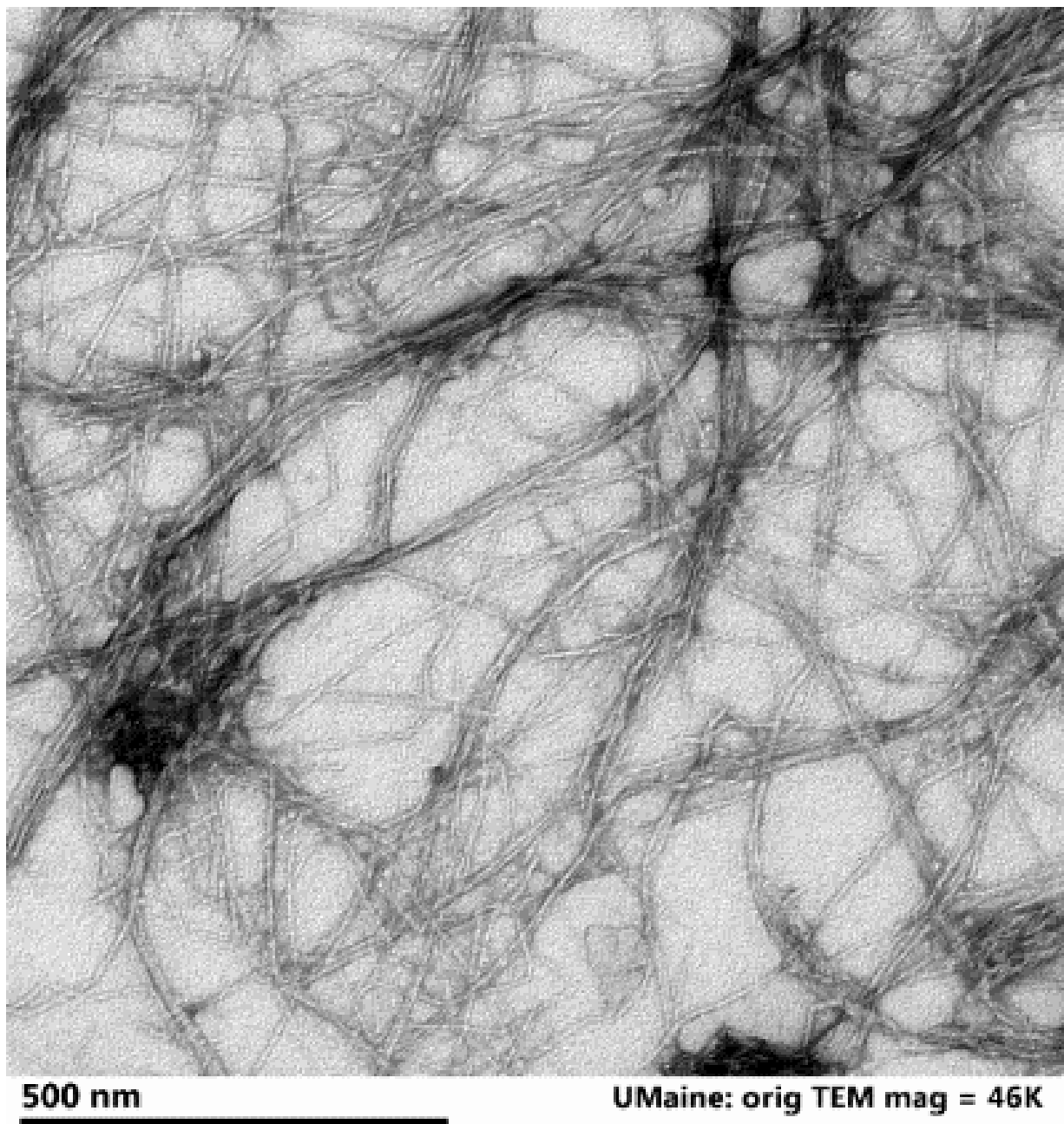


Figure A. 1 TEM image of the CNF fibrils used to make the sheets. The diameter of the fibrils was measured with imageJ an open source software. Note, individual fibrils were measured rather than the agglomerated structures that appear as darker regions. TEM image is courtesy of Youngblood's research group.

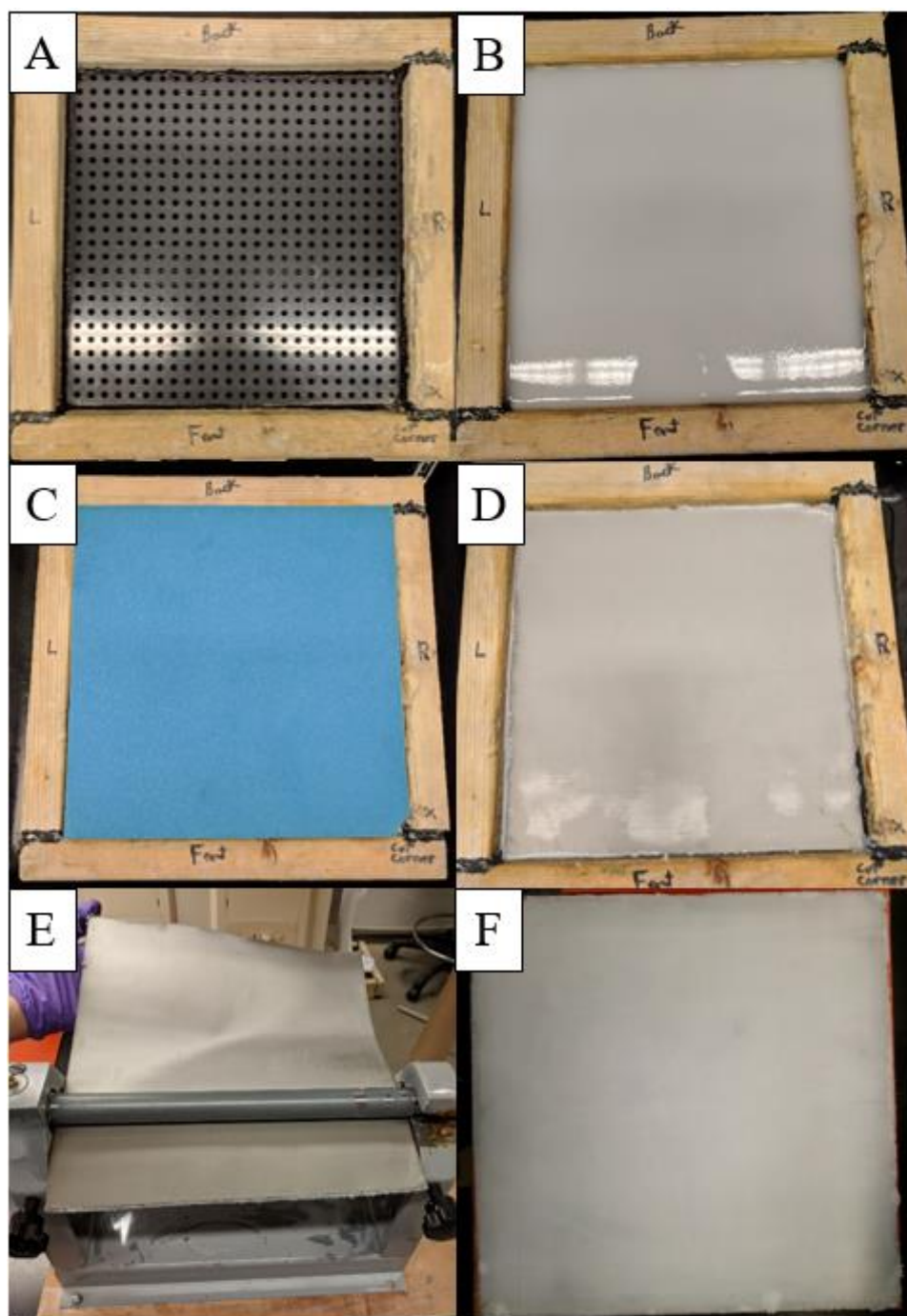


Figure A. 2 The process of making a single layer of CNF. A) empty wooden frame with perforated PVC sheet on the bottom, B) poured 1 wt.% CNF mixture on top of the felt filter and metal mesh, C) metal filter mesh and sponge laid on top of CNF slurry, D) consolidated ~7 wt.% CNF between metal filter meshes, E) CNF sandwich passed through the slip roller to a solids loading of ~10 wt.%, F) final wet CNF single layer with the top metal mesh removed. The process continues in Figure A. 3.

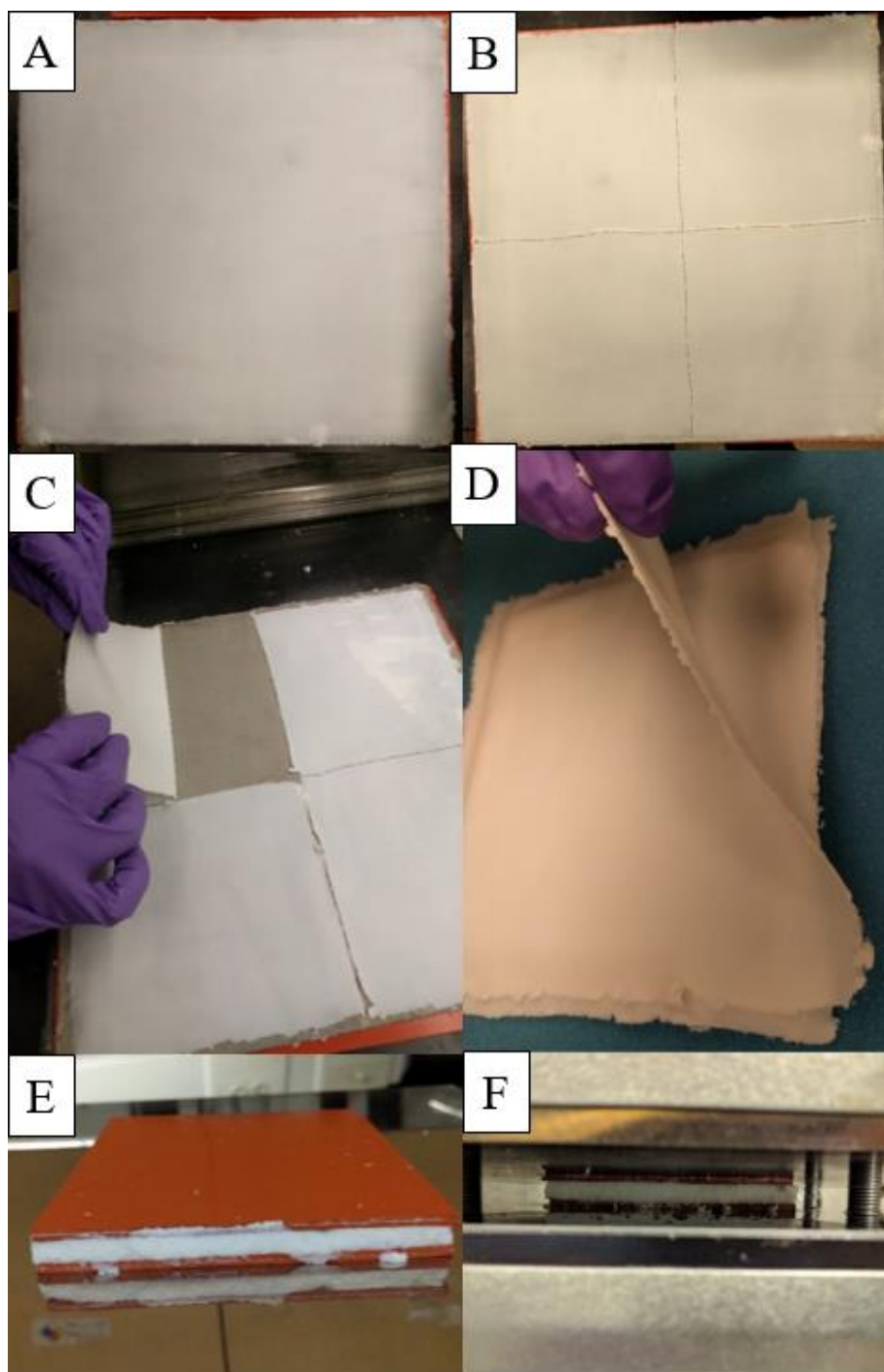


Figure A. 3 Making thick CNF sheets from the single layer prepared in Figure S3. A) the produced square single layer had a side length of 12 inches, B) the single layer was sectioned into four 6x6 inch squares, C) the single layers were removed from the supporting filtering metal mesh by hand D) stacked on top of each other, E) the sides were trimmed and rubber pads sandwiched the structure and F) hot pressed for final consolidation.

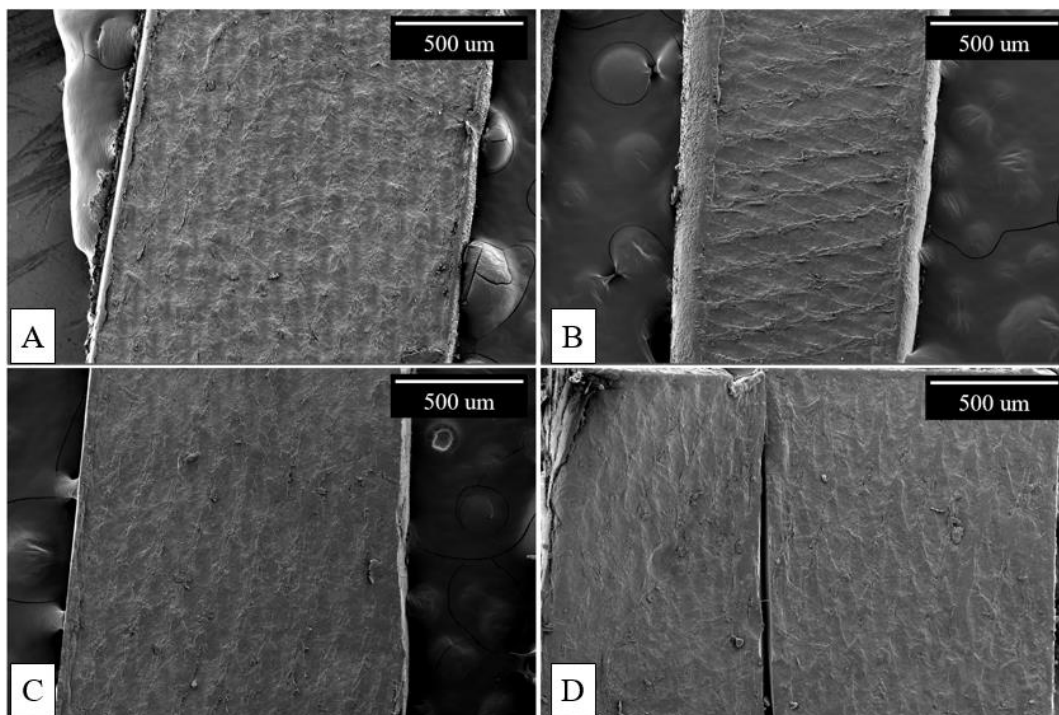


Figure A. 4 SEM of sheet surfaces of varying thickness; A) 1-layer, B) 2-layer, C) 6-layer, and D) 8-layer.

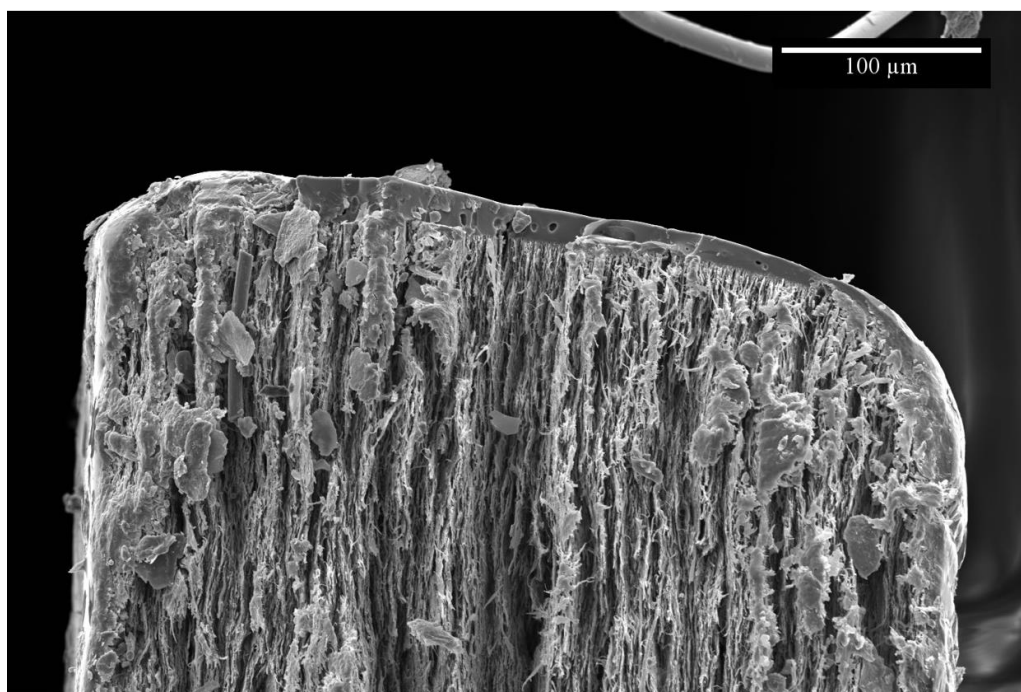


Figure A. 5 SEM microphotography of the fracture surface edge of a 6-layer sheet. The surface damage caused by laser cutting can be seen on the edge of the specimen.

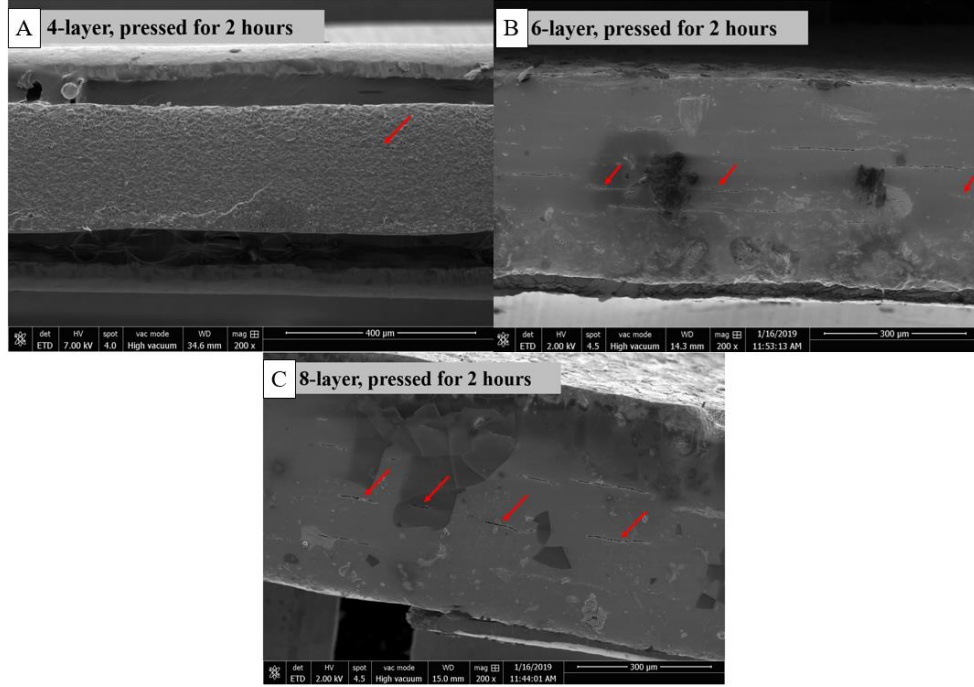


Figure A. 6 Cross-sectional area of a A) 4-layer, B) 6-layer, and C) 8-layer specimen pressed for two hours. The red highlight the flat defects.

Equation A. 1

$$\sigma_{ULT} \cong \frac{1}{\sqrt{D_{fibril}}}$$

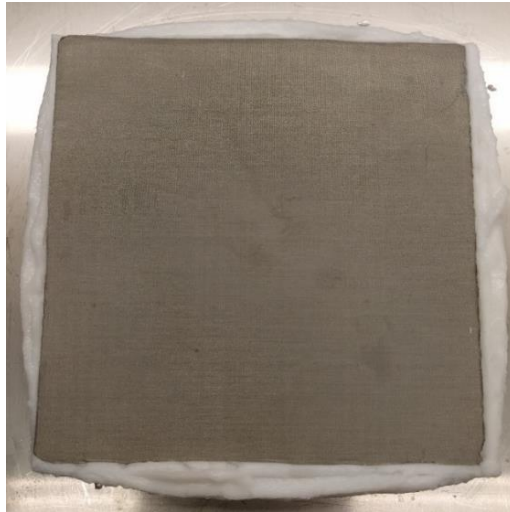


Figure A. 7 Top view of an 8-layer CNF cake that has been pressed at ~0.36 MPa but not fully dry. The CNF layers started sliding out of the mold during pressing due to fast pressing. The filtering mesh is still attached to the top of the cake to appreciate the degree of displacement.

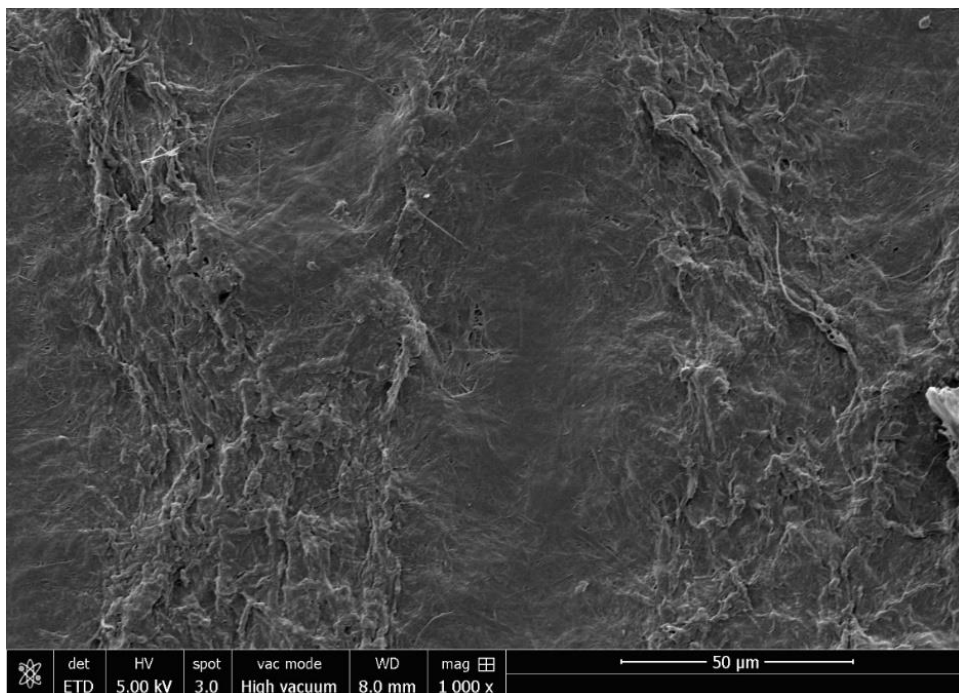


Figure A. 8 Surface texture of a 1-layer sheet. The fibrils appear to be randomly oriented. Rougher patches on the surface originate due to the contact with the woven mesh during hot pressing.

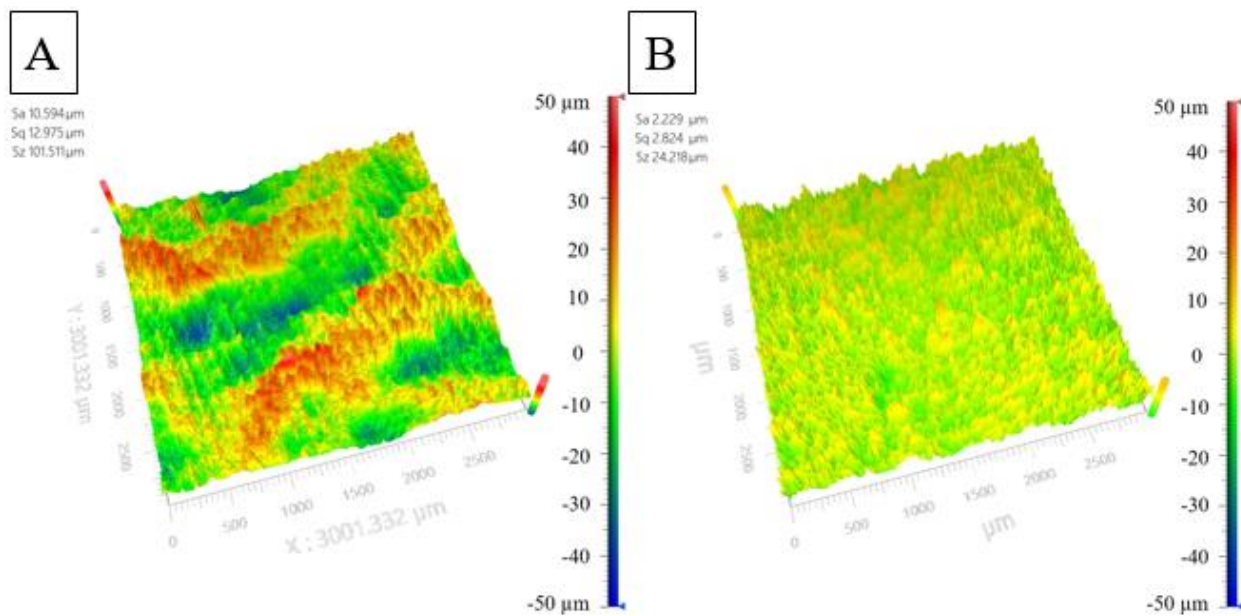


Figure A. 9 Optical profilometry (2.75x) of the edge of the 20 second fast pressed sheet (A) and the 4 minutes slow pressed sheet (B). The surface roughness increased significantly for the fast-pressed sheet ($Sq = 12.975 \mu\text{m}$ versus $Sq = 2.824 \mu\text{m}$).

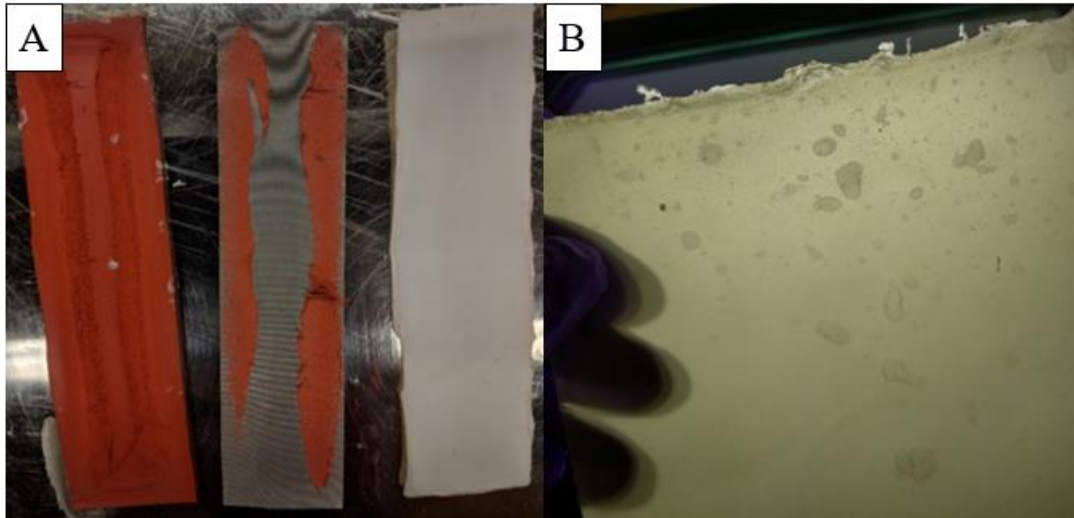


Figure A. 10 Four-layer CNF sheet pressed at A) ~ 5.17 MPa and B) ~ 0 MPa. To achieve higher pressures the dimensions of the sheet were reduced to 2.54 cm wide and 10.16 cm long before final press dry. The loosely pressed (~ 0 MPa) sheet experienced the formation of interlayer bubbles due to the semi-unconstrained drying as the water vapor escaped the web. On the other hand, pressing pressures of ~ 5.17 MPa damaged the rubber pads, filtering mesh, and CNF web.

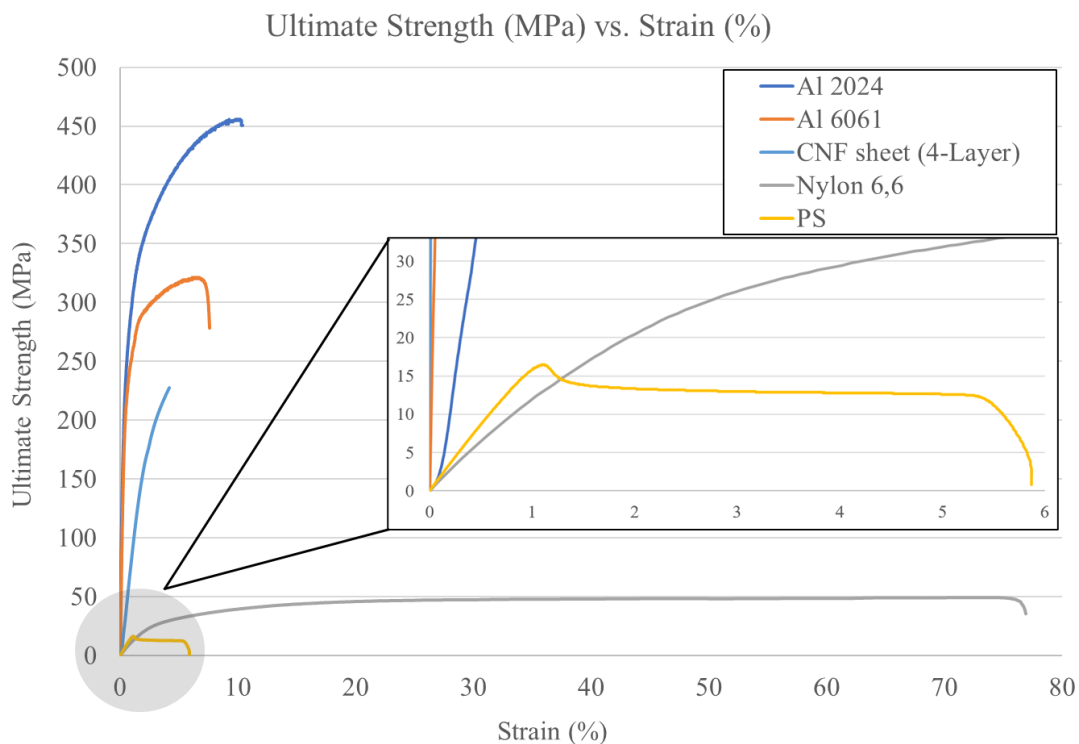


Figure A. 11 Tensile response (Ultimate strength (MPa) versus strain (%)) for different materials. The inset gives a closer look to the behavior of polystyrene (PS) as well as the different elastic modulus observed for the other materials, respectively. (Al = aluminum). This plot shows the response of a single sample from its respective group.

APPENDIX B. CONTINUOUS PROCESSING OF CNF SHEETS



Figure B. 1 CNF/aPAM paste mixed in the Brabender at a dry weight ratio of 0.05:1. Clumps or grainy texture can be clearly appreciated instead of a homogenous/creamy texture. The torque plateaus for this paste were not reached even though the mixing times was extended for over an hour instead of the typical ~40 minutes.

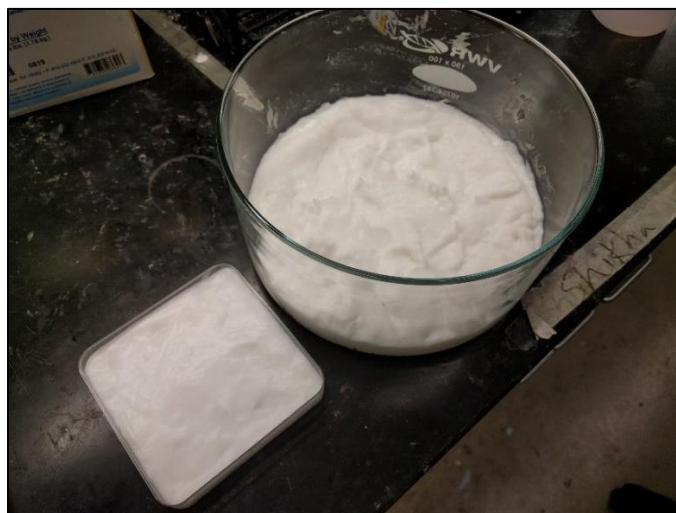


Figure B. 2 Air dried CNF/CMC paste prepared by air drying the watery CNF+CMC suspension in a humidity controlled oven long periods of time. The suspension was cast in either square polypropylene petri dishes or in a large crystallization dish as shown. The current state of the paste shown is of a ~10 wt.% solids concentration.

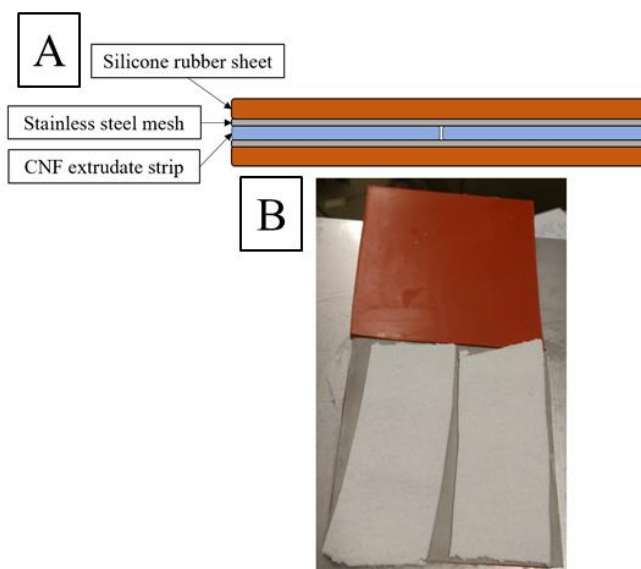


Figure B. 3 Graphical representation of the pressing configuration used to fully consolidate the extrudates (A) which shows the different components used and B) an actual photograph of a CNF/CMC extrudate before pressing at 126 °C for 30 minutes.

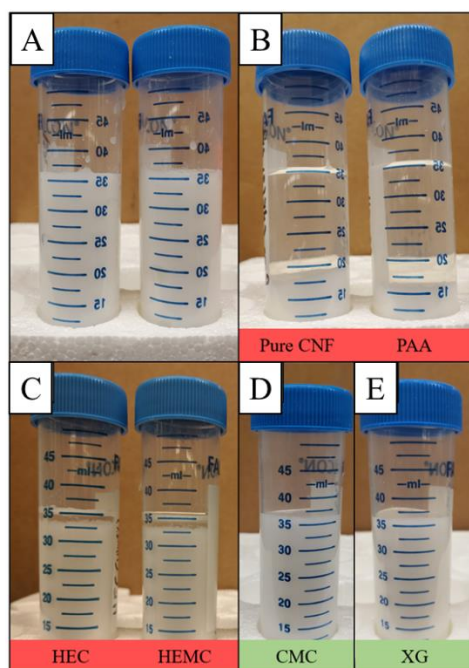


Figure B. 4 Few examples of centrifuge tubes filled with CNF plus processing aid mixtures (A) before centrifugation and (B, C, D, E) after centrifugation. For pure CNF and PAA roughly 20 ml of water was separated while for HEC and HEMC roughly 2 to 3 ml of water was separated. CMC and XG mixtures did not dewater in any perceivable manner.

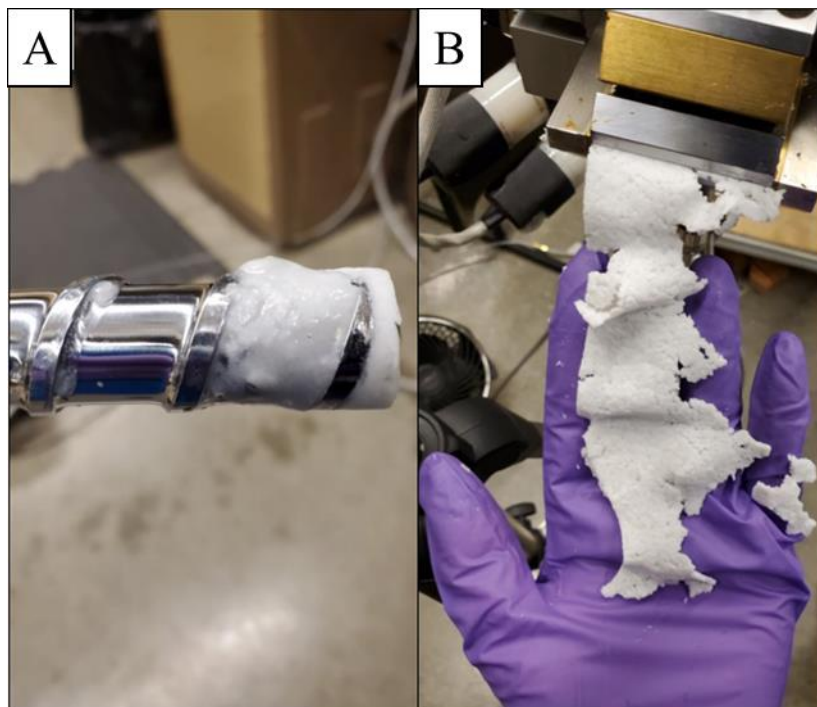


Figure B. 5 Dewatering observed at the end of the screw after extrusion of a CNF/aPAM paste with an aid to CNF dry weight ratio of 0.013:1 (A), and fractured extrudate during extrusion of the same paste (B). A similar dewatering behavior and formation of a fractured extrudate was experienced for pastes of CNF/CMC and CNF/XG with a polymer to dry weight ratio of 0.05:1.

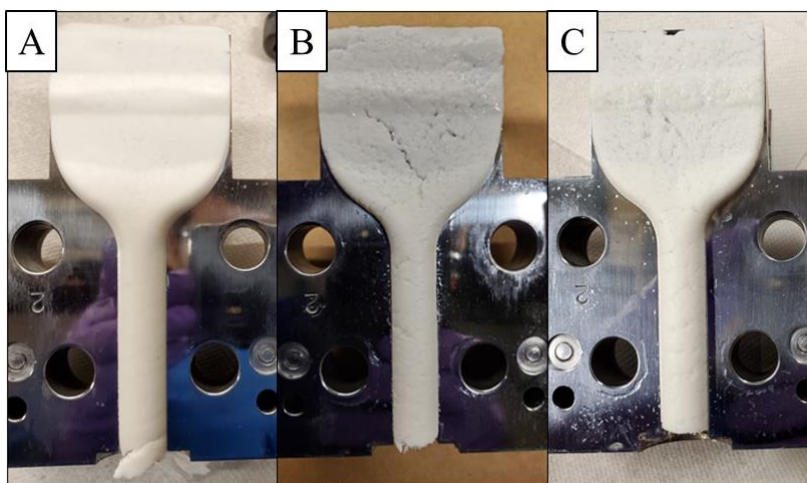


Figure B. 6 View from the inside of the slot or sheet die after the extrusion of a CNF/CMC paste (A), CNF/XG paste (B), and CNF/aPAM paste (C) at a ratio of 0.1:1 for CNF/CMC and CNF/XG and a ratio of 0.026:1 for CNF/aPAM.

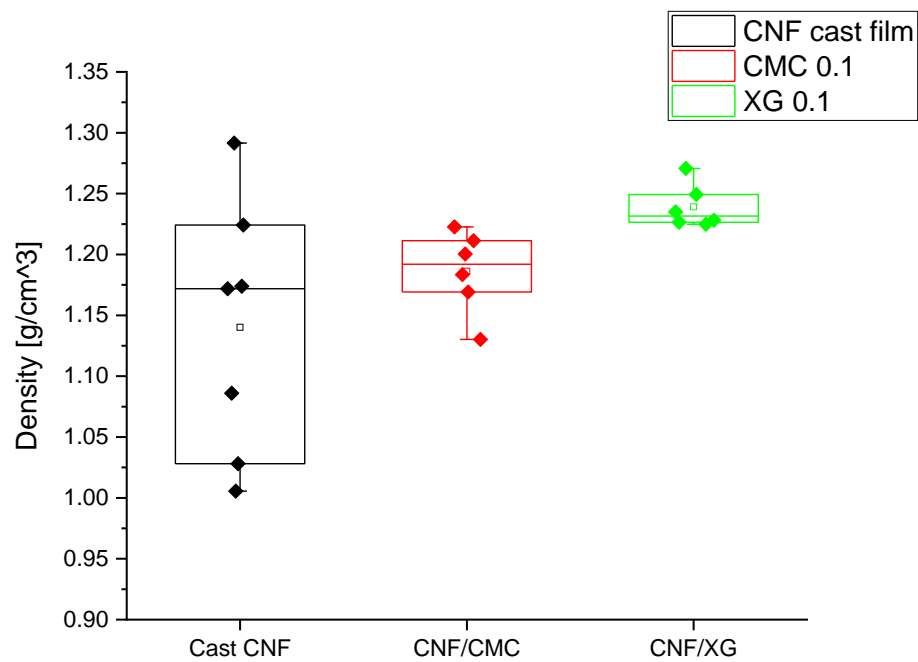


Figure B. 7 Boxplot of the density data for cast CNF films and extruded sheets of CNF/CMC and CNF/XG. The filled points represent the actual sample units while the middle unfilled square represents the mean of the sample.

Table B. 6-1 Complete summary of the mechanical performance of pressed extruded sheets prepared using different paste types. Paste types denoted with “_AD” were prepared by air drying in a humidity controlled oven while all others were prepared using the Brabender. Solution cast CNF films are also shown for comparison purposes. All the values are displayed as: mean \pm (1 STD)

Paste Type	Total Solids Concentration	Processing aid to CNF ratio	Ultimate Strength	Young's Modulus	Strain to Failure	Density	Specific Strength	Specific Modulus
	(wt.%)	[aid to CNF]*	[MPa]	[GPa]	[%]	[g/cm ³]	MPa/(g/cm ³)	GPa/(g/cm ³)
Cast CNF	3	0 : 1	110.29 \pm 8.23	11.35 \pm 1.5	2.57 \pm 0.60	1.13 \pm 0.11	96.07 \pm 13.38	9.95 \pm 1.77
CNF/CMC	15.32	0.1 : 1	110.57 \pm 7.30	9.36 \pm 0.57	1.80 \pm 0.08	1.19 \pm 0.03	93.21 \pm 5.46	7.90 \pm 0.56
CNF/CMC	19	0.1 : 1	109.62 \pm 13.10	10.67 \pm 0.87	1.54 \pm 0.30	1.26 \pm 0.02	87.21 \pm 10.15	8.50 \pm 0.73
CNF/CMC	25	0.1 : 1	100.84 \pm 14.12	8.57 \pm 0.65	1.29 \pm 0.26	1.37 \pm 0.02	73.87 \pm 10.59	6.27 \pm 0.44
CNF/CMC	15.32	0.15 : 1	82.27 \pm 13.30	9.23 \pm 0.91	1.03 \pm 0.22	1.03 \pm 0.13	78.54 \pm 15.11	8.78 \pm 1.12
CNF/CMC_AD	15.32	0.1 : 1	111.23 \pm 9.73	9.48 \pm 0.39	1.41 \pm 0.20	1.32 \pm 0.03	84.55 \pm 6.86	7.21 \pm 0.37
CNF/CMC_AD	20	0.1 : 1	106.93 \pm 16.13	11.03 \pm 0.66	1.16 \pm 0.24	1.36 \pm 0.04	78.91 \pm 11.31	8.15 \pm 0.44
CNF/CMC_AD	24	0.1 : 1	70.35 \pm 7.76	8.24 \pm 0.51	0.80 \pm 0.12	1.36 \pm 0.01	51.56 \pm 5.54	6.04 \pm 0.36
CNF/XG	15.32	0.1 : 1	60.08 \pm 19.51	10.01 \pm 0.45	0.75 \pm 0.26	1.24 \pm 0.02	48.58 \pm 16.01	8.08 \pm 0.37
CNF/XG	15.32	0.15 : 1	84.53 \pm 10.66	11.32 \pm 0.64	0.79 \pm 0.17	1.28 \pm 0.03	66.20 \pm 8.65	8.86 \pm 0.40

* The ratio is in terms of dry weight of both components

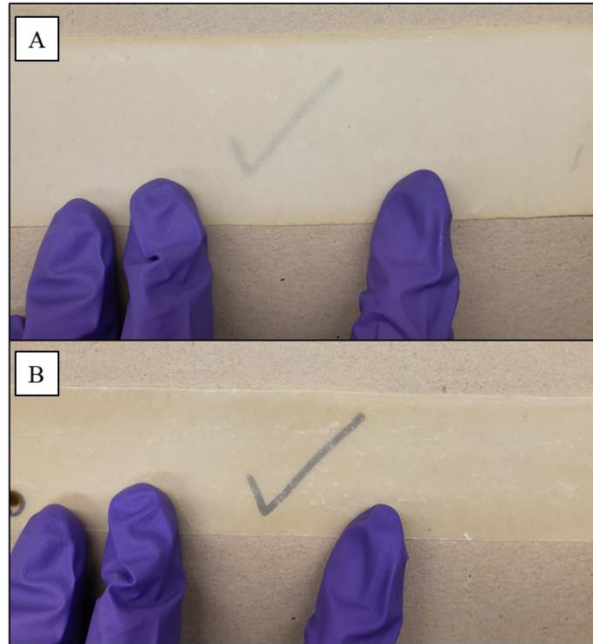


Figure B. 8 Two different consolidation procedures used to fully dry an extruded CNF/CMC paste through pressing and heating (A) and heated calendering (B). Note that the same check mark can be viewed more easily with the calendered sheet.

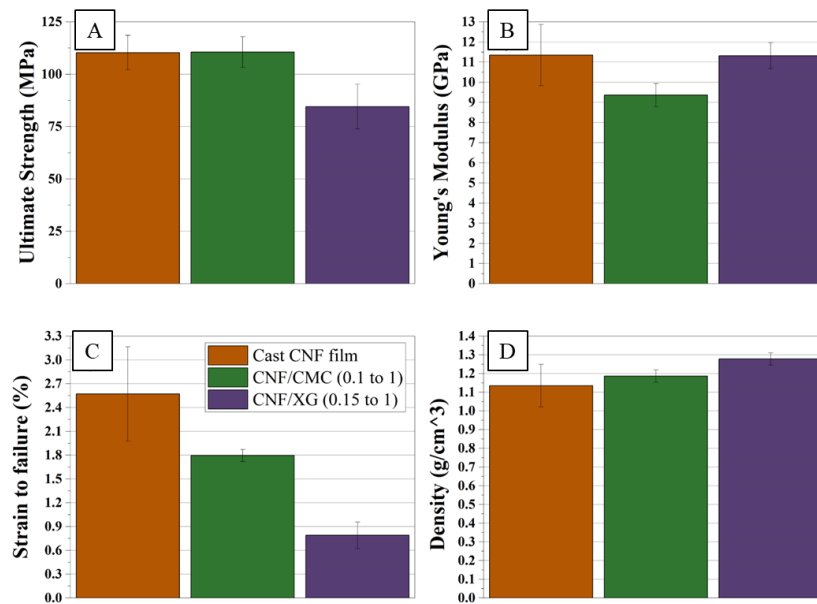


Figure B. 9 Tensile mechanical response of cast CNF films, extruded CNF/CMC sheets, and extruded CNF/XG sheets at two different processing to CNF dry weight ratios. The error bars represent one standard deviation away from the mean. The recorded responses are A) ultimate strength, B) Young's modulus, C) strain to failure, and D) density.

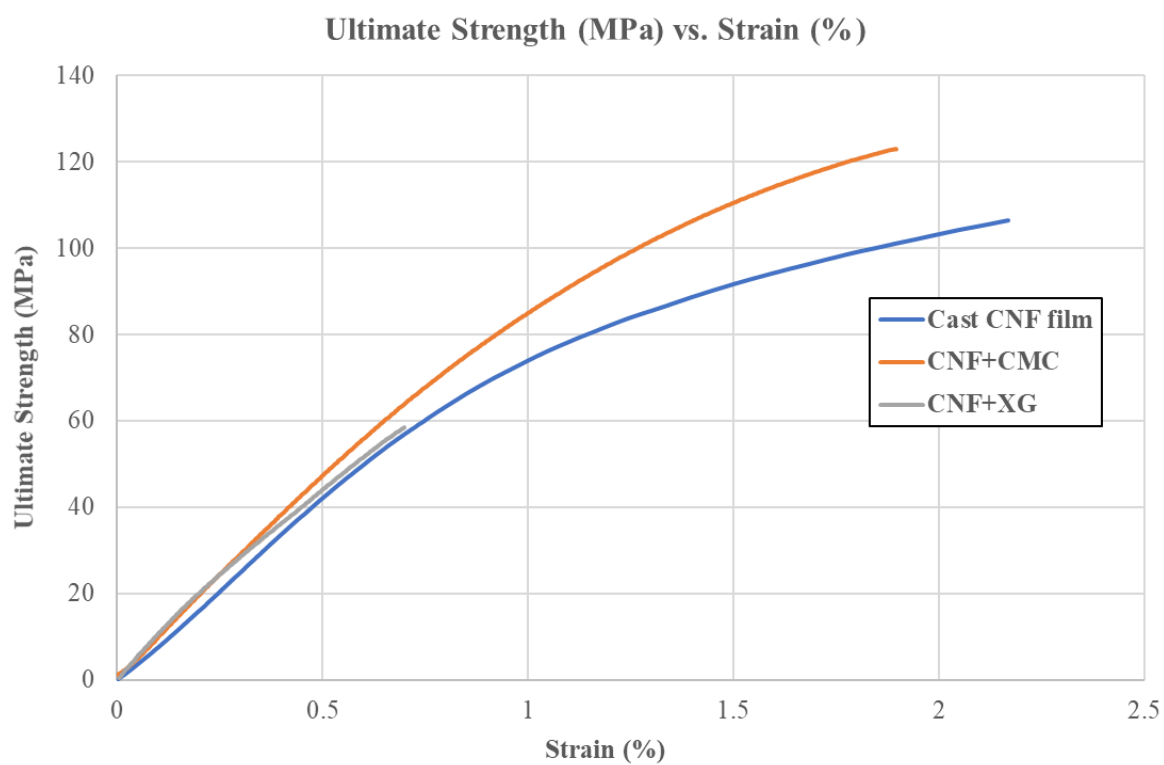


Figure B. 10 Tensile response (Ultimate strength (MPa) versus strain (%)) for a cast CNF film, and extruded CNF+CMC and CNF+XG sheets. This plot shows the response of a single sample from its respective group.

APPENDIX C. CONTROLLED DISPERSION AND SETTING OF CNF+CMC PASTES

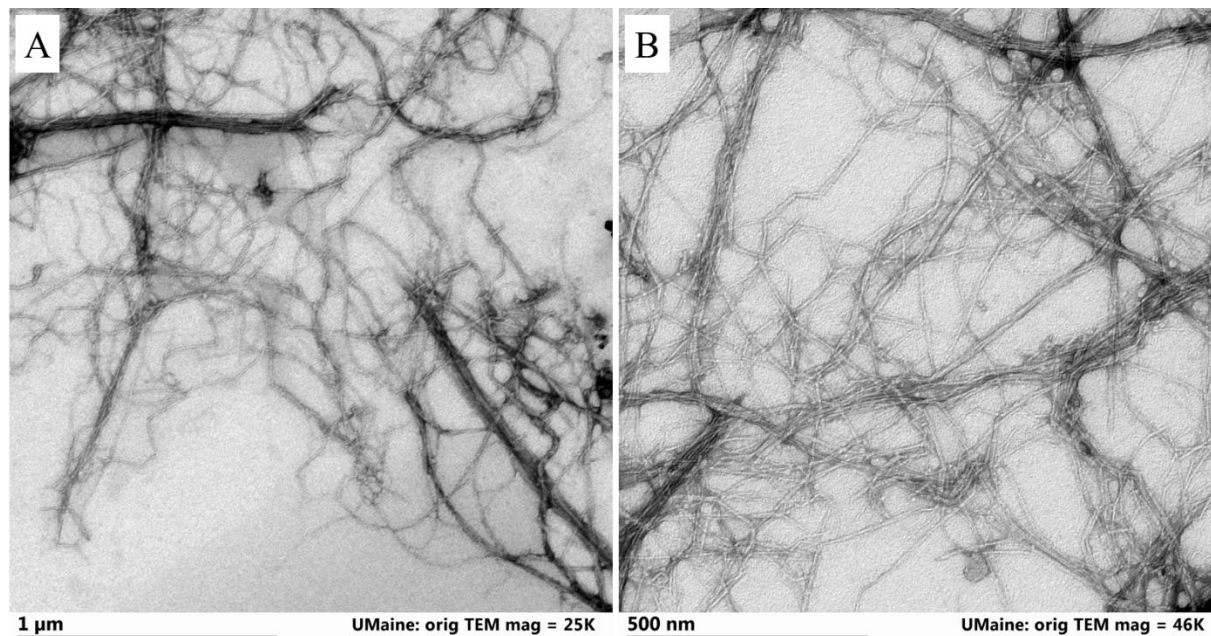


Figure C. 1 TEM images at two different magnifications (A = 25,000x, and B = 46,000x) of mechanically fibrillated CNF fibrils. CNF was procured from University of Maine and used as received. The TEM images were taken from a different batch of material but they should still be representative of the material used for the experiments.



Figure C. 2 CNF+CMC paste extruded into a ~ 100 mm long wet cord (a), and room temperature dried CNF+CMC cord (b). The approximate wet cord diameter is 2 mm while the dry cord had an approximate diameter of ~1 mm.

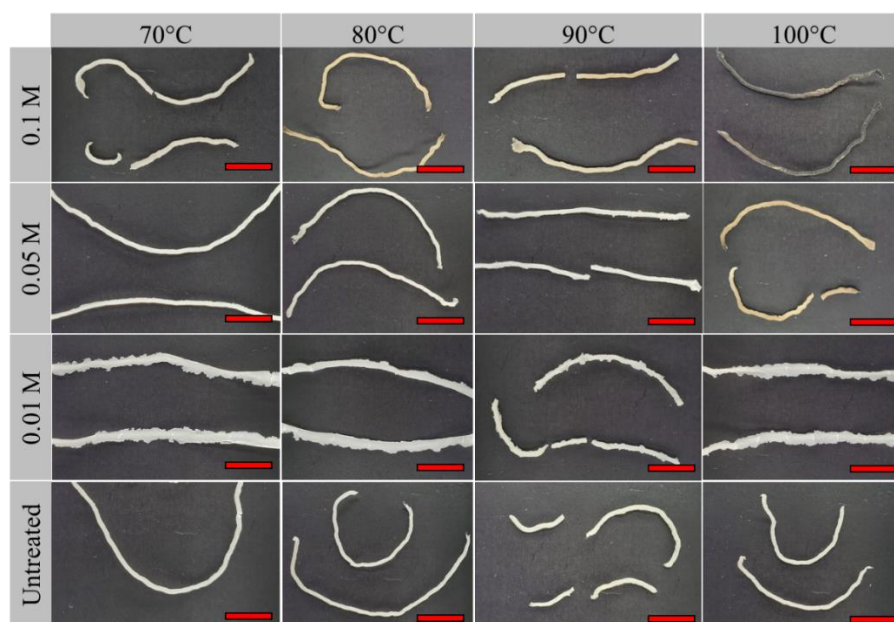


Figure C. 3 CNF+CMC treated cord segments at different acid concentrations (0.01 M, 0.05 M, and 0.1 M) and different drying temperatures (70 °C, 80 °C, 90 °C, and 100 °C). For all cases, CMC with a D.S. of 0.7 was used. The scale bars shown in red have a length of 10.5 mm. A cure temperature of 70°C was selected to avoid oxidation of the cord.

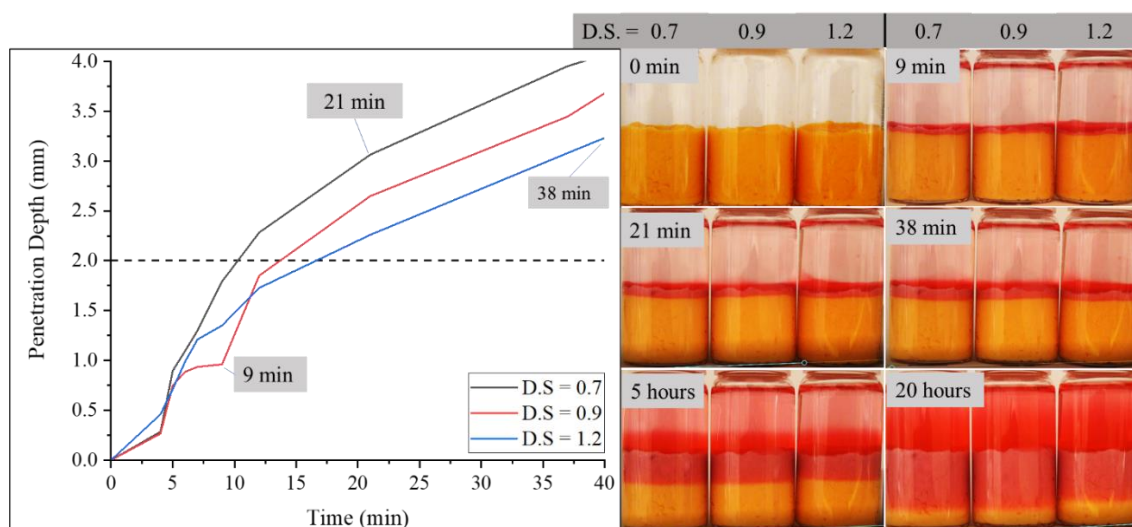


Figure C. 4 Acid penetration depth (mm) versus time (min) for HCl into a ~18 wt.% CNF+CMC paste with CMC at three different degrees of substitution (D.S. = 0.7, 0.9, and 1.2) (left). The CNF+CMC pastes (10 g) shown inside the vials (right) were mixed with 0.5 mL of 0.15 % methyl orange which served as an indicator for pH change due to the acid penetration into the paste. The dashed line on the plot to the left represents the 2 mm depth which corresponded with the desired cord diameter; hence a 20 min soak was selected for further treatments.

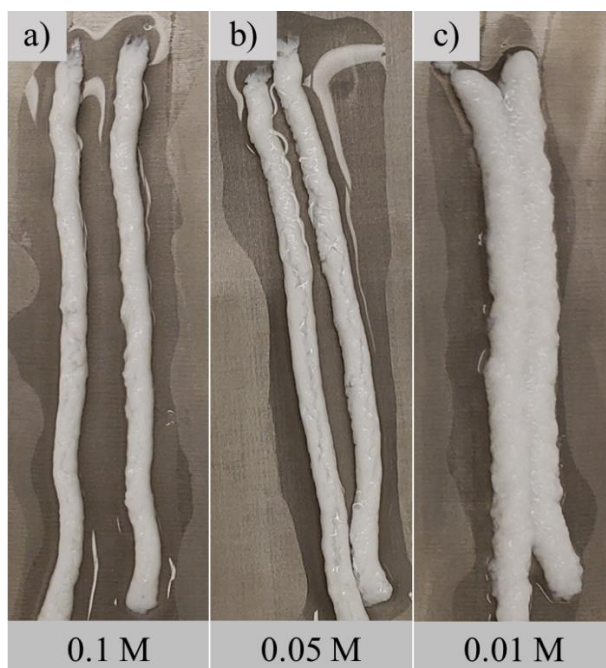


Figure C. 5 Wet CNF+CMC (D.S. = 0.7) cord segments (~100 mm long) being soaked/treated with different HCl concentrations. The lower acid molarity caused a distortion of the cord's dimension due to water absorption, hence 0.1 M was selected as the treatment concentration.

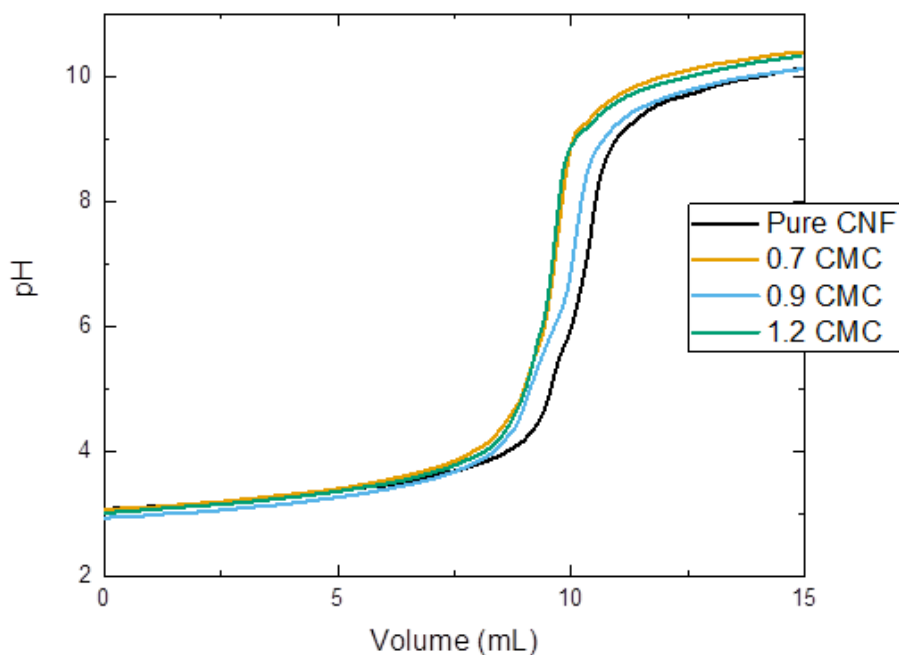


Figure C. 6 Representative titration curves (pH versus volume) of three different CNF+CMC suspensions prepared with a varying CMC D.S. of 0.7, 0.9, and 1.2 as well as a control group of pure CNF. The suspensions were titrated with 5 mM NaOH. The difference in volume between the inflection points in the curve correspond to the COOH concentration of the CNF suspensions.

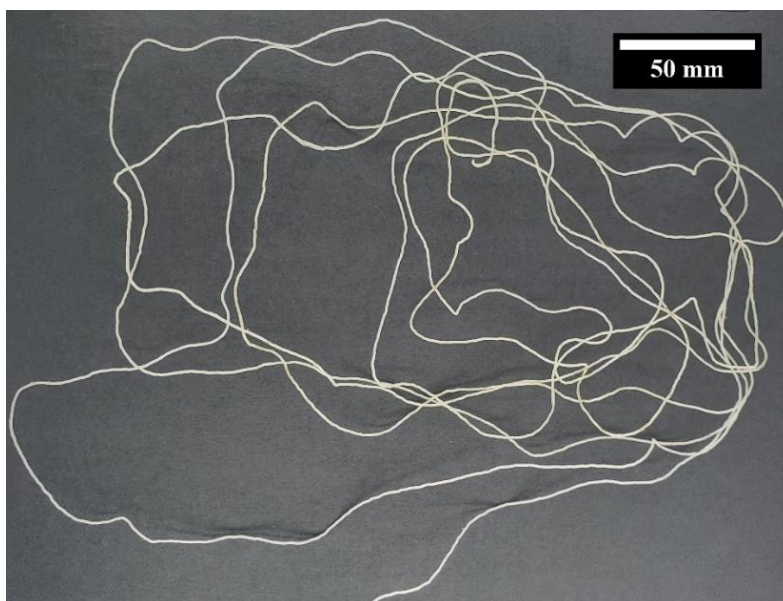


Figure C. 7 Free/unconstrained dried CNF+CMC cord (CMC D.S. = 0.7). The cord was dried at 35 °C overnight.

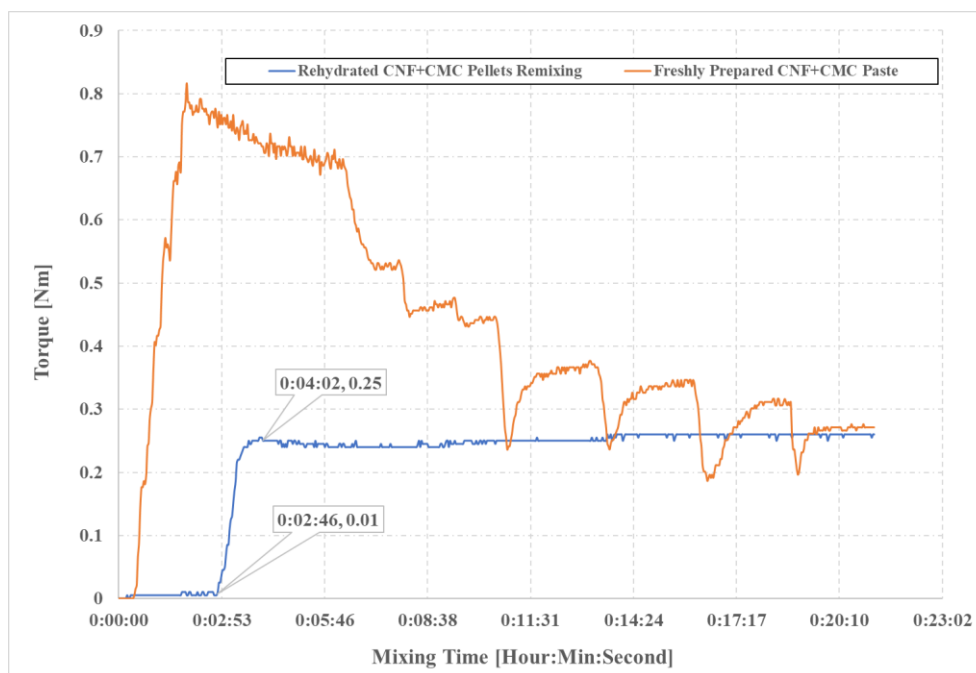


Figure C. 8 Plastogram of CNF+CMC (D.S. = 0.7) mixing in a Banbury shear mixer. The orange curve represents the typical torque response observed when preparing new CNF+CMC pastes. The blue curve represents the torque response of rehydrated CNF+CMC pellets which were mixed using the same configuration (120 rpm, 55 °C). Note that both curves reach a plateau of about ~0.27 Nm which signals complete mixing, yet the rehydrated pellet remixing reached it in approximately 1 min.

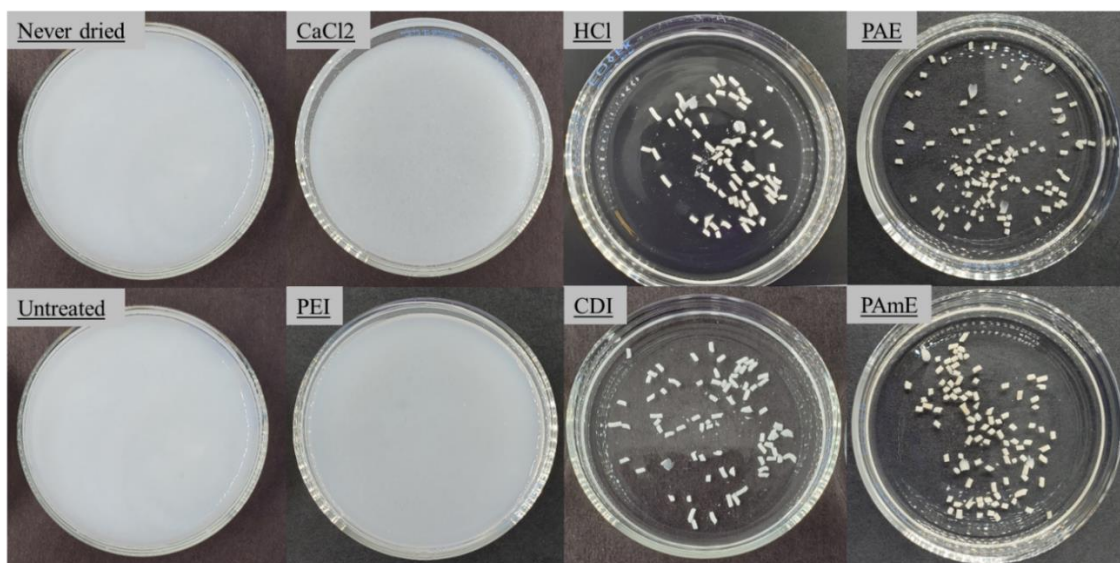


Figure C. 9 Redisperison behavior of treated and untreated CNF+CMC pellets in purified water. CMC with a D.S. of 0.7 was used for all samples. The pellets were stirred for 24 h at 25 °C. After stirring the suspensions were cast in a glass petri dish (diameter of 50 mm). The labels on the top-left of each figure represent the respective treatment used.

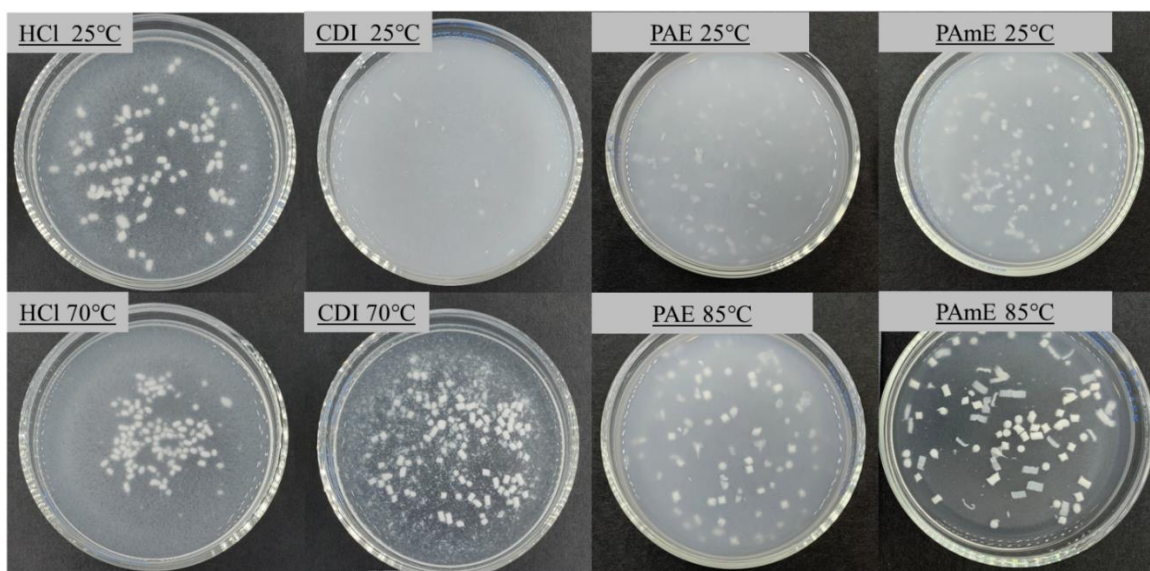


Figure C. 10 Redisperison behavior of treated CNF+CMC in 0.1 M NaOH. CMC with a D.S. of 0.7 was used for all samples. The pellets were stirred for 24 h at 25 °C. After stirring the suspensions were cast in a glass petri dish (diameter of 50 mm). The labels on the top-left of each figure represent the respective treatment and cure temperature used.

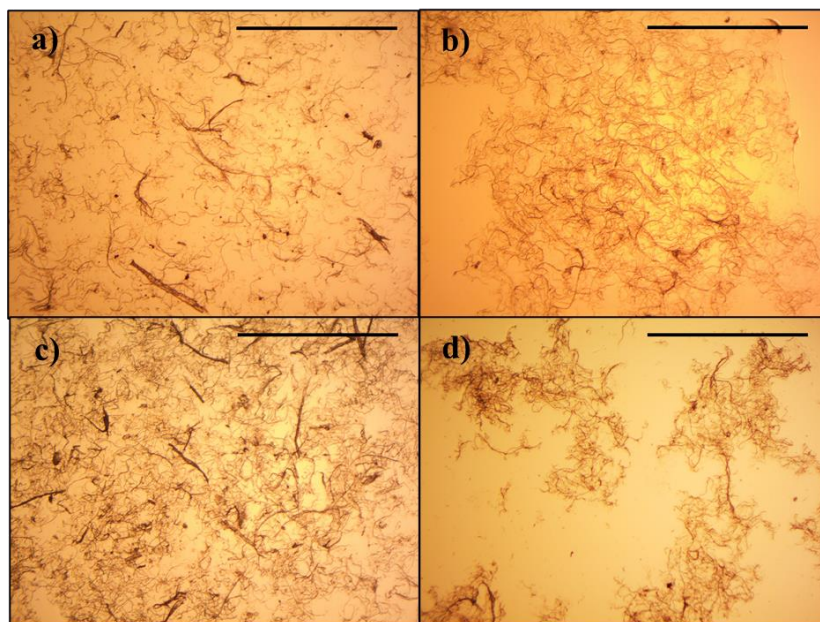


Figure C. 11 Optical micrographs of redispersed dried-untreated CNF+CMC (a), dispersed never-dried pure CNF (b), CaCl₂ treated CNF+CMC (c), and PEI treated CNF+CMC (d), all dispersed in water. For all samples CMC with a D.S. of 0.7 was used. The scale bar in the top right has a length of 1 mm. Agglomeration of the CNF fibrils is clearly appreciated for the PEI treatment.

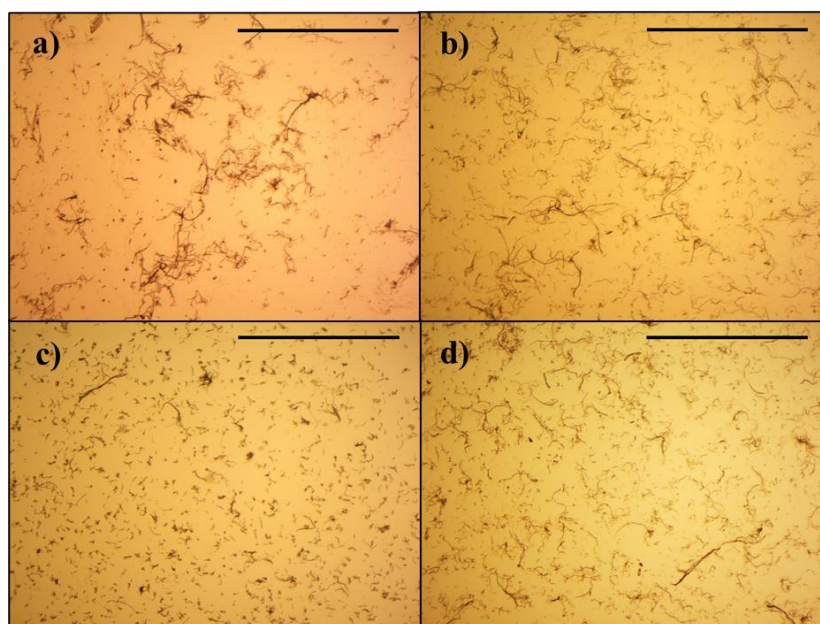


Figure C. 12 Optical micrographs of dispersed CNF+CMC treated with CDI cured at 70 °C (a), treated with PAE cured at 85 °C (b), treated with HCl cured at 70 °C (c), and treated with PAmE cured at 85 °C (d) all dispersed in 0.1 M NaOH. For all samples CMC with a D.S. of 0.7 was used. The scale bar in the top right has a length of 1 mm.

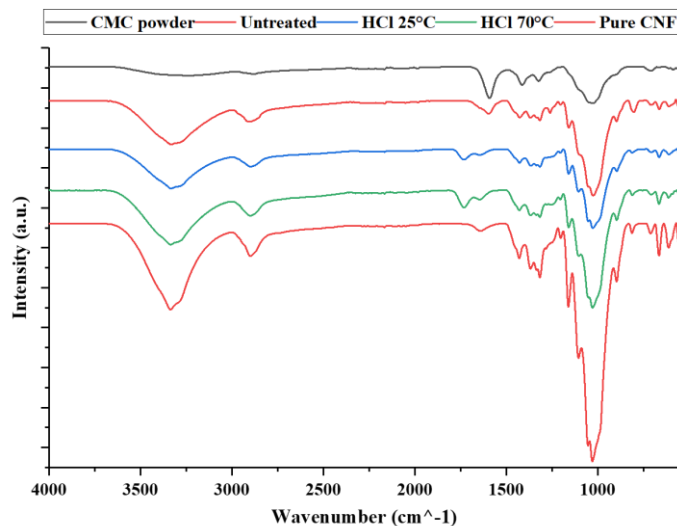


Figure C. 13 FTIR spectra of CNF+CMC treated with HCl cured at 25 °C and 70 °C, pure CMC powder, dried-untreated CNF+CMC, and pure CNF. 20 sample scans were collected, and the background was subtracted before each sample, respectively. Baseline correction was used for all spectra. For all samples CMC with a D.S. of 0.7 was used. The spectra shown was not normalized.

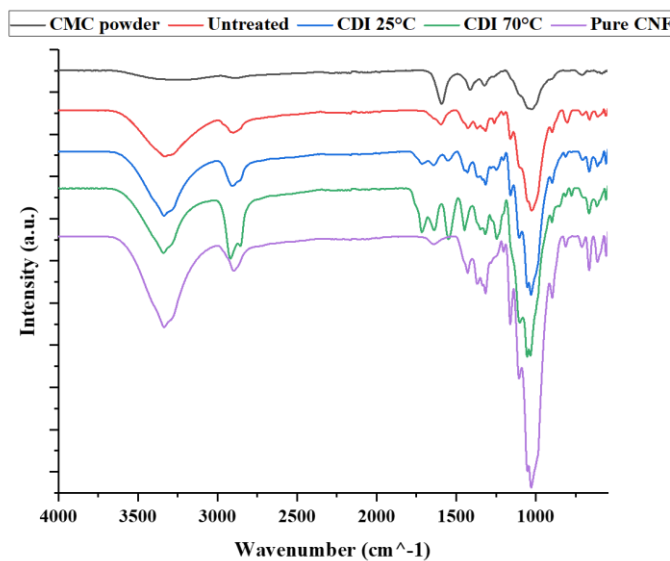


Figure C. 14 FTIR spectra of CNF+CMC treated with CDI cured at 25 °C and 70 °C, pure CMC powder, dried-untreated CNF+CMC, and pure CNF. 20 sample scans were collected, and the background was subtracted before each sample, respectively. Baseline correction was used for all spectra. For all samples CMC with a D.S. of 0.7 was used. The spectra shown was not normalized.

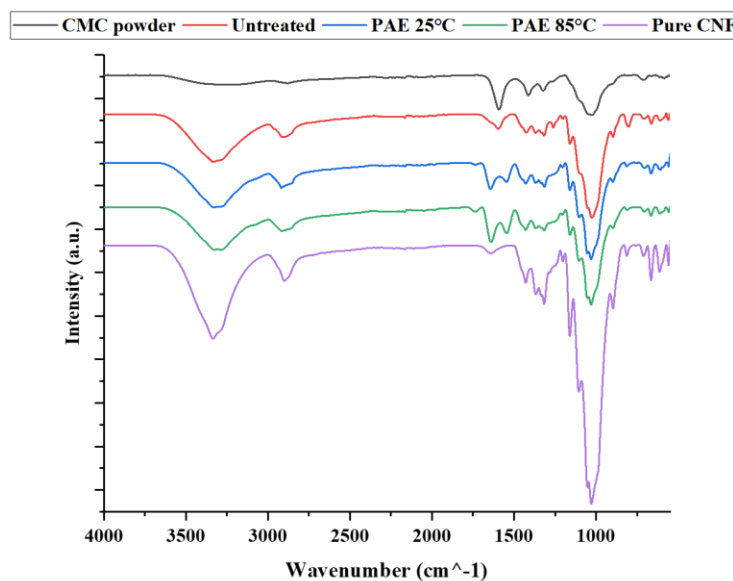


Figure C. 15 FTIR spectra of CNF+CMC treated with PAE cured at 25 °C and 85 °C, pure CMC powder, dried-untreated CNF+CMC, and pure CNF. 20 sample scans were collected, and the background was subtracted before each sample, respectively. Baseline correction was used for all spectra. For all samples CMC with a D.S. of 0.7 was used. The spectra shown was not normalized.

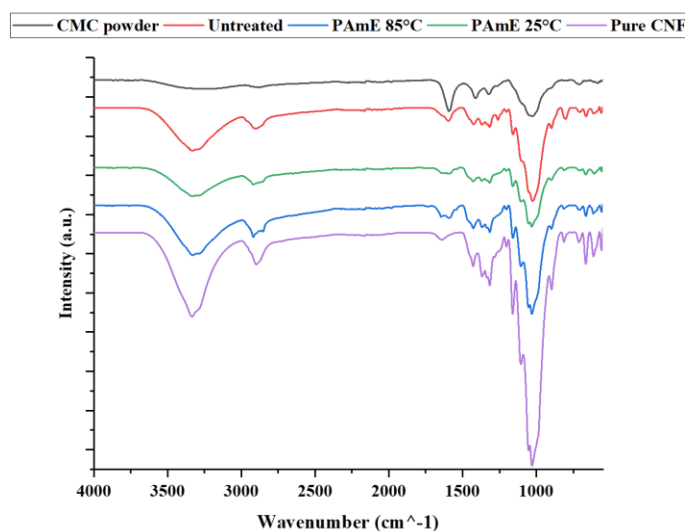


Figure C. 16 FTIR spectra of CNF+CMC treated with PAmE cured at 25 °C and 85 °C, pure CMC powder, dried-untreated CNF+CMC, and pure CNF. 20 sample scans were collected, and the background was subtracted before each sample, respectively. Baseline correction was used for all spectra. For all samples CMC with a D.S. of 0.7 was used. The spectra shown was not normalized.

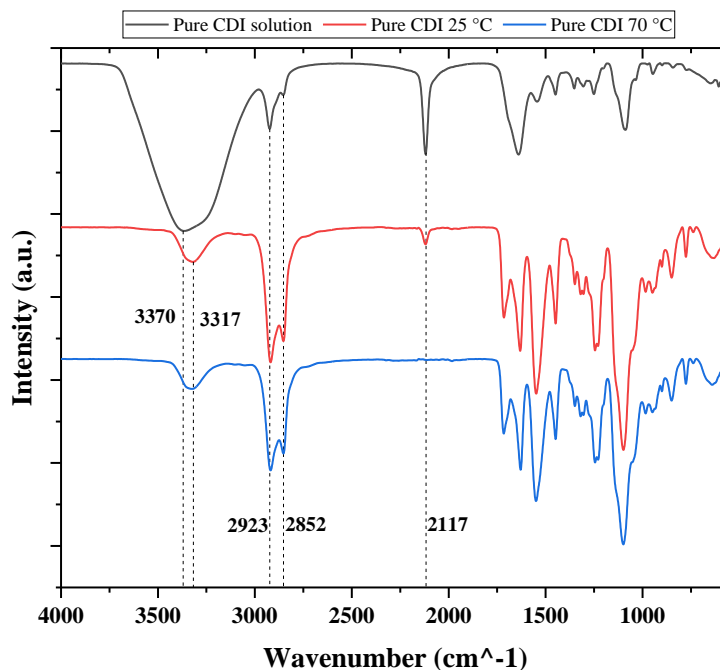


Figure C. 17 FTIR spectra of a concentrated uncured solution of CDI, cured CDI at 25 °C, and CDI cured at 70°C. 20 sample scans were collected, and the background was subtracted before each sample, respectively. Baseline correction was used for all spectra. The spectra shown was not normalized.

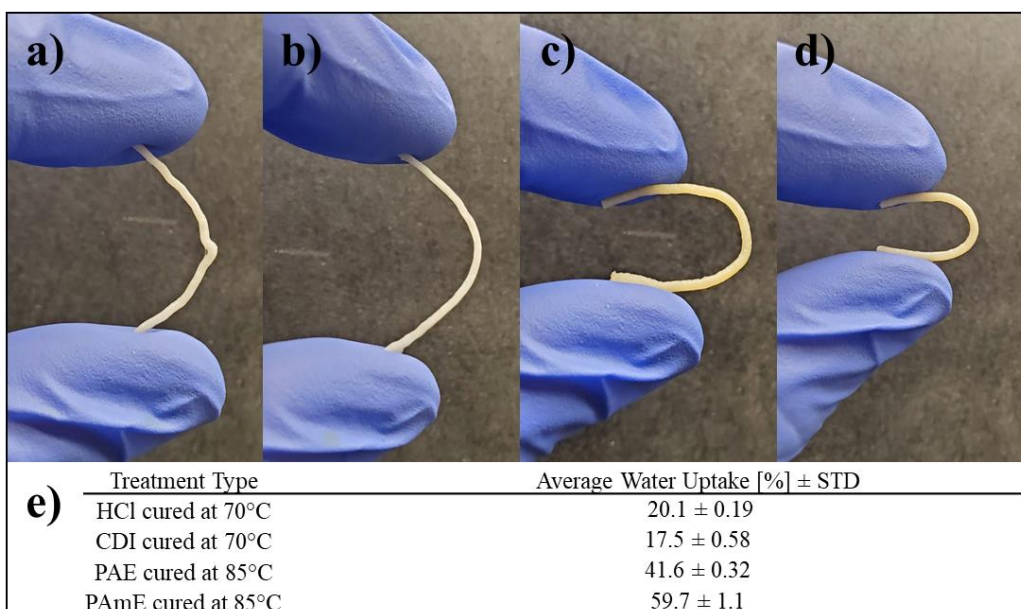


Figure C. 18 Bending of hydrated CNF+CMC treated with HCl (a), CDI (b), PAE (c), PAmE (d), and water uptake of the respective materials after 24 h submersion (e). The cord segments of HCl and CDI would fracture in half if bent further while PAE and PAmE treated cords could be fully bent onto itself without fracturing. For all samples CMC with a D.S. of 0.7 was used.

APPENDIX D. PROCESSING OF FIBER REINFORCED CELLULOSE NANOFIBRILS COMPOSITES (FR-CNF)

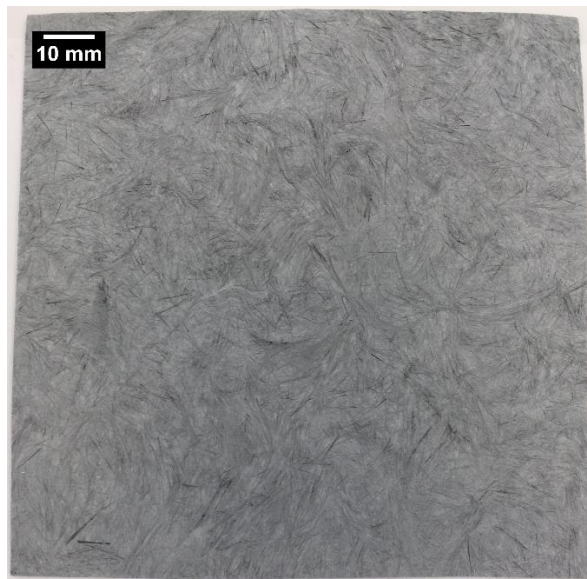


Figure D. 1 Three layer carbon fiber reinforce CNF composite. 30 wt.% fiber reinforcement was used in the laminate shown. The fiber length was 6.35 mm. Clear fiber bundles can be observed without using a strong back light.

REFERENCES

- (1) Moon, R. J.; Martini, A.; Nairn, J.; Simonsen, J.; Youngblood, J. Cellulose Nanomaterials Review: Structure, Properties and Nanocomposites. *Chem. Soc. Rev.* **2011**, *40* (7), 3941–3994. <https://doi.org/10.1039/c0cs00108b>.
- (2) Turbak, A. F.; Snyder, F. W.; Sandberg, K. R. Microfibrillated Cellulose, a New Cellulose Product: Properties, Uses, and Commercial Potential. *J. Appl. Polym. Sci.* **1983**, *37*, 815.
- (3) Herrik, F. W. Process For Preparing Microfibrillated Cellulose. 4,481,077, 1984.
- (4) Moon, R. J.; Schueneman, G. T.; Simonsen, J. Overview of Cellulose Nanomaterials, Their Capabilities and Applications. *JOM* **2016**, *68* (9), 2383–2394. <https://doi.org/10.1007/s11837-016-2018-7>.
- (5) Maren, R. Toxicity of Cellulose Nanocrystals: A Review. *Ind. Biotechnol.* **2015**, *11* (1), 25–33. <https://doi.org/10.1089/ind.2014.0024>.
- (6) Lin, N.; Dufresne, A. Nanocellulose in Biomedicine: Current Status and Future Prospect. *Eur. Polym. J.* **2014**, *59*, 302–325. <https://doi.org/10.1016/j.eurpolymj.2014.07.025>.
- (7) Axelsson, L.; Franzén, M.; Ostwald, M.; Berndes, G.; Lakshmi, G.; Ravindranath, N. H. Perspective: Jatropha Cultivation in Southern India: Assessing Farmers’ Experiences. *Biofuels, Bioprod. Biorefining* **2012**, *6* (3), 246–256. <https://doi.org/10.1002/bbb>.
- (8) Assis, C. A. de; Iglesias, M. C.; Bilodeau, M.; Johnson, D.; Phillips, R.; Peresin, M. S.; Bilek, E. M. (Ted); Rojas, O. J.; Venditti, R.; Gonzalez, R. Cellulose Micro- and Nanofibrils (CMNF) Manufacturing - Financial and Risk Assessment. *Biofuels, Bioprod. Biorefining* **2018**, *12* (2), 251–264. <https://doi.org/10.1002/bbb.1835>.
- (9) Foster, E. J.; Moon, R. J.; Agarwal, U. P.; Bortner, M. J.; Bras, J.; Camarero-Espinosa, S.; Chan, K. J.; Clift, M. J. D.; Cranston, E. D.; Eichhorn, S. J.; et al. Current Characterization Methods for Cellulose Nanomaterials. *Chem. Soc. Rev.* **2018**, *47* (8), 2609–2679. <https://doi.org/10.1039/c6cs00895j>.
- (10) Clarkson, C. M.; El Awad Azrak, S.; Forti, E.; Schueneman, G. T.; Moon, R. J.; Youngblood, J. P. Progress Report on Recent Developments in Cellulose Nanomaterial Composites. *Adv. Mater.* **2020**, *2000718*, 14–17. <https://doi.org/adma.202000718R1>.

- (11) Henriksson, M.; Henriksson, G.; Berglund, L. A.; Lindström, T. An Environmentally Friendly Method for Enzyme-Assisted Preparation of Microfibrillated Cellulose (MFC) Nanofibers. *Eur. Polym. J.* **2007**, *43* (8), 3434–3441. <https://doi.org/10.1016/j.eurpolymj.2007.05.038>.
- (12) El Awad Azrak, S. M.; Clarkson, C. M.; Moon, R. J.; Schueneman, G. T.; Youngblood, J. P. Wet-Stacking Lamination of Multilayer Mechanically Fibrillated Cellulose Nanofibril (CNF) Sheets with Increased Mechanical Performance for Use in High-Strength and Lightweight Structural and Packaging Applications. *ACS Appl. Polym. Mater.* **2019**, *1* (9), 2525–2534. <https://doi.org/10.1021/acsapm.9b00635>.
- (13) Saito, T.; Kimura, S.; Nishiyama, Y.; Isogai, A. Cellulose Nanofibers Prepared by TEMPO-Mediated Oxidation of Native Cellulose. *Biomacromolecules* **2007**, *8* (8), 2485–2491. <https://doi.org/10.1021/bm0703970>.
- (14) Saito, T.; Nishiyama, Y.; Putaux, J. L.; Vignon, M.; Isogai, A. Homogeneous Suspensions of Individualized Microfibrils from TEMPO-Catalyzed Oxidation of Native Cellulose. *Biomacromolecules* **2006**, *7* (6), 1687–1691. <https://doi.org/10.1021/bm060154s>.
- (15) Mascheroni, E.; Rampazzo, R.; Ortenzi, M. A.; Piva, G.; Bonetti, S.; Piergiovanni, L. Comparison of Cellulose Nanocrystals Obtained by Sulfuric Acid Hydrolysis and Ammonium Persulfate, to Be Used as Coating on Flexible Food-Packaging Materials. *Cellulose* **2016**, *23* (1), 779–793. <https://doi.org/10.1007/s10570-015-0853-2>.
- (16) Eichhorn, S. J. Cellulose Nanowhiskers: Promising Materials for Advanced Applications. *Soft Matter* **2011**, *7* (2), 303–315. <https://doi.org/10.1039/c0sm00142b>.
- (17) Vanderfleet, O. M.; Osorio, D. A.; Cranston, E. D. Optimization of Cellulose Nanocrystal Length and Surface Charge Density through Phosphoric Acid Hydrolysis. *Philos. Trans. R. Soc. A Math. Phys. Eng. Sci.* **2018**, *376* (2112). <https://doi.org/10.1098/rsta.2017.0041>.
- (18) Clarkson, C. M.; El Awad Azrak, S. M.; Chowdhury, R.; Shuvo, S. N.; Snyder, J.; Schueneman, G.; Ortalan, V.; Youngblood, J. P. Melt Spinning of Cellulose Nanofibril/Polylactic Acid (CNF/PLA) Composite Fibers For High Stiffness. *ACS Appl. Polym. Mater.* **2019**, *1* (2), 160–168. <https://doi.org/10.1021/acsapm.8b00030>.
- (19) Chowdhury, R. A.; Clarkson, C.; Youngblood, J. Continuous Roll-to-Roll Fabrication of Transparent Cellulose Nanocrystal (CNC) Coatings with Controlled Anisotropy. *Cellulose* **2018**, *25* (3), 1769–1781. <https://doi.org/10.1007/s10570-018-1688-4>.

- (20) Sehaqui, H.; Liu, A.; Zhou, Q.; Berglund, L. A. Fast Preparation Procedure for Large, Flat Cellulose and Cellulose/Inorganic Nanopaper Structures. *Biomacromolecules* **2010**, *11* (9), 2195–2198. <https://doi.org/10.1021/bm100490s>.
- (21) Osong, S. H.; Norgren, S.; Engstrand, P. Processing of Wood-Based Microfibrillated Cellulose and Nanofibrillated Cellulose, and Applications Relating to Papermaking: A Review. *Cellulose* **2016**, *23* (1), 93–123. <https://doi.org/10.1007/s10570-015-0798-5>.
- (22) Chowdhury, R. A.; Clarkson, C. M.; Shrestha, S.; El Awad Azrak, S. M.; Mavlan, M.; Youngblood, J. P. High-Performance Waterborne Polyurethane Coating Based on a Blocked Isocyanate with Cellulose Nanocrystals (CNC) as the Polyol. *ACS Appl. Polym. Mater.* **2020**, *2* (2), 385–393. <https://doi.org/10.1021/acsapm.9b00849>.
- (23) Clarkson, C. M.; El Awad Azrak, S. M.; Schueneman, G. T.; Snyder, J. F.; Youngblood, J. P. Crystallization Kinetics and Morphology of Small Concentrations of Cellulose Nanofibrils (CNFs) and Cellulose Nanocrystals (CNCs) Melt-Compounded into Poly(Lactic Acid) (PLA) with Plasticizer. *Polymer (Guildf)*. **2020**, *187* (October 2019), 122101. <https://doi.org/10.1016/j.polymer.2019.122101>.
- (24) Qiu, X.; Hu, S. “Smart” Materials Based on Cellulose: A Review of the Preparations, Properties, and Applications. *Materials (Basel)*. **2013**, *6* (3), 738–781. <https://doi.org/10.3390/ma6030738>.
- (25) Saito, T.; Hirota, M.; Tamura, N.; Kimura, S.; Fukuzumi, H.; Heux, L.; Isogai, A. Individualization of Nano-Sized Plant Cellulose Fibrils by Direct Surface Carboxylation Using TEMPO Catalyst under Neutral Conditions. *Biomacromolecules* **2009**, *10* (7), 1992–1996. <https://doi.org/10.1021/bm900414t>.
- (26) Clarkson, C. M.; El Awad Azrak, S. M.; Chowdhury, R.; Shuvo, S. N.; Snyder, J.; Schueneman, G.; Ortalan, V.; Youngblood, J. P. Melt Spinning of Cellulose Nanofibril/Poly(lactic Acid) (CNF/PLA) Composite Fibers For High Stiffness. *ACS Appl. Polym. Mater.* **2019**, *acsapm.8b00030*. <https://doi.org/10.1021/acsapm.8b00030>.
- (27) Clarkson, C. M.; El Awad Azrak, S. M.; Schueneman, G. T.; Snyder, J. F.; Youngblood, J. P. Crystallization Kinetics and Morphology of Small Concentrations of Cellulose Nanofibrils (CNFs) and Cellulose Nanocrystals (CNCs) Melt-Compounded into Poly(Lactic Acid) (PLA) with Plasticizer. *Polymer (Guildf)*. **2020**, *187* (December 2019), 122101. <https://doi.org/10.1016/j.polymer.2019.122101>.

- (28) Clarkson, C. M.; El Awad Azrak, S. M.; Forti, E. S.; Schueneman, G. T.; Moon, R. J.; Youngblood, J. P. Recent Developments in Cellulose Nanomaterial Composites. *Advanced Materials*. 2020. <https://doi.org/10.1002/adma.202000718>.
- (29) Zhang, Y.; Nypelö, T.; Salas, C.; Arboleda, J.; Hoeger, I. C.; Rojas, O. J. Cellulose Nanofibrils: From Strong Materials to Bioactive Surfaces. *J. Renew. Mater.* **2013**, *1* (3), 195–211. <https://doi.org/10.7569/JRM.2013.634115>.
- (30) Henriksson, M.; Berglund, L. A. Structure and Properties of Cellulose Nanocomposite Films Containing Melamine Formaldehyde. *J. Appl. Polym. Sci.* **2007**, *106*, 2817–2824. <https://doi.org/10.1002/app.26946>.
- (31) Chowdhury, R. A.; Clarkson, C.; Apalangya, V. A.; Islam, S. M. N.; Youngblood, J. P. Roll-to-Roll Fabrication of Cellulose Nanocrystal-Poly(Vinyl Alcohol) Composite Coatings with Controlled Anisotropy. *Cellulose* **2018**, *25* (11), 6547–6560. <https://doi.org/10.1007/s10570-018-2019-5>.
- (32) Peng, S. X.; Shrestha, S.; Yoo, Y.; Youngblood, J. P. Enhanced Dispersion and Properties of a Two-Component Epoxy Nanocomposite Using Surface Modified Cellulose Nanocrystals. *Polymer (Guildf)*. **2017**, *112*, 359–368. <https://doi.org/10.1016/j.polymer.2017.02.016>.
- (33) Oksman, K.; Aitomäki, Y.; Mathew, A. P.; Siqueira, G.; Zhou, Q.; Butylina, S.; Tanpichai, S.; Zhou, X.; Hooshmand, S. Review of the Recent Developments in Cellulose Nanocomposite Processing. *Compos. Part A Appl. Sci. Manuf.* **2016**, *83*, 2–18. <https://doi.org/10.1016/j.compositesa.2015.10.041>.
- (34) Forti, E. S.; Moon, R. J.; Schueneman, G. T.; Youngblood, J. P. Transparent Tempco Oxidized Cellulose Nanofibril (TOCNF) Composites with Increased Toughness and Thickness by Lamination. *Cellulose* **2020**, *27* (8), 4389–4405. <https://doi.org/10.1007/s10570-020-03107-8>.
- (35) Henriksson, M.; Berglund, L. A.; Isaksson, P.; Lindstro, T.; Nishino, T. Cellulose Nanopaper Structures of High Toughness Cellulose Nanopaper Structures of High Toughness. *Biomacromolecules* **2008**, *9* (May), 1579–1585. <https://doi.org/10.1021/bm800038n>.

- (36) Claro, P.; de Campos, A.; Corrêa, A.; Rodrigues, V.; Luchesi, B.; Silva, L.; Tonoli, G.; Mattoso, L.; Marconcini, J. Curaua and Eucalyptus Nanofiber Films by Continuous Casting: Mixture of Cellulose Nanocrystals and Nanofibrils. *Cellulose* **2019**, *26* (4), 2453–2470. <https://doi.org/10.1007/s10570-019-02280-9>.
- (37) Claro, P. I. C.; Corrêa, A. C.; de Campos, A.; Rodrigues, V. B.; Luchesi, B. R.; Silva, L. E.; Mattoso, L. H. C.; Marconcini, J. M. Curaua and Eucalyptus Nanofibers Films by Continuous Casting: Mechanical and Thermal Properties. *Carbohydr. Polym.* **2018**, *181*, 1093–1101. <https://doi.org/10.1016/J.CARBPOL.2017.11.037>.
- (38) Otoni, C. G.; Lodi, B. D.; Lorevice, M. V.; Leitão, R. C.; Ferreira, M. D.; Moura, M. R. d.; Mattoso, L. H. C. Optimized and Scaled-up Production of Cellulose-Reinforced Biodegradable Composite Films Made up of Carrot Processing Waste. *Ind. Crops Prod.* **2018**, *121* (May), 66–72. <https://doi.org/10.1016/j.indcrop.2018.05.003>.
- (39) Balea, A.; Sanchez-Salvador, J. L.; Monte, M. C.; Merayo, N.; Negro, C.; Blanco, A. In Situ Production and Application of Cellulose Nanofibers to Improve Recycled Paper Production. *Molecules* **2019**, *24* (9), 1–13. <https://doi.org/10.3390/molecules24091800>.
- (40) Douglass, E. F.; Avci, H.; Boy, R.; Rojas, O. J.; Kotek, R. A Review of Cellulose and Cellulose Blends for Preparation of Bio-Derived and Conventional Membranes, Nanostructured Thin Films, and Composites. *Polym. Rev.* **2018**, *58* (1), 102–163. <https://doi.org/10.1080/15583724.2016.1269124>.
- (41) Böhmendorfer, S.; Hosoya, T.; Röder, T.; Potthast, A.; Rosenau, T. A Cautionary Note on Thermal Runaway Reactions in Mixtures of 1-Alkyl-3-Methylimidazolium Ionic Liquids and N-Methylmorpholine-N-Oxide. *Cellulose* **2017**, *24* (5), 1927–1932. <https://doi.org/10.1007/s10570-017-1257-2>.
- (42) Fu, F.; Guo, Y.; Wang, Y.; Tan, Q.; Zhou, J.; Zhang, L. Structure and Properties of the Regenerated Cellulose Membranes Prepared from Cellulose Carbamate in NaOH/ZnO Aqueous Solution. *Cellulose* **2014**, *21* (4), 2819–2830. <https://doi.org/10.1007/s10570-014-0297-0>.
- (43) Illiam, O.; Brilhart; LeRoy; Galian; And; James; N.; Carver; Fredericksburg; et al. Cellophane Coating Having Improved Wet Stretch At Low Temperatures. 2,950,992, 1960.

- (44) Taylor; Grantham, W. G. Dimensionally Stable, Nitrocellulose Coated Cellophane. 4,072,785, 1978.
- (45) Chavan, P. A.; Shinde, B. S.; Bhagwat, V. N.; Shinde, P. P.; Patil, B. D. Pocket Ventilation System In Dryer Section Of Paper Machine : A Review. *Int. J. Technol. Enhanc. Emerg. Eng. Res.* **2015**, 3 (03), 11–14.
- (46) Sehaqui, H.; Zhou, Q.; Ikkala, O.; Berglund, L. A. Strong and Tough Cellulose Nanopaper with High Specific Surface Area and Porosity. *Biomacromolecules* **2011**, 12, 3638–3644. <https://doi.org/10.1021/bm2008907>.
- (47) Syverud, K.; Stenius, P. Strength and Barrier Properties of MFC Films. *Cellulose* **2009**, 16 (1), 75–85. <https://doi.org/10.1007/s10570-008-9244-2>.
- (48) Przybysz, P.; Dubowik, M.; Kucner, M. A.; Przybysz, K.; Buzala, K. P. Contribution of Hydrogen Bonds to Paper Strength Properties. *PLoS One* **2016**, 11 (5), 1–10. <https://doi.org/10.1371/journal.pone.0155809>.
- (49) Ghosh, A. K. *Fundamentals of Paper Drying – Theory and Application from Industrial Perspective*; InTech, 2011.
- (50) Weise, U. Characterization and Mechanism of Changes in Wood Pulp Fibres Caused by Water Removal. *Acta Polytech. Scand. Chem. Technol. Ser.* **1997**, No. 249.
- (51) TAPPI. Forming Handsheets for Physical Tests of Pulp. Test Method TAPPI/ANSI T 205 Sp-18. *Tappi* **2002**, 1–9.
- (52) Peng, Y.; Gardner, D. J.; Han, Y. Drying Cellulose Nanofibrils: In Search of a Suitable Method. *Cellulose* **2012**, 19 (1), 91–102. <https://doi.org/10.1007/s10570-011-9630-z>.
- (53) Cheng, W.; Dunn, P. F.; Brach, R. M. SURFACE ROUGHNESS EFFECTS ON MICROPARTICLE ADHESION Modeling of Adhesion for Smooth Surfaces. **2002**, No. 96, 929–965. <https://doi.org/10.1080/00218460290010584>.
- (54) Bardet, R.; Reverdy, C.; Belgacem, N.; Leirset, I.; Syverud, K.; Bardet, M.; Bras, J. Substitution of Nanoclay in High Gas Barrier Films of Cellulose Nanofibrils with Cellulose Nanocrystals and Thermal Treatment. *Cellulose* **2015**, 22 (2), 1227–1241. <https://doi.org/10.1007/s10570-015-0547-9>.
- (55) Zhang, X.; Yu, Y.; Jiang, Z.; Wang, H. Influence of Thickness and Moisture Content on the Mechanical Properties of Microfibrillated Cellulose (MFC) Films. *Wood Res.* **2016**, 61 (6), 851–860.

- (56) Zhu, H.; Zhu, S.; Jia, Z.; Parvinian, S.; Li, Y.; Vaaland, O.; Hu, L.; Li, T. Anomalous Scaling Law of Strength and Toughness of Cellulose Nanopaper. *Proc. Natl. Acad. Sci.* **2015**, *112* (29), 8971–8976. <https://doi.org/10.1073/pnas.1502870112>.
- (57) Alcalá, M.; González, I.; Boufi, S.; Vilaseca, F.; Mutjé, P. All-Cellulose Composites from Unbleached Hardwood Kraft Pulp Reinforced with Nanofibrillated Cellulose. *Cellulose* **2013**, *20* (6), 2909–2921. <https://doi.org/10.1007/s10570-013-0085-2>.
- (58) Chun, S. J.; Lee, S. Y.; Doh, G. H.; Lee, S.; Kim, J. H. Preparation of Ultrastrength Nanopapers Using Cellulose Nanofibrils. *J. Ind. Eng. Chem.* **2011**, *17* (3), 521–526. <https://doi.org/10.1016/j.jiec.2010.10.022>.
- (59) González, I.; Alcalà, M.; Chinga-Carrasco, G.; Vilaseca, F.; Boufi, S.; Mutjé, P. From Paper to Nanopaper: Evolution of Mechanical and Physical Properties. *Cellulose* **2014**, *21* (4), 2599–2609. <https://doi.org/10.1007/s10570-014-0341-0>.
- (60) Kulachenko, A.; Denoyelle, T.; Galland, S.; Lindstrom, S. B. Elastic Properties of Cellulose Nanopaper. *Cellulose* **2012**, *19* (3), 793–807. <https://doi.org/10.1007/s10570-012-9685-5>.
- (61) Griffith, A. A. The Phenomena of Rupture and Flow in Solids. *Philos. Trans. R. Soc. A* **1920**, *221* (582–593). <https://doi.org/10.1098/rsta.1921.0006>.
- (62) Singh, A. P.; Rey, A. D. Computer Simulation of Dynamics and Morphology of Discotic Mesophases in Extensional Flows. *Liq. Cryst.* **1995**, *18* (2), 219–230. <https://doi.org/10.1080/02678299508036617>.
- (63) Report, A. *Alcoa Annual Report*; 2017.
- (64) Kumar, V.; Bollström, R.; Yang, A.; Chen, Q.; Chen, G.; Salminen, P.; Bousfield, D.; Toivakka, M. Comparison of Nano- and Microfibrillated Cellulose Films. *Cellulose* **2014**, *21* (5), 3443–3456. <https://doi.org/10.1007/s10570-014-0357-5>.
- (65) Rantanen, J.; Maloney, T. C. Press Dewatering and Nip Rewetting of Paper Containing Nano- and Microfibril Cellulose. *Nord. Pulp Pap. Res. J.* **2013**, *28* (4), 582–587. <https://doi.org/10.3183/NPPRJ-2013-28-04-p582-587>.
- (66) Wang, Q.; Yao, Q.; Liu, J.; Sun, J.; Zhu, Q.; Chen, H. Processing Nanocellulose to Bulk Materials: A Review. *Cellulose* **2019**, *26* (13–14), 7585–7617. <https://doi.org/10.1007/s10570-019-02642-3>.

- (67) Hietala, M.; Mathew, A. P.; Oksman, K. Bionanocomposites of Thermoplastic Starch and Cellulose Nanofibers Manufactured Using Twin-Screw Extrusion. *Eur. Polym. J.* **2013**, *49* (4), 950–956. <https://doi.org/10.1016/j.eurpolymj.2012.10.016>.
- (68) Gong, G.; Pyo, J.; Mathew, A. P.; Oksman, K. Tensile Behavior, Morphology and Viscoelastic Analysis of Cellulose Nanofiber-Reinforced (CNF) Polyvinyl Acetate (PVAc). *Compos. Part A Appl. Sci. Manuf.* **2011**, *42* (9), 1275–1282. <https://doi.org/10.1016/j.compositesa.2011.05.009>.
- (69) Jonoobi, M.; Harun, J.; Mathew, A. P.; Oksman, K. Mechanical Properties of Cellulose Nanofiber (CNF) Reinforced Polylactic Acid (PLA) Prepared by Twin Screw Extrusion. *Compos. Sci. Technol.* **2010**, *70* (12), 1742–1747. <https://doi.org/10.1016/j.compscitech.2010.07.005>.
- (70) Herrera, N.; Mathew, A. P.; Oksman, K. Plasticized Polylactic Acid/Cellulose Nanocomposites Prepared Using Melt-Extrusion and Liquid Feeding: Mechanical, Thermal and Optical Properties. *Compos. Sci. Technol.* **2015**, *106*, 149–155. <https://doi.org/10.1016/j.compscitech.2014.11.012>.
- (71) Picker, K. M.; Hoag, S. W. Characterization of the Thermal Properties of Microcrystalline Cellulose by Modulated Temperature Differential Scanning Calorimetry. *J. Pharm. Sci.* **2002**, *91* (2), 342–349. <https://doi.org/10.1002/jps.10018>.
- (72) Borsoi, C.; Zimmermann, M. V. G.; Zattera, A. J.; Santana, R. M. C.; Ferreira, C. A. Thermal Degradation Behavior of Cellulose Nanofibers and Nanowhiskers. *J. Therm. Anal. Calorim.* **2016**, *126* (3), 1867–1878. <https://doi.org/10.1007/s10973-016-5653-x>.
- (73) Beck, S.; Bouchard, J.; Berry, R. Dispersibility in Water of Dried Nanocrystalline Cellulose. *Biomacromolecules* **2012**, *13* (5), 1486–1494. <https://doi.org/10.1021/bm300191k>.
- (74) Fairman, E. Avoiding Aggregation During Drying and Rehydration of Nanocellulose, University of Maine, 2014.
- (75) Nechyporchuk, O.; Belgacem, M. N.; Pignon, F. Current Progress in Rheology of Cellulose Nanofibril Suspensions. *Biomacromolecules* **2016**, *17* (7), 2311–2320. <https://doi.org/10.1021/acs.biomac.6b00668>.
- (76) Hubbe, M. A.; Nanko, H.; McNeal, M. R. Retention Aid Polymer Interactions with Cellulosic Surfaces and Suspensions: A Review. *BioResources* **2009**, *4* (2), 850–906. <https://doi.org/10.15376/biores.4.2.850-906>.

- (77) Kang, K. S.; Pettitt, D. J. Xanthan, Gellan, Welan, and Rhamsan. In *Industrial Gums: Polysaccharides and Their Derivatives: Third Edition*; WHISTLER, R. L., BEMILLER, J. N., Eds.; ACADEMIC PRESS, INC., 2012; pp 341–397. <https://doi.org/10.1016/B978-0-08-092654-4.50017-6>.
- (78) Maine, U. of. Order Nanocellulose <https://umaine.edu/pdc/nanocellulose/order-nanocellulose/>.
- (79) Xu, X.; Hilmas, G. E. The Rheological Behavior of Ceramic/Polymer Mixtures for Coextrusion Processing. *J. Mater. Sci.* **2007**, 42 (4), 1381–1387. <https://doi.org/10.1007/s10853-006-1221-2>.
- (80) Samaniuk, J. R.; Scott, C. T.; Root, T. W.; Klingenberg, D. J. Rheological Modification of Corn Stover Biomass at High Solids Concentrations. *J. Rheol. (N. Y. N. Y.)*. **2012**, 56 (3), 649–665. <https://doi.org/10.1122/1.3702101>.
- (81) Goodrich, J. E.; Porter, R. S. A Rheological Interpretation of Torque-rheometer Data. *Polym. Eng. Sci.* **1967**, 7 (1), 45–51. <https://doi.org/10.1002/pen.760070112>.
- (82) Beeaff, D. R.; Hilmas, G. E. Rheological Behavior of Coextruded Multilayer Architectures. *J. Mater. Sci.* **2002**, 37 (6), 1259–1264. <https://doi.org/10.1023/A:1014392111303>.
- (83) Bousmina, M.; Ait-Kadi, A.; Faisant, J. B. Determination of Shear Rate and Viscosity from Batch Mixer Data. *J. Rheol. (N. Y. N. Y.)*. **1999**, 43 (2), 415–433. <https://doi.org/10.1122/1.551044>.
- (84) Blyler, L. L.; Daane, J. H. An Analysis of Brabender Torque Rheometer Data. *Polym. Eng. Sci.* **1967**, 7 (3), 178–181. <https://doi.org/10.1002/pen.760070309>.
- (85) Marquez, A.; Quijano, J.; Gaulin, M. A Calibration Technique to Evaluate the Power-Law Parameters of Polymer Melts Using a Torque-Rheometer. *Polym. Eng. Sci.* **1996**, 36 (20), 2556–2563. <https://doi.org/10.1002/pen.10655>.
- (86) Santi, C. R.; Jr., E. H.; Correa, C. A.; Vlachopoulos, J. Torque Viscometry of Molten Polymers and Composites. *Appl. Rheol.* **2009**, 19 (1), 1–7.
- (87) Costakis, W. J.; Schlup, A. P.; Youngblood, J. P.; Trice, R. W. Aligning α -Alumina Platelets via Uniaxial Pressing of Ceramic-Filled Polymer Blends for Improved Sintered Transparency. **2019**, *Accepted*.

- (88) Brancato, A.; Walsh, F. L.; Sabo, R.; Banerjee, S. Effect of Recycling on the Properties of Paper Surfaces. *Ind. Eng. Chem. Res.* **2007**, *46* (26), 9103–9106. <https://doi.org/10.1021/ie070826a>.
- (89) Howard, R. . The Effects of Recycling on Paper Quality. *J. Pulp Pap. Sci.* **1990**, *16* (5), 143–149.
- (90) Kulkarni, V. S.; Shaw, C.; Kulkarni, V. S.; Shaw, C. Use of Polymers and Thickeners in Semisolid and Liquid Formulations. In *Essential Chemistry for Formulators of Semisolid and Liquid Dosages*; Academic Press, 2016; pp 43–69. <https://doi.org/10.1016/B978-0-12-801024-2.00005-4>.
- (91) Saha, D.; Bhattacharya, S. Hydrocolloids as Thickening and Gelling Agents in Food: A Critical Review. *Journal of Food Science and Technology*. Springer December 2010, pp 587–597. <https://doi.org/10.1007/s13197-010-0162-6>.
- (92) Brady, J.; Drig, T.; Lee, P. I.; Li, J. X. Polymer Properties and Characterization. In *Developing Solid Oral Dosage Forms: Pharmaceutical Theory and Practice: Second Edition*; Qiu, Y., Zhang, G. G. Z., Mantri, R. V., Chen, Y., Yu, L., Eds.; Elsevier Inc., 2017; pp 181–223. <https://doi.org/10.1016/B978-0-12-802447-8.00007-8>.
- (93) Liimatainen, H.; Haavisto, S.; Haapala, A.; Niinimäki, J. Influence of Adsorbed and Dissolved Carboxymethyl Cellulose on Fibre Suspension Dispersing, Dewaterability, and Fines Retention. *BioResources* **2009**, *4* (1), 321–340.
- (94) Lee, P. F. W.; Lindstrom, T. Effect of High Molecular Mass Anionic Polymers on Paper Sheet Formation. *Nord. Pulp Pap. Res. J.* **1989**, *4* (2), 61–70. <https://doi.org/10.3183/npprj-1989-04-02-p061-070>.
- (95) Scott, C. T. Pulp Extrusion at Ultra-High Consistencies: Selection of Water-Soluble Polymers for Process Optimization. In *TAPPI Fall technical Conference and Trade Fair*; 2002; pp 1621–1629.
- (96) Lafleur, P. G.; Vergnes, B. Single-Screw Extrusion. In *Polymer Extrusion*; ISTE Ltd and John Wiley & Sons, Inc, 2014; pp 37–108.
- (97) Fang, S.; Chen, L.; Zhu, F. Studies on the Theory of Single Screw Plasticating Extrusion. Part II: Non-plug Flow Solid Conveying. *Polym. Eng. Sci.* **1991**, *31* (15), 1117–1122. <https://doi.org/10.1002/pen.760311508>.

- (98) Derakhshandeh, B.; Kerekes, R. J.; Hatzikiriakos, S. G.; Bennington, C. P. J. Rheology of Pulp Fibre Suspensions: A Critical Review. *Chem. Eng. Sci.* **2011**, *66* (15), 3460–3470. <https://doi.org/10.1016/J.CES.2011.04.017>.
- (99) Dealy, J. M.; Wang, J. Role of Rheology in Melt Processing. In *Melt Rheology and its Applications in the Plastics Industry*; 2013; pp 205–260. <https://doi.org/10.1007/978-94-007-6395-1>.
- (100) Williams, P. A.; Phillips, G. O. Introduction to Food Hydrocolloids. In *Handbook of Hydrocolloids: Second Edition*; Woodhead Publishing Limited, 2009; pp 1–22. <https://doi.org/10.1533/9781845695873.1>.
- (101) Sworn, G. Xanthan Gum. In *Handbook of Hydrocolloids*; Woodhead Publishing, 2009; pp 186–203. <https://doi.org/10.1533/9781845695873.186>.
- (102) Imeson, A. *Food Stabilisers, Thickeners and Gelling Agents*; Imeson, A., Ed.; John Wiley & Sons, Ltd, 2009. <https://doi.org/10.1002/9781444314724>.
- (103) Ellwood, K. R. J.; Papanastasiou, T. C.; Wilkes, J. O. Three-dimensional Streamlined Finite Elements: Design of Extrusion Dies. *Int. J. Numer. Methods Fluids* **1992**, *14* (1), 13–24. <https://doi.org/10.1002/fld.1650140103>.
- (104) Hall, L. K.; Rosen, M. Polyglycerol Plastic Lubricants. 4,481,324, 1984.
- (105) Butchosa, N.; Zhou, Q. Water Redispersible Cellulose Nanofibrils Adsorbed with Carboxymethyl Cellulose. *Cellulose* **2014**, *21* (6), 4349–4358. <https://doi.org/10.1007/s10570-014-0452-7>.
- (106) Yan, H.; Lindström, T.; Christiernin, M. Some Ways to Decrease Fibre Suspension Flocculation and Improve Sheet Formation. *Nord. Pulp Pap. Res. J.* **2006**, *21* (1), 36–43.
- (107) Beghello, L.; Lindstrom, T. The Influence of Carboxymethylation on the Fiber Flocculation Process. *Nord. Pulp Pap. Res. J.* **1998**, *13* (4). <https://doi.org/10.3183/npprj-1998-13-04-p269-273>.
- (108) Watanabe, M.; Gondo, T.; Kitao, O. Advanced Wet-End System with Carboxymethyl-Cellulose. *Tappi* **2004**, *3* (5), 15–19.
- (109) Stickel, J. J.; Knutsen, J. S.; Liberatore, M. W.; Luu, W.; Bousfield, D. W.; Klingenberg, D. J.; Scott, C. T.; Root, T. W.; Ehrhardt, M. R.; Monz, T. O. Rheology Measurements of a Biomass Slurry: An Inter-Laboratory Study. *Rheol. Acta* **2009**, *48* (9), 1005–1015. <https://doi.org/10.1007/s00397-009-0382-8>.

- (110) Samaniuk, J. R.; Wang, J.; Root, T. W.; Scott, C. T.; Klingenberg, D. J. Rheology of Concentrated Biomass. *Korea Aust. Rheol. J.* **2011**, *23* (4), 237–245. <https://doi.org/10.1007/s13367-011-0029-z>.
- (111) Samaniuk, J. R.; Scott, C. T.; Root, T. W.; Klingenberg, D. J. Effects of Process Variables on the Yield Stress of Rheologically Modified Biomass. *Rheol. Acta* **2015**, *54* (11–12), 941–949. <https://doi.org/10.1007/s00397-015-0884-5>.
- (112) Schmid, C. F.; Klingenberg, D. J. Properties of Fiber Flocs with Frictional and Attractive Interfiber Forces. *J. Colloid Interface Sci.* **2000**, *226* (1), 136–144. <https://doi.org/10.1006/jcis.2000.6803>.
- (113) de Britto, D.; Assis, O. B. G. Thermal Degradation of Carboxymethylcellulose in Different Salty Forms. *Thermochim. Acta* **2009**, *494* (1–2), 115–122. <https://doi.org/10.1016/j.tca.2009.04.028>.
- (114) Fukuzumi, H.; Saito, T.; Isogai, A. Influence of TEMPO-Oxidized Cellulose Nanofibril Length on Film Properties. *Carbohydr. Polym.* **2013**, *93* (1), 172–177. <https://doi.org/10.1016/j.carbpol.2012.04.069>.
- (115) Lin, X.; Li, Y.; Chen, Z.; Zhang, C.; Luo, X.; Du, X.; Huang, Y. Synthesis, Characterization and Electrospinning of New Thermoplastic Carboxymethyl Cellulose (TCMC). *Chem. Eng. J.* **2013**, *215–216*, 709–720. <https://doi.org/10.1016/j.cej.2012.10.089>.
- (116) Murray, J. C. F. Cellulosics. In *Handbook of Hydrocolloids: Second Edition*; 2009; pp 710–723. <https://doi.org/10.1533/9781845695873.710>.
- (117) Feddersen, R. L.; Thorp, S. N. Sodium Carboxymethylcellulose. In *Industrial Gums: Polysaccharides and Their Derivatives: Third Edition*; ACADEMIC PRESS, INC., 2012; pp 537–578. <https://doi.org/10.1016/B978-0-08-092654-4.50024-3>.
- (118) El Awad Azrak, S. M.; Costakis, W. J.; Moon, R. J.; Schueneman, G. T.; Youngblood, J. P. Continuous Processing of Cellulose Nanofibril Sheets Through Conventional Single-Screw Extrusion. *ACS Appl. Polym. Mater.* **2020**, *2* (8), 3365–3377. <https://doi.org/10.1021/acsapm.0c00477>.
- (119) Liimatainen, H.; Haavisto, S.; Haapala, A.; Niinimäki, J. Influence of Adsorbed and Dissolved Carboxymethyl Cellulose on Fibre Suspension Dispersing, Dewaterability, and Fines Retention. *BioResources* **2009**, *4* (1), 321–340. <https://doi.org/10.15376/biores.4.1.321-340>.

- (120) Beghelli, L.; Lindström, T. The Influence of Carboxymethylation on the Fiber Flocculation Process. *Nord. Pulp Pap. Res. J.* **1998**, *13* (4), 269–273.
- (121) Lundahl, M. J.; Klar, V.; Wang, L.; Ago, M.; Rojas, O. J. Spinning of Cellulose Nanofibrils into Filaments: A Review. *Ind. Eng. Chem. Res.* **2017**, *56* (1), 8–19. <https://doi.org/10.1021/acs.iecr.6b04010>.
- (122) Mather, R. R.; Wardman, R. H. *The Chemistry of Textile Fibres*; Royal Society of Chemistry, 2011.
- (123) Kafy, A.; Kim, H. C.; Zhai, L.; Kim, J. W.; Hai, L. Van; Kang, T. J.; Kim, J. Cellulose Long Fibers Fabricated from Cellulose Nanofibers and Its Strong and Tough Characteristics. *Sci. Rep.* **2017**, *7* (1), 1–8. <https://doi.org/10.1038/s41598-017-17713-3>.
- (124) Håkansson, K. M. O.; Fall, A. B.; Lundell, F.; Yu, S.; Krywka, C.; Roth, S. V.; Santoro, G.; Kvik, M.; Prahl Wittberg, L.; Wågberg, L.; et al. Hydrodynamic Alignment and Assembly of Nanofibrils Resulting in Strong Cellulose Filaments. *Nat. Commun.* **2014**, *5*. <https://doi.org/10.1038/ncomms5018>.
- (125) Kim, H. C.; Kim, D.; Lee, J. Y.; Zhai, L.; Kim, J. Effect of Wet Spinning and Stretching to Enhance Mechanical Properties of Cellulose Nanofiber Filament. *Int. J. Precis. Eng. Manuf. - Green Technol.* **2019**, *6* (3), 567–575. <https://doi.org/10.1007/s40684-019-00070-z>.
- (126) Cai, Y.; Geng, L.; Chen, S.; Shi, S.; Hsiao, B. S.; Peng, X. Hierarchical Assembly of Nanocellulose into Filaments by Flow-Assisted Alignment and Interfacial Complexation: Conquering the Conflicts between Strength and Toughness. *ACS Appl. Mater. Interfaces* **2020**, *12* (28), 32090–32098. <https://doi.org/10.1021/acsami.0c04504>.
- (127) Duker, E.; Brännvall, E.; Lindström, T. The Effects of CMC Attachment onto Industrial and Laboratory-Cooked Pulps. *Nord. Pulp Pap. Res. J.* **2007**, *22* (3), 356–363. <https://doi.org/10.3183/npprj-2007-22-03-p356-363>.
- (128) Liu, Z.; Choi, H.; Gatenholm, P.; Esker, A. R. Quartz Crystal Microbalance with Dissipation Monitoring and Surface Plasmon Resonance Studies of Carboxymethyl Cellulose Adsorption onto Regenerated Cellulose Surfaces. *Langmuir* **2011**, *27* (14), 8718–8728. <https://doi.org/10.1021/la200628a>.
- (129) Lasseguette, E. Grafting onto Microfibrils of Native Cellulose. *Cellulose* **2008**, *15* (4), 571–580. <https://doi.org/10.1007/s10570-008-9200-1>.

- (130) Jiang, F.; Hsieh, Y. Lo. Self-Assembling of TEMPO Oxidized Cellulose Nanofibrils As Affected by Protonation of Surface Carboxyls and Drying Methods. *ACS Sustain. Chem. Eng.* **2016**, *4* (3), 1041–1049. <https://doi.org/10.1021/acssuschemeng.5b01123>.
- (131) Moser, C.; Lindström, M. E.; Henriksson, G. Toward Industrially Feasible Methods for Following the Process of Manufacturing Cellulose Nanofibers. *BioResources* **2015**, *10* (2), 2360–2375. <https://doi.org/10.15376/biores.10.2.2360-2375>.
- (132) Desmaisons, J.; Boutonnet, E.; Rueff, M.; Dufresne, A.; Bras, J. A New Quality Index for Benchmarking of Different Cellulose Nanofibrils. *Carbohydr. Polym.* **2017**, *174*, 318–329. <https://doi.org/10.1016/j.carbpol.2017.06.032>.
- (133) Uetani, K.; Yano, H. Zeta Potential Time Dependence Reveals the Swelling Dynamics of Wood Cellulose Nanofibrils. *Langmuir* **2012**, *28* (1), 818–827. <https://doi.org/10.1021/la203404g>.
- (134) Fernandes Diniz, J. M. B.; Gil, M. H.; Castro, J. A. A. M. Hornification - Its Origin and Interpretation in Wood Pulps. *Wood Sci. Technol.* **2004**, *37* (6), 489–494. <https://doi.org/10.1007/s00226-003-0216-2>.
- (135) Hospodarova, V.; Singovszka, E.; Stevulova, N. Characterization of Cellulosic Fibers by FTIR Spectroscopy for Their Further Implementation to Building Materials. *Am. J. Anal. Chem.* **2018**, *09* (06), 303–310. <https://doi.org/10.4236/ajac.2018.96023>.
- (136) Aguayo, M. G.; Pérez, A. F.; Reyes, G.; Oviedo, C.; Gacitúa, W.; Gonzalez, R.; Uyarte, O. Isolation and Characterization of Cellulose Nanocrystals from Rejected Fibers Originated in the Kraft Pulping Process. *Polymers (Basel)*. **2018**, *10* (10). <https://doi.org/10.3390/polym10101145>.
- (137) Müller, Y.; Tot, I.; Potthast, A.; Rosenau, T.; Zimmermann, R.; Eichhorn, K. J.; Nitschke, C.; Scherr, G.; Freudenberg, U.; Werner, C. The Impact of Esterification Reactions on Physical Properties of Cellulose Thin Films. *Soft Matter* **2010**, *6* (15), 3680–3684. <https://doi.org/10.1039/c0sm00005a>.
- (138) Cuba-Chiem, L. T.; Huynh, L.; Ralston, J.; Beattie, D. A. In Situ Particle Film ATR FTIR Spectroscopy of Carboxymethyl Cellulose Adsorption on Talc: Binding Mechanism, PH Effects, and Adsorption Kinetics. *Langmuir* **2008**, *24* (15), 8036–8044. <https://doi.org/10.1021/la800490t>.

- (139) Eyholzer, C.; Bordeanu, N.; Lopez-Suevos, F.; Rentsch, D.; Zimmermann, T.; Oksman, K. Preparation and Characterization of Water-Redispersible Nanofibrillated Cellulose in Powder Form. *Cellulose* **2010**, *17* (1), 19–30. <https://doi.org/10.1007/s10570-009-9372-3>.
- (140) Onyianta, A. J.; Dorris, M.; Williams, R. L. Aqueous Morpholine Pre-Treatment in Cellulose Nanofibril (CNF) Production: Comparison with Carboxymethylation and TEMPO Oxidisation Pre-Treatment Methods. *Cellulose* **2018**, *25* (2), 1047–1064. <https://doi.org/10.1007/s10570-017-1631-0>.
- (141) Pantze, A.; Karlsson, O.; Westermarck, U. Esterification of Carboxylic Acids on Cellulosic Material: Solid State Reactions. *Holzforschung* **2008**, *62* (2), 136–141. <https://doi.org/10.1515/HF.2008.027>.
- (142) Carrillo, I.; Mendonça, R. T.; Ago, M.; Rojas, O. J. Comparative Study of Cellulosic Components Isolated from Different Eucalyptus Species. *Cellulose* **2018**, *25* (2), 1011–1029. <https://doi.org/10.1007/s10570-018-1653-2>.
- (143) Rosa, M. F.; Medeiros, E. S.; Malmonge, J. A.; Gregorski, K. S.; Wood, D. F.; Mattoso, L. H. C.; Glenn, G.; Orts, W. J.; Imam, S. H. Cellulose Nanowhiskers from Coconut Husk Fibers: Effect of Preparation Conditions on Their Thermal and Morphological Behavior. *Carbohydr. Polym.* **2010**, *81* (1), 83–92. <https://doi.org/10.1016/j.carbpol.2010.01.059>.
- (144) Hesselmanns, L. C. J.; Derksen, A. J.; Van Den Goorbergh, J. A. M. Polycarbodiimide Crosslinkers. *Prog. Org. Coatings* **2006**, *55* (2), 142–148. <https://doi.org/10.1016/j.porgcoat.2005.08.011>.
- (145) Posthumus, W.; Derksen, A. J.; van den Goorbergh, J. A. M.; Hesselmanns, L. C. J. Crosslinking by Polycarbodiimides. *Prog. Org. Coatings* **2007**, *58* (2–3), 231–236. <https://doi.org/10.1016/j.porgcoat.2006.09.031>.
- (146) Derksen, A. J. *Polycarbodiimides as Classification-Free and Easy to Use Crosslinkers for Water-Based Coatings*; Waalwijk, The Netherlands, 2017; Vol. 14.
- (147) Lu, P.; Zhang, Y.; Jia, C.; Li, Y.; Mao, Z. Use of Polyurea from Urea for Coating of Urea Granules. *Springerplus* **2016**, *5* (1). <https://doi.org/10.1186/s40064-016-2120-x>.
- (148) Piasek Z.; Urbanski T. The Infrared Absorption Spectrum and Structure of Urea. *Bul. L' Acad. Pol. Des Sci.* **1962**, *X* (3), 113–120.
- (149) Mojarradi, H. Coupling of Substances Containing a Primary Amine to Hyaluronan via Carbodiimide-Mediated Amidation, Uppsala University, 2011.

- (150) Pham, H. H.; Winnik, M. A. Polymer Interdiffusion vs Cross-Linking in Carboxylic Acid-Carbodiimide Latex Films. Effect of Annealing Temperature, Reactive Group Concentration, and Carbodiimide Substituent. *Macromolecules* **2006**, 39 (4), 1425–1435. <https://doi.org/10.1021/ma051685w>.
- (151) Obokata, T.; Isogai, A. The Mechanism of Wet-Strength Development of Cellulose Sheets Prepared with Polyamideamine-Epichlorohydrin (PAE) Resin. *Colloids Surfaces A Physicochem. Eng. Asp.* **2007**, 302 (1–3), 525–531. <https://doi.org/10.1016/j.colsurfa.2007.03.025>.
- (152) Yang, W.; Bian, H.; Jiao, L.; Wu, W.; Deng, Y.; Dai, H. High Wet-Strength, Thermally Stable and Transparent TEMPO-Oxidized Cellulose Nanofibril Film: Via Cross-Linking with Poly-Amide Epichlorohydrin Resin. *RSC Adv.* **2017**, 7 (50), 31567–31573. <https://doi.org/10.1039/c7ra05009g>.
- (153) Sharma, S.; Deng, Y. Dual Mechanism of Dry Strength Improvement of Cellulose Nanofibril Films by Polyamide-Epichlorohydrin Resin Cross-Linking. *Ind. Eng. Chem. Res.* **2016**, 55 (44), 11467–11474. <https://doi.org/10.1021/acs.iecr.6b02910>.
- (154) Siqueira, E. J.; Salon, M.-C. B.; Belgacem, M. N.; Mauret, E. Carboxymethylcellulose (CMC) as a Model Compound of Cellulose Fibers and Polyamideamine Epichlorohydrin (PAE)-CMC Interactions as a Model of PAE-Fibers Interactions of PAE-Based Wet Strength Papers. *J. Appl. Polym. Sci.* **2015**, 132 (26), n/a-n/a. <https://doi.org/10.1002/app.42144>.
- (155) Yang, D.; Diflavio, J. L.; Gustafsson, E.; Pelton, R. Wet-Peel: A Tool for Comparing Wet-Strength Resins. *Nord. Pulp Pap. Res. J.* **2018**, 33 (4), 632–646. <https://doi.org/10.1515/npprj-2018-0013>.
- (156) Siqueira, E. J. Polyamideamine Epichlorohydrin-Based Papers: Mechanisms of Wet Strength Development and Paper Repulping, Universite de Grenoble, 2014. <https://doi.org/tel-00952991>.
- (157) Chattopadhyay, S.; Keul, H.; Moeller, M. Synthesis of Azetidinium-Functionalized Polymers Using a Piperazine Based Coupler. *Macromolecules* **2013**, 46 (3), 638–646. <https://doi.org/10.1021/ma302008s>.

- (158) Lionetto, F.; Del Sole, R.; Cannoletta, D.; Vasapollo, G.; Maffezzoli, A. Monitoring Wood Degradation during Weathering by Cellulose Crystallinity. *Materials (Basel)*. **2012**, *5* (10), 1910–1922. <https://doi.org/10.3390/ma5101910>.
- (159) Colom, X.; Carrillo, F.; Nogués, F.; Garriga, P. Structural Analysis of Photodegraded Wood by Means of FTIR Spectroscopy. *Polym. Degrad. Stab.* **2003**, *80* (3), 543–549. [https://doi.org/10.1016/S0141-3910\(03\)00051-X](https://doi.org/10.1016/S0141-3910(03)00051-X).
- (160) Ku, H.; Wang, H.; Pattarachaiyakoo, N.; Trada, M. A Review on the Tensile Properties of Natural Fiber Reinforced Polymer Composites. *Compos. Part B Eng.* **2011**, *42* (4), 856–873. <https://doi.org/10.1016/j.compositesb.2011.01.010>.
- (161) Herrera-Franco, P. J.; Valadez-González, A. A Study of the Mechanical Properties of Short Natural-Fiber Reinforced Composites. *Compos. Part B Eng.* **2005**, *36* (8), 597–608. <https://doi.org/10.1016/j.compositesb.2005.04.001>.
- (162) Mallick, P. . *Fiber-Reinforced Composites Materials, Manufacturing and Design*; CRC Press, 2007.
- (163) Lieder, M.; Rashid, A. Towards Circular Economy Implementation: A Comprehensive Review in Context of Manufacturing Industry. *J. Clean. Prod.* **2016**, *115*, 36–51. <https://doi.org/10.1016/j.jclepro.2015.12.042>.
- (164) Li, M.; Pu, Y.; Thomas, V. M.; Yoo, C. G.; Ozcan, S.; Deng, Y.; Nelson, K.; Ragauskas, A. J. Recent Advancements of Plant-Based Natural Fiber–Reinforced Composites and Their Applications. *Compos. Part B Eng.* **2020**, *200* (August). <https://doi.org/10.1016/j.compositesb.2020.108254>.
- (165) Sela, N.; Ishai, O. Interlaminar Fracture Toughness and Toughening of Laminated Composite Materials: A Review. *Composites* **1989**, *20* (5), 423–435. [https://doi.org/10.1016/0010-4361\(89\)90211-5](https://doi.org/10.1016/0010-4361(89)90211-5).
- (166) Russo, C. J.; Harmer, M. P.; Chan, H. M.; Miller, G. A. Design of a Laminated Ceramic Composite for Improved Strength and Toughness. *J. Am. Ceram. Soc.* **1992**, *75* (12), 3396–3400. <https://doi.org/10.1111/j.1151-2916.1992.tb04440.x>.
- (167) Cantwell, W. J.; Morton, J. The Impact Resistance of Composite Materials - a Review. *Composites* **1991**, *22* (5), 347–362. [https://doi.org/10.1016/0010-4361\(91\)90549-V](https://doi.org/10.1016/0010-4361(91)90549-V).

- (168) Aji, I. S.; Zainudin, E. S.; Khalina, A.; Sapuan, S. M.; Khairul, M. D. Studying the Effect of Fiber Size and Fiber Loading on the Mechanical Properties of Hybridized Kenaf/PALF-Reinforced HDPE Composite. *J. Reinf. Plast. Compos.* **2011**, *30* (6), 546–553. <https://doi.org/10.1177/0731684411399141>.
- (169) Rasheed, A.; Howe, J. Y.; Dadmun, M. D.; Britt, P. F. The Efficiency of the Oxidation of Carbon Nanofibers with Various Oxidizing Agents. *Carbon N. Y.* **2007**, *45* (5), 1072–1080. <https://doi.org/10.1016/j.carbon.2006.12.010>.
- (170) Yu, J.; Meng, L.; Fan, D.; Zhang, C.; Yu, F.; Huang, Y. The Oxidation of Carbon Fibers through K₂S₂O₈/AgNO₃ System That Preserves Fiber Tensile Strength. *Compos. Part B Eng.* **2014**, *60*, 261–267. <https://doi.org/10.1016/J.COMPOSITESB.2013.12.037>.
- (171) Mashudi; Wicaksono, S. T.; Ardhyanta, H. Effect of Surfactants on Carbon Fiber Dispersion of Cement Carbon Fiber Reinforced Composite for Self-Monitoring Applications. *AIP Conf. Proc.* **2018**, *2014* (September), 1–7. <https://doi.org/10.1063/1.5054515>.
- (172) Pozegic, T. R.; Huntley, S.; Longana, M. L.; He, S.; Bandara, R. M. I.; King, S. G.; Hamerton, I. Improving Dispersion of Recycled Discontinuous Carbon Fibres to Increase Fibre Throughput in the HiPerDiF Process. *Materials (Basel)*. **2020**, *13* (7). <https://doi.org/10.3390/ma13071544>.
- (173) Drzal, L. T. The Role of the Fiber-Matrix Interphase on Composite Properties. *Vacuum* **1990**, *41* (7–9), 1615–1618. [https://doi.org/10.1016/0042-207X\(90\)94034-N](https://doi.org/10.1016/0042-207X(90)94034-N).
- (174) Li, S.; Cui, C.; Hou, H.; Wu, Q.; Zhang, S. The Effect of Hyperbranched Polyester and Zirconium Slag Nanoparticles on the Impact Resistance of Epoxy Resin Thermosets. *Compos. Part B Eng.* **2015**, *79*, 342–350. <https://doi.org/10.1016/j.compositesb.2015.04.048>.
- (175) Li, S.; Cui, H.; Hou, H. Synthesis of Core–Shell Particles Based on Hyperbranched Polyester and Zirconium Slag Nanoparticles and Its Influence on the Impact Resistance of Epoxy Resin Thermosets. *Polym. Compos.* **2017**, *38* (3), 441–451. <https://doi.org/10.1002/pc.23602>.
- (176) Reale Batista, M. D.; Drzal, L. T. Carbon Fiber/Epoxy Matrix Composite Interphases Modified with Cellulose Nanocrystals. *Compos. Sci. Technol.* **2018**, *164* (December 2017), 274–281. <https://doi.org/10.1016/j.compscitech.2018.05.010>.

PUBLICATIONS

- **El Awad Azrak, S.M.**, Clarkson C. M., Moon R. J., Schueneman G. T., and Youngblood J. P.; Wet-Stacking Lamination of Multilayer Mechanically Fibrillated Cellulose Nanofibril (CNF) Sheets with Increased Mechanical Performance for Use in High-Strength and Lightweight Structural and Packaging Applications. ACS Applied Polymer Materials 2019 1 (9), 2525-2534, <https://doi.org/10.1021/acsapm.9b00635>.
- **El Awad Azrak, S.M.**, Costakis W. J., Moon R. J., Schueneman G. T., and Youngblood J. P.; Continuous Processing of Cellulose Nanofibril (CNF) Sheets Through Conventional Single-Screw Extrusion. ACS Applied Polymer Materials. 2020 2 (8), 3365–3377, <https://doi.org/10.1021/acsapm.0c00477>
- **El Awad Azrak, S.M.**, Gohl J. A., Moon R. J., Davis C. S., Schueneman G. T., and Youngblood J. P.; Controlled Dispersion and Setting of Cellulose Nanofibril (CNF) - Carboxymethyl Cellulose (CMC) Pastes. (*Manuscript submitted to Cellulose and is under review, March 2021)
- Clarkson, C. M.; **El Awad Azrak, S.M.**; Forti, E. S.; Schueneman, G. T.; Moon, R. J.; Youngblood, J. P. Progress Report on Recent Developments in Cellulose Nanomaterial Composites. Advanced Materials 2020, 2000718, 14–17. <https://doi.org/10.1002/adma.202000718>
- Clarkson, C. M.; **El Awad Azrak, S. M.**; Schueneman, G. T.; Snyder, J. F.; Youngblood, J. P. Crystallization Kinetics and Morphology of Small Concentrations of Cellulose Nanofibrils (CNFs) and Cellulose Nanocrystals (CNCs) Melt-Compounded into Poly(Lactic Acid) (PLA) with Plasticizer. Polymer. 2020, 187 (October 2019), 122101. <https://doi.org/10.1016/j.polymer.2019.122101>.
- Clarkson, C. M.; **El Awad Azrak, S. M.**; Chowdhury, R.; Shuvo, S. N.; Snyder, J.; Schueneman, G.; Ortalan, V.; Youngblood, J. P. Melt Spinning of Cellulose Nanofibril/Poly(lactic Acid) (CNF/PLA) Composite Fibers for High Stiffness. ACS Appl. Polym. Mater. 2019, acsapm.8b00030. <https://doi.org/10.1021/acsapm.8b00030>.

- Forti E. S., **El Awad Azrak, S. M.**, Ng X. Y., Moon R. J., Schueneman G. T., and Youngblood J. P.; Mechanical Enhancement of Cellulose Nanofibril (CNF) Films Through the Addition of Water-soluble Polymers. (*Under review in Cellulose, temporary DOI: 10.21203/rs.3.rs-162652/v1).
- Rencheck, M. L.; Weiss, A. J.; **El Awad Azrak, S. M.**; Forti, E. S.; Nuruddin, M.; Youngblood, J. P.; Davis, C. S. Nanocellulose Film Modulus Determination via Buckling Mechanics Approaches. ACS Appl. Polym. Mater. 2020, 2 (2), 578–584. <https://doi.org/10.1021/acsapm.9b00969>.
- Chowdhury, R. A.; Clarkson, C. M.; Shrestha, S.; **El Awad Azrak, S. M.**; Mavlan, M.; Youngblood, J. P. High-Performance Waterborne Polyurethane Coating Based on a Blocked Isocyanate with Cellulose Nanocrystals (CNC) as the Polyol. ACS Appl. Polym. Mater. 2020, 2 (2), 385–393. <https://doi.org/10.1021/acsapm.9b00849>.